

**A Showcase of Functional Fluorous Materials  
and Their Applications**

by

Kosuke Yoshinaga

B. Eng. in Chemistry and Biotechnology  
The University of Tokyo, 2012

Submitted to the Department of Chemistry  
in Partial Fulfillment of the Requirements for the Degree of

DOCTOR OF PHILOSOPHY IN CHEMISTRY  
at the  
MASSACHUSETTS INSTITUTE OF TECHNOLOGY

September 2021

© 2021, Massachusetts Institute of Technology. All Rights Reserved.

Signature of Author.....  
Department of Chemistry  
August 13, 2021

Certified by: .....  
Timothy M. Swager  
John D. MacArthur Professor  
Thesis Supervisor

Accepted by: .....  
Adam Willard  
Associate Professor  
Graduate Officer





## SIGNATURE PAGE

This doctoral thesis has been examined by a committee of the  
Department of Chemistry as follows:

Professor Jeremiah A. Johnson.....  
Thesis Committee Chair  
Professor of Chemistry

Professor Timothy M. Swager.....  
Thesis Supervisor  
John D. MacArthur Professor of Chemistry

Professor Bradley D. Olsen.....  
Thesis Committee Member  
Professor of Chemical Engineering

# **DEDICATION**

*For my family, and Anna*

# **A Showcase of Functional Fluorous Materials and Their Applications**

by

Kosuke Yoshinaga

Submitted to the Department of Chemistry in September 2021  
in Partial Fulfillment of the Requirements for the Degree of  
Doctor of Philosophy in Chemistry

## **ABSTRACT**

This thesis highlights conjugated organic materials functionalized with fluoroalkyl chains and explores their applications in material chemistry. In Chapter 1, we begin with a brief introduction of incorporation of fluorine into materials and its effect on materials properties. An introduction to dynamically reconfigurable complex emulsions reported by our group and their applications in sensing is also provided. In Chapter 2, we disclose the synthesis and photophysical properties of “fluorofluorescent” perylene bisimides, where fluoro- refers to both fluorine and fluorescence. These perylene bisimides were utilized to realize the concept of a fluorofluorescent solar concentrator. In Chapter 3, we report the synthesis and photophysical properties of fluorous phthalocyanines and subphthalocyanines. We then explored these molecules’ Faraday rotation properties in organic and fluorous solvents. In Chapter 4, we describe the applications of the perylene bisimide and subphthalocyanine dyes by incorporating them into fluorescent Janus emulsions. We also report the synthesis of fluorous soluble black hole quencher dyes, which were found to be more absorptive than fluorous soluble subphthalocyanines. The emulsions were engineered to function as biosensors for the detection of Salmonella, Zika virus, Listeria, and anti-SARS-CoV-2 spike antibody. In Chapter 5, we report the utilization of the Heck reaction for facile access to functional fluorous materials. We also showcase how this fluoroalkenyl side chain turns out to be an important functional group for lithium primary batteries.

Thesis Supervisor: Timothy M. Swager  
Title: John D. MacArthur Professor of Chemistry

## TABLE OF CONTENTS

	Page
<b>Title Page</b> .....	<b>- 1 -</b>
<b>Signature Page</b> .....	<b>- 3 -</b>
<b>Dedication</b> .....	<b>- 4 -</b>
<b>Abstract</b> .....	<b>- 5 -</b>
<b>List of Figures</b> .....	<b>- 9 -</b>
<b>List of Schemes</b> .....	<b>- 24 -</b>
<b>List of Tables</b> .....	<b>- 26 -</b>
<b>List of Equations</b> .....	<b>- 27 -</b>
<b>CHAPTER 1: Introduction and Background</b> .....	<b>- 28 -</b>
1.1 Abstract .....	- 29 -
1.2 Introduction .....	- 29 -
1.3 Incorporation of Fluorine in Conjugated Organic Materials.....	- 30 -
1.4 “Fluorous” Chemistry and Fluorous Partition.....	- 31 -
1.5 Fluorescence and Fluorofluorescent Molecules.....	- 35 -
1.6 Dynamically Reconfigurable Complex Emulsions .....	- 37 -
<b>CHAPTER 2: Synthesis of Fluorofluorescent Perylene Bisimides: Applications in Luminescent Solar Concentrators</b> .....	<b>- 40 -</b>
2.1 Abstract .....	- 41 -
2.2 Introduction .....	- 41 -
2.3 Results and Discussion.....	- 43 -
2.3.1 Synthesis of FF-PBI-1 .....	- 43 -
2.3.2 Properties of FF-PBI-1 .....	- 45 -
2.3.3 Synthesis of FF-PBI-2 .....	- 50 -

2.3.4 Properties of FF-PBI-2 .....	- 52 -
2.3.5 Luminescent Solar Concentrators .....	- 55 -
2.4 Conclusions .....	- 58 -
2.5 Experimental .....	- 58 -
2.5.1 General .....	- 58 -
2.5.2 Synthetic Procedures .....	- 59 -
2.6 Appendix for CHAPTER 2 .....	- 69 -

**CHAPTER 3: Synthesis of Fluorous Phthalocyanines and Subphthalocyanines: Applications in Faraday Rotation .....** - 81 -

3.1 Abstract .....	- 82 -
3.2 Introduction .....	- 82 -
3.3 Results and Discussion.....	- 84 -
3.3.1 Synthesis of F-PCs .....	- 84 -
3.3.2 Properties of F-PCs .....	- 84 -
3.3.3 Synthesis of F-SubPCs .....	- 87 -
3.3.4 Properties of F-SubPCs .....	- 88 -
3.3.5 Faraday Rotation Properties of F-PCs and F-SubPCs.....	- 90 -
3.4 Conclusions .....	- 94 -
3.5 Experimental .....	- 94 -
3.5.1 General .....	- 94 -
3.5.2 Synthetic Procedures .....	- 96 -
3.6 Appendix for CHAPTER 3 .....	- 104 -
3.6.1 Instrumental Setup for Faraday Rotation Measurement.....	- 105 -

**CHAPTER 4: Adding Color to Dynamically Reconfigurable Complex Emulsions .....** - 117 -

4.1 Abstract .....	- 118 -
4.2 Introduction .....	- 118 -
4.3 Results and Discussion.....	- 122 -
4.3.1 Combination of Perylene and FF-PBI-2 in Emulsions.....	- 123 -
4.3.2 Combination of SubPC and FF-PBI-2 in Emulsions .....	- 127 -
4.3.3 Combination of Lumogen F Orange 240 and F-SubPC-1 in Emulsions.....	- 132 -

4.3.4 Synthesis of F-BHQs.....	- 135 -
4.3.5 Combination of Lumogen F Orange 240 and F-BHQ-2 in Emulsions .....	- 138 -
4.4 Conclusions .....	- 141 -
4.5 Experimental .....	- 142 -
4.5.1 General .....	- 142 -
4.5.2 Synthetic Procedures .....	- 144 -
4.6 Appendix for CHAPTER 4 .....	- 149 -
<b>CHAPTER 5: Revisiting the Heck Reaction for Fluorous Materials Applications.....</b>	<b>- 157 -</b>
5.1 Abstract .....	- 158 -
5.2 Introduction .....	- 158 -
5.3 Results and Discussion.....	- 160 -
5.3.1 Heck Reaction: Substrate Scope.....	- 160 -
5.3.2 Brominations of FAA-Functionalized Thiophenes .....	- 162 -
5.3.3 Synthesis and Properties of FAA-Functionalized Terthiophenes .....	- 163 -
5.3.4 Synthesis and Properties of FAA-Functionalized Polythiophenes.....	- 165 -
5.3.5 Synthesis and Properties of Fluorous-Soluble Polythiophenes.....	- 166 -
5.3.6 Fluorous Aromatics in Lithium Primary Batteries .....	- 169 -
5.3.7 Synthesis of Fluorous Aromatics .....	- 171 -
5.3.8 Discharge Profiles of Fluorous Aromatics in Lithium Primary Batteries .....	- 173 -
5.4 Conclusions .....	- 178 -
5.5 Experimental .....	- 179 -
5.5.1 General .....	- 179 -
5.5.2 Synthetic Procedures .....	- 182 -
5.6 Appendix for CHAPTER 5 .....	- 206 -
<b>References.....</b>	<b>- 253 -</b>
<b>Curriculum Vitae.....</b>	<b>- 264 -</b>
<b>ACKNOWLEDGMENTS .....</b>	<b>- 267 -</b>

## List of Figures

Figure	Page
<b>Figure 1.1</b> General schematic image of a fluorous biphasic reaction system. ....	<b>32 -</b>
<b>Figure 1.2</b> Summary of representative examples of highly fluorinated polymers. (a) Chemical structure of semifluorinated polyquaterthiophene (SFA-PQT). <sup>11</sup> (b) Image of an inverter using orthogonal patterning. <sup>11</sup> (c) Schematic procedure for an orthogonally hydrophobic patterned complementary inverter consisting of SFA-PQT and ActivInk N2200 (P(NDI2OD-T2)) layers. Figures adapted with permission. <sup>11</sup> Copyright © 2013, John Wiley and Sons. (d) Chemical structure of fluorinated polyfluorene and an image of orthogonally patterned light-emitting pixels. Figure adapted with permission. <sup>12</sup> Copyright © 2010, American Chemical Society. ....	<b>34 -</b>
<b>Figure 1.3</b> A Jablonski diagram describing the photochemical processes. ....	<b>36 -</b>
<b>Figure 1.4</b> Examples of fluorous soluble conjugated materials from the Swager group. (a) Chemical structure of a fluorous soluble polyphenylene ethynylene and an image of an emulsion containing the polymer. Figure adapted with permission. <sup>13</sup> Copyright © 2010, John Wiley and Sons. (b) Chemical structure of a fluorous soluble n-type semiconducting polymer with air stability. Figure adapted with permission. <sup>14</sup> Copyright © 2012, John Wiley and Sons. (c) Synthesis of a panel of “fluorofluorophores” from a common aminophenol precursor. Various fluorous emulsions containing the fluorofluorophores could be obtained. Figure adapted with permission. <sup>15</sup> Copyright © 2014, American Chemical Society. ....	<b>37 -</b>
<b>Figure 1.5</b> (a) Fabrication of the complex emulsion. The hydrocarbon phase contains Nile Red. Figure adapted with permission. <sup>16</sup> Copyright © 2015, Springer Nature. (b) Chemical structures of typical hydrocarbon and fluorocarbon surfactants. (c) Schematic image of the emulsions undergoing reversible morphology change. ....	<b>39 -</b>
<b>Figure 2.1</b> Chemical structures of fluorofluorescent PBIs in this report. Figure adapted with permission. <sup>36</sup> Copyright © 2018, Georg Thieme Verlag KG. ....	<b>43 -</b>

**Figure 2.2** (a) Synthetic scheme of **FF-PBI-1'**. (b) Photographs of **FF-PBI-1'** (0.5 mg) in CH<sub>2</sub>Cl<sub>2</sub> (0.5 mL) and C<sub>6</sub>F<sub>14</sub> (0.5 mL), and after adding TFA. .... - 45 -

**Figure 2.3** Demonstration of solubility of **FF-PBI-1** and its response to TFA under ambient light (left) and UV light (right,  $\lambda_{\text{ex}} = 365$  nm). (a) Photographs of **FF-PBI-1** (0.5 mg) in CH<sub>2</sub>Cl<sub>2</sub> (0.5 mL), (b) after adding C<sub>6</sub>F<sub>14</sub> (0.5 mL), and (c) after adding TFA. (d) Photographs of the heterogeneous mixture of **FF-PBI-1** (1.0 mg) and C<sub>6</sub>F<sub>14</sub> (1.0 mL) and (e) the sample after adding TFA. Figure adapted with permission.<sup>36</sup> Copyright © 2018, Georg Thieme Verlag KG. .... - 47 -

**Figure 2.4** Photophysical properties of **FF-PBI-1**. (a) Absorbance spectra and (b) relative fluorescence (FL) spectra ( $\lambda_{\text{ex}} = 500$  nm) of **FF-PBI-1** in CH<sub>2</sub>Cl<sub>2</sub> at different concentrations of TFA. Inset: Fluorescence intensity at 584 nm at different concentrations of TFA. Black arrows indicate spectral change with increasing concentration of TFA. Figure adapted with permission.<sup>36</sup> Copyright © 2018, Georg Thieme Verlag KG. .... - 49 -

**Figure 2.5** Photographs of **FF-PBI-2** under ambient light (left) and UV light (right,  $\lambda_{\text{ex}} = 365$  nm). (a) Photographs of **FF-PBI-2** (0.5 mg) in CH<sub>2</sub>Cl<sub>2</sub> (0.5 mL). (b) Photographs of the sample after adding C<sub>6</sub>F<sub>14</sub> (0.5 mL). Figure adapted with permission.<sup>36</sup> Copyright © 2018, Georg Thieme Verlag KG. .... - 52 -

**Figure 2.6** Chemical structures of the **FF-PBI-2** series and their solubilities. A check (✓) indicates the molecule is soluble in the respective solvent. .... - 53 -

**Figure 2.7** Photophysical properties of **FF-PBI-2** in C<sub>6</sub>F<sub>14</sub> and CH<sub>2</sub>Cl<sub>2</sub>. (a) Absorbance spectra and (b) relative fluorescence spectra ( $\lambda_{\text{ex}} = 500$  nm) of samples at different concentrations in C<sub>6</sub>F<sub>14</sub>. (c) Absorbance spectra and (d) relative fluorescence spectra ( $\lambda_{\text{ex}} = 500$  nm) of samples at different concentrations in CH<sub>2</sub>Cl<sub>2</sub>. Black arrows indicate spectral change with increasing concentration. Figure adapted with permission.<sup>36</sup> Copyright © 2018, Georg Thieme Verlag KG. .... - 54 -

**Figure 2.8** (a) Schematic diagram of building-integrated photovoltaics, and (b) loss mechanisms of luminescent solar concentrators. .... - 56 -



<b>Figure 2.9</b> Device architecture and external quantum efficiency experimental setup. (a) Dimensions of the fabricated PMMA device. (b) A picture of the device in ambient environment. (c) Schematic representation of the edge emission measurement. (d) Absorbance and EQE spectra of the device. ....	- 57 -
<b>Figure 2.10</b> Normalized absorbance and fluorescence spectra of <b>FF-PBI-1</b> in CH <sub>2</sub> Cl <sub>2</sub> + TFA and C <sub>6</sub> F <sub>14</sub> + TFA. ....	- 69 -
<b>Figure 2.11</b> Normalized absorbance and fluorescence spectra of <b>FF-PBI-1</b> in CH <sub>2</sub> Cl <sub>2</sub> and its change upon addition of TFA and Et <sub>3</sub> N.....	- 69 -
<b>Figure 2.12</b> Quantum yield ( $\Phi_F$ ) of <b>FF-PBI-2</b> in CH <sub>2</sub> Cl <sub>2</sub> and C <sub>6</sub> F <sub>14</sub> at different concentrations. $\Phi_F$ was determined by using an integrating sphere. The error bars represent values of $\Phi_F$ measured at three different excitation wavelengths. ....	- 70 -
<b>Figure 2.13</b> Compound <b>FF-PBI-1</b> <sup>1</sup> H NMR (500 MHz, CD <sub>2</sub> Cl <sub>2</sub> , 25 °C).....	- 70 -
<b>Figure 2.14</b> Compound <b>FF-PBI-1</b> <sup>19</sup> F NMR (470 MHz, CD <sub>2</sub> Cl <sub>2</sub> , 25 °C) .....	- 71 -
<b>Figure 2.15</b> Compound <b>5</b> <sup>1</sup> H NMR (500 MHz, CDCl <sub>3</sub> , 25 °C) .....	- 71 -
<b>Figure 2.16</b> Compound <b>5</b> <sup>13</sup> C NMR (125 MHz, CDCl <sub>3</sub> , 25 °C) .....	- 72 -
<b>Figure 2.17</b> Compound <b>FF-PBI-2</b> <sup>1</sup> H NMR (500 MHz, CD <sub>2</sub> Cl <sub>2</sub> , 25 °C).....	- 72 -
<b>Figure 2.18</b> Compound <b>FF-PBI-2</b> <sup>19</sup> F NMR (470 MHz, CD <sub>2</sub> Cl <sub>2</sub> , 25 °C) .....	- 73 -
<b>Figure 2.19</b> Compound <b>FF-PBI-2</b> COSY NMR (500 MHz, CD <sub>2</sub> Cl <sub>2</sub> , 25 °C) .....	- 73 -
<b>Figure 2.20</b> Compound <b>6</b> <sup>1</sup> H NMR (500 MHz, CDCl <sub>3</sub> , 25 °C) .....	- 74 -
<b>Figure 2.21</b> Compound <b>6</b> HRMS (ESI) .....	- 74 -
<b>Figure 2.22</b> Single crystal X-ray structure of compound <b>6</b> . Hydrogen atoms and solvent atoms are omitted for clarity. ....	- 75 -
<b>Figure 2.23</b> Compound <b>7</b> <sup>1</sup> H NMR (500 MHz, CDCl <sub>3</sub> , 25 °C) .....	- 76 -

<b>Figure 2.24</b> Compound <b>7</b> $^{19}\text{F}$ NMR (470 MHz, $\text{CDCl}_3$ , 25 °C).....	- 76 -
<b>Figure 2.25</b> Compound <b>FF-PBI-2'</b> $^1\text{H}$ NMR (500 MHz, $\text{CDCl}_3$ , 25 °C).....	- 77 -
<b>Figure 2.26</b> Compound <b>FF-PBI-2'</b> $^{19}\text{F}$ NMR (471 MHz, $\text{CDCl}_3$ , 25 °C) .....	- 77 -
<b>Figure 2.27</b> Compound <b>8</b> $^1\text{H}$ NMR (500 MHz, $\text{CD}_2\text{Cl}_2$ , 25 °C).....	- 78 -
<b>Figure 2.28</b> Compound <b>8</b> HRMS (ESI) .....	- 78 -
<b>Figure 2.29</b> Compound <b>FF-PBI-2''</b> $^1\text{H}$ NMR (500 MHz, $\text{CDCl}_3$ , 25 °C) .....	- 79 -
<b>Figure 2.30</b> Compound <b>FF-PBI-2''</b> $^{19}\text{F}$ NMR (471 MHz, $\text{CDCl}_3$ , 25 °C).....	- 79 -
<b>Figure 3.1</b> Chemical structure and fluorous partition of (a) <b>F-PC-1</b> , (b) <b>F-PC-2</b> , and (c) <b>F-PC-3</b> . Figure adapted with permission. <sup>77</sup> Copyright © 2020, World Scientific Publishing. ....	- 85 -
<b>Figure 3.2</b> Overlaid normalized absorbance spectra of (a) <b>F-PC-1</b> , (b) <b>F-PC-2</b> , and (c) <b>F-PC-3</b> in organic solvent THF and in fluorous solvent HFE-7500. Spectra for <b>F-PC-1</b> obtained by heating the solutions to their boiling temperatures (66 °C for THF, 128 °C for HFE-7500). Figure adapted with permission. <sup>77</sup> Copyright © 2020, World Scientific Publishing. ....	- 86 -
<b>Figure 3.3</b> Chemical structure and fluorous partition of (a) <b>F-SubPC-1</b> , (b) <b>F-SubPC-2</b> , and (c) <b>F-SubPC-3</b> . Absorbance and emission spectra of (d) <b>F-SubPC-1</b> , (e) <b>F-SubPC-2</b> , and (f) <b>F-SubPC-3</b> . Scheme adapted with permission. <sup>77</sup> Copyright © 2020, World Scientific Publishing.....	- 90 -
<b>Figure 3.4</b> Schematic image of magneto-optical material displaying a Faraday rotation. The degree of rotation ( $\theta$ ) is governed by the materials' Verdet Constant ( <b>V</b> ), strength of magnetic field ( <b>B</b> ), and the thickness of the material ( <b>d</b> ). Scheme adapted with permission. <sup>77</sup> Copyright © 2020, World Scientific Publishing. ....	- 91 -
<b>Figure 3.5</b> Faraday rotation properties of <b>F-PCs</b> and <b>F-SubPCs</b> . Molar specific magnetic rotation of (a) <b>F-PC-2</b> and (b) <b>F-PC-3</b> in THF. Molar specific magnetic rotation of (c) <b>F-SubPC-1</b> and (d) <b>F-SubPC-2</b> in PFMCH. Molar specific magnetic rotation of (e) <b>F-SubPC-2</b> and (f) <b>F-SubPC-3</b>	

in PhMe. Spectra for **F-PC-1** obtained by heating the solution to its boiling temperature (66 °C). Scheme adapted with permission.<sup>77</sup> Copyright © 2020, World Scientific Publishing. .... - 93 -

**Figure 3.6** (a) Chemical structure of **F-PC-1**. (b) Fluorous partition of **F-PC-1** in DEB and HFE-7500 (left), and observation of precipitates after a few hours (right). (c) UV/Vis absorbance spectra of a heated solution of **F-PC-1** in HFE-7500 (red) and the same cooled solution (blue)..... - 104 -

**Figure 3.7** (a) Chemical structure of **F-SubPC-1** and its fluorous partition in diethylbenzene (DEB) and HFE-7500. (b) UV/Vis absorbance and fluorescence spectra of **F-SubPC-1** (solvent: HFE-7500). (c) Chemical structure of **F-SubPC-2** and its fluorous partition in DEB and HFE-7500. (d) Chemical structure of **F-SubPC-3** and its fluorous partition in DEB and HFE-7500..... - 104 -

**Figure 3.8** FT-IR spectra of (a) **F-PC-1**, (b) **F-PC-2**, (c) **F-PC-3**, (d) **F-SubPC-1**, (e) **F-SubPC-2**, and (f) **F-SubPC-3**. F-SubPCs were deposited on KBr pellets. .... - 105 -

**Figure 3.9** Schematic of the instrument for Faraday rotation measurement. .... - 106 -

**Figure 3.10** Compound **3** <sup>1</sup>H NMR (500 MHz, acetone-*d*<sub>6</sub>, 25 °C) ..... - 107 -

**Figure 3.11** Compound **3** <sup>13</sup>C NMR (126 MHz, acetone-*d*<sub>6</sub>, 25 °C) ..... - 107 -

**Figure 3.12** Compound **3** <sup>19</sup>F NMR (471 MHz, acetone-*d*<sub>6</sub>, 25 °C) ..... - 108 -

**Figure 3.13** Compound **3** DART MS..... - 108 -

**Figure 3.14** **F-PC-2** MALDI TOF-MS spectra..... - 109 -

**Figure 3.15** **F-PC-3** MALDI TOF-MS spectra..... - 110 -

**Figure 3.16** **F-SubPC-1** MALDI TOF-MS spectra ..... - 111 -

**Figure 3.17** **F-SubPC-2** <sup>1</sup>H NMR (500 MHz, CDCl<sub>3</sub>, 25 °C) ..... - 112 -

**Figure 3.18** **F-SubPC-2** <sup>19</sup>F NMR (476 MHz, CDCl<sub>3</sub>, 25 °C) ..... - 112 -

**Figure 3.19** **F-SubPC-2** MALDI TOF-MS spectra ..... - 113 -

**Figure 3.20 F-SubPC-3**  $^1\text{H}$  NMR (500 MHz,  $\text{CDCl}_3$ , 25 °C)..... - 114 -

**Figure 3.21 F-SubPC-3**  $^{19}\text{F}$  NMR (476 MHz,  $\text{CDCl}_3$ , 25 °C) ..... - 114 -

**Figure 3.22 F-SubPC-3** MALDI TOF-MS spectra ..... - 115 -

**Figure 3.23** MALDI TOF-MS isotope distribution comparisons of (a) **F-PC-2**, (b) **F-PC-3**, (c) **F-SubPC-1**, (d) **F-SubPC-2**, and (e) **F-SubPC-3**, with their respective simulated mass spectra. MALDI TOF-MS spectra could not be obtained for **F-PC-1**, presumably due to aggregation..... - 116 -

**Figure 4.1** (a) Fabrication of the complex emulsion. The hydrocarbon phase contains Nile Red. Figure adapted with permission.<sup>16</sup> Copyright © 2015, Springer Nature. (b) Chemical structures of typical hydrocarbon and fluorocarbon surfactants. (c) Schematic image of the emulsions undergoing reversible morphology change..... - 120 -

**Figure 4.2** Janus emulsions for the detection of ConA. (a) Chemical structure of the surfactants to fabricate the Janus emulsions and an illustration of the emulsion. (b) Cartoon and top-view microscope images of the emulsions before and after addition of ConA. (c) QR code placed under the sample for the agglutination detection scheme. The sample becomes opaque upon agglutination, rendering the QR code to be unreadable. Figure adapted with permission.<sup>98</sup> Copyright © 2017, American Chemical Society. .... - 121 -

**Figure 4.3** Chemical structures of dyes discussed in this chapter..... - 123 -

**Figure 4.4** Schematic diagram of the emulsions using the inner filter effect. (a) Diagram of naturally oriented emulsions and its optical path. (b) Diagram of agglutinated emulsions and its optical path. (c) Normalized emission intensity ratio  $I_H/I_F$  in correlation with the concentration of streptavidin. Figure adapted with permission.<sup>99</sup> Copyright © 2019, American Chemical Society..... - 124 -

**Figure 4.5** Intensity distribution around the droplet determined by 2D raytracing for varying emulsion morphologies. Figure adapted with permission.<sup>100</sup> Copyright © 2019, American Chemical Society. .... - 125 -

**Figure 4.6** Conceptual sketch of the mechanism for the detection of *Salmonella enterica* cells using boronic acid-functionalized complex emulsions with reversible assembly of carbohydrate or IgG antibody. (a) Changes in the droplet morphology, induced by reversible assembly of carbohydrates or IgG antibodies at the hydrocarbon (HC, red) water (W) interface and upon removal by competitive binding to *Salmonella* cells. (b) Light-curve: Boronic acid-functionalized emulsions are initialized to yield the highest emission intensity (1); upon reversible binding to carbohydrates or antibodies the emission intensity decreases by up to 60% resulting from the reconfiguration to the Janus morphology (2); the emission intensity transitions back to the high original state upon removal of the carbohydrates or antibodies by *Salmonella* cells (3). (c) Normalized emission intensities of polydisperse droplets containing perylene dye in the hydrocarbon phase ( $\lambda = 475$  nm) and **FF-PBI-2** in the fluorocarbon phase ( $\lambda = 580$  nm). The ratio between the two emissions was used as a ratiometric read-out for the detection of live *Salmonella* bacteria. Figures adapted with permission.<sup>100</sup> Copyright © 2019, American Chemical Society.

.....- 126 -

**Figure 4.7** Photophysical properties of the dyes in solution and in emulsions. (a) Schematic image of the emulsions and the chemical structure of the dyes incorporated in the emulsions. (b) Normalized absorbance and fluorescence spectra of **FF-PBI-2** in HFE-7500, overlaid with absorbance spectra of **SubPC** in DEB. (c) Molar extinction coefficient ratio of **SubPC** ( $\epsilon_H$ ) and **FF-PBI-2** ( $\epsilon_F$ ) plotted against the wavelength. (d) Fluorescence spectra of emulsions containing **FF-PBI-2** in the fluorocarbon phase with and without **SubPC** in the hydrocarbon phase. Figures adapted with permission.<sup>101</sup> Copyright © 2020, National Academy of Sciences. ....- 128 -

**Figure 4.8** (a) Measurement scheme showing excitation and monitoring of the fluorescence coming from the dyed emulsions. (b and c) Confocal microscope image of (b) nonagglutinated emulsion (without addition of *Listeria*) and (c) agglutinated emulsions (with the addition of *Listeria* at 100 CFU/mL), with sub-PC dye in the hydrocarbon phase and F-PBI dye in the fluorocarbon phase. (d) Schematic illustration of agglutinated emulsions. (e) Fluorescence spectra ( $\lambda_{ex} = 361$  nm) of droplet containing Poly-TCO and sub-PC dye in the hydrocarbon phase and F-PBI dye in the fluorocarbon phase after addition of heat-killed *Listeria* at different concentrations. (f) Correlation of concentration of heat-killed *Listeria* and relative fluorescence intensity at 580

nm (three replicate measurements were performed for the error bars,  $**p \leq 0.01$ ). Figures adapted with permission.<sup>101</sup> Copyright © 2020, National Academy of Sciences. ....- 130 -

**Figure 4.9** Detection of anti-SARS-CoV-2 spike antibody. (a) Agglutination scheme of emulsions functionalized with SARS-CoV-2 spike receptor binding domain and Goat Anti-Human IgG antibody. (b) Fluorescence spectra ( $\lambda_{\text{ex}} = 361$  nm) of 1:1 mixture of dye containing fully bioconjugated Janus emulsions with addition of anti-SARS-CoV-2 spike antibody at different concentrations. Note that the fluorescence intensity increases with concentration. (c) Correlation of concentration of anti-SARS-CoV-2 spike antibody and relative fluorescence intensity at 580 nm. All error bars are calculated from three independent experiments ( $n = 3$ ), and  $**$  represent statistical significance ( $**p \leq 0.01$ ). Figures adapted with permission.<sup>102</sup> Copyright © 2021, American Chemical Society. ....- 132 -

**Figure 4.10** (a) Schematic image of the emulsions and the chemical structure of the dyes incorporated in the emulsions. (b) Normalized absorbance and fluorescence spectra of Lumogen Orange in DEB, overlaid with absorbance spectra of **F-SubPC-1** in HFE-7500. (c) Molar extinction coefficient ratio of **F-SubPC-1** ( $\epsilon_{\text{F}}$ ) and Lumogen Orange ( $\epsilon_{\text{H}}$ ) plotted against the wavelength. (d) Fluorescence spectra ( $\lambda_{\text{ex}} = 398$  nm) of emulsions containing Poly-TCO and Lumogen Orange in the hydrocarbon phase and **F-SubPC-1** in the fluorocarbon phase after addition of *Listeria* at different concentrations. (e) Correlation of concentration of *Listeria* and relative fluorescence intensity at 535 nm (three replicate measurements were performed for the error bars,  $**p \leq 0.01$ ). Figures adapted with permission.<sup>101</sup> Copyright © 2020, National Academy of Sciences.....- 134 -

**Figure 4.11** (a) Chemical structure and picture showing fluorous partitioning of **F-BHQ-1**. (b) Chemical structure and picture showing fluorous partitioning of **F-BHQ-2**. (c) Normalized absorbance spectra of **F-BHQ-1** and **F-BHQ-2** in HFE-7500. ....- 138 -

**Figure 4.12** (a) Schematic image of the emulsions and the chemical structure of the dyes incorporated in the emulsions. (b) Normalized absorbance and fluorescence spectra of Lumogen Orange in DEB, overlaid with absorbance spectra of **F-BHQ-2** in HFE-7500. (c) Molar extinction

coefficient ratio of **F-BHQ-2** ( $\epsilon_F$ ) and Lumogen Orange ( $\epsilon_H$ ) plotted against the wavelength. Figures adapted with permission.<sup>102</sup> Copyright © 2021, American Chemical Society. .... - 139 -

**Figure 4.13** (a) Schematic illustrations of the sensing device using the emulsions containing the two dyes. (b) Fluorescence spectra ( $\lambda_{ex} = 400$  nm) of 1:1 mixture of bioconjugated Janus droplets containing of F-BHQ dye in the fluorocarbon phase, P-TCO and Lumogen Orange dye in the hydrocarbon phase, after addition of anti-SARS-CoV-2 spike antibody at different concentrations. (c) Correlation of concentration of anti-SARS-CoV-2 spike antibody and relative fluorescence intensity at 535 nm. All error bars are calculated from three independent experiments ( $n = 3$ ), and \*\* represent statistical significance (\*\* $p \leq 0.01$ ). Figures adapted with permission.<sup>102</sup> Copyright © 2021, American Chemical Society. .... - 141 -

**Figure 4.14** Compound **SubPC**  $^1\text{H}$  NMR (600 MHz, chloroform-*d*, 20 °C)..... - 149 -

**Figure 4.15** Compound **SubPC**  $^{13}\text{C}$  NMR (151 MHz, chloroform-*d*, 20 °C) ..... - 149 -

**Figure 4.16** MALDI-TOF mass spectrometry spectrum of **SubPC** shown in blue. Simulated isotopic distribution for  $\text{C}_{144}\text{H}_{156}\text{BCIN}_6\text{S}_{12}$  shown in red. .... - 150 -

**Figure 4.17** Compound **2**  $^1\text{H}$  NMR (500 MHz,  $\text{CDCl}_3$ , 20 °C) ..... - 150 -

**Figure 4.18** Compound **2**  $^{13}\text{C}$  NMR (126 MHz,  $\text{CDCl}_3$ , 20 °C) ..... - 151 -

**Figure 4.19** Compound **2**  $^{19}\text{F}$  NMR (471 MHz,  $\text{CDCl}_3$ , 20 °C)..... - 151 -

**Figure 4.20** Compound **2** DART MS..... - 152 -

**Figure 4.21** Compound **3**  $^1\text{H}$  NMR (500 MHz, acetone-*d*<sub>6</sub>, 20 °C) ..... - 152 -

**Figure 4.22** Compound **3**  $^{19}\text{F}$  NMR (471 MHz, acetone-*d*<sub>6</sub>, 20 °C) ..... - 153 -

**Figure 4.23** Compound **3** DART MS..... - 153 -

**Figure 4.24** Compound **F-BHQ-2**  $^1\text{H}$  NMR (500 MHz, acetone-*d*<sub>6</sub>, 20 °C) ..... - 154 -

**Figure 4.25** Compound **F-BHQ-2**  $^{19}\text{F}$  NMR (471 MHz, acetone-*d*<sub>6</sub>, 20 °C) ..... - 154 -

**Figure 4.26** Compound **F-BHQ-2** MALDI TOF-MS (Matrix: DCTB) ..... - 155 -

**Figure 4.27** MALDI TOF-MS isotope distribution comparison of **F-BHQ-2**. ..... - 155 -

**Figure 5.1** Summary of perfluoroalkyl precursor installation. (a) Commercially available iodides and thiols. (b) Recent 5-step synthesis of branched perfluoroalkyl chains from perfluorohexyl ethyl iodide.<sup>69</sup> Functional groups besides thiol could be obtained in fewer steps. (c) Commercially available perfluoroalkyl alkenes. The listed prices are obtained from a June 15, 2021 web search.<sup>119</sup> Scheme of the fluororous Heck reaction described in this work. Figure adapted with permission.<sup>120</sup> Copyright © 2021, Georg Thieme Verlag KG. .... - 160 -

**Figure 5.2** (a) Chemical structure and (b) UV/vis absorbance and fluorescence spectra of compounds **11**, **12**, **3T-C<sub>12</sub>**, and **3T** in toluene solution. Excitation wavelength = 330 nm. Figure adapted with permission.<sup>120</sup> Copyright © 2021, Georg Thieme Verlag KG. .... - 165 -

**Figure 5.3** (a) Chemical Structure of **F-PT-1 (100/0)** and **F-PT-2**. (b) Normalized absorbance and fluorescence spectra of **F-PT-1 (100/0)** and **F-PT-2** in HFE-7500 solution. Figure adapted with permission.<sup>120</sup> Copyright © 2021, Georg Thieme Verlag KG. .... - 168 -

**Figure 5.4** Theoretical voltages and cell capacities of Li primary batteries and metal–O<sub>2</sub> and Li–S batteries. Reprinted with permission.<sup>138</sup> Copyright © 2018, American Chemical Society. ... - 170 -

**Figure 5.5** Galvanostatic discharge properties of **Ph-CN–C8(p)**. (a) Galvanostatic discharge profile of **Ph-CN–C8(p)** at 50 °C with varying discharge rate. (b) Scanning electron microscope image of the discharged carbon cathode. (c) Powder X-ray diffraction pattern of the discharged carbon cathode. .... - 174 -

**Figure 5.6** Discharge performance of the synthesized molecules. (a) Chemical structures and the respective computed LUMO values. (b) Galvanostatic discharge profiles of the synthesized molecules. All discharge experiments were performed at 50 °C. (c) Correlation plot of the discharge voltage and the computed LUMO values of the molecules. .... - 176 -

**Figure 5.7** Galvanostatic discharge profile of 0.1 M **Ph-NO<sub>2</sub>–C6(o)** performed at 50 °C. Galvanostatic discharge profile of 1 M **Ph-NO<sub>2</sub>–C6(o)** performed at RT. .... - 177 -



<b>Figure 5.8</b> (a) A Ragone plot comparing the projected discharge performances of Li-fluoroaromatic cells and Li-CF <sub>x</sub> cells at 50 °C. (b) Galvanostatic discharge profile of 1 M Ph-NO <sub>2</sub> -C6(o) performed at 50 °C. ....	- 178 -
<b>Figure 5.9</b> Single crystal X-ray structure and packing of compound 4. (a) ORTEP diagram of compound 4, shown at 50% ellipticity. (b) View along the <i>b</i> axis of the crystal packing. Hydrogen atoms are omitted for clarity. ....	- 206 -
<b>Figure 5.10</b> Fluorous Partition of compounds. Solvents diethylbenzene (DEB) and 2-(trifluoromethyl)-3-ethoxydodecafluorohexane (HFE-7500) were chosen as a result of their low interfacial tension and low upper critical mixing temperature. ....	- 208 -
<b>Figure 5.11</b> Gel Permeation Chromatogram of F-PT-1(25/75) and F-PT-1(50/50). ....	- 208 -
<b>Figure 5.12</b> Cyclic voltammetry of F-PT-1(25/75) and F-PT-1(50/50). ....	- 209 -
<b>Figure 5.13</b> UV/vis absorption and fluorescence spectra of F-PT-1(25/75) and F-PT-1(50/50) in chloroform solution and in film. Films were prepared by dropcasting a chloroform solution of the polymers onto a glass slide. ....	- 209 -
<b>Figure 5.14</b> Wide angle X-ray scattering of F-PT-1(25/75) and F-PT-1(50/50). ....	- 210 -
<b>Figure 5.15</b> Study of photostability of fluorous thiophenes by using fluorescence spectra. Samples were continuously irradiated in the fluorimeter for 120 minutes and the intensity was recorded every 1 minute. Excitation slit width: 14 nm; Emission slit width: 1 nm. ....	- 210 -
<b>Figure 5.16</b> Galvanostatic discharge of control compounds. (a) Galvanostatic discharge profile of (perfluorohexyl)benzene. (b) Galvanostatic discharge profile of 1 <i>H</i> ,1 <i>H</i> ,2 <i>H</i> -perfluoro-1-octene. (c) Galvanostatic discharge profile of a mixture of benzonitrile and 1 <i>H</i> ,1 <i>H</i> ,2 <i>H</i> -perfluoro-1-octene. All discharges were performed at 50 °C. ....	- 211 -
<b>Figure 5.17</b> Galvanostatic discharge profile of 1-Naph-C6 and 2-Naph-C6 performed at 50 °C. ....	- 211 -
<b>Figure 5.18</b> Compound 1 <sup>1</sup> H NMR (500 MHz, CDCl <sub>3</sub> ).....	- 212 -

<b>Figure 5.19</b> Compound <b>1</b> $^{13}\text{C}$ NMR (126 MHz, $\text{CDCl}_3$ ) .....	- 212 -
<b>Figure 5.20</b> Compound <b>1</b> $^{19}\text{F}$ NMR (471 MHz, $\text{CDCl}_3$ ).....	- 213 -
<b>Figure 5.21</b> Compound <b>1</b> DART MS.....	- 213 -
<b>Figure 5.22</b> Compound <b>2</b> $^1\text{H}$ NMR (500 MHz, $\text{CDCl}_3$ ).....	- 214 -
<b>Figure 5.23</b> Compound <b>2</b> $^{19}\text{F}$ NMR (471 MHz, $\text{CDCl}_3$ ).....	- 214 -
<b>Figure 5.24</b> Compound <b>2</b> $^{13}\text{C}$ NMR (126 MHz, $\text{CDCl}_3$ ) .....	- 215 -
<b>Figure 5.25</b> Compound <b>2</b> DART MS.....	- 215 -
<b>Figure 5.26</b> Compound <b>3</b> $^1\text{H}$ NMR (500 MHz, $\text{CDCl}_3$ ).....	- 216 -
<b>Figure 5.27</b> Compound <b>3</b> $^{13}\text{C}$ NMR (126 MHz, $\text{CDCl}_3$ ) .....	- 216 -
<b>Figure 5.28</b> Compound <b>3</b> $^{19}\text{F}$ NMR (471 MHz, $\text{CDCl}_3$ ).....	- 217 -
<b>Figure 5.29</b> Compound <b>3</b> DART MS.....	- 217 -
<b>Figure 5.30</b> Compound <b>4</b> $^1\text{H}$ NMR (500 MHz, $\text{CDCl}_3$ ).....	- 218 -
<b>Figure 5.31</b> Compound <b>4</b> $^{13}\text{C}$ NMR (126 MHz, $\text{CDCl}_3$ ) .....	- 218 -
<b>Figure 5.32</b> Compound <b>4</b> $^{19}\text{F}$ NMR (471 MHz, $\text{CDCl}_3$ ).....	- 219 -
<b>Figure 5.33</b> Compound <b>4</b> DART MS.....	- 219 -
<b>Figure 5.34</b> Compound <b>6</b> $^1\text{H}$ NMR (500 MHz, $\text{CDCl}_3$ ).....	- 220 -
<b>Figure 5.35</b> Compound <b>6</b> $^{13}\text{C}$ NMR (126 MHz, $\text{CDCl}_3$ ) .....	- 220 -
<b>Figure 5.36</b> Compound <b>6</b> $^{19}\text{F}$ NMR (471 MHz, $\text{CDCl}_3$ ).....	- 221 -
<b>Figure 5.37</b> Compound <b>6</b> DART MS.....	- 221 -
<b>Figure 5.38</b> Compound <b>7</b> $^1\text{H}$ NMR (500 MHz, $\text{CDCl}_3$ ).....	- 222 -

<b>Figure 5.39</b> Compound <b>7</b> $^{13}\text{C}$ NMR (126 MHz, $\text{CDCl}_3$ ) .....	- 222 -
<b>Figure 5.40</b> Compound <b>7</b> $^{19}\text{F}$ NMR (471 MHz, $\text{CDCl}_3$ ).....	- 223 -
<b>Figure 5.41</b> Compound <b>7</b> DART MS.....	- 223 -
<b>Figure 5.42</b> Compound <b>8</b> $^1\text{H}$ NMR (500 MHz, $\text{CDCl}_3$ ).....	- 224 -
<b>Figure 5.43</b> Compound <b>8</b> $^{13}\text{C}$ NMR (126 MHz, $\text{CDCl}_3$ ) .....	- 224 -
<b>Figure 5.44</b> Compound <b>8</b> $^{19}\text{F}$ NMR (471 MHz, $\text{CDCl}_3$ ).....	- 225 -
<b>Figure 5.45</b> Compound <b>8</b> DART MS.....	- 225 -
<b>Figure 5.46</b> Compound <b>9</b> $^1\text{H}$ NMR (500 MHz, $\text{CDCl}_3$ ).....	- 226 -
<b>Figure 5.47</b> Compound <b>9</b> $^{13}\text{C}$ NMR (126 MHz, $\text{CDCl}_3$ ) .....	- 226 -
<b>Figure 5.48</b> Compound <b>9</b> $^{19}\text{F}$ NMR (471 MHz, $\text{CDCl}_3$ ).....	- 227 -
<b>Figure 5.49</b> Compound <b>9</b> DART MS.....	- 227 -
<b>Figure 5.50</b> Compound <b>10</b> $^1\text{H}$ NMR (500 MHz, $\text{CDCl}_3$ ).....	- 228 -
<b>Figure 5.51</b> Compound <b>10</b> $^{13}\text{C}$ NMR (126 MHz, $\text{CDCl}_3$ ) .....	- 228 -
<b>Figure 5.52</b> Compound <b>10</b> $^{19}\text{F}$ NMR (471 MHz, $\text{CDCl}_3$ ).....	- 229 -
<b>Figure 5.53</b> Compound <b>10</b> DART MS.....	- 229 -
<b>Figure 5.54</b> Compound <b>11</b> $^1\text{H}$ NMR (500 MHz, $\text{CDCl}_3$ ).....	- 230 -
<b>Figure 5.55</b> Compound <b>11</b> $^{13}\text{C}$ NMR (126 MHz, $\text{CDCl}_3$ ) .....	- 230 -
<b>Figure 5.56</b> Compound <b>11</b> $^{19}\text{F}$ NMR (471 MHz, $\text{CDCl}_3$ ).....	- 231 -
<b>Figure 5.57</b> Compound <b>11</b> DART MS.....	- 231 -
<b>Figure 5.58</b> Compound <b>12</b> $^1\text{H}$ NMR (500 MHz, $\text{CDCl}_3$ ).....	- 232 -

<b>Figure 5.59</b> Compound <b>12</b> $^{13}\text{C}$ NMR (126 MHz, $\text{CDCl}_3$ ) .....	- 232 -
<b>Figure 5.60</b> Compound <b>12</b> $^{19}\text{F}$ NMR (471 MHz, $\text{CDCl}_3$ ).....	- 233 -
<b>Figure 5.61</b> Compound <b>12</b> DART MS.....	- 233 -
<b>Figure 5.62</b> <b>F-PT-1(25/75)</b> $^1\text{H}$ NMR (500 MHz, $\text{CDCl}_3$ ) .....	- 234 -
<b>Figure 5.63</b> <b>F-PT-1(25/75)</b> $^{19}\text{F}$ NMR (471 MHz, $\text{CDCl}_3$ ).....	- 234 -
<b>Figure 5.64</b> <b>F-PT-1(50/50)</b> $^1\text{H}$ NMR (500 MHz, $\text{CDCl}_3$ ) .....	- 235 -
<b>Figure 5.65</b> <b>F-PT-1(50/50)</b> $^{19}\text{F}$ NMR (471 MHz, $\text{CDCl}_3$ ).....	- 235 -
<b>Figure 5.66</b> Compound <b>Py-C6</b> $^1\text{H}$ NMR (500 MHz, $\text{CDCl}_3$ , 20 °C).....	- 236 -
<b>Figure 5.67</b> Compound <b>Py-C6</b> $^{13}\text{C}$ NMR (126 MHz, $\text{CDCl}_3$ , 20 °C) .....	- 236 -
<b>Figure 5.68</b> Compound <b>Py-C6</b> $^{19}\text{F}$ NMR (471 MHz, $\text{CDCl}_3$ , 20 °C).....	- 237 -
<b>Figure 5.69</b> Compound <b>Py-C6</b> DART MS .....	- 237 -
<b>Figure 5.70</b> Compound <b>Ph-CN-C6 (p)</b> $^1\text{H}$ NMR (500 MHz, $\text{CDCl}_3$ , 20 °C).....	- 238 -
<b>Figure 5.71</b> Compound <b>Ph-CN-C6 (p)</b> $^{13}\text{C}$ NMR (126 MHz, $\text{CDCl}_3$ , 20 °C) .....	- 238 -
<b>Figure 5.72</b> Compound <b>Ph-CN-C6 (p)</b> $^{19}\text{F}$ NMR (471 MHz, $\text{CDCl}_3$ , 20 °C).....	- 239 -
<b>Figure 5.73</b> Compound <b>Ph-CN-C6 (p)</b> DART MS .....	- 239 -
<b>Figure 5.74</b> Compound <b>Ph-CN-C6 (o)</b> $^1\text{H}$ NMR (500 MHz, $\text{CDCl}_3$ , 20 °C).....	- 240 -
<b>Figure 5.75</b> Compound <b>Ph-CN-C6 (o)</b> $^{13}\text{C}$ NMR (126 MHz, $\text{CDCl}_3$ , 20 °C) .....	- 240 -
<b>Figure 5.76</b> Compound <b>Ph-CN-C6 (o)</b> $^{19}\text{F}$ NMR (471 MHz, $\text{CDCl}_3$ , 20 °C).....	- 241 -
<b>Figure 5.77</b> Compound <b>Ph-CN-C6 (o)</b> DART MS .....	- 241 -
<b>Figure 5.78</b> Compound <b>Ph-NO<sub>2</sub>-C6 (o)</b> $^1\text{H}$ NMR (500 MHz, $\text{CDCl}_3$ , 20 °C) .....	- 242 -

<b>Figure 5.79</b> Compound <b>Ph-NO<sub>2</sub>-C6 (o)</b> <sup>19</sup> F NMR (471 MHz, CDCl <sub>3</sub> , 20 °C) .....	- 242 -
<b>Figure 5.80</b> Compound <b>Ph-NO<sub>2</sub>-C6 (o)</b> <sup>13</sup> C NMR (126 MHz, CDCl <sub>3</sub> , 20 °C).....	- 243 -
<b>Figure 5.81</b> Compound <b>Ph-NO<sub>2</sub>-C6 (o)</b> DART MS.....	- 243 -
<b>Figure 5.82</b> Compound <b>Ph-CF<sub>3</sub>-C6 (o)</b> <sup>1</sup> H NMR (500 MHz, CDCl <sub>3</sub> , 20 °C).....	- 244 -
<b>Figure 5.83</b> Compound <b>Ph-CF<sub>3</sub>-C6 (o)</b> <sup>13</sup> C NMR (126 MHz, CDCl <sub>3</sub> , 20 °C).....	- 244 -
<b>Figure 5.84</b> Compound <b>Ph-CF<sub>3</sub>-C6 (o)</b> <sup>19</sup> F NMR (471 MHz, CDCl <sub>3</sub> , 20 °C) .....	- 245 -
<b>Figure 5.85</b> Compound <b>Ph-CF<sub>3</sub>-C6 (o)</b> DART MS .....	- 245 -
<b>Figure 5.86</b> Compound <b>Ph-CF<sub>3</sub>-C6 (p)</b> <sup>1</sup> H NMR (500 MHz, CDCl <sub>3</sub> , 20 °C).....	- 246 -
<b>Figure 5.87</b> Compound <b>Ph-CF<sub>3</sub>-C6 (p)</b> <sup>13</sup> C NMR (126 MHz, CDCl <sub>3</sub> , 20 °C).....	- 246 -
<b>Figure 5.88</b> Compound <b>Ph-CF<sub>3</sub>-C6 (p)</b> <sup>19</sup> F NMR (471 MHz, CDCl <sub>3</sub> , 20 °C) .....	- 247 -
<b>Figure 5.89</b> Compound <b>Ph-CF<sub>3</sub>-C6 (p)</b> DART MS .....	- 247 -
<b>Figure 5.90</b> Compound <b>1-Naph-C6</b> <sup>1</sup> H NMR (500 MHz, CDCl <sub>3</sub> , 20 °C) .....	- 248 -
<b>Figure 5.91</b> Compound <b>1-Naph-C6</b> <sup>13</sup> C NMR (126 MHz, CDCl <sub>3</sub> , 20 °C) .....	- 248 -
<b>Figure 5.92</b> Compound <b>1-Naph-C6</b> <sup>19</sup> F NMR (471 MHz, CDCl <sub>3</sub> , 20 °C).....	- 249 -
<b>Figure 5.93</b> Compound <b>1-Naph-C6</b> DART MS.....	- 249 -
<b>Figure 5.94</b> Compound <b>2-Naph-C6</b> <sup>1</sup> H NMR (500 MHz, CDCl <sub>3</sub> , 20 °C) .....	- 250 -
<b>Figure 5.95</b> Compound <b>2-Naph-C6</b> <sup>13</sup> C NMR (126 MHz, CDCl <sub>3</sub> , 20 °C) .....	- 250 -
<b>Figure 5.96</b> Compound <b>2-Naph-C6</b> <sup>19</sup> F NMR (471 MHz, CDCl <sub>3</sub> , 20 °C).....	- 251 -
<b>Figure 5.97</b> Compound <b>2-Naph-C6</b> DART MS.....	- 251 -

## List of Schemes

Scheme	Page
<b>Scheme 2.1</b> Synthesis of <b>FF-PBI-1</b> . Scheme adapted with permission. <sup>36</sup> Copyright © 2018, Georg Thieme Verlag KG.....	- 44 -
<b>Scheme 2.2</b> Synthesis of <b>FF-PBI-2</b> . Scheme adapted with permission. <sup>36</sup> Copyright © 2018, Georg Thieme Verlag KG.....	- 50 -
<b>Scheme 2.3</b> Synthesis of <b>FF-PBI-2'</b> .....	- 51 -
<b>Scheme 2.4</b> Synthesis of <b>FF-PBI-2''</b> .....	- 51 -
<b>Scheme 3.1</b> Synthesis of fluorous phthalocyanines ( <b>F-PCs: F-PC-1, F-PC-2, F-PC-3</b> ). Scheme adapted with permission. <sup>77</sup> Copyright © 2020, World Scientific Publishing .....	- 84 -
<b>Scheme 3.2</b> Synthesis of fluorous subphthalocyanines ( <b>F-SubPCs</b> ). Scheme adapted with permission. <sup>77</sup> Copyright © 2020, World Scientific Publishing. ....	- 87 -
<b>Scheme 3.3</b> Unsuccessful alternative synthetic scheme to obtain <b>F-SubPC-1</b> in an $S_NAr$ reaction installing the fluoroalkyl thiols on halogenated subphthalocyanines. ....	- 88 -
<b>Scheme 4.1</b> Synthesis of <b>F-BHQ-1</b> .....	- 136 -
<b>Scheme 4.2</b> Synthesis of <b>F-BHQ-2</b> .....	- 137 -
<b>Scheme 5.1</b> Fluorous Heck Reaction for the Synthesis of FAA-Functionalized Thiophenes. Scheme adapted with permission. <sup>120</sup> Copyright © 2021, Georg Thieme Verlag KG.....	- 162 -
<b>Scheme 5.2</b> Brominations of FAA-Functionalized Thiophenes. Scheme adapted with permission. <sup>120</sup> Copyright © 2021, Georg Thieme Verlag KG.....	- 163 -
<b>Scheme 5.3</b> Synthesis of FAA-Functionalized Terthiophenes. Scheme adapted with permission. <sup>120</sup> Copyright © 2021, Georg Thieme Verlag KG. ....	- 164 -

**Scheme 5.4** Synthesis of **F-PT-1 (x/1-x)**. Scheme adapted with permission.<sup>120</sup> Copyright © 2021, Georg Thieme Verlag KG..... - **166** -

**Scheme 5.5** Synthesis of fluorous soluble polymers **F-PT-1 (100/0)** and **F-PT-2**. The photographs show samples under ambient light (left) and handheld UV lamp (right, excitation: 365 nm) and their fluorous partition behavior. Scheme adapted with permission.<sup>120</sup> Copyright © 2021, Georg Thieme Verlag KG..... - **168** -

**Scheme 5.6** Hypothetical mechanism of fluoride reduction of the FAA-functionalized molecules ..... - **171** -

**Scheme 5.7** Synthesis of FAA-functionalized molecules described in this work..... - **172** -

**Scheme 5.8** Synthesis of perfluoroalkyl naphthalenes ..... - **173** -

## List of Tables

Table	Page
<b>Table 2.1</b> Photophysical Properties of <b>FF-PBI-1</b> in CH <sub>2</sub> Cl <sub>2</sub> and C <sub>6</sub> F <sub>14</sub> (+ TFA) .....	- 48 -
<b>Table 2.2</b> Crystal data and structure refinement for compound <b>6</b> .....	- 75 -
<b>Table 3.1</b> Summary of photophysical properties of <b>F-PCs</b> .....	- 86 -
<b>Table 3.2</b> Summary of photophysical properties of <b>F-SubPCs</b> .....	- 89 -
<b>Table 5.1</b> Crystal data and structure refinement for compound <b>4</b> .....	- 206 -
<b>Table 5.2</b> Photophysical summary of compounds <b>11</b> , <b>12</b> , <b>3T-C<sub>12</sub></b> , and <b>3T</b> in toluene solution. .....	- 207 -
<b>Table 5.3</b> Property summary of <b>F-PT(x/1-x)</b> .....	- 207 -



## List of Equations

Equation	Page
<b>Equation 1.1</b> $\log P = \log \left( \frac{[\text{solute}]_{\text{fluorocarbon}}}{[\text{solute}]_{\text{hydrocarbon}}} \right)$ .....	<b>32</b> -
<b>Equation 2.1</b> Maximum Edge EQE = $1 - \left( \frac{1}{n^2} \right)^{1/2}$ , where n = 1.49 for PMMA.....	<b>57</b> -

**CHAPTER 1:**  
**Introduction and Background**

## 1.1 Abstract

In this chapter, the basic concepts explored in this thesis are described. First, the basic property of fluorine is summarized. Then, a review of the incorporation of fluorine in conjugated materials is described. The origin of “fluorous” chemistry is defined and applications involving fluorous partition are shown. The work in this thesis emphasizes fluorous partition, rather than fluorous solubility. Dynamically reconfigurable complex emulsions, in which the emulsions consist of equal volume of hydrocarbon and fluorocarbon, are introduced. Molecules that exhibit good fluorous partition show great utility in the emulsions as discussed in later chapters. The central theme of the thesis is to elucidate the effect of fluorine functionalization on materials’ properties. This thesis provides insights on the design and synthesis of fluorous conjugated materials, which lays the foundation for future discovery of applications.

## 1.2 Introduction

Fluorine is the most electronegative atom in the periodic table, and thus endows various unique properties to a molecule. Fluorine ranks 13<sup>th</sup> in the abundance of elements in Earth’s crust, mostly in the form of calcium fluoride.<sup>1</sup> Calcium fluoride is industrially converted to hydrogen fluoride which serves as a precursor to organic fluorides. Owing to its high electronegativity, fluorine is a very reactive atom. Conversely, compounds containing carbon-fluorine bonds often possess high chemical and thermal stability. One of the most famous fluorine-containing materials, poly(tetrafluoroethylene) (PTFE), is often used in coatings for optical fibers and non-stick frying pans.<sup>2</sup> In 2018, 28% of the pharmaceutical drugs approved by the U.S. Food and Drug Administration contained fluorine in their structures.<sup>3</sup> Fluorine incorporation in to conjugated

organic materials has been trending in recent materials chemistry due to its positive impact on hydrophobicity, rigidity, and thermal stability. Details are further described in section 1.3.

### 1.3 Incorporation of Fluorine in Conjugated Organic Materials

Fluorine has found unique yet versatile applications *via* its incorporation into conjugated organic materials. For example, exchanging a single hydrogen for a fluorine has great impact on a molecule's solubility, molecular packing, and electronic properties.<sup>4</sup> Molecules containing fluorine have also shown greater photochemical and thermal stability over their counterparts, making fluorine an attractive functional group to incorporate into molecular electronic devices.<sup>5</sup> This has been especially true in organic photovoltaics, where one of the highest performing organic solar cells features fluorination on both the donor and the non-fullerene acceptor.<sup>6</sup> Fluorination in this context often refers to attaching fluorine atoms to the conjugated backbone of molecules, and much attention has been paid towards precise tuning of the energy level of the molecular orbitals of molecules. Such engineering often significantly increases the synthetic complexity of the target compound. Since the aryl fluoride starting reagents are also strikingly expensive, much work needs to be done to commercialize any high-performing fluorinated organic devices.

Besides attaching fluorine directly to the conjugated backbone, attaching semifluoroalkyl or perfluoroalkyl chains have also found applications in materials chemistry. For example, attaching semifluoroalkyl or perfluoroalkyl chains have been found to induce self-assembly in conjugated materials due to fluorine-fluorine interactions. Schmidt *et al.* reported that perylene bisimides with different perfluorinated residues afforded several derivatives with excellent electron carrier mobility and on-to-off current ratios in organic thin film transistors.<sup>7</sup> Kang *et al.* found that strong self-organization of these fluoroalkyl side chains induced a high degree of order in the attached polymer backbones by forming a superstructure composed of “backbone crystals”

and “side-chain crystals.”<sup>8</sup> This phenomenon was shown to greatly enhance the ordering along the backbone direction, and the resulting polymers thus exhibited unipolar n-channel transport in field-effect transistors with remarkably high electron mobility.<sup>8</sup>

This thesis focuses on conjugated materials functionalized with semifluoroalkyl or perfluoroalkyl chains due to the straightforward and more synthetically accessible procedures. Materials described in this thesis have multiple fluoroalkyl chains attached to them so that the materials could be soluble in fluoruous solvents, as defined in the next section.

#### **1.4 “Fluorous” Chemistry and Fluorous Partition**

When the fluorine content of the molecule becomes high, typically over 60 weight percent of fluorine (wt% F), the molecule shows a unique behavior of phase separating from organic and aqueous solutions. Examples of such molecules include perfluoromethoxybutane and perfluorohexane, sold by 3M as HFE-7100 and FC-770, respectively. The utility of such solvents were demonstrated by Horváth and Rábai in 1994, when the term “fluorous” was first coined.<sup>9</sup> In their work, they described a catalyst soluble in perfluorinated solvents, and showed its utility in a biphasic reaction. When the reaction mixture was heated, the organic and fluoruous phases mixed, and the reaction proceeded. Upon completion, the reaction was cooled again for the two phase to separate. The product in the organic phase could be easily isolated, while the catalyst could be easily recycled. A fluoruous phase provides advantages over other biphasic systems in that they improve stability of the catalyst in its resting state and is miscible with organic solvents at elevated temperatures. Thus, a fluoruous catalyst could combine the advantages of one-phase catalysis with biphasic product separation by running the reaction at higher temperatures and separating the products at lower temperatures.

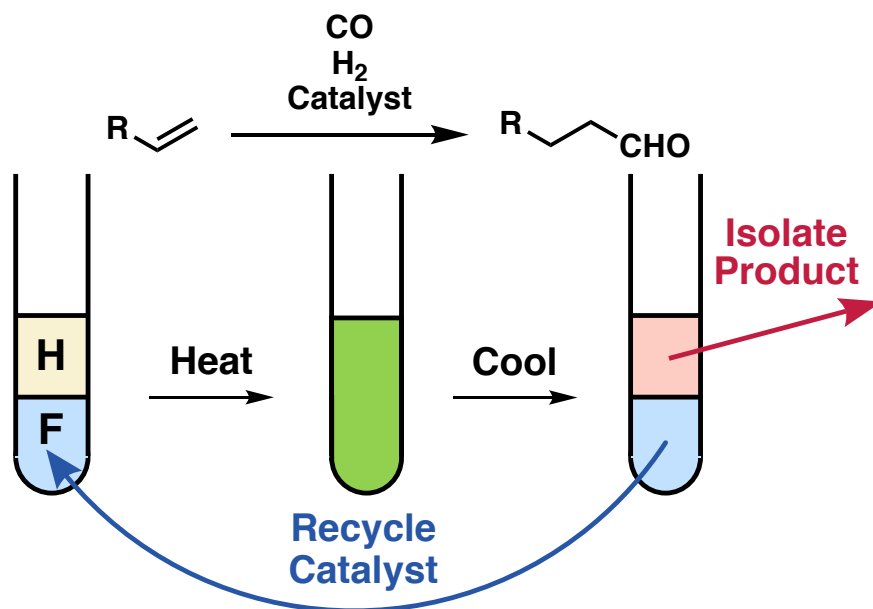


**Figure 1.1** General schematic image of a fluoruous biphasic reaction system.

Fluorous partition describes the tendency of a molecule preferring to reside in the fluorocarbon phase over the hydrocarbon phase (or any other phases) when subjected to the two phases. The fluorous partition coefficient, abbreviated  $P$ , is defined as the ratio of concentrations of a compound in a mixture of perfluorocarbon and a hydrocarbon, typically in perfluoro(methylcyclohexane) and toluene, respectively.<sup>10</sup> The fluorous partition coefficient is often given as  $\log P$  (**Equation 1.1**) or as a ratio normalized to 100. Both descriptions for fluorous partition coefficient are listed when they were measured in this thesis.

$$\text{Equation 1.1} \quad \log P = \log \left( \frac{[\text{solute}]_{\text{fluorocarbon}}}{[\text{solute}]_{\text{hydrocarbon}}} \right)$$

Solubilities in fluorous solvents are largely determined by two parameters: solute polarity and size. The first is an extension of the familiar “like dissolves like” paradigm. The second is uniquely important to perfluorinated solvents, which because of low intermolecular forces have large cavities (free volumes) that can accommodate small molecules. Noteworthy, a molecule possessing high fluorous solubility is a necessary but not sufficient condition for a molecule to

have high fluorine partition. In other words, a molecule showing high solubility in fluorine solvents does not necessarily show high fluorine partition. This becomes crucial later in this thesis when a high fluorine partition of a molecule is desired for targeted applications. A reasonable strategy to confer high fluorine partition relies on the installation of fluorine “ponytails” on a molecule. Typical fluorine ponytails have the formula of  $\text{CF}_3(\text{CF}_2)_n(\text{CH}_2)_m\text{-R}$  ( $n \approx 8$ ,  $m \approx 3$ ; R = arbitrary functional group). Because the fluoroalkyl groups can be electron-withdrawing, a short alkyl group serves as an insulating group to reduce any undesired electronic influence. Such ponytails are often referred to as semifluoroalkyl chains because the chains are not fully fluorinated, while fully fluorinated ponytails are referred to as perfluoroalkyl chains.

The fluorine phase separation behavior is also frequently applied to orthogonal processing techniques. Jeong *et al.* reported a semifluorinated alkyl-polyquaterthiophene (SFA-PQT, **Figure 1.2a**) that is insoluble in most solvents at room temperature but is soluble in orthodichlorobenzene at elevated temperatures.<sup>11</sup> The self-organizing behavior of the semifluoroalkyl groups provided a morphology that allowed efficient charge transport even without thermal annealing. This proved to be a major advantage because, in addition to simplifying the process, a process free of thermal annealing eliminates the chance of thermal damage to the underlying layers such as plastic substrates, interfacial layers, and active layers. The hydrophobicity of SFA-PQT facilitated a simple patterning process, resulting in selectively patterned complementary inverters that solve the problems of large-voltage consumption, a broad transition zone, low-gain values, and hysteresis. The actual patterning is shown in **Figure 1.2b** and the schematic process is shown in **Figure 1.2c**. In another work, Lee *et al.* synthesized semifluoroalkyl polyfluorenes for orthogonal patterning of organic electronic devices (**Figure 1.2d**, left).<sup>12</sup> Solution processing of organic electronic materials is a highly attractive processing option for many applications,

particularly organic light emitting diodes for display and solid-state lighting. While highly efficient full color displays are rather straightforward to fabricate *via* vacuum-assisted shadow mask deposition of organic small molecules, the standard solvents used in the processing of photosensitive materials can damage the organic light-emitting materials used as active layers. The semifluoroalkyl polyfluorenes were synthesized to achieve the formation of a multi-layer solution-processed device and direct photolithographic patterning of light-emitting layers without compromising the device efficiency.

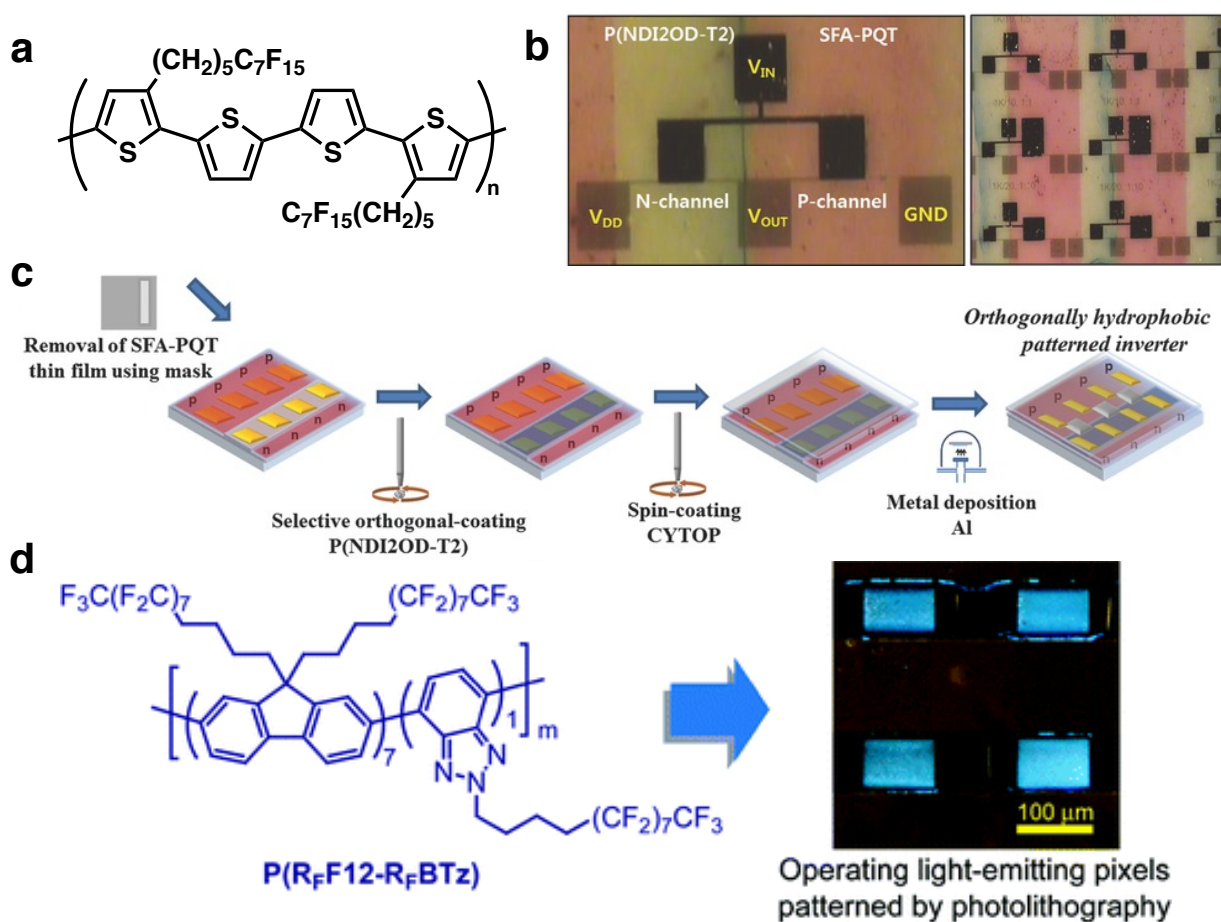


**Figure 1.2** Summary of representative examples of highly fluorinated polymers. (a) Chemical structure of semifluorinated polyquaterthiophene (SFA-PQT).<sup>11</sup> (b) Image of an inverter using orthogonal patterning.<sup>11</sup> (c) Schematic procedure for an orthogonally hydrophobic patterned complementary inverter consisting of SFA-PQT and ActivInk N2200 (P(NDI2OD-T2)) layers. Figures adapted with permission.<sup>11</sup> Copyright © 2013, John Wiley and Sons. (d) Chemical structure of fluorinated polyfluorene and an image of orthogonally patterned light-emitting pixels. Figure adapted with permission.<sup>12</sup> Copyright © 2010, American Chemical Society.



## 1.5 Fluorescence and Fluorofluorescent Molecules

This thesis involves the development and application of organic molecules that undergo photoluminescence, or luminescence resulting from the absorption of light. When absorption occurs, an electron lying in the ground state of the photoluminescent molecule is promoted to a higher-energy excited state. After a period known as the luminescence lifetime, this higher-energy electron will transition back to the ground state, causing the residual energy produced as a result of this relaxation to be ejected from the molecule in the form of a photon.

After a molecule absorbs a photon with sufficient energy to promote one of its electrons to an excited state, several processes may occur prior to relaxation. Such photophysical phenomena may be conveniently described with a Jablonski diagram, a scheme commonly employed by scientists to depict the landscape of a molecule's electronic excited states and the possible mechanisms by which photoluminescence can occur. A Jablonski diagram for a conventional, closed-shell single organic molecule is shown in **Figure 1.3**. Prior to absorption, the molecule resides in a ground state in which all electrons are spin-paired (i.e., the spin multiplicity is zero). Such a configuration is termed a singlet state. The ground state is therefore the lowest energy singlet electronic state and denoted as  $S_0$  with higher-level states listed as  $S_n$ , where  $n$  is an integer greater than zero. In the case where the excited-state electron is unpaired, the resulting electronic configuration is termed a triplet state, or  $T_n$  (i.e., the spin multiplicity is one). Additionally, the coupling of these electronic states with vibrational wavefunctions associated with relevant chemical bonds in the molecule gives rise to discrete energy levels that an electron may occupy depending on the energy of light absorbed. Thus, individual singlet and triplet manifolds are often depicted as Morse potential wells to account for these vibrational couplings.

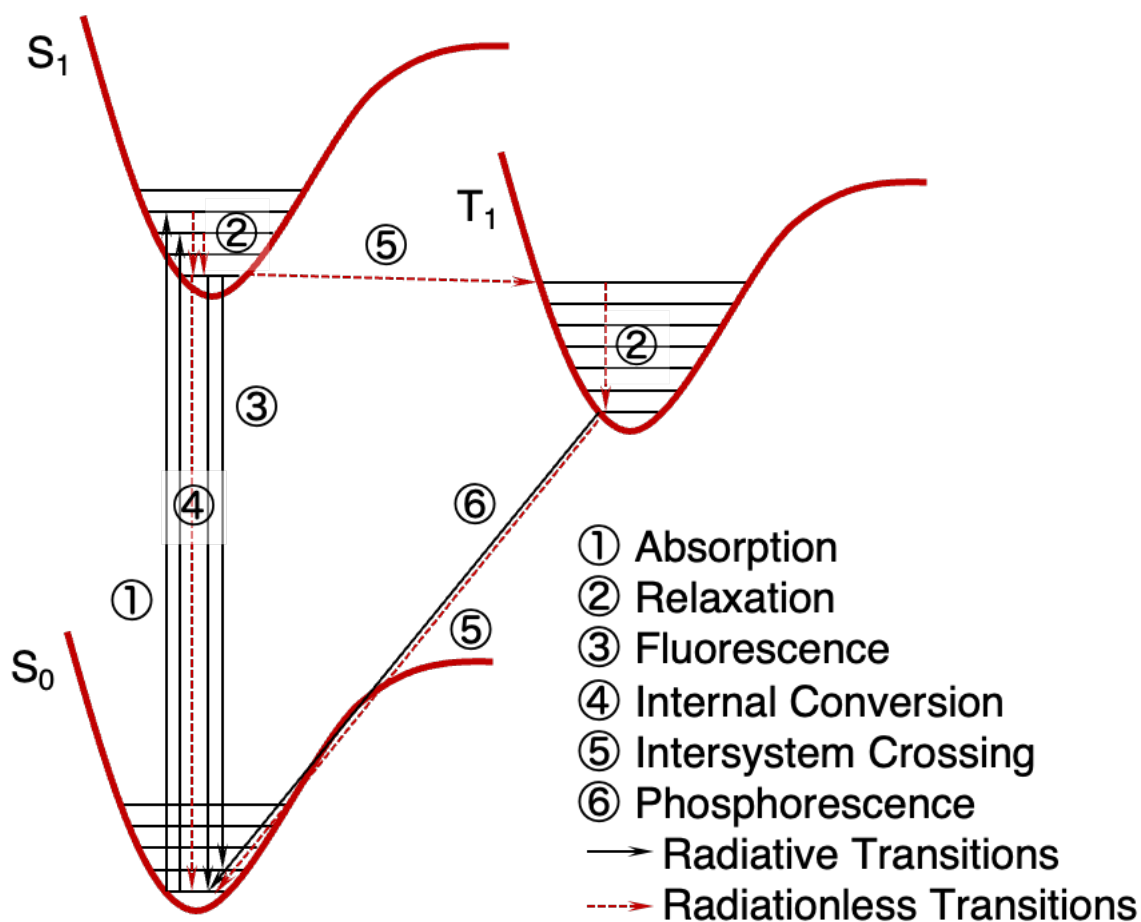


**Figure 1.3** A Jablonski diagram describing the photochemical processes.

“Fluoro” can refer to both fluorine and fluorescence, however very few fluorescent molecules are soluble in perfluorinated solvents. This fact is surprising since the orthogonality of fluorinated materials is a commonly exploited strategy in synthetic chemistry, materials science, and chemical biology, as mentioned in section 1.2. Seminal work from the Swager group is summarized in **Figure 1.4** and the group has addressed this shortage by synthesizing conjugated polymers<sup>13,14</sup> and a panel of “fluorofluorophores,”<sup>15</sup> all containing high weight percent fluorine with optical properties spanning the visible to near-infrared spectrum. These examples represent only a few unique highlights of the fluorinated phase and new discoveries will be enabled by access to an expanded portfolio of fluorinated materials. This is demonstrated in **Chapter 2** and **Chapter 3**

where fluorofluorescent perylene bisimides, phthalocyanines, and subphthalocyanines are introduced, as well as their applications enabled by their unique fluorophilic partition properties.

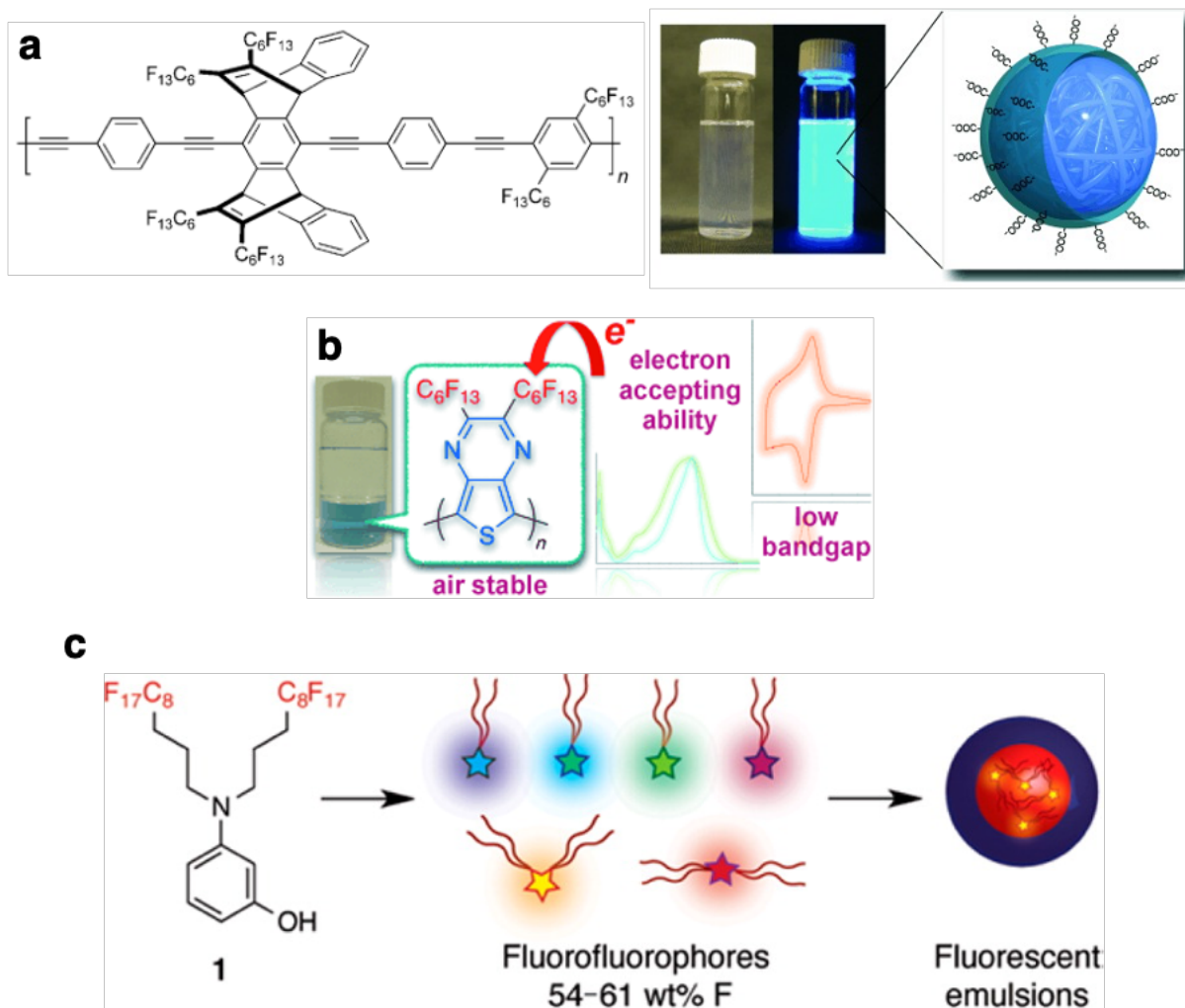


**Figure 1.4** Examples of fluorophilic soluble conjugated materials from the Swager group. (a) Chemical structure of a fluorophilic soluble polyphenylene ethynylene and an image of an emulsion containing the polymer. Figure adapted with permission.<sup>13</sup> Copyright © 2010, John Wiley and Sons. (b) Chemical structure of a fluorophilic soluble n-type semiconducting polymer with air stability. Figure adapted with permission.<sup>14</sup> Copyright © 2012, John Wiley and Sons. (c) Synthesis of a panel of “fluorofluorophores” from a common aminophenol precursor. Various fluorophilic emulsions containing the fluorofluorophores could be obtained. Figure adapted with permission.<sup>15</sup> Copyright © 2014, American Chemical Society.

## 1.6 Dynamically Reconfigurable Complex Emulsions

In recent years, Swager and coworkers have pioneered a novel class of emulsions: complex emulsions that dynamically reconfigure in response to external stimuli.<sup>16</sup> Nominally double

emulsions comprising two immiscible oils (e.g. hydrocarbon (H) and fluorocarbon (F) oils) dispersed in water (W), these emulsions change morphologies from encapsulated to Janus configurations by tuning interfacial tensions at the H/W and F/W interfaces ( $\gamma_{H/W}$  and  $\gamma_{F/W}$ , respectively). When  $\gamma_{H/W} = \gamma_{F/W}$ , a perfect Janus morphology (equal hemispheres) is achieved. When  $\gamma_{H/W} \gg \gamma_{F/W}$ , the higher interfacial tension at the H/W interface results in a minimization of H/W interfacial area, and a H-in-F-in-W (H/F/W) encapsulated morphology is preferred. The inverse ( $\gamma_{H/W} \ll \gamma_{F/W}$ ) is necessary for F-in-H-in-W (F/H/W) double emulsions.

The fabrication of the complex emulsions is achieved through temperature-induced phase separation emulsification (**Figure 1.5a**). Briefly, equal volumes of H and F oils are heated above their critical solution temperature to generate a homogenous phase and subsequently emulsified in a surfactant-enriched aqueous continuous phase by conventional or microfluidic techniques. The H oil contains a Nile Red dye for visual demonstration purposes. Upon cooling, the two oils phase separate to yield double emulsions with uniform compositions and morphologies.

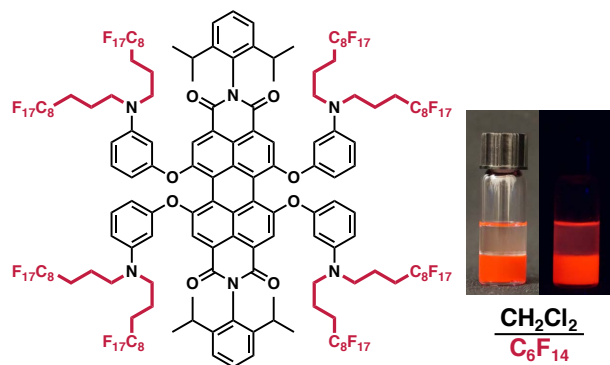
The morphology of the emulsions can be tuned along the continuum between H/F/W and F/H/W encapsulated structures. For example, adjusting surfactant concentration ratios of H- and F-surfactants can induce morphology changes. A typical H-surfactant, sodium dodecyl sulfate, and a typical F-surfactant, Zonyl, are shown in **Figure 1.5b**. As depicted in **Figure 1.5c**, as the concentration of the H-surfactant increases, the H/F/W emulsion undergoes a morphology change to the Janus morphology and eventually to the F/H/W morphology. The morphology change is reversible: as the concentration of the F-surfactant increases, the F/H/W emulsion undergoes a morphology change to the Janus morphology and eventually back to the H/F/W morphology. Other strategies like changing surfactant strength with external stimuli (e.g., light and pH) will induce



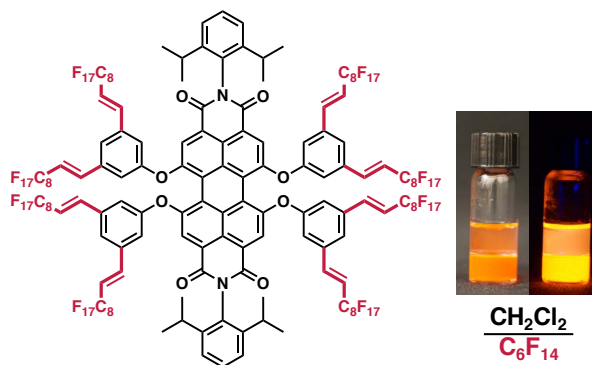
## CHAPTER 2:

### Synthesis of Fluorofluorescent Perylene Bisimides:

### Applications in Luminescent Solar Concentrators



**54 wt% F**



**56 wt% F**

Parts of this chapter were adapted and reprinted with permission from:

Yoshinaga, K.; Swager, T. M. Fluorofluorescent Perylene Bisimides. *Synlett* **2018**, 29, 2509.  
Copyright © 2018, Georg Thieme Verlag KG.

## 2.1 Abstract

Perfluorinated liquids can exhibit immiscibility with organic and aqueous solvents and provide orthogonal opportunities to applications in organic and aqueous environments. Examples of emissive dyes that display only fluoruous phase solubility are limited, despite the many potential applications. Perylene bisimides are among the most versatile dyes and are known for their outstanding stability and high quantum yields. Herein, we report the synthesis of two new “fluorofluorescent” perylene bisimide dyes, designed to be soluble in the fluoruous phase. These two dyes possess unique properties, including dramatic increases in fluorescence quantum yields when treated with Brønsted acids as well as aggregation in the fluoruous phase. We demonstrate the concept of a fluorofluorescent solar concentrator by fabricating a device made from poly(methyl methacrylate). The edge external quantum efficiency of the device is measured to be 33% at 566 nm.

## 2.2 Introduction

The “fluoruous” phase, which can include perfluorinated alkanes, ethers, or amines, has found unique opportunities in chemistry as a result of the ability to phase-separate from polar and nonpolar phases.<sup>17</sup> The term “fluoruous” was coined by Horváth and Rábai in 1994, when they demonstrated the utility of fluoruous biphasic catalysis.<sup>9</sup> Fluoruous molecules tend to exhibit improved photochemical, thermal, and chemical stability compared to their hydrocarbon counterparts, since C–F bonds are more stronger than C–H bonds.<sup>5</sup> Fluoruous compounds have attracted attention for applications<sup>18</sup> such as coating materials,<sup>19</sup> organic electronics,<sup>7,12,20,21</sup> perfluorocarbon nanoemulsions for *in vivo* drug delivery<sup>22</sup> and cell tracking,<sup>23</sup> and fluorescent recognition in the fluoruous phase.<sup>24–26</sup> These examples represent only a few unique highlights of

fluorous-phase chemistry and suggest that important new discoveries could be enabled by access to an expanded portfolio of fluorous materials.

Fluorous solubility is well-predicted by the fluorine content of the molecule, typically requiring >50 weight percent fluorine (wt% F) and extended perfluoroalkyl chains.<sup>17</sup> Examples of dyes that exhibit fluorous solubility are extremely limited.<sup>27</sup> To address this shortage, our group has previously synthesized fluorous soluble conjugated polymers,<sup>13,14</sup> as well as an array of “fluorofluorophores”, in which “fluoro” refers to both fluorescence and fluorination.<sup>15</sup> However, to date only a small area of chemical space has been explored and there are vast uncharted territories of electronic molecules to be discovered.

We targeted perylene bisimides (PBIs) as a result of their wide utility as organic semiconductors,<sup>28</sup> supramolecular building blocks,<sup>29</sup> and fluorophores.<sup>30</sup> Previous examples of the incorporation of fluorinated groups in PBIs have been demonstrated to provide air-stable n-type semiconductors.<sup>7,21,31–33</sup> However, the fluorine content of these examples was less than 50 wt% F. Examples of PBIs with higher wt% F have been reported to self-assemble into ordering structures.<sup>34,35</sup> However, their fluorous solubilities and the photophysical properties of the fluorinated molecules were not studied in detail.

Herein, we disclose two synthetic approaches to obtain fluorofluorescent PBI dyes **FF-PBI-1** and **FF-PBI-2**, both requiring only four facile steps from a commercial starting material (**Figure 2.1**). **FF-PBI-1**, which possesses 54 wt% F, initially shows moderate solubility in both organic and fluorous solvents, but the solubility in fluorous solvents is significantly improved upon addition of a Brønsted acid. On the other hand, **FF-PBI-2**, which possesses 56 wt% F, shows good solubility in both organic and fluorous solvents. The photophysical properties of the two **FF-PBIs**



are also distinctly unusual; **FF-PBI-1** shows a response to acidity, whereas **FF-PBI-2** shows concentration dependence.

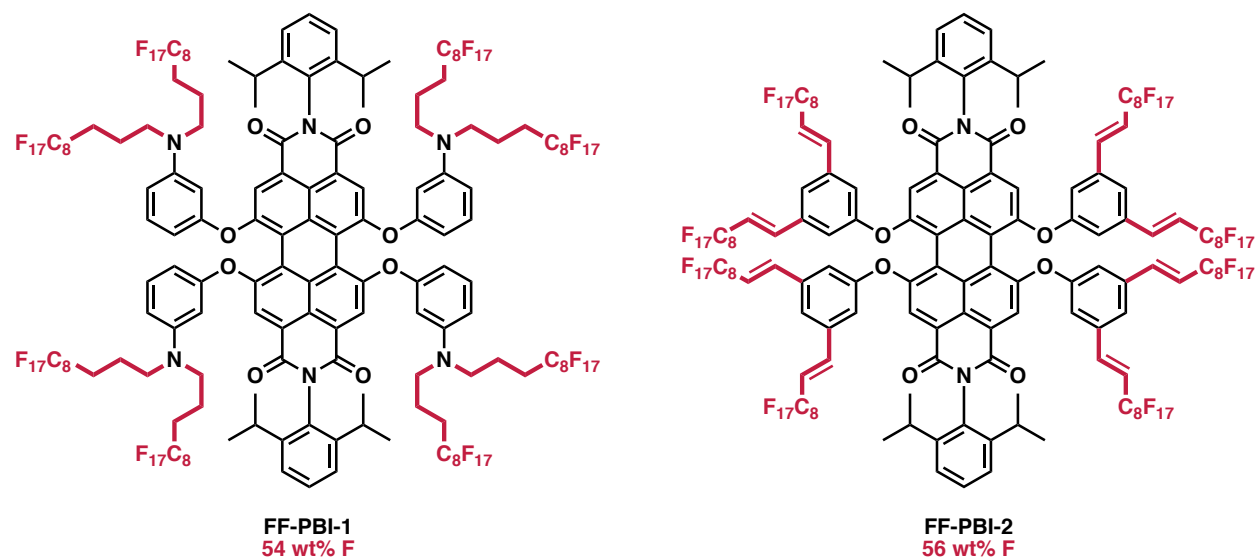


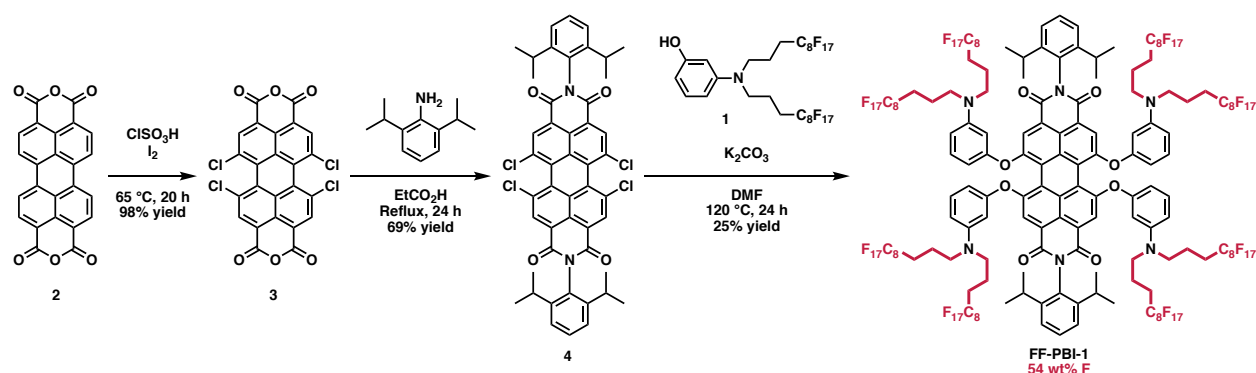
**Figure 2.1** Chemical structures of fluorofluorescent PBIs in this report. Figure adapted with permission.<sup>36</sup> Copyright © 2018, Georg Thieme Verlag KG.

## 2.3 Results and Discussion

### 2.3.1 Synthesis of FF-PBI-1

The synthesis of **FF-PBI-1** is shown in **Scheme 2.1**. Fluoroalkylated aminophenol **1**, compound **3**, and compound **4** were prepared according to previous reports.<sup>15,37,38</sup> A nucleophilic aromatic substitution ( $S_NAr$ ) reaction of **4** with **1** produced the target perylene bisimide **FF-PBI-1** in 25% isolated yield. The crude  $^1H$  NMR suggested full conversion with minor amounts of impurities. The product was purified by chromatography on silica gel, but its poor solubility in most solvents presumably contributed to the low isolated yield.<sup>39</sup> **FF-PBI-1** was fully characterized by  $^1H$  and  $^{19}F$  nuclear magnetic resonance (NMR) spectroscopy, matrix assisted laser

desorption/ionization time-of-flight mass spectrometry (MALDI TOF-MS), and elemental analysis.



**Scheme 2.1** Synthesis of **FF-PBI-1**. Scheme adapted with permission.<sup>36</sup> Copyright © 2018, Georg Thieme Verlag KG.

We initially attempted the synthesis of **FF-PBI-1'** in a similar manner as shown in **Figure 2.2a** due to the availability of the regioisomeric mixture of dibrominated perylene bisimide synthesized by Gutierrez.<sup>40</sup> An  $S_NAr$  reaction of the precursor with **1** produced the target perylene bisimide **FF-PBI-1'** in 18% yield. The two regioisomeric product co-eluted on high-performance liquid chromatography and could not be separated. **FF-PBI-1'** possesses 47 wt% F and was not soluble in fluorous solvents such as perfluorohexane and perfluorodecalin. **FF-PBI-1'** served as an important control molecule to demonstrate the necessity of high fluorine content to render fluorous solubility. This molecule also did not fluoresce in ambient conditions. However, upon addition of an acid such as TFA, the fluorescence of the molecule was turned on (**Figure 2.2b**).

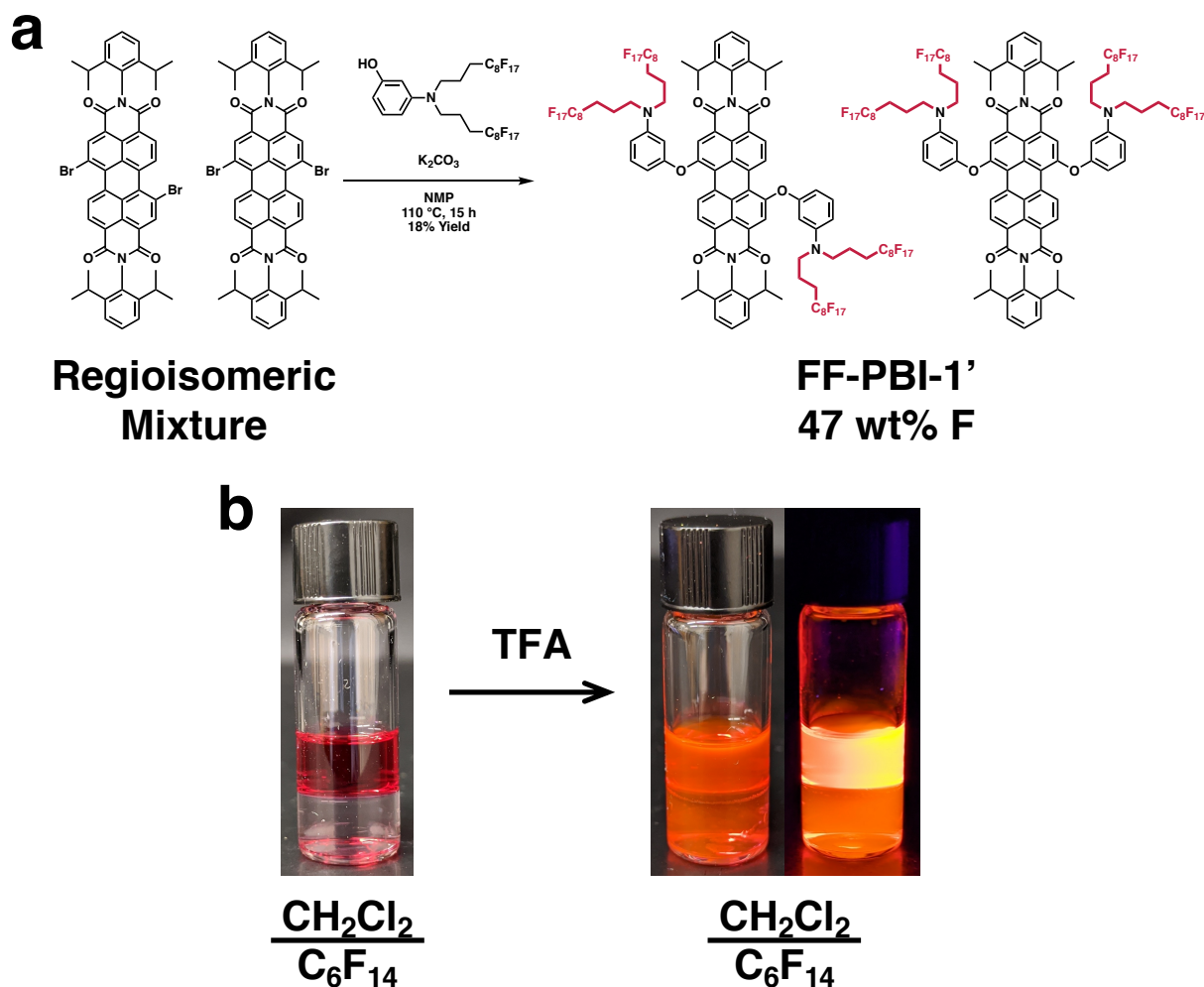


**Figure 2.2** (a) Synthetic scheme of **FF-PBI-1'**. (b) Photographs of **FF-PBI-1'** (0.5 mg) in  $\text{CH}_2\text{Cl}_2$  (0.5 mL) and  $\text{C}_6\text{F}_{14}$  (0.5 mL), and after adding TFA.

### 2.3.2 Properties of **FF-PBI-1**

We sought to gain a better understanding of the solubility of **FF-PBI-1**, which showed moderate solubility ( $\sim 1.0$  mg/mL;  $\sim 2.1 \times 10^2$   $\mu\text{M}$ ) in organic solvents such as dichloromethane ( $\text{CH}_2\text{Cl}_2$ ) (**Figure 2.3a**), toluene, chloroform, acetone, and ethyl acetate. Interestingly, when perfluorohexane ( $\text{C}_6\text{F}_{14}$ ) was added to a solution of **FF-PBI-1** in  $\text{CH}_2\text{Cl}_2$ , we visually observed the partition of **FF-PBI-1** in both  $\text{CH}_2\text{Cl}_2$  and  $\text{C}_6\text{F}_{14}$  layers (**Figure 2.3b**). Despite the high wt% F, **FF-PBI-1** was insoluble in pure perfluorinated solvents such as  $\text{C}_6\text{F}_{14}$  (**Figure 2.3d**), as well as

perfluorodecalin. This contradicts the observation of **FF-PBI-1** partitioning in both  $\text{CH}_2\text{Cl}_2$  and  $\text{C}_6\text{F}_{14}$  layers as shown in **Figure 2.3b**. We hypothesize the minute amount of  $\text{CH}_2\text{Cl}_2$  dissolved in  $\text{C}_6\text{F}_{14}$  upon partition increased the solubility of **FF-PBI-1** in  $\text{C}_6\text{F}_{14}$ , however, the fluororous partition coefficient of **FF-PBI-1** should be measured for further discussion.

To our surprise, we found that addition of a Brønsted acid improved the solubility of **FF-PBI-1** in fluororous solvents. For instance, when trifluoroacetic acid (TFA) was added to the solution of **FF-PBI-1** in  $\text{CH}_2\text{Cl}_2/\text{C}_6\text{F}_{14}$  mixture, the color of the  $\text{CH}_2\text{Cl}_2$  layer turned from turbid purple to colorless transparent, while that of the  $\text{C}_6\text{F}_{14}$  layer turned from turbid purple to a brilliant fluorescent red (**Figure 2.3c**). When TFA was added to the heterogeneous mixture of **FF-PBI-1** (1.0 mg) and  $\text{C}_6\text{F}_{14}$  (1.0 mL), the mixture became homogeneously red and fluorescent, thereby confirming that this effect is not dependent on the organic solvent (**Figure 2.3d, e**). Other Brønsted acids such as hydrochloric acid and perfluorononanoic acid also elicited a similar response. The fluorescence of **FF-PBI-1** was also increased upon protonation with these other acids and the resulting compound exhibited preferential solubility for fluororous solvents over organic solvents.

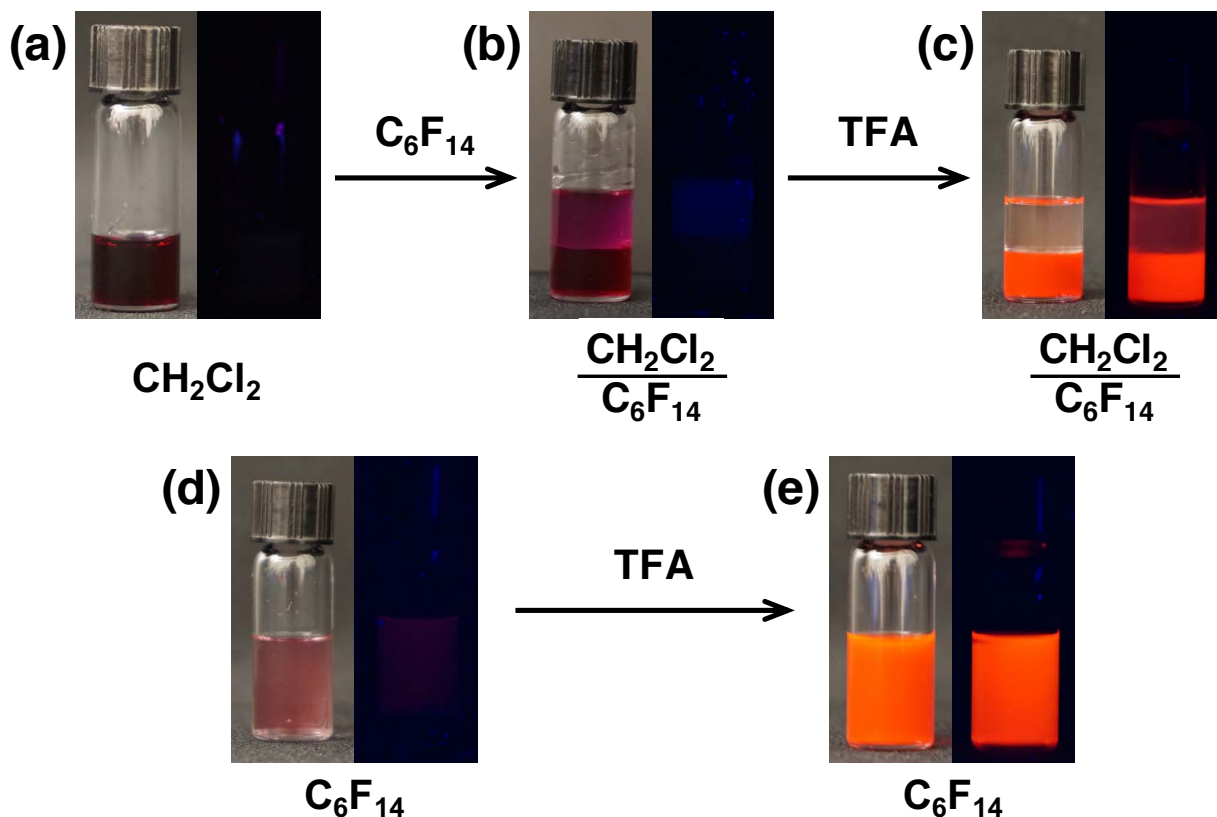


**Figure 2.3** Demonstration of solubility of **FF-PBI-1** and its response to TFA under ambient light (left) and UV light (right,  $\lambda_{ex} = 365$  nm). (a) Photographs of **FF-PBI-1** (0.5 mg) in  $\text{CH}_2\text{Cl}_2$  (0.5 mL), (b) after adding  $\text{C}_6\text{F}_{14}$  (0.5 mL), and (c) after adding TFA. (d) Photographs of the heterogeneous mixture of **FF-PBI-1** (1.0 mg) and  $\text{C}_6\text{F}_{14}$  (1.0 mL) and (e) the sample after adding TFA. Figure adapted with permission.<sup>36</sup> Copyright © 2018, Georg Thieme Verlag KG.

We further investigated the photophysical properties of **FF-PBI-1** in  $\text{CH}_2\text{Cl}_2$  (2.1  $\mu\text{M}$ ) by monitoring the absorbance and fluorescence and the changes upon gradual addition of TFA. With increasing acidity, the absorbance spectra showed a hypsochromic shift (**Figure 2.4a**), and the fluorescence spectra showed an enhanced intensity (**Figure 2.4b**). Plotting the concentration of TFA against the fluorescence intensity at 584 nm (**Figure 2.4b**, inset) gives a sigmoidal shape. We observed a saturation of fluorescence intensity when the concentration of TFA was increased to  $\sim 9$  mM. The quantum yield of **FF-PBI-1** in  $\text{CH}_2\text{Cl}_2$  increased from 6.1% to 54% upon excess addition of TFA (**Table 2.1**). The quantum yield of **FF-PBI-1** in  $\text{C}_6\text{F}_{14}$  with excess TFA was 76%.

The red shifted spectra and higher quantum yields in fluoruous phases highlight the uniqueness of the fluoruous environments (also see **Figure 2.10**).

We attribute the initial fluorescence quenching of **FF-PBI-1** to photo-induced electron transfer (PET) from the peripheral lone pairs of the nitrogen on the aminophenolic groups.<sup>41-46</sup> Upon addition of acid, PET is attenuated as a result of protonation of the aminophenolic groups. This protonation also likely causes the absorbance to shift to a shorter wavelength, because the HOMO of **FF-PBI-1** is also lowered with the decreased electron donation by the protonated pendant aminophenolic groups. The saturation of the fluorescence intensity is perhaps due to full protonation of the aminophenolic groups. The proton induced photophysical change in **FF-PBI-1** is also reversible. Addition of triethylamine to the acidic sample restores the original absorbance and fluorescence spectra to their original shape (**Figure 2.11**).

**Table 2.1** Photophysical Properties of **FF-PBI-1** in CH<sub>2</sub>Cl<sub>2</sub> and C<sub>6</sub>F<sub>14</sub> (+ TFA)

Solvent	$\lambda_{\max}$ (Abs) (nm)	$\lambda_{\max}$ (Em) (nm)	$\Phi_F$ (%)
CH <sub>2</sub> Cl <sub>2</sub>	584	616 <sup>b</sup>	6.1
CH <sub>2</sub> Cl <sub>2</sub> + TFA <sup>a</sup>	549	584 <sup>c</sup>	54
C <sub>6</sub> F <sub>14</sub> + TFA <sup>a</sup>	562	594 <sup>c</sup>	76

<sup>a</sup>Excess TFA was added to the sample. <sup>b</sup> $\lambda_{\text{ex}} = 570$  nm. <sup>c</sup> $\lambda_{\text{ex}} = 500$  nm.

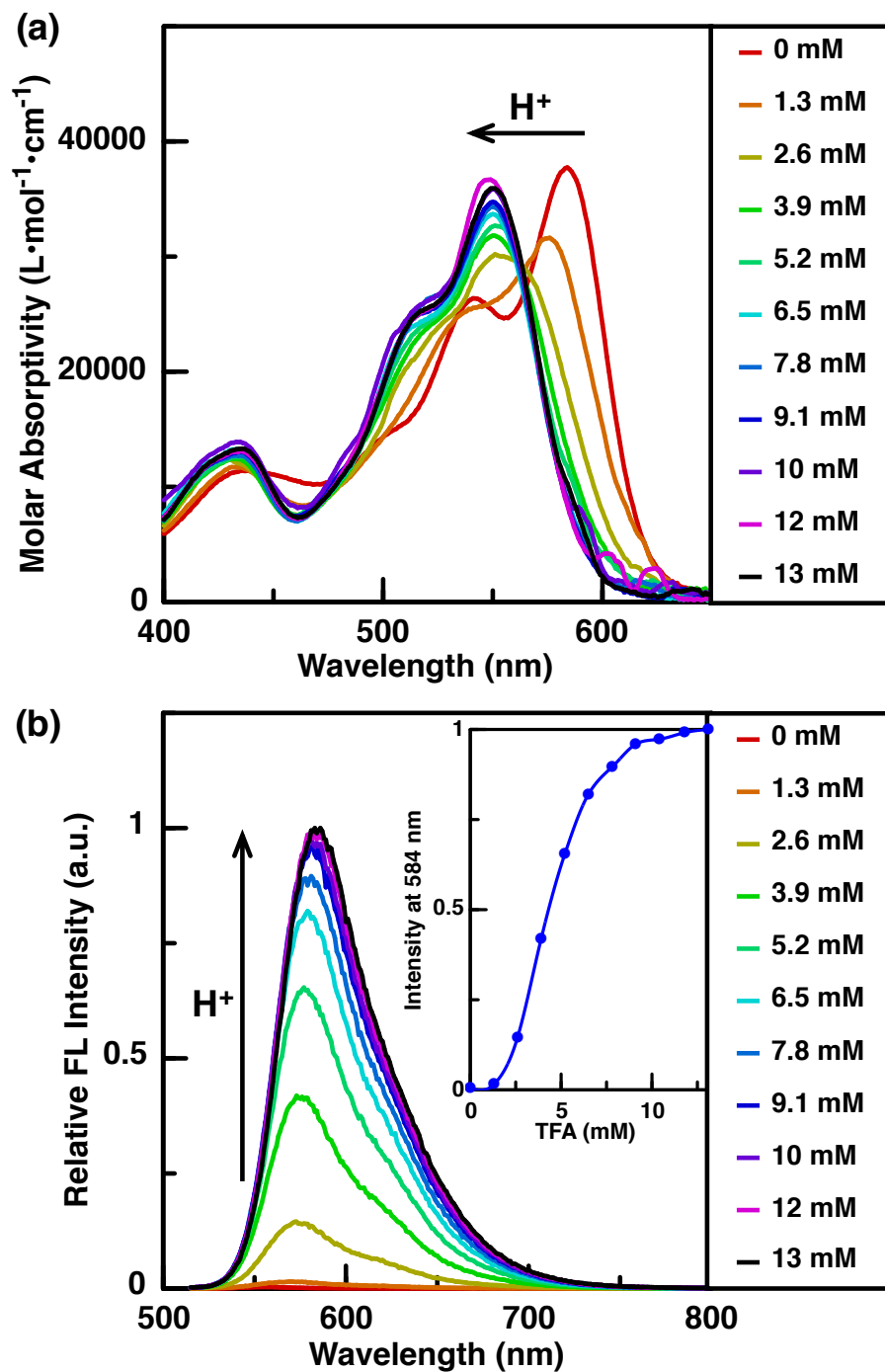
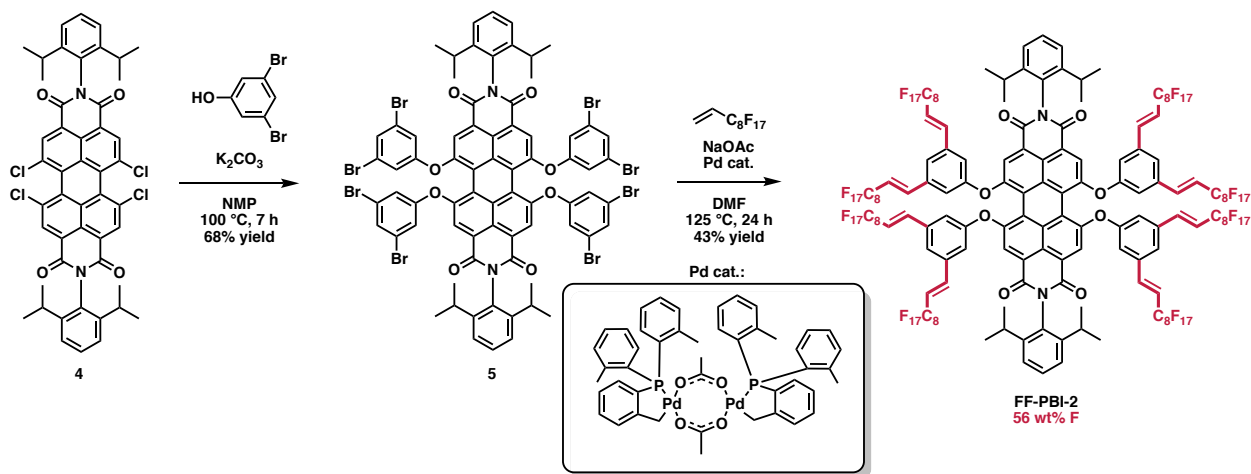


**Figure 2.4** Photophysical properties of FF-PBI-1. (a) Absorbance spectra and (b) relative fluorescence (FL) spectra ( $\lambda_{\text{ex}} = 500 \text{ nm}$ ) of FF-PBI-1 in CH<sub>2</sub>Cl<sub>2</sub> at different concentrations of TFA. Inset: Fluorescence intensity at 584 nm at different concentrations of TFA. Black arrows indicate spectral change with increasing concentration of TFA. Figure adapted with permission.<sup>36</sup> Copyright © 2018, Georg Thieme Verlag KG.

### 2.3.3 Synthesis of FF-PBI-2

Although the protonation of **FF-PBI-1** led to interesting properties such as improved fluororous solubility and fluorescence, we also studied alternative structures of highly fluorinated PBIs that lack basic nitrogens. Beginning with intermediate **4**, we synthesized octabrominated PBI **5** via an  $S_NAr$  reaction with 3,5-dibromophenol in 68% yield (**Scheme 2.2**). We targeted compound **5** as a useful intermediate for subsequent metal-catalyzed cross-coupling reactions. Indeed, compound **5** successfully underwent an eight-fold Herrmann's palladacycle-catalyzed Heck reaction<sup>47,48</sup> between 1*H*,1*H*,2*H*-perfluoro-1-decene to provide the desired product **FF-PBI-2** in 43% yield.<sup>49</sup> **FF-PBI-2** was fully characterized by <sup>1</sup>H, COSY, <sup>19</sup>F NMR spectroscopy, MALDI TOF-MS, and elemental analysis. This efficient eight-fold reaction produces only the all-*trans* product, which is readily isolated by column chromatography.

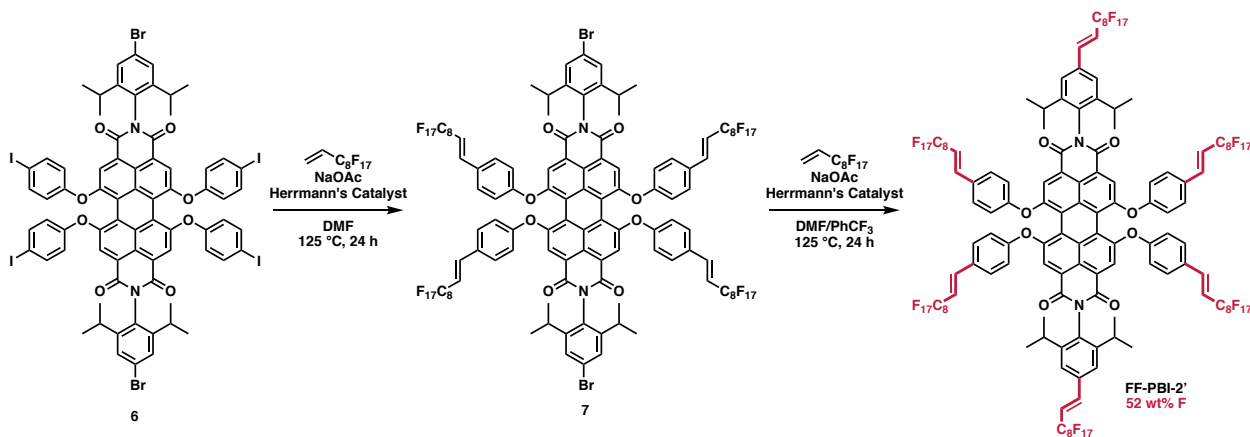


**Scheme 2.2** Synthesis of **FF-PBI-2**. Scheme adapted with permission.<sup>36</sup> Copyright © 2018, Georg Thieme Verlag KG.

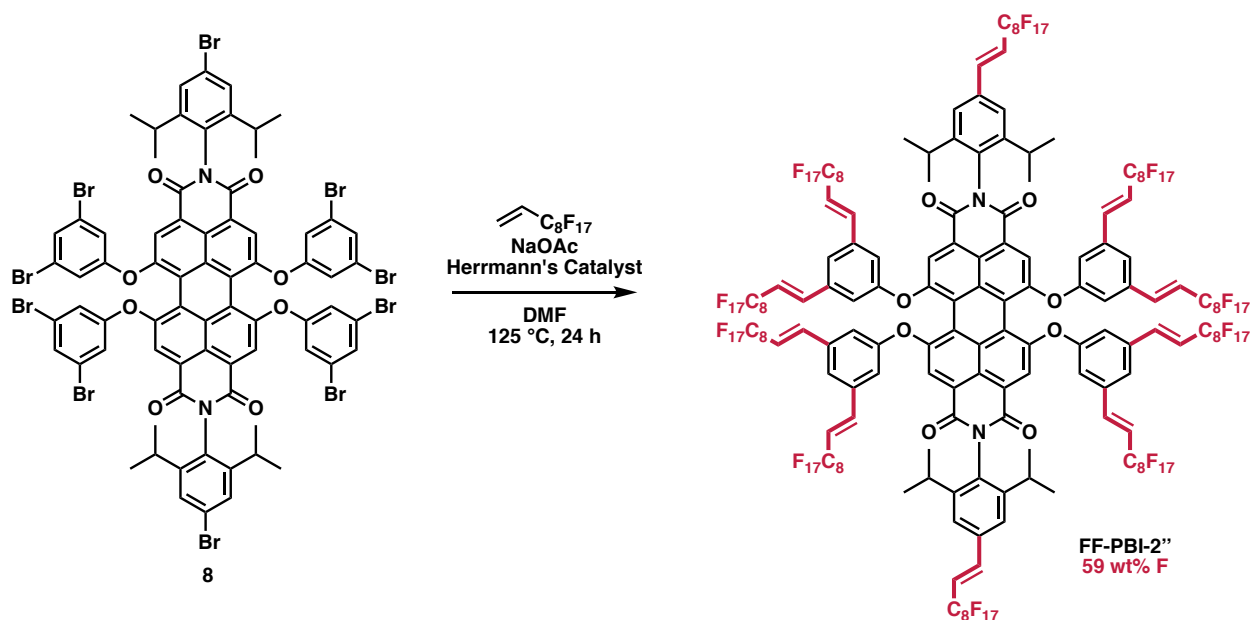
**FF-PBI-2'** and **FF-PBI-2''** were synthesized by an analogous route for comparison. For **FF-PBI-2'**, 4-bromo-2,6-diisopropylaniline<sup>50</sup> and 4-iodophenol was utilized for the imidization and  $S_NAr$  reaction, respectively. When we attempted the fluororous Heck reaction shown in **Scheme 2.3**, we only saw reaction of the iodides by <sup>1</sup>H NMR, even with excess reagents. Thus, a two-step



Heck reaction procedure was required, where the first step couples the iodides, and the second reaction takes place at the bromides. For **FF-PBI-2''**, 4-bromo-2,6-diisopropylaniline and 3,5-dibromophenol was utilized for the imidization and  $S_NAr$  reaction, respectively (**Scheme 2.4**). Surprisingly, the isolation of these products was not straightforward and ultimately unsuccessful.



**Scheme 2.3** Synthesis of **FF-PBI-2'**



**Scheme 2.4** Synthesis of **FF-PBI-2''**

### 2.3.4 Properties of FF-PBI-2

In contrast to **FF-PBI-1**, **FF-PBI-2** showed good solubility ( $>1.0$  mg/mL;  $>2.2 \times 10^2$   $\mu$ M) in common organic solvents such as  $\text{CH}_2\text{Cl}_2$ , toluene, chloroform, acetone, and ethyl acetate. Intriguingly, **FF-PBI-2** also showed good solubility in perfluoroalkanes such as  $\text{C}_6\text{F}_{14}$  and perfluorodecalin. When  $\text{C}_6\text{F}_{14}$  was added to a solution of **FF-PBI-2** in  $\text{CH}_2\text{Cl}_2$ , we observed the extraction of **FF-PBI-2** into the  $\text{C}_6\text{F}_{14}$  layer (**Figure 2.5**). This result illustrates that **FF-PBI-2** has a higher preference towards fluoruous solvents over organic solvents.

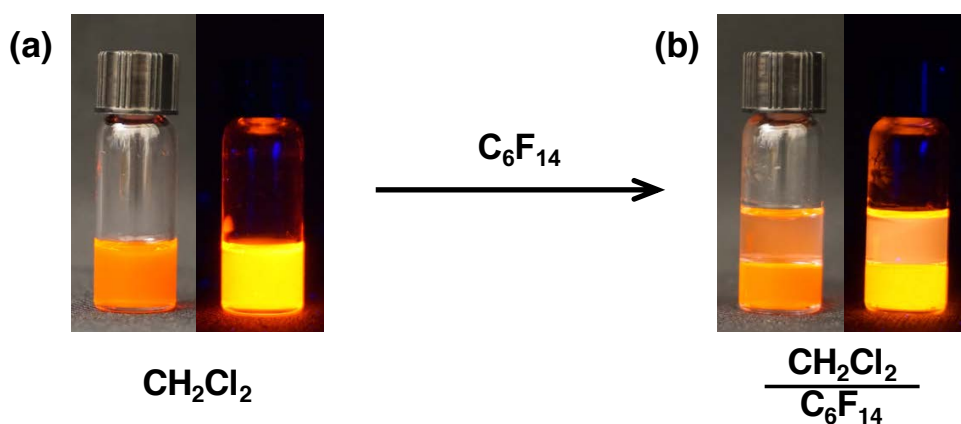


**Figure 2.5** Photographs of **FF-PBI-2** under ambient light (left) and UV light (right,  $\lambda_{\text{ex}} = 365$  nm). (a) Photographs of **FF-PBI-2** (0.5 mg) in  $\text{CH}_2\text{Cl}_2$  (0.5 mL). (b) Photographs of the sample after adding  $\text{C}_6\text{F}_{14}$  (0.5 mL). Figure adapted with permission.<sup>36</sup> Copyright © 2018, Georg Thieme Verlag KG.

The solubility of **FF-PBI-2'** and **FF-PBI-2''** was also investigated, and the results are briefly summarized in **Figure 2.6**. **FF-PBI-2'** showed good solubility in organic solvents such as chloroform; however, it did not dissolve in perfluorinated solvents such as perfluorohexanes. On the other hand, **FF-PBI-2''** showed good solubility in perfluorohexanes, however did not show good solubility in chloroform. The results support in part that a higher wt% F leads to better fluoruous solubility. All three molecules were soluble in hydrofluoroethers such as HFE-7500. The comparison highlights the amphiphilic solubility properties of **FF-PBI-2**, and thus this molecule was selected for further studies.

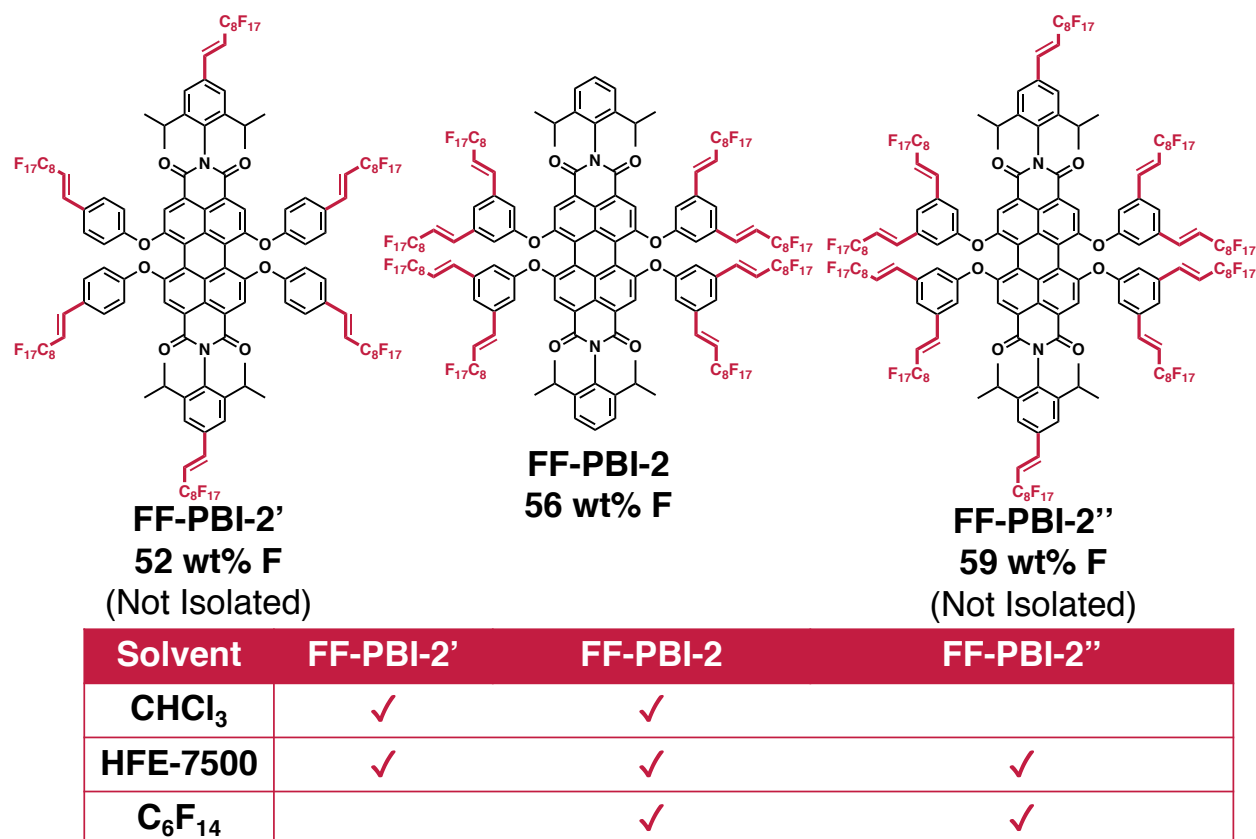


**Figure 2.6** Chemical structures of the **FF-PBI-2** series and their solubilities. A check (✓) indicates the molecule is soluble in the respective solvent.

**FF-PBI-2** was found to exhibit concentration-dependent photophysical properties in C<sub>6</sub>F<sub>14</sub>. **Figure 2.7a** shows the absorbance spectra of **FF-PBI-2** at different concentrations. A peak at 525 nm was observed in the dilute solution. However, a large bathochromic peak at 567 nm develops in concentrated solutions, which is characteristic of a J-aggregation.<sup>51–53</sup> In the fluorescence spectra, in addition to the peak at 558 nm, a large bathochromic peak at 595 nm was observed when the concentration of the solution was increased (**Figure 2.7b**). The quantum yields of **FF-PBI-2** in C<sub>6</sub>F<sub>14</sub> at different concentrations were maintained near 75% (**Figure 2.12**). The red-shifted spectra, increase in the molar absorptivity, and the increased quantum yield for emission all support a J-aggregation. Similar measurements of **FF-PBI-2** in CH<sub>2</sub>Cl<sub>2</sub> showed a completely different trend. In the absorbance spectra, no new peaks were observed when the concentration of

the solution was increased (**Figure 2.7c**). In the fluorescence spectra, the peak at 595 nm simply gradually enhanced in intensity (**Figure 2.7d**). This suggests that the aggregation is exclusively observed in fluoruous solvents. Recently, Cao and Sletten reported the first cyanine dye showing aggregation in the fluoruous phase;<sup>54</sup> however, they utilize 1% CH<sub>2</sub>Cl<sub>2</sub> and a mixture of methoxy- and ethoxynonafluorobutane as their solvent system. Therefore, **FF-PBI-2** presents a unique example of aggregation in pure perfluorinated solvents.

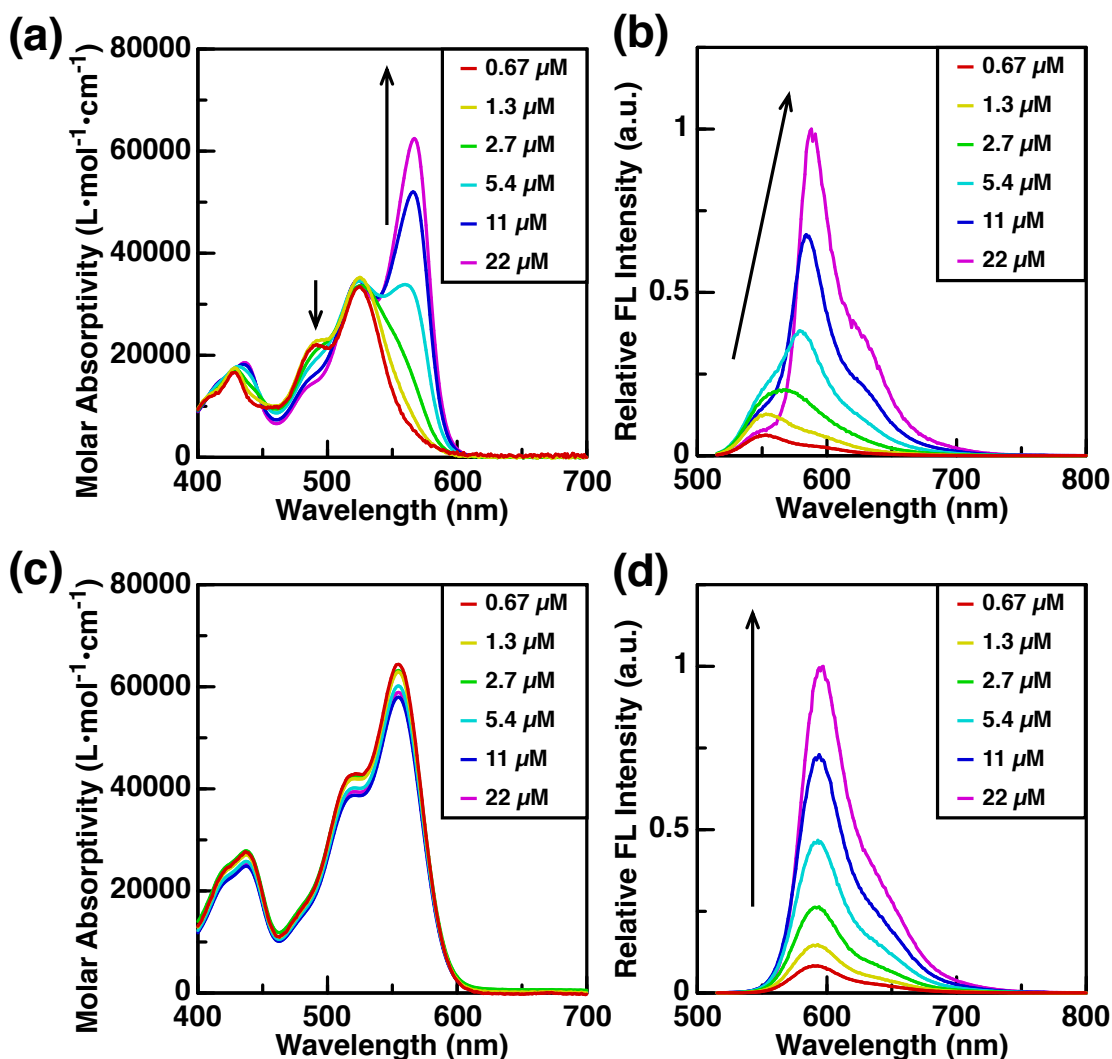


**Figure 2.7** Photophysical properties of **FF-PBI-2** in C<sub>6</sub>F<sub>14</sub> and CH<sub>2</sub>Cl<sub>2</sub>. (a) Absorbance spectra and (b) relative fluorescence spectra ( $\lambda_{\text{ex}} = 500 \text{ nm}$ ) of samples at different concentrations in C<sub>6</sub>F<sub>14</sub>. (c) Absorbance spectra and (d) relative fluorescence spectra ( $\lambda_{\text{ex}} = 500 \text{ nm}$ ) of samples at different concentrations in CH<sub>2</sub>Cl<sub>2</sub>. Black arrows indicate spectral change with increasing concentration. Figure adapted with permission.<sup>36</sup> Copyright © 2018, Georg Thieme Verlag KG.

### 2.3.5 Luminescent Solar Concentrators

Luminescent solar concentrators (LSCs) are a class of materials that can realize the concept of building-integrated photovoltaics (BIPVs), in which photovoltaics (PVs) become a part of the building.<sup>55,56</sup> This technology is ideally suited for solar energy production in urban settings because of the limited area available for installation of PVs and high energy consumption. Typically, LSCs consist of a polymer nanocomposite doped with light-absorbing fluorescent dyes, and small PVs placed at the edge. The PVs convert the fluorescence of the dyes that is guided to the edges by total internal reflection into electricity (**Figure 2.8a**). Unique materials such as quantum dots,<sup>57,58</sup> near-infrared harvesting dyes,<sup>59,60</sup> and aggregation-induced emitting dyes<sup>61,62</sup> have been demonstrated as useful LSCs. From the Swager group, a  $\pi$ -conjugated polymer thin film has been reported as a emissive matrix for energy transfer to perylene bisimide dyes.<sup>63</sup>

We propose the concept of a solution-based archetype, the fluorofluorescent solar concentrator (FSC), in which “fluoro” refers to both fluorescent and fluorine. Solution-based LSCs are interesting because the device architecture can be flexible, and the solvent can be distilled and recycled to minimize waste when replaced. Perfluorinated or “fluorous”<sup>9</sup> solvents are suitable for widespread use because they are odorless, inflammable, nontoxic, photochemically stable, and commercially available.<sup>5</sup> We targeted PBIs as the class of fluorophore for our FSC because they possess attractive photophysical properties such as broad absorbance across the solar spectrum, high fluorescence quantum yield, and photochemical robustness.<sup>28–30</sup> Here, we attempted to utilize **FF-PBI-2** to realize the concept of FSCs.

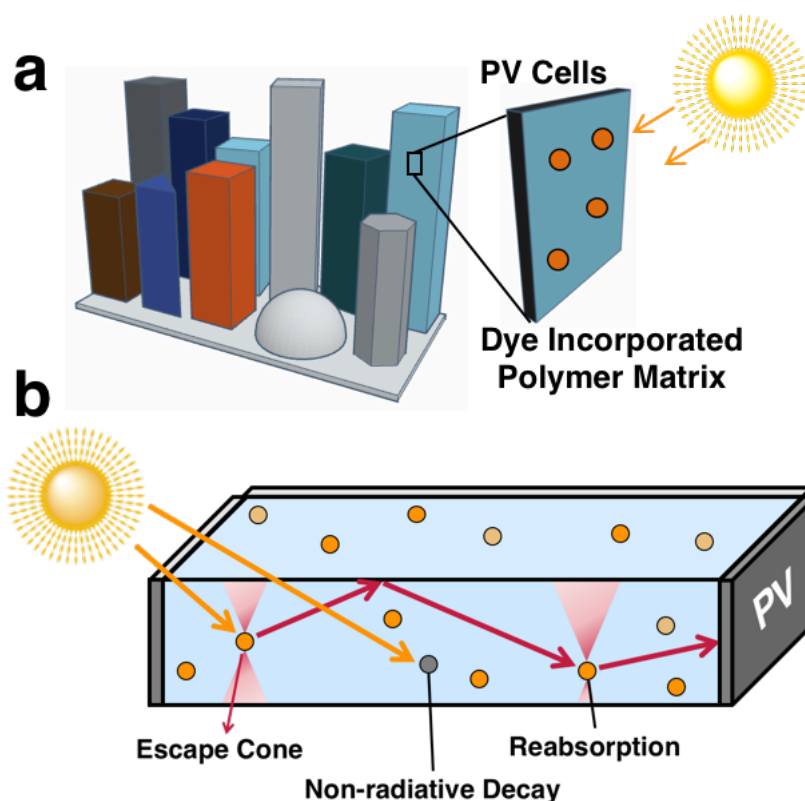


**Figure 2.8** (a) Schematic diagram of building-integrated photovoltaics, and (b) loss mechanisms of luminescent solar concentrators.

A major loss mechanism in LSCs is reabsorption of the fluorescence of the dyes, leading to lower efficiency at higher concentrations and in larger devices (**Figure 2.8b**). This crucially limits the utility of certain LSCs in urban settings where larger devices need to be employed. However, because **FF-PBI-2** was able to retain its high fluorescence quantum yield at high concentrations due to J-aggregation, it may be a promising means to realize the concept for an FSC. We fabricated a device made of poly(methyl methacrylate) (PMMA) with a  $1.1 \times 10^2 \mu\text{M}$  solution of **FF-PBI-2** in FC-770, a fluoruous solvent commonly used in industrial applications (**Figure 2.9a, b**). To test the efficiency of our device, external quantum efficiency (EQE), defined as the fraction of incident photons emanating from the device, was measured according to a scheme reported by Coropceanu and Bawendi (**Figure 2.9c**).<sup>58</sup> We first measured the EQE of the entire device emission (PL1). As shown in **Figure 2.9d**, the EQE spectra of the device matches the

absorbance spectra well, suggesting a high quantum yield at this concentration. We then covered the edges to obtain EQE from the face emission (PL2). By subtracting PL2 from PL1, we obtain the edge EQE. The highest edge EQE was found to be 33% (observed at 566 nm), which was lower than our previous example (40%, observed at 405 nm).<sup>63</sup> A direct comparison of the two LSCs is not feasible since the overall performance depends on the choice of the PV cell. For materials based on PMMA, the maximum theoretical edge EQE is 74%, as defined by Snell's Law shown in **Equation 2.1**.<sup>57</sup> Future work will focus on optimizing the edge EQE of our device at different concentrations. Monte Carlo simulations to predict the edge EQE of larger devices are also ongoing in the Bawendi group.

$$\text{Equation 2.1} \quad \text{Maximum Edge EQE} = 1 - \left(\frac{1}{n^2}\right)^{1/2}, \text{ where } n = 1.49 \text{ for PMMA}$$

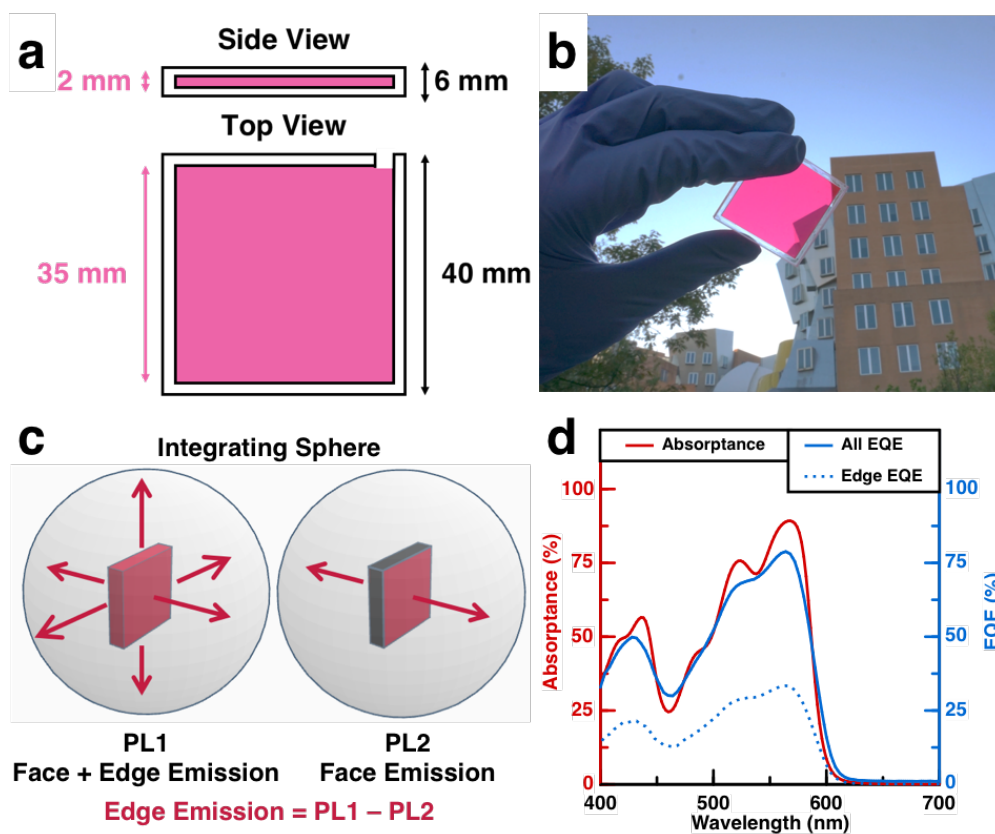


**Figure 2.9** Device architecture and external quantum efficiency experimental setup. (a) Dimensions of the fabricated PMMA device. (b) A picture of the device in ambient environment. (c) Schematic representation of the edge emission measurement. (d) Absorbance and EQE spectra of the device.

## 2.4 Conclusions

In conclusion, we have disclosed two synthetic methods to obtain fluorofluorescent perylene bisimides. **FF-PBI-1** only showed moderate solubility in both organic and fluorous solvents, but the solubility could be improved upon addition of Brønsted acid. On the other hand, **FF-PBI-2** showed useful solubility in both organic and fluorous solvents. Titration measurements of **FF-PBI-1** and concentration-dependent measurements of **FF-PBI-2** demonstrate the interesting and potentially useful photophysical properties of the fluorofluorescent PBIs. For example, **FF-PBI-2** was utilized to develop a fluorofluorescent solar concentrator, where an edge EQE of 33% at 566 nm was achieved. We envision these dyes will enable promising applications in the fluorous phase, including the incorporation of fluorofluorescent PBIs in the fluorous phase of dynamically reconfigurable complex emulsions<sup>16</sup> and LSCs.

## 2.5 Experimental

### 2.5.1 General

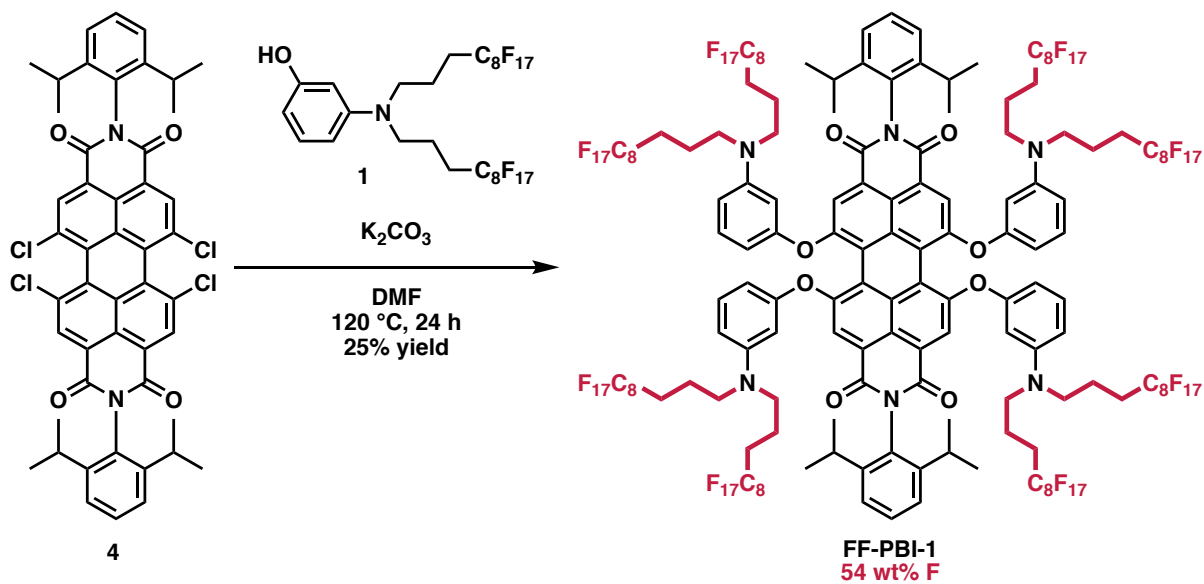
All chemical reagents were purchased from Sigma-Aldrich, Synquest Laboratories, or TCI, and used without purification unless noted otherwise. Thin layer chromatography was performed with Baker-flex Silica Gel 1B-F plates (JT Baker). Flash chromatography was performed using technical grade silica gel with 60 Å pores and 230–400 mesh particle size (Sigma-Aldrich, 717185). PMMA sheets were purchased from McMaster-Carr.

<sup>1</sup>H, <sup>13</sup>C, and <sup>19</sup>F NMR spectra were recorded on a JEOL model JNM-ECZ500R/S1 spectrometer operating at 500, 126, and 470 MHz, respectively. For <sup>1</sup>H, <sup>13</sup>C NMR spectra, deuterated solvent references were used as internal standards (<sup>1</sup>H: 7.26 ppm for CDCl<sub>3</sub>, 5.32 ppm for CD<sub>2</sub>Cl<sub>2</sub>; <sup>13</sup>C: 77.16 ppm for CDCl<sub>3</sub>). For <sup>19</sup>F NMR spectra, α,α,α-trifluorotoluene was added

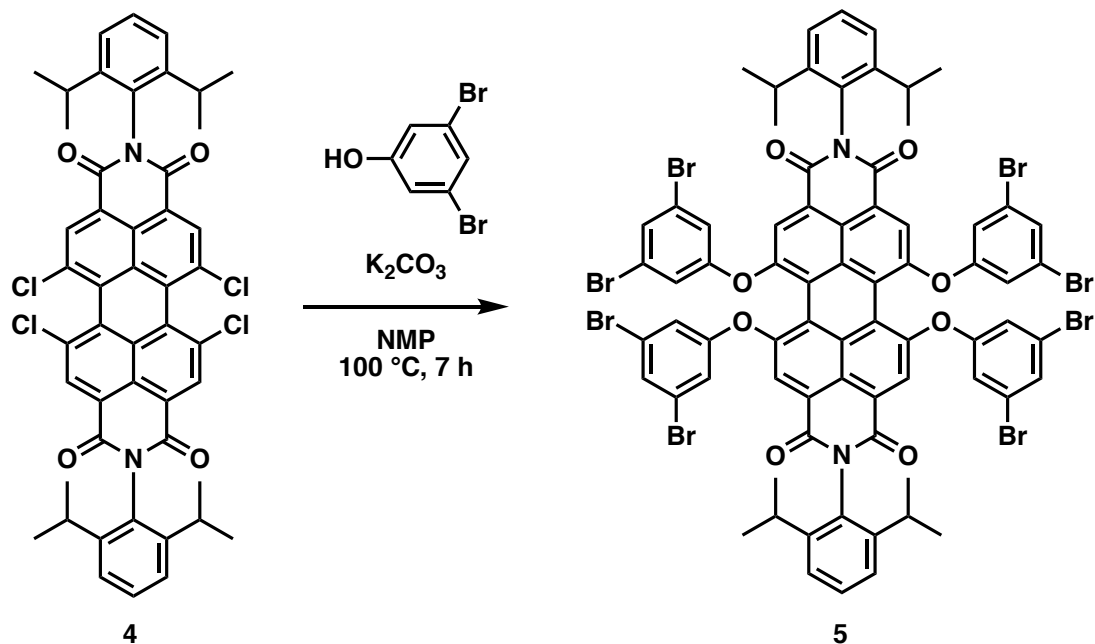


as an internal standard and the spectra was referenced to  $-63.72$  ppm. Multiplicities are abbreviated as singlet (s), doublet (d), triplet (t), septet (sep), multiplet (m). Matrix-assisted laser desorption/ionization time-of-flight (MALDI-TOF) mass spectra were obtained at the Massachusetts Institute of Technology Biopolymers & Proteomics Core Laboratory. Electrospray ionization (ESI) high-resolution mass spectra (HRMS) were obtained at the MIT Department of Chemistry Instrumentation Facility. Elemental analysis data were obtained by Robertson Microlit Laboratories. Absorbance spectra were obtained at room temperature on a Cary 4000 UV/Vis spectrophotometer (Agilent Technologies) with a scan rate of  $600$  nm/min. The instrument was blanked on the solvent prior to obtaining a spectrum. Fluorescence spectra were obtained at room temperature on a Horiba Jobin Yvon SPEX Fluorolog- $\tau 3$  fluorimeter (model FL-321, 450 W Xenon lamp). Quantum yields were determined by using Horiba Quanta- $\phi$  integrating sphere. Absorbance and fluorescence data were collected in a quartz cuvette (1 cm path length). EQE measurements were conducted in the Baldo group (MIT).

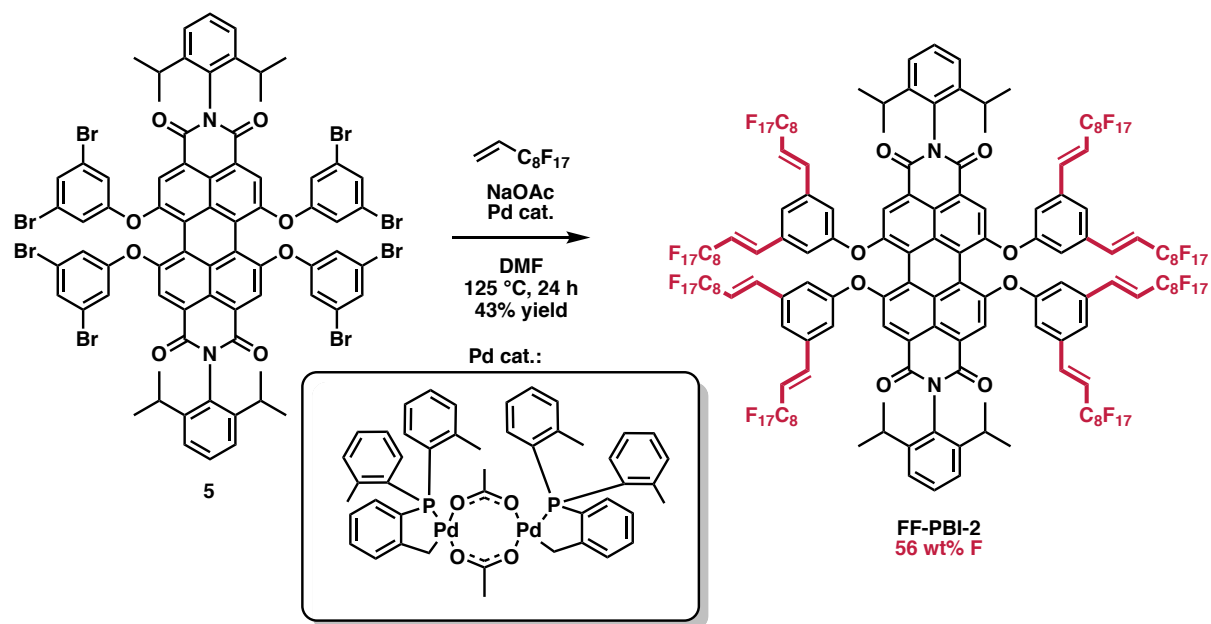
### 2.5.2 Synthetic Procedures



**FF-PBI-1.** A mixture of compound **4** (0.150 g, 0.176 mmol), compound **1** (1.04 g, 1.01 mmol), and anhydrous K<sub>2</sub>CO<sub>3</sub> (0.123 g, 0.892 mmol) in anhydrous *N,N*-dimethylformamide (DMF) (6 mL) was stirred at 120 °C under Ar for 24 h. Then, the reaction was cooled to room temperature. The precipitated product was filtered under suction, washed three times with water (100 mL), and dried under vacuum. The residue was chromatographed on silica gel using hexanes/ CH<sub>2</sub>Cl<sub>2</sub> (2:1 v/v) as an eluent, and the fraction containing **FF-PBI-1** (R<sub>f</sub> = 0.50) was collected and evaporated to dryness to provide a purple solid (0.212 g, 0.0440 mmol, 25% yield). <sup>1</sup>H NMR (500 MHz, CD<sub>2</sub>Cl<sub>2</sub>, 25 °C): δ (ppm) 8.20 (s, 4H), 7.46 (t, *J* = 7.5 Hz, 2H), 7.29 (d, *J* = 8.0 Hz, 4H), 7.17 (t, *J* = 8.0 Hz, 4H), 6.47 (d, *J* = 8.0 Hz, 4H), 6.39 (d, *J* = 8.0 Hz, 4H), 6.33 (s, 4H), 3.21 (d, *J* = 6.5 Hz, 16H), 2.67 (sep, *J* = 7.0 Hz, 4H), 1.96–2.10 (m, 16H), 1.72–1.83 (m, 16H), 1.06 (d, *J* = 6.5 Hz, 24H). <sup>19</sup>F NMR (470 MHz, CD<sub>2</sub>Cl<sub>2</sub>, 25 °C): δ (ppm) -82.00 (t, 9.4 Hz, 24F), -114.84 (br, 16F), -122.84 (br, 16F), -123.02 (br, 32F), -123.81 (br, 16F), -124.47 (br, 16F), -127.24 (br, 16F). MALDI-TOF MS: *m/z* calcd. for C<sub>160</sub>H<sub>102</sub>F<sub>136</sub>N<sub>6</sub>O<sub>8</sub>+H<sup>+</sup> [M+H]<sup>+</sup>: 4819.5678, found: 4819.80. Anal. calcd. for C<sub>160</sub>H<sub>102</sub>F<sub>136</sub>N<sub>6</sub>O<sub>8</sub> (%): C, 39.87; H, 2.13; N, 1.74. Found: C, 39.35; H, 2.08; N, 1.65.

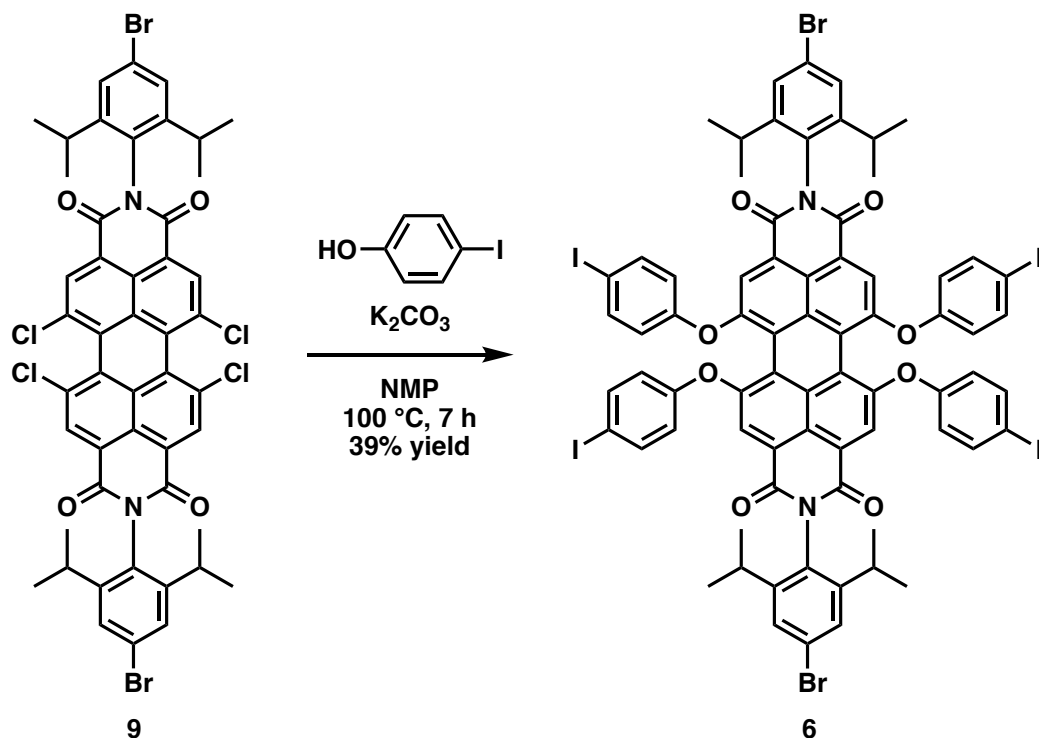


**Compound 5.** A mixture of compound **4** (0.320 g, 0.377 mmol), 3,5-dibromophenol (0.907 g, 3.60 mmol), and anhydrous  $K_2CO_3$  (0.256 g, 1.85 mmol) in anhydrous 1-methyl-2-pyrrolidinone (NMP) (4 mL) was stirred at 100 °C under Ar for 7 h. Then, the reaction mixture was cooled to room temperature and poured into hydrochloric acid (30 mL, 1 M). The precipitated product was filtered under suction, washed three times with water (100 mL), and dried under vacuum. The residue was chromatographed on silica gel using toluene as an eluent, and the fraction containing compound **5** ( $R_f = 0.70$ ) was collected and evaporated to dryness under reduced pressure to provide a pink-red solid (0.440 g, 0.257 mmol, 68% yield).  $^1H$  NMR (500 MHz,  $CDCl_3$ , 25 °C):  $\delta$  (ppm) 8.33 (s, 4H), 7.48 (t,  $J = 8.0$  Hz, 2H), 7.45 (t,  $J = 1.5$  Hz, 4H), 7.32 (d,  $J = 8.0$  Hz, 4H), 7.03 (d,  $J = 1.5$  Hz, 8H), 2.71 (sep,  $J = 7.0$  Hz, 4H), 1.15 (d,  $J = 7.0$  Hz, 24H).  $^{13}C$  NMR (126 MHz,  $CDCl_3$ , 25 °C):  $\delta$  (ppm) 162.73, 156.66, 154.52, 145.70, 133.12, 130.48, 130.14, 129.94, 124.26, 124.01, 123.89, 121.98, 121.76, 121.53, 121.34, 29.32, 24.17. HRMS (ESI):  $m/z$  calcd. for  $C_{72}H_{50}Br_8N_2O_8 + H^+$   $[M+H]^+$ : 1710.7057, found: 1710.7048.



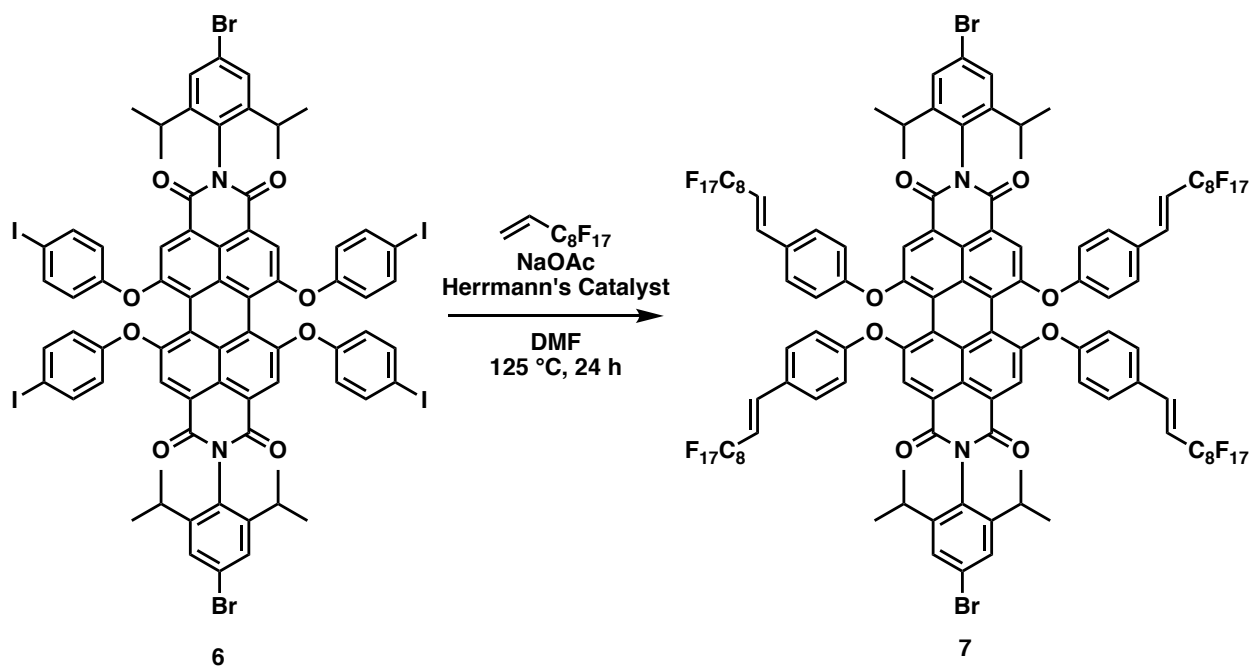
**FF-PBI-2.** A mixture of compound **5** (0.439 g, 0.257 mmol), 1H,1H,2H-perfluoro-1-decene (1.44 g, 3.23 mmol), NaOAc (0.256 g, 3.04 mmol), and anhydrous DMF (5 mL) was treated with three freeze-pump-thaw cycles. Then, Herrmann's catalyst (50.2 mg, 0.0535 mmol) was added to the mixture and it was stirred for 24 h at 125 °C. Upon cooling the reaction mixture to room temperature, the residue was dissolved in AcOEt (100 mL) and HCl (1 M, 100 mL). The organic layer was separated, washed with water (100 mL  $\times$  3) and brine (100 mL), dried with MgSO<sub>4</sub>, and evaporated to dryness under reduced pressure. The residue was chromatographed on silica gel using CHCl<sub>3</sub> as an eluent, and the fraction containing **FF-PBI-2** ( $R_f = 0.50$ ) was collected and evaporated to dryness to provide a pink-red solid (0.517 g, 0.112 mmol, 43% yield). <sup>1</sup>H NMR (500 MHz, CD<sub>2</sub>Cl<sub>2</sub>, 25 °C):  $\delta$  (ppm) 8.31 (s, 4H), 7.47 (t,  $J = 7.5$  Hz, 2H), 7.30–7.31 (m, 8H), 7.03–7.06 (m, 16H), 5.98–6.06 (m, 8H), 2.67 (sep, 7.0 Hz, 4H), 1.07 (d, 7.0 Hz, 24H). <sup>19</sup>F NMR (470 MHz, CD<sub>2</sub>Cl<sub>2</sub>, 25 °C,  $\alpha,\alpha,\alpha$ -trifluorotoluene was added as an internal standard and was referenced to -63.72 ppm):  $\delta$  (ppm) -81.98 (t, 9.9 Hz, 24F), -112.78 (br, 16F), -122.52 (br, 16F), -122.99 (br, 32F), -123.80 (br, 16F), -123.96 (br, 16F), -127.22 (br, 16F). MALDI-TOF MS:  $m/z$  calcd. for

C<sub>152</sub>H<sub>66</sub>F<sub>136</sub>N<sub>2</sub>O<sub>8</sub>: 4630.2648, found: 4630.13. Anal. calcd. for C<sub>152</sub>H<sub>66</sub>F<sub>136</sub>N<sub>2</sub>O<sub>8</sub> (%): C, 39.41; H, 1.44; N, 0.60. Found: C, 39.40; H, 1.33; N, 0.60.



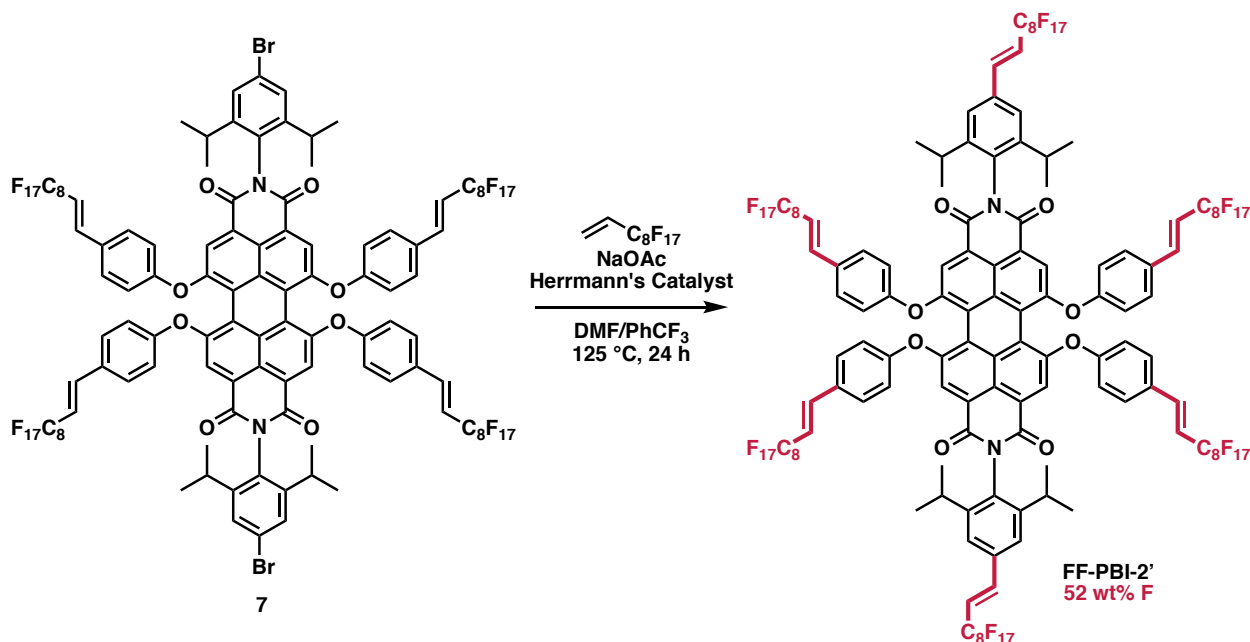
**Compound 6 (not isolated).** A mixture of compound **9** (0.910 g, 0.904 mmol), 4-iodophenol (1.72 g, 7.82 mmol), and anhydrous K<sub>2</sub>CO<sub>3</sub> (0.616 g, 4.46 mmol) in anhydrous 1-methyl-2-pyrrolidinone (NMP) (25 mL) was stirred at 100 °C under Ar for 7 h. Then, the reaction mixture was cooled to room temperature and poured into hydrochloric acid (100 mL, 1 M). The precipitated product was filtered under suction, washed three times with water (100 mL), and dried under vacuum. The residue was chromatographed on silica gel using chloroform as an eluent, and the fraction containing compound **6** (R<sub>f</sub> = 0.75) was collected and evaporated to dryness under reduced pressure to provide a pink-red solid (0.610 g, 0.350 mmol, 39% yield). <sup>1</sup>H NMR (500 MHz, CDCl<sub>3</sub>, 25 °C): δ (ppm) 8.22 (s, 4H), 7.60 (d, *J* = 8.8 Hz, 8H), 7.39 (s, 4H), 6.69 (d, *J* = 8.8 Hz, 8H), 2.59-2.66 (m, 4H), 1.11 (d, *J* = 6.9 Hz, 24H). <sup>13</sup>C NMR could not be obtained. HRMS (ESI): *m/z* calcd.

for  $[C_{72}H_{52}Br_2I_4N_2O_8 + H]^+$ : 1738.8348; found: 1738.84. Single crystal could be obtained by slow diffusion of methanol into a toluene solution of compound **6**.



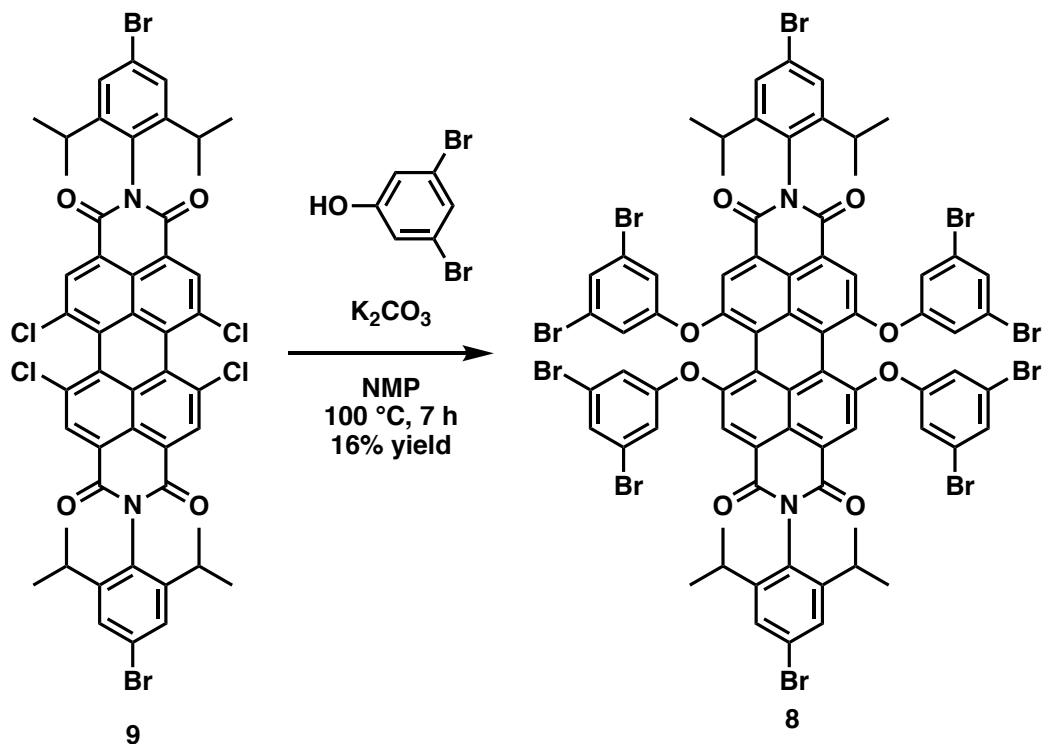
**Compound 7 (not isolated).** A mixture of compound **6** (0.429 g, 0.246 mmol), 1H,1H,2H-perfluoro-1-decene (2.25 g, 5.04 mmol), NaOAc (0.412 g, 5.02 mmol), and anhydrous DMF (5 mL) was treated with three freeze-pump-thaw cycles. Then, Herrmann's catalyst (47.0 mg, 0.0501 mmol) was added to the mixture, and it was stirred for 24 h at 125 °C. Upon cooling the reaction mixture to room temperature, the residue was dissolved in AcOEt (100 mL) and HCl (1 M, 100 mL). The organic layer was separated, washed with water (100 mL  $\times$  3) and brine (100 mL), dried with  $MgSO_4$ , and evaporated to dryness under reduced pressure. The residue was chromatographed on silica gel using  $CHCl_3$  as an eluent, and the fraction containing compound **7** ( $R_f = 0.55$ ) was collected and evaporated to dryness to provide a pink-red solid (0.600 g, 0.112 mmol, 81% yield).  $^1H$  NMR (500 MHz,  $CDCl_3$ , 25 °C):  $\delta$  (ppm) 8.29 (s, 4H), 7.40 (m, 12H), 7.10 (d,  $J = 16.4$  Hz, 4H), 6.96 (d,  $J = 8.0$  Hz, 8H), 6.11 (dt,  $J = 28.4, 12.4$  Hz, 4H), 2.60-2.68 (m, 4H), 1.11 (d,  $J = 5.3$

Hz, 24H).  $^{19}\text{F}$  NMR (470 MHz,  $\text{CDCl}_3$ , 25 °C):  $\delta$  (ppm) -80.68 (t,  $J = 9.8$  Hz, 3F), -111.07 (m, 2F), -121.33 (m, 2F), -121.86 (m, 4F), -122.65 (m, 2F), -123.01 (m, 2F), -126.06 (m, 2F).



**Compound FF-PBI-2' (not isolated).** A mixture of compound **6** (81.2 mg, 0.0269 mmol), 1H,1H,2H-perfluoro-1-decene (230 mg, 0.516 mmol), NaOAc (42.2 mg, 0.514 mmol),  $\text{PhCF}_3$  (1 mL), and anhydrous DMF (1 mL) was treated with three freeze-pump-thaw cycles. Then, Herrmann's catalyst (5.0 mg, 0.00533 mmol) was added to the mixture, and it was stirred for 24 h at 125 °C. Upon cooling the reaction mixture to room temperature, the residue was dissolved in AcOEt (100 mL) and HCl (1 M, 10 mL). The organic layer was separated, washed with water (10 mL  $\times$  3) and brine (10 mL), dried with  $\text{MgSO}_4$ , and evaporated to dryness under reduced pressure. The residue was chromatographed on silica gel using  $\text{CHCl}_3$  as an eluent, and the fraction containing compound **7** ( $R_f = 0.55$ ) was collected and evaporated to dryness to provide a pink-red solid (0.600 g, 0.112 mmol, 81% yield).  $^1\text{H}$  NMR (500 MHz,  $\text{CDCl}_3$ , 25 °C): 8.30 (s, 4H), 7.38-7.41 (m, 12H), 7.23 (d,  $J = 16.0$  Hz, 2H), 7.10 (d,  $J = 16.0$  Hz, 4H), 6.97 (dd,  $J = 8.8, 1.9$  Hz, 8H),

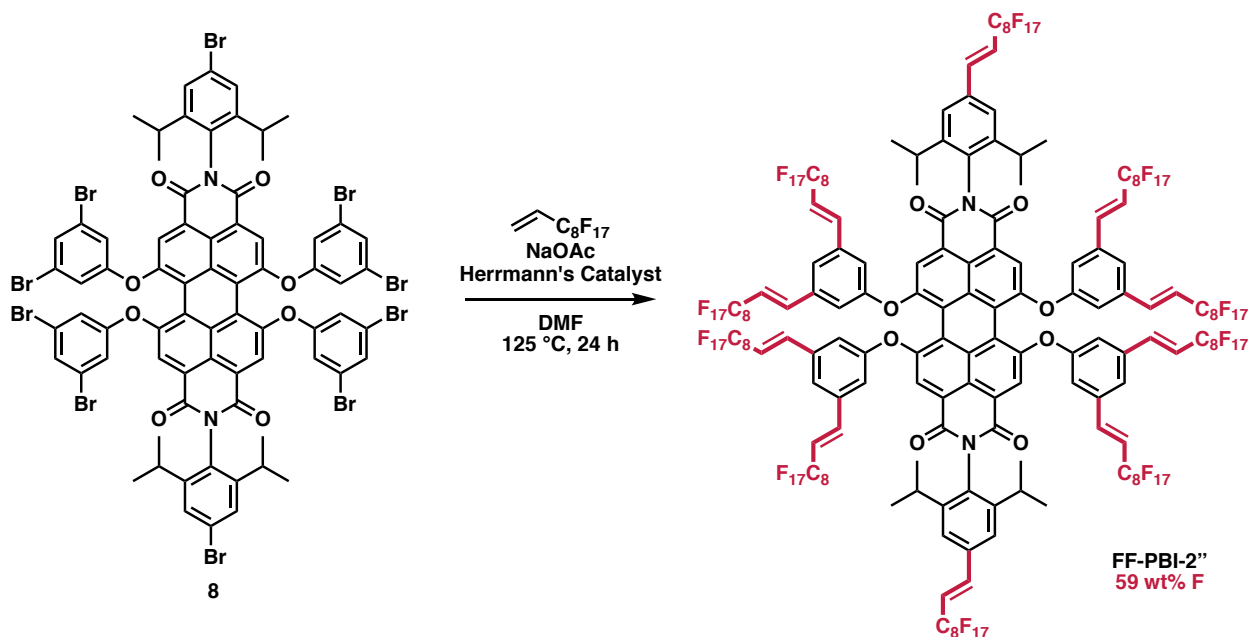
6.20-6.28 (m, 2H), 6.07-6.15 (m, 4H), 2.68-2.74 (m, 4H), 1.12-1.16 (m, 24H).  $^{19}\text{F}$  NMR (470 MHz,  $\text{CDCl}_3$ , 25 °C):  $\delta$  (ppm) -80.67 (t,  $J = 9.8$  Hz, 6F), -80.73 (t,  $J = 10.5$  Hz, 12F), -110.88 (d,  $J = 11.2$  Hz, 4F), -111.12 (d,  $J = 11.2$  Hz, 8F), -121.30 (m, 12F), -121.87 (m, 24F), -122.75 (m, 16F), -123.04 (m, 8F), -126.06 (m, 12F).



**Compound 8 (not isolated).** A mixture of compound **9** (0.103 g, 0.102 mmol), 3,5-dibromophenol (0.263 g, 1.04 mmol), and anhydrous  $\text{K}_2\text{CO}_3$  (0.096 g, 0.695 mmol) in anhydrous 1-methyl-2-pyrrolidinone (NMP) (25 mL) was stirred at 100 °C under Ar for 7 h. Then, the reaction mixture was cooled to room temperature and poured into hydrochloric acid (100 mL, 1 M). The precipitated product was filtered under suction, washed three times with water (100 mL), and dried under vacuum. The residue was chromatographed on silica gel using chloroform as an eluent, and the fraction containing compound **6** ( $R_f = 0.75$ ) was collected and evaporated to dryness under reduced pressure to provide a pink-red solid (30.9 g, 0.0165 mmol, 16% yield).  $^1\text{H}$  NMR (500 MHz,  $\text{CDCl}_3$ ,



25 °C):  $\delta$  (ppm) 8.30 (s, 4H), 7.49 (s, 4H), 7.45 (s, 4H), 7.08 (d,  $J = 1.5$  Hz, 8H), 2.64-2.72 (m, 4H), 1.11 (d,  $J = 6.9$  Hz, 24H).  $^{13}\text{C}$  NMR could not be obtained. HRMS (ESI):  $m/z$  calcd. for  $[\text{C}_{72}\text{H}_{48}\text{Br}_{10}\text{N}_2\text{O}_8 + \text{H}]^+$ : 1868.5248; found: 1868.5202.



**Compound FF-PBI-2'' (not isolated).** A mixture of compound **6** (81.2 mg, 0.0269 mmol), 1H,1H,2H-perfluoro-1-decene (230 mg, 0.516 mmol), NaOAc (42.2 mg, 0.514 mmol),  $\text{PhCF}_3$  (1 mL), and anhydrous DMF (1 mL) was treated with three freeze-pump-thaw cycles. Then, Herrmann's catalyst (5.0 mg, 0.00533 mmol) was added to the mixture, and it was stirred for 24 h at 125 °C. Upon cooling the reaction mixture to room temperature, the residue was dissolved in AcOEt (10 mL) and HCl (1 M, 10 mL). The organic layer was separated, washed with water (10 mL  $\times$  3) and brine (10 mL), dried with  $\text{MgSO}_4$ , and evaporated to dryness under reduced pressure. The residue was chromatographed on silica gel using  $\text{CHCl}_3$  as an eluent, and the fraction containing compound **FF-PBI-2''** ( $R_f = 0.55$ ) was collected and evaporated to dryness to provide a pink-red solid (trace).  $^1\text{H}$  NMR (500 MHz,  $\text{CDCl}_3$ , 25 °C): 8.31 (s, 4H), 7.40 (s, 4H), 7.27 (s,

4H), 7.00 (m, 18H), 6.20-6.28 (m, 2H), 5.93-6.00 (m, 8H), 2.60-2.65 (m, 4H), 1.08 (d,  $J = 6.9$  Hz, 24H).  $^{19}\text{F}$  NMR (470 MHz,  $\text{CDCl}_3$ , 25 °C):  $\delta$  (ppm) -80.74 (m, 30F), -111.85 (m, 20F), -121.53 (m, 20F), -121.92 (m, 40F), -122.78 (m, 40F), -126.13 (m, 20F).

## 2.6 Appendix for CHAPTER 2

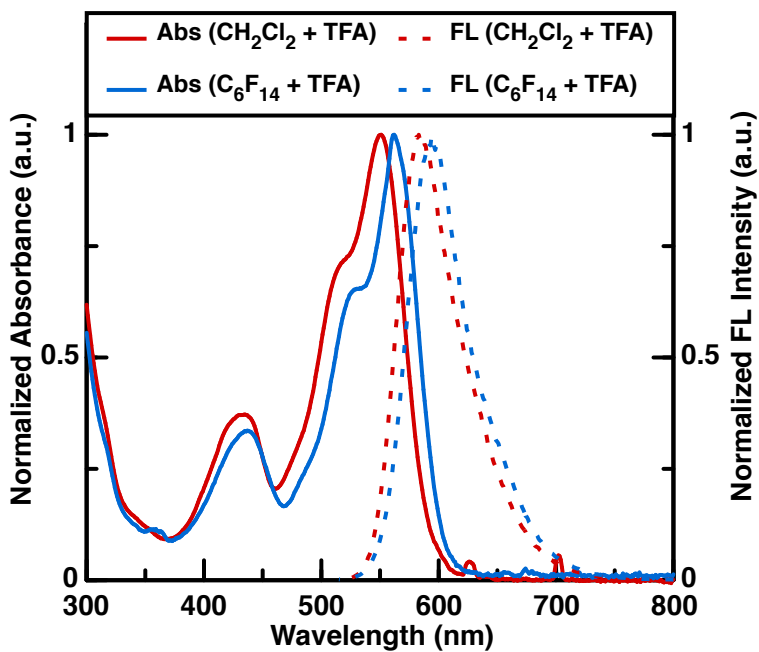


**Figure 2.10** Normalized absorbance and fluorescence spectra of **FF-PBI-1** in CH<sub>2</sub>Cl<sub>2</sub> + TFA and C<sub>6</sub>F<sub>14</sub> + TFA.

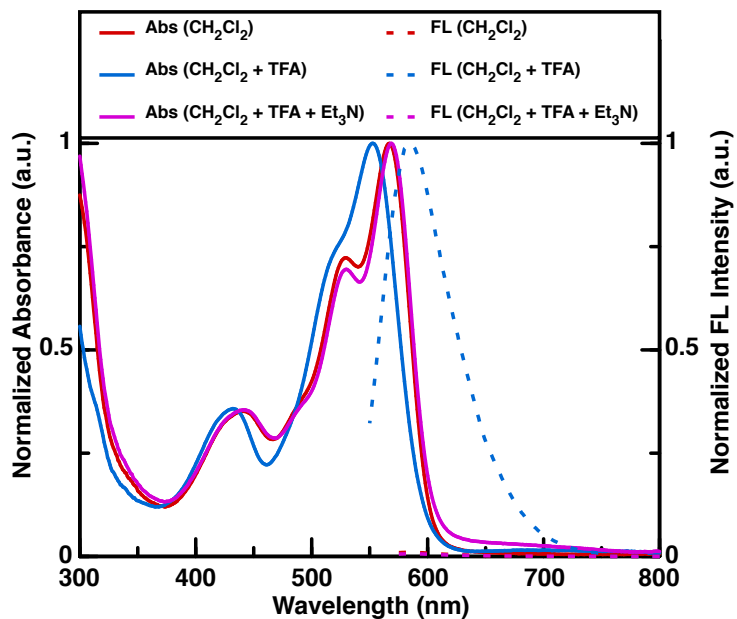


**Figure 2.11** Normalized absorbance and fluorescence spectra of **FF-PBI-1** in CH<sub>2</sub>Cl<sub>2</sub> and its change upon addition of TFA and Et<sub>3</sub>N.

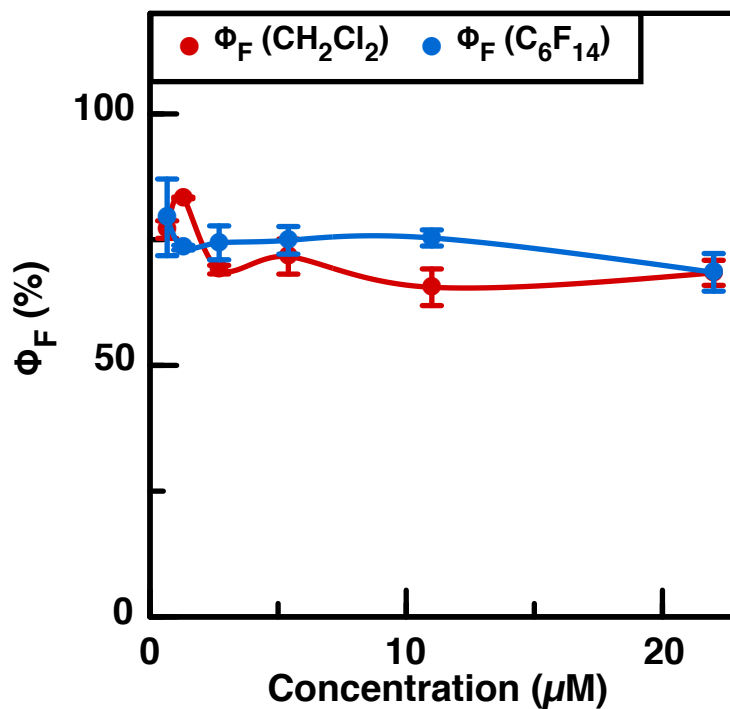


**Figure 2.12** Quantum yield ( $\Phi_F$ ) of FF-PBI-2 in  $\text{CH}_2\text{Cl}_2$  and  $\text{C}_6\text{F}_{14}$  at different concentrations.  $\Phi_F$  was determined by using an integrating sphere. The error bars represent values of  $\Phi_F$  measured at three different excitation wavelengths.

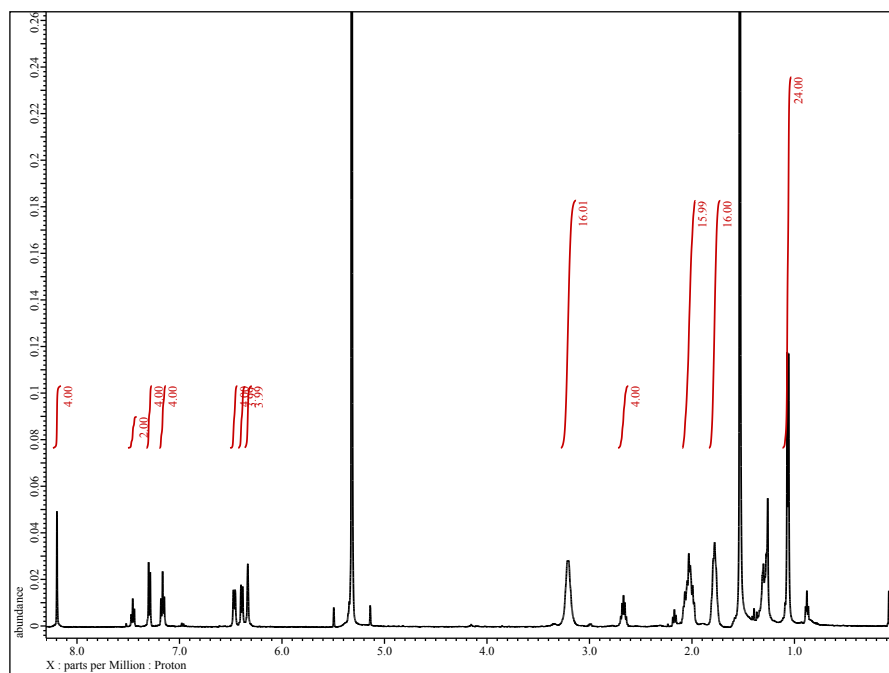


**Figure 2.13** Compound FF-PBI-1  $^1\text{H}$  NMR (500 MHz,  $\text{CD}_2\text{Cl}_2$ , 25 °C)

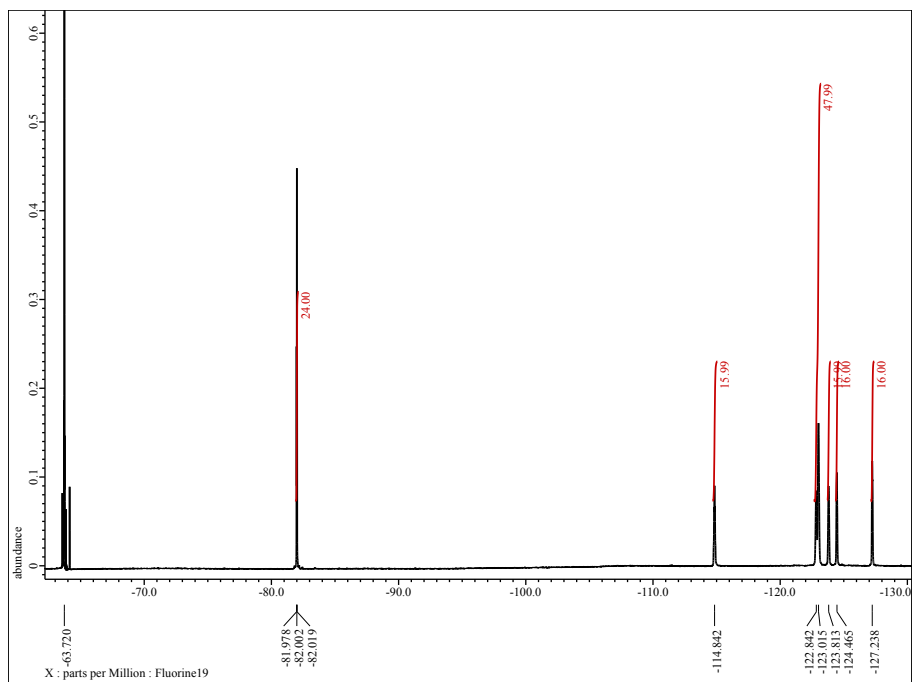


**Figure 2.14** Compound **FF-PBI-1**  $^{19}\text{F}$  NMR (470 MHz,  $\text{CD}_2\text{Cl}_2$ , 25 °C)

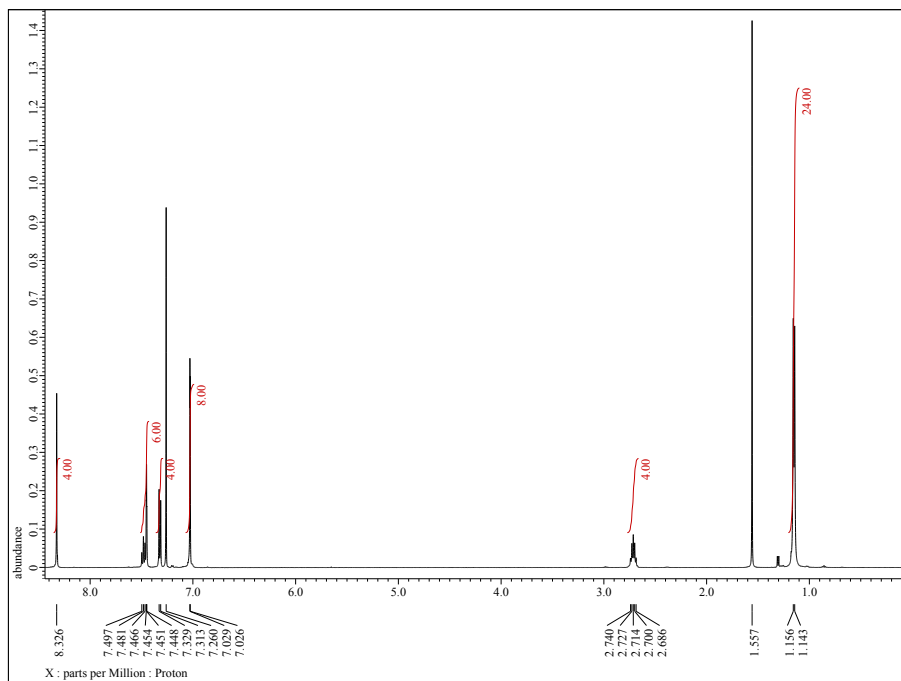


**Figure 2.15** Compound **5**  $^1\text{H}$  NMR (500 MHz,  $\text{CDCl}_3$ , 25 °C)

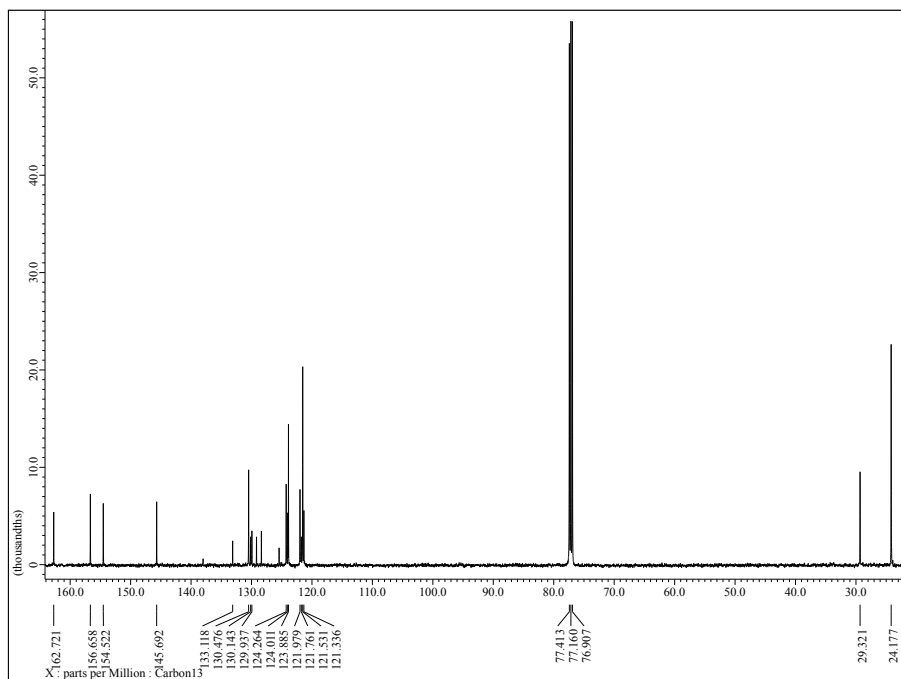


Figure 2.16 Compound **5**  $^{13}\text{C}$  NMR (125 MHz,  $\text{CDCl}_3$ , 25 °C)

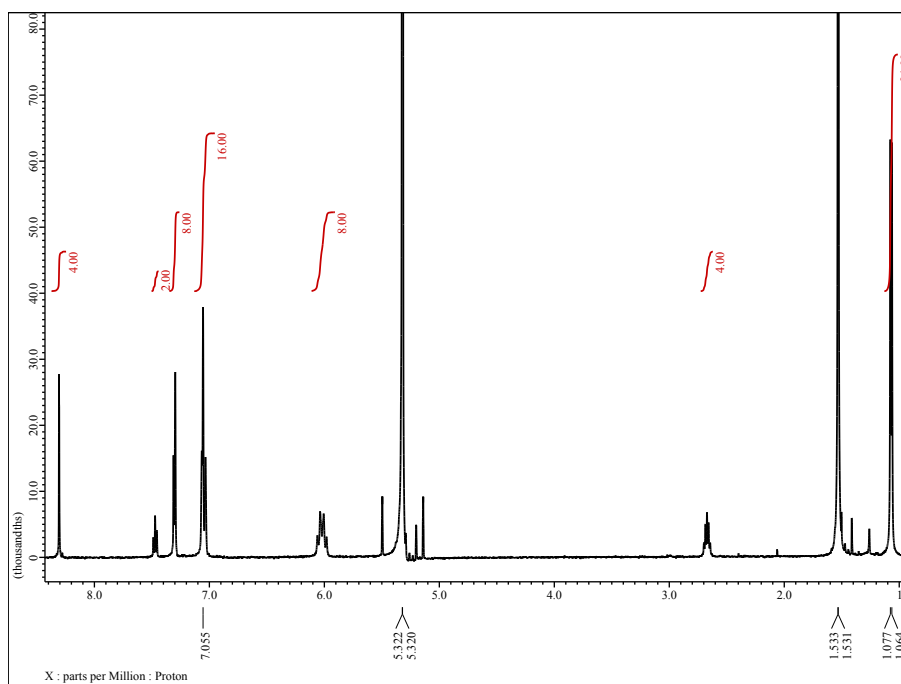
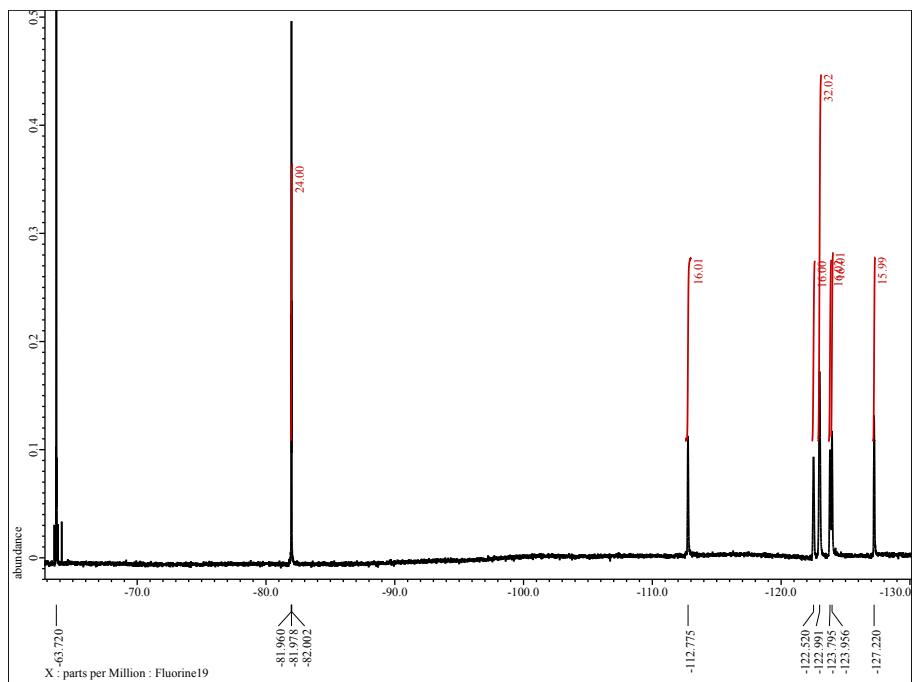
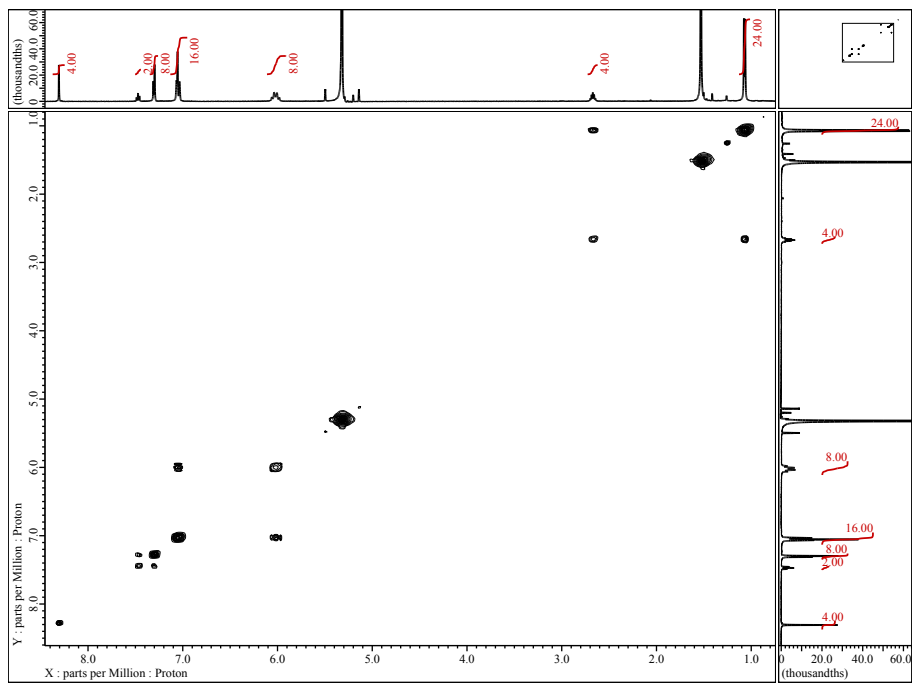


Figure 2.17 Compound **FF-PBI-2**  $^1\text{H}$  NMR (500 MHz,  $\text{CD}_2\text{Cl}_2$ , 25 °C)



**Figure 2.18** Compound **FF-PBI-2**  $^{19}\text{F}$  NMR (470 MHz,  $\text{CD}_2\text{Cl}_2$ , 25 °C)



**Figure 2.19** Compound **FF-PBI-2** COSY NMR (500 MHz,  $\text{CD}_2\text{Cl}_2$ , 25 °C)

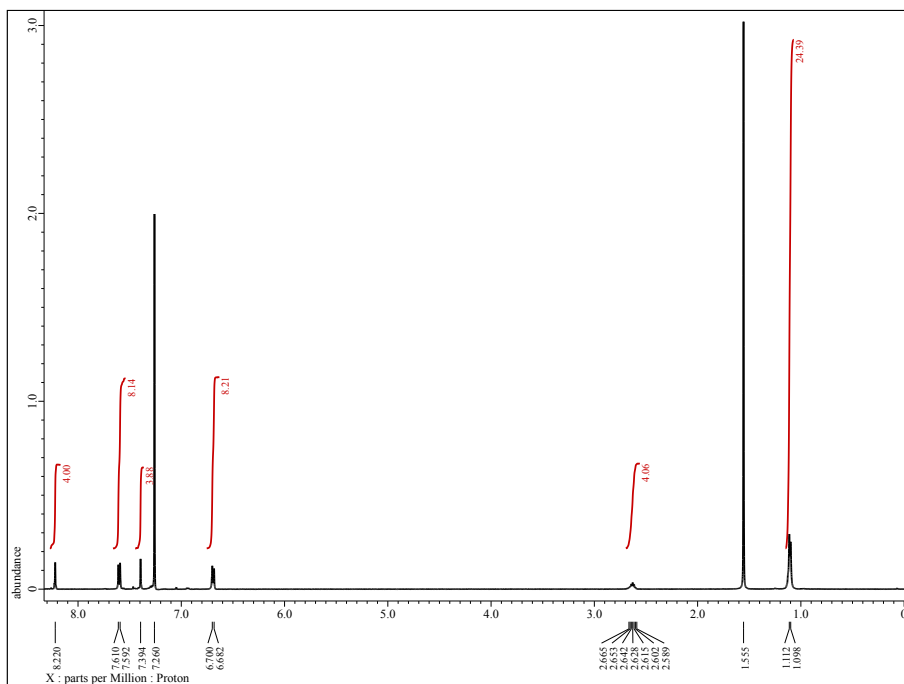


**Figure 2.20** Compound 6  $^1\text{H}$  NMR (500 MHz,  $\text{CDCl}_3$ , 25  $^\circ\text{C}$ )

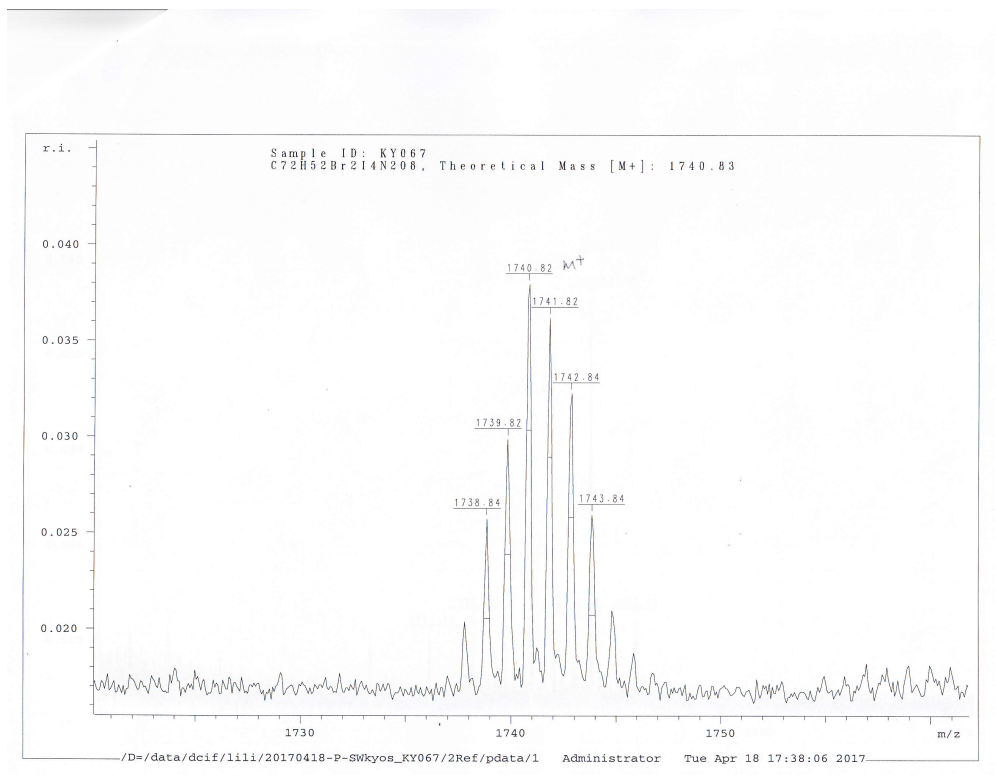


**Figure 2.21** Compound 6 HRMS (ESI)



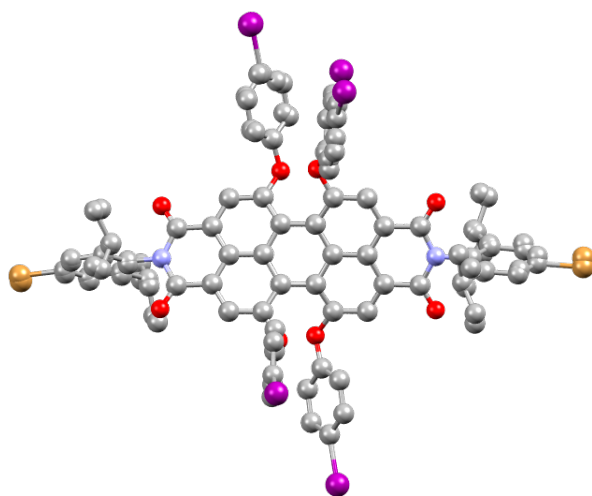


**Figure 2.22** Single crystal X-ray structure of compound **6**. Hydrogen atoms and solvent atoms are omitted for clarity.

**Table 2.2** Crystal data and structure refinement for compound **6**

Empirical formula	C <sub>72</sub> H <sub>52</sub> Br <sub>2</sub> I <sub>4</sub> N <sub>2</sub> O <sub>8</sub>
Formula weight	1740.64
Temperature	100(2) K
Wavelength	0.71073 Å
Crystal system	Triclinic
Space group	P-1 (2)
Lattice parameters	
a	12.5381 (17) Å
b	13.1960 (18) Å
c	23.925 (3) Å
$\alpha$	95.833(2)°
$\beta$	92.458(2)°
$\gamma$	102.757(2)°
Volume	3832.0(9)
Z	2
$2\theta_{\max}$	29.87°
Number of reflections	167635
Independent reflections	23367
Number of parameters	1282
$R_{\text{int}}$	0.0389
Completeness to $\theta$	1.000
$R_1 [I > 2\sigma(I)]$	0.0459
$wR_2$ (all data)	0.1250
Largest diff. peak	1.384 e.Å <sup>3</sup>
Largest diff. hole	-1.614 e.Å <sup>3</sup>
Goodness-of-fit	1.062

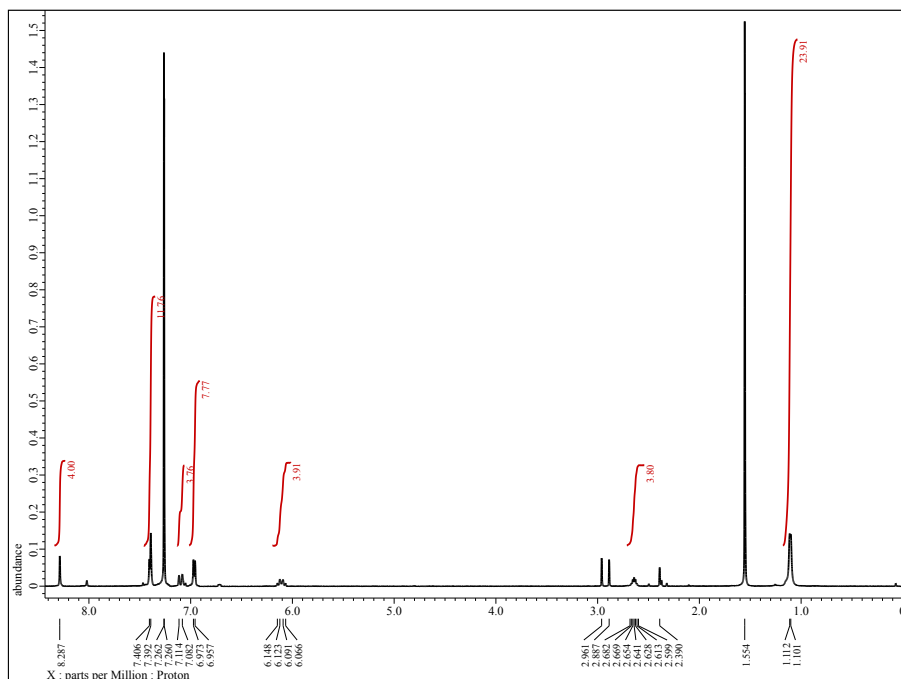


**Figure 2.23** Compound 7  $^1\text{H}$  NMR (500 MHz,  $\text{CDCl}_3$ , 25 °C)

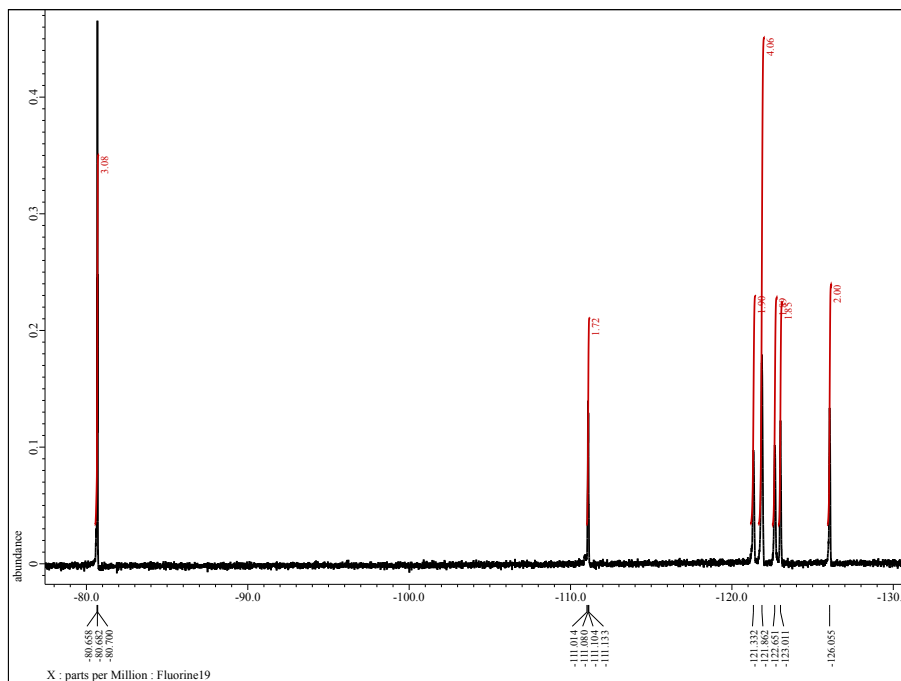


**Figure 2.24** Compound 7  $^{19}\text{F}$  NMR (470 MHz,  $\text{CDCl}_3$ , 25 °C)

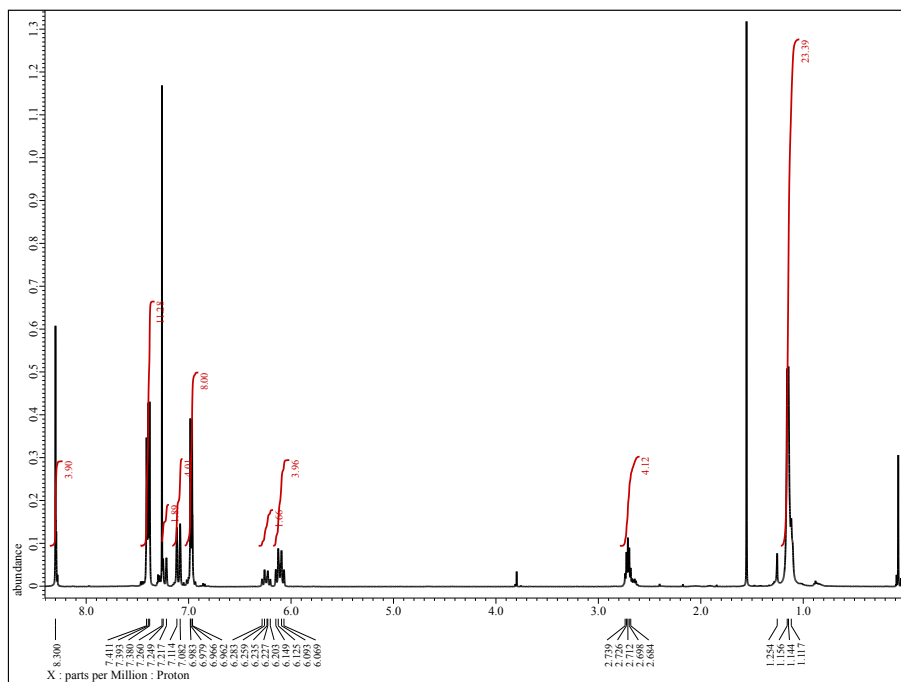


Figure 2.25 Compound FF-PBI-2' <sup>1</sup>H NMR (500 MHz, CDCl<sub>3</sub>, 25 °C)

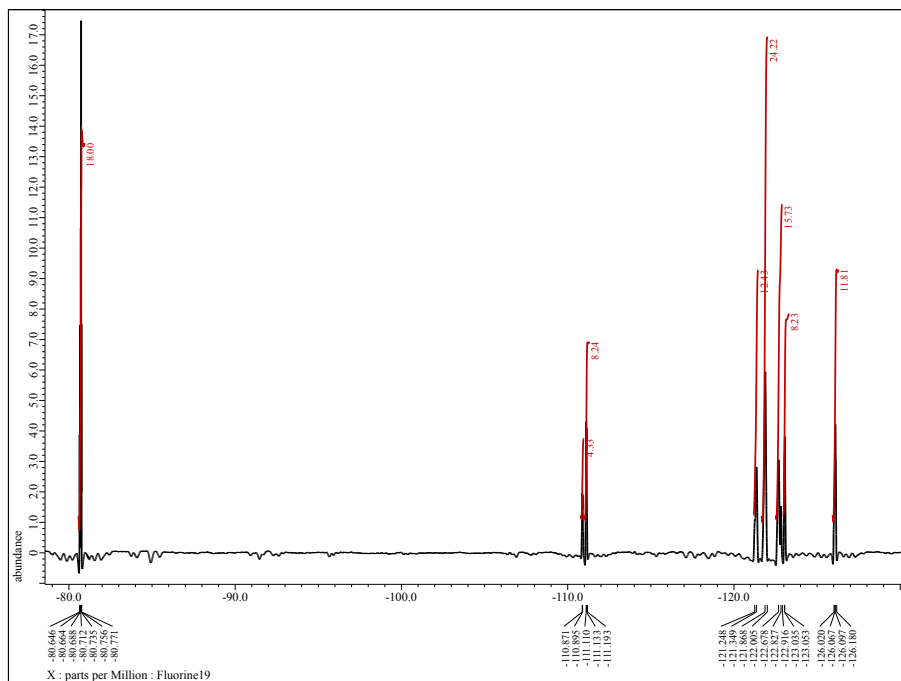


Figure 2.26 Compound FF-PBI-2' <sup>19</sup>F NMR (471 MHz, CDCl<sub>3</sub>, 25 °C)

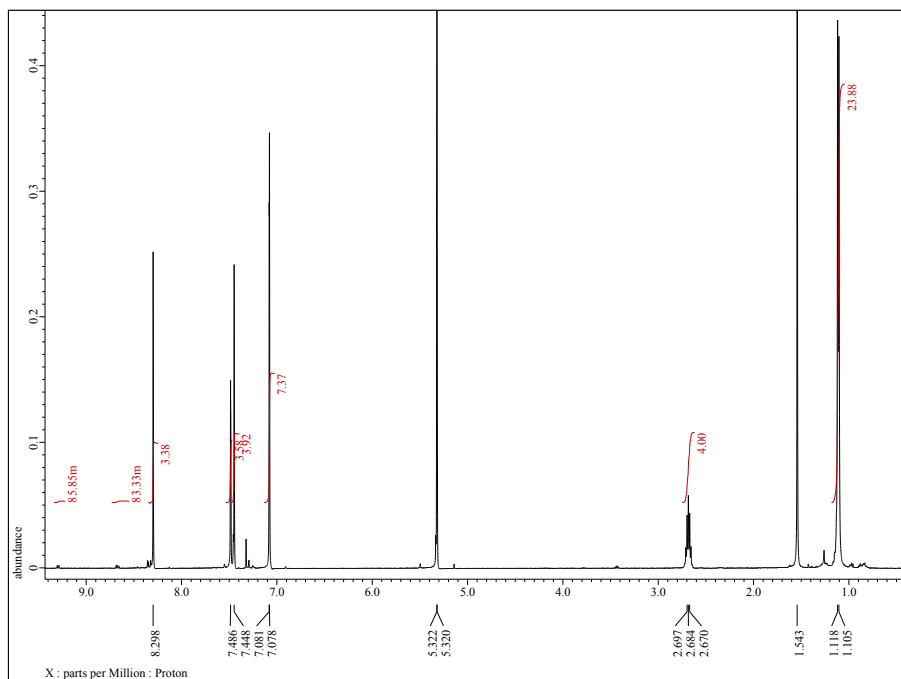


Figure 2.27 Compound 8  $^1\text{H}$  NMR (500 MHz,  $\text{CD}_2\text{Cl}_2$ , 25  $^\circ\text{C}$ )

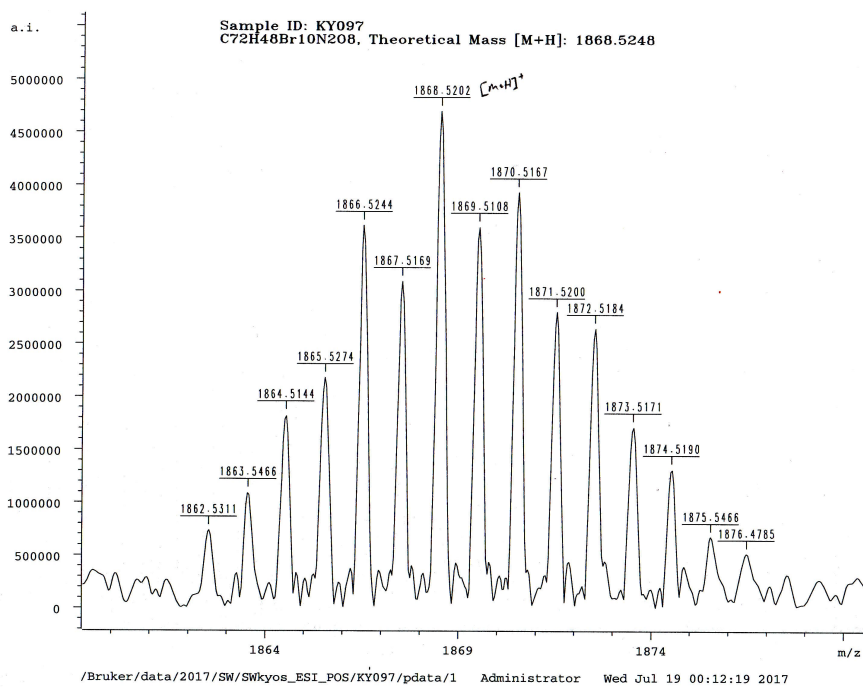
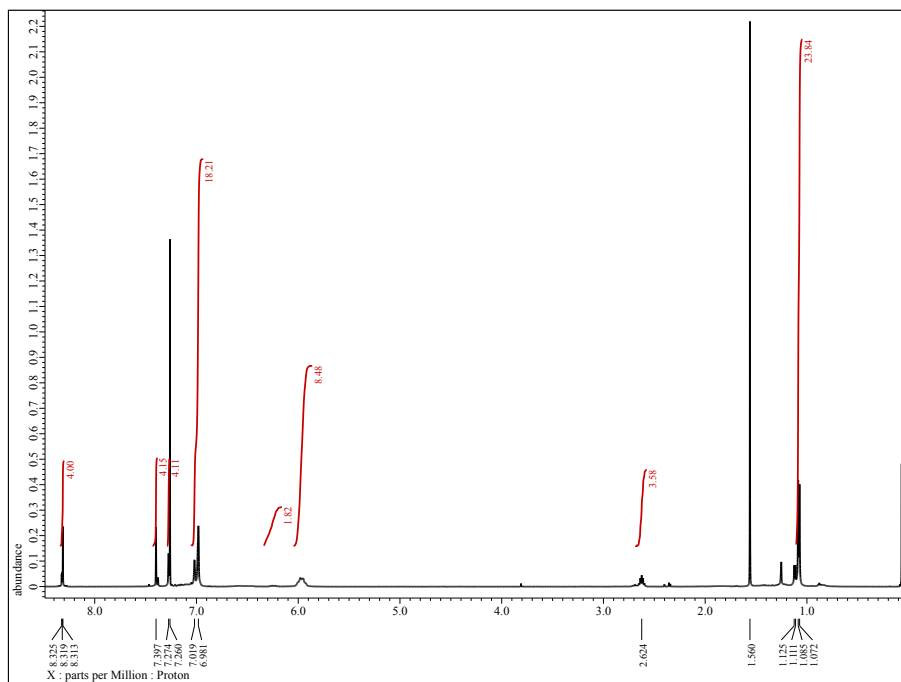
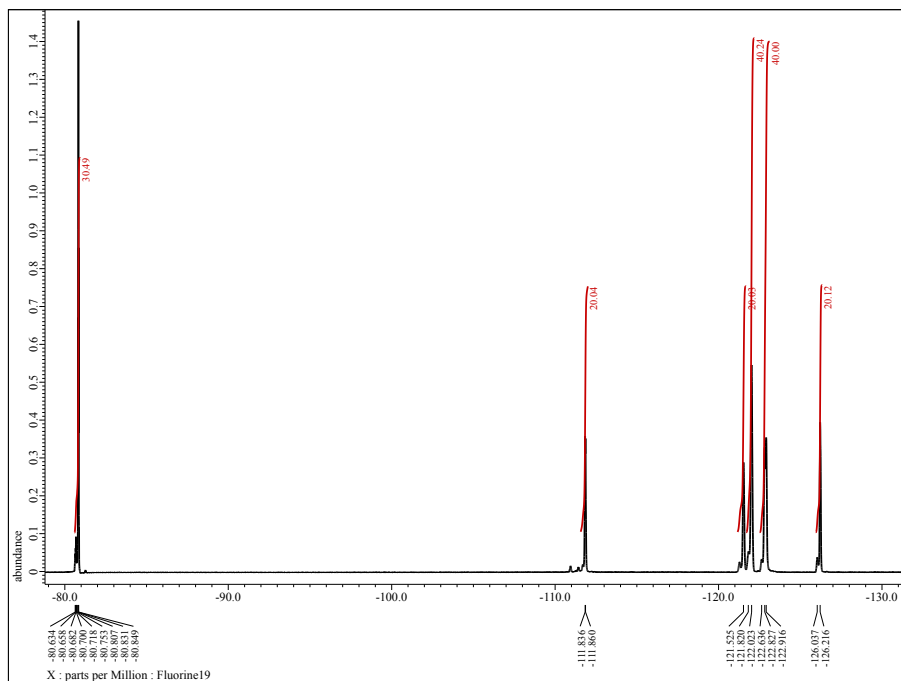


Figure 2.28 Compound 8 HRMS (ESI)



**Figure 2.29** Compound FF-PBI-2'' <sup>1</sup>H NMR (500 MHz, CDCl<sub>3</sub>, 25 °C)



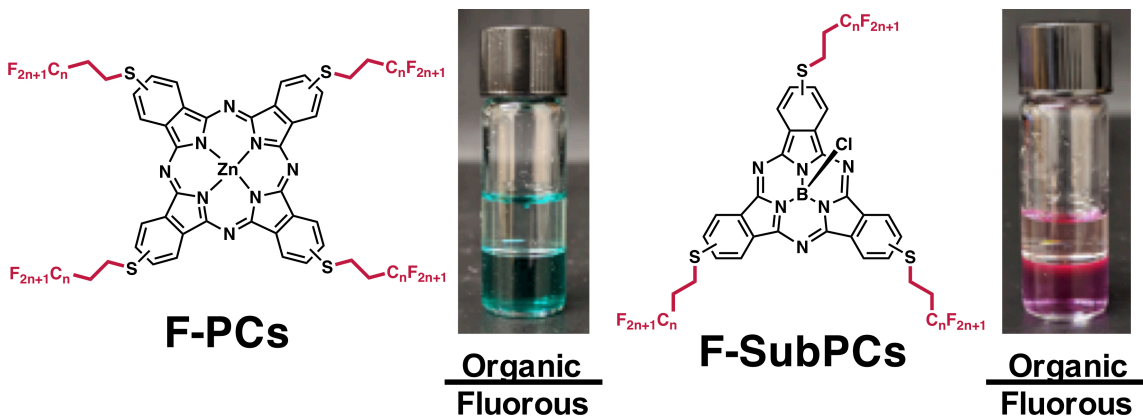
**Figure 2.30** Compound FF-PBI-2'' <sup>19</sup>F NMR (471 MHz, CDCl<sub>3</sub>, 25 °C)



## CHAPTER 3:

### Synthesis of Fluorous Phthalocyanines and Subphthalocyanines:

#### Applications in Faraday Rotation



- ✓ **>50 wt% F**
- ✓ **Photophysical Studies in Fluorous Solvents**
- ✓ **Faraday Rotation Properties**

Parts of this chapter were adapted and reprinted with permission from:

Yoshinaga, K.; Delage-Laurin, L.; Swager, T. M. Fluorous Phthalocyanines and Subphthalocyanines. *J. Porphyr. Phthalocyanines* **2020**, *24*, 1074. Copyright © 2020, World Scientific Publishing. K.Y. and T.M.S. designed research; K.Y. and L.D.L. performed research; all authors analyzed data; all authors contributed to the writing of the paper.

### 3.1 Abstract

Incorporating fluorine atoms into a molecule can endow it with unique properties that enable materials applications. Selective solubility in fluoruous solvents is achieved by a high fluorine content and selective partitioning into perfluorinated liquids over organic and aqueous phases provides orthogonal opportunities for chemistry and materials assembly. Although there are a growing number of partially fluorinated molecules, very few structural design principles exist to produce heavily fluorinated dyes. Herein, we report the synthesis of six fluoruous phthalocyanine and subphthalocyanine dyes and study their photophysical properties in the fluoruous phase. Phthalocyanines generally display limited solubility and we also observe apparent aggregation in the fluoruous phase, whereas the nonplanar subphthalocyanines show greater solubility in both organic and fluoruous solvents. Subphthalocyanines also display fluorescence in selected solvents, and their emissive properties are investigated. The materials described in this work expand the library of fluoruous dyes and provide insights for the design of new molecules with fluoruous solubility.

### 3.2 Introduction

Fluorine incorporation provides properties of importance to materials chemistry, and has found applications in coating materials,<sup>19</sup> pharmaceuticals,<sup>64</sup> *in vivo* drug delivery with perfluorocarbon nanoemulsions,<sup>65</sup> and organic electronics.<sup>66</sup> Owing to fluorine's electronegativity and hydrophobicity, introducing even a single fluorine atom into a molecule can vastly influence its solubility and dipole moment.<sup>4</sup> As a result, there is a growing interest in incorporating fluorine into organic semiconducting materials to enhance device performance. Incorporation of fluorine has also been found to improve chemical, thermal, and photochemical stability.<sup>5</sup> In some cases



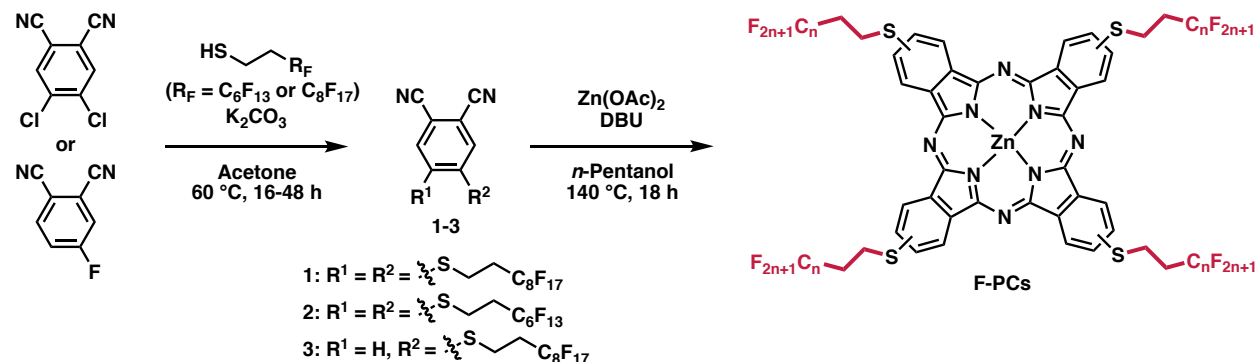
when the incorporation of fluorine atoms is high, compounds can phase separate from organic and aqueous phases.<sup>17</sup> In 1994, Horváth and Rábai labeled liquids displaying this phase separation as "fluorous" phases, and demonstrated their utility in fluorous biphasic catalysis.<sup>9</sup> Strategies to promote fluorous phase formation and solubility therein mainly rely on the fluorine content of the molecule, and the typical requirement is that there is >50 weight percent fluorine (wt% F).<sup>67</sup> However, as of 2020, examples of dyes that partition to fluorous phases over organic phases are scarce.<sup>68</sup> The Swager group has been interested in expanding this area and we have produced fluorous soluble conjugated polymers,<sup>13,14</sup> an array of fluorofluorophores,<sup>15</sup> and fluorofluorescent perylene bisimides.<sup>36</sup> Additionally, Sletten and coworkers have recently demonstrated the opportunities of fluorous character in molecules and reported the first J-aggregate in fluorous media,<sup>54</sup> and the synthesis of a branched fluorous tag to create a fluorous soluble porphyrin.<sup>69</sup> All these examples gave rise to noteworthy materials properties, which highlights the uniqueness of the fluorous phase. As a result, we believe many applications await the synthesis and development of novel fluorous materials.

Fluorous phthalocyanines and subphthalocyanines have attracted our interest as a result of their applications in organic field-effect transistors,<sup>70</sup> organic light-emitting diodes,<sup>71</sup> photovoltaics,<sup>72</sup> nonlinear optical materials,<sup>73</sup> and photodynamic therapy.<sup>74</sup> To date there are limited reports describing the properties of phthalocyanines and subphthalocyanines in the fluorous phase.<sup>75,76</sup> Herein, we report the synthesis of six fluorous soluble phthalocyanines (**F-PCs**) and subphthalocyanines (**F-SubPCs**), and elaborate on their structure-property relationship in the fluorous phase.

### 3.3 Results and Discussion

#### 3.3.1 Synthesis of F-PCs

The synthesis of **F-PCs**, as shown in **Scheme 3.1**, was accomplished by adaptation of a previous literature report.<sup>75</sup> In brief, phthalonitriles **1-3** were reacted with zinc acetate and 1,8-diazabicyclo[5.4.0]undec-7-ene (DBU) in *n*-pentanol to provide the desired **F-PCs** in 32-43% yields. **F-PCs** were characterized by MALDI-TOF MS, UV/vis absorbance spectroscopy, FT-IR, and elemental analysis. The low solubility of **F-PCs** in deuterated solvents and fluorous solvents prevented the acquisition of nuclear magnetic resonance (NMR) characterization.



**Scheme 3.1** Synthesis of fluorinated phthalocyanines (**F-PCs**: **F-PC-1**, **F-PC-2**, **F-PC-3**). Scheme adapted with permission.<sup>77</sup> Copyright © 2020, World Scientific Publishing.

#### 3.3.2 Properties of F-PCs

The **F-PCs** displayed almost no solubility in any organic solvents, regardless of wt% F. THF was the only solvent that showed any, albeit low solubility (< 0.1 mg/mL) of **F-PCs**. **Figure 3.2a–c** shows the **F-PCs** partitioning into the fluorous solvent 2-(trifluoromethyl)-3-ethoxydodecafluorohexane (HFE-7500) rather than dissolving in the organic solvent diethylbenzene (DEB). HFE-7500 and DEB is a convenient solvent combination to study the fluorous partition by visual inspection because it has a low interfacial tension and low upper critical mixing temperature. Although the **F-PCs** partitioned into HFE-7500, we observed precipitation **F-**

**PC-1** and **F-PC-2** solutions from this solvent at room temperature (**Figure 3.6**). This was confirmed by the observation that when solutions of **F-PC-1** and **F-PC-2** were passed through a 0.2  $\mu\text{m}$  syringe filter, the filtered solution was colorless, implying that they likely form aggregates larger than 0.2  $\mu\text{m}$ . The solubility of **F-PCs** can be increased to  $\sim 0.1$  mg/mL by heating the THF and HFE-7500 solutions to their boiling temperatures (66  $^{\circ}\text{C}$  and 128  $^{\circ}\text{C}$ , respectively). **F-PC-3** is slightly more soluble in THF and HFE-7500 than **F-PC-1** and **F-PC-2**, displaying a solubility of  $\sim 1$  mg/mL.

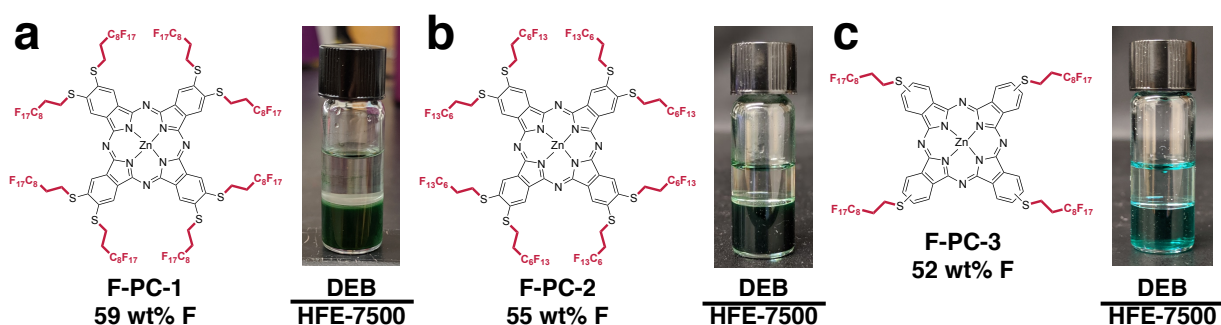


**Figure 3.1** Chemical structure and fluorine partitioning of (a) **F-PC-1**, (b) **F-PC-2**, and (c) **F-PC-3**. Figure adapted with permission.<sup>77</sup> Copyright © 2020, World Scientific Publishing.

The photophysical properties of **F-PCs** are summarized in **Table 3.1** and **Figure 3.2a–c**. **F-PC-1** is scarcely soluble in heated THF and HFE-7500, and as a result its absorbance spectra were taken in THF and HFE-7500 heated to near boiling temperatures. When solutions are cooled, the spectra broaden and decrease in intensity (**Figure 3.6**). The heated solutions could be passed through a 0.2  $\mu\text{m}$  syringe filter, however after cooling no perceptible color was observed in filtered solutions, thereby indicating that **F-PC-1** precipitates. The absorbance spectra of **F-PC-2** and **F-PC-3** were also taken in THF and HFE-7500. The absorbance spectra of **F-PC-2** in THF resembles were in accordance with previously reported spectra.<sup>75</sup> The absorbance of **F-PCs** in THF showed the typical Soret and Q absorbance bands for phthalocyanines, however a significant and consistent difference in the absorbance spectra was observed for all of the **F-PCs** in HFE-7500. Specifically,

the relative peak intensity of the Q band at ~690 nm decreased, while the relative peak intensities of the Soret band at ~360 nm as well as the shoulder at ~650 nm increased. A decreased intensity at the  $S_0 \rightarrow S_1$  band ( $\lambda_{\text{abs}} \approx 690$  nm) and an increased intensity of the absorbance at ~650 nm is suggestive of H-aggregation in fluorous solvents.<sup>78,79</sup>

**Table 3.1** Summary of photophysical properties of F-PCs

Compound	$\lambda_{\text{abs}}$ (nm)	Molar Extinction Coefficient
		at $\lambda_{\text{abs}}$ ( $10^5 \text{ L} \cdot \text{mol}^{-1} \cdot \text{cm}^{-1}$ )
<b>F-PC-1</b>	698 (THF)	1.67 (THF)
	650 (HFE-7500)	
<b>F-PC-2</b>	698 (THF)	2.37 (THF)
	650 (HFE-7500)	
<b>F-PC-3</b>	683 (THF)	2.84 (THF)
	624 (HFE-7500)	

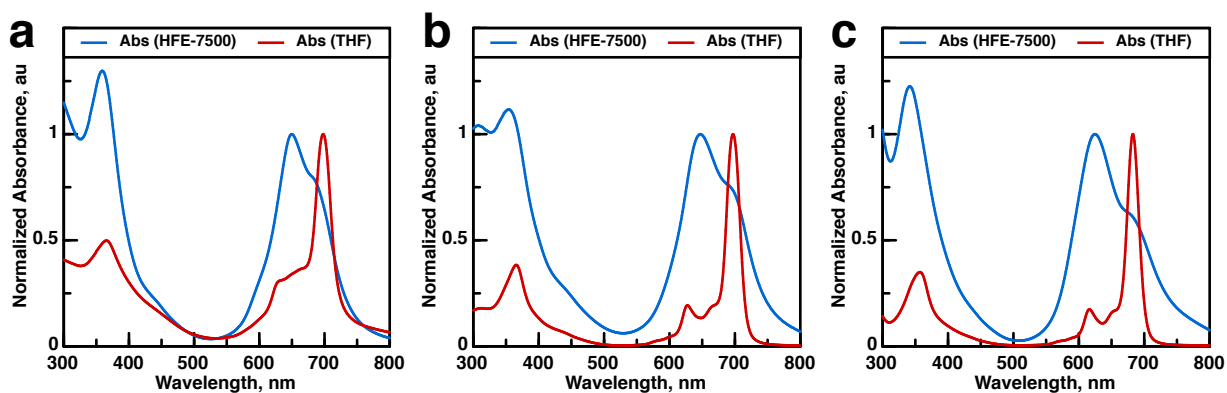
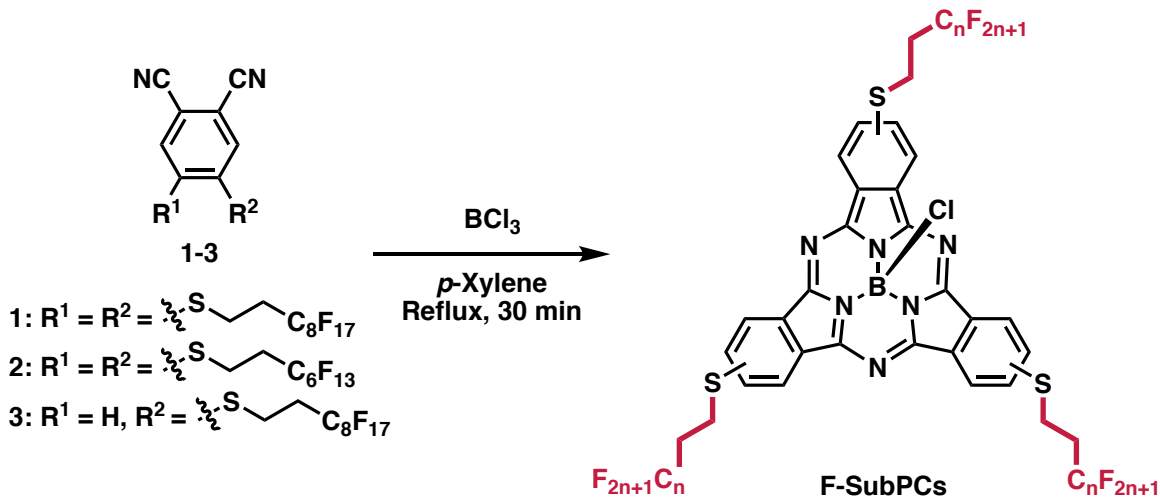


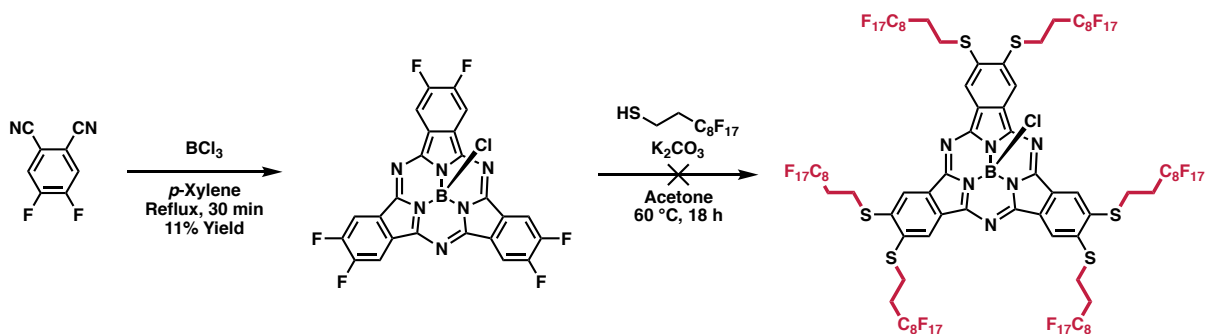
**Figure 3.2** Overlaid normalized absorbance spectra of (a) **F-PC-1**, (b) **F-PC-2**, and (c) **F-PC-3** in organic solvent THF and in fluorous solvent HFE-7500. Spectra for **F-PC-1** obtained by heating the solutions to their boiling temperatures (66 °C for THF, 128 °C for HFE-7500). Figure adapted with permission.<sup>77</sup> Copyright © 2020, World Scientific Publishing.

### 3.3.3 Synthesis of F-SubPCs



**Scheme 3.2** Synthesis of fluorinated subphthalocyanines (**F-SubPCs**). Scheme adapted with permission.<sup>77</sup> Copyright © 2020, World Scientific Publishing.

The synthesis of **F-SubPCs**, as shown in **Scheme 3.2**, was accomplished by adapting previous literature procedures.<sup>80</sup> In brief, the phthalonitrile precursors **1–3** were prepared by an  $\text{S}_{\text{N}}\text{Ar}$  reaction of the fluoroalkyl thiols and halogenated phthalonitriles. Phthalonitriles **1–3** were then reacted with  $\text{BCl}_3$  to provide the desired **F-SubPCs** in 13–29% yields. We note that an alternative synthetic scheme wherein the  $\text{S}_{\text{N}}\text{Ar}$  reaction installing the fluoroalkyl thiols directly on the halogenated subphthalocyanines did not produce the desired **F-SubPCs** (**Scheme 3.3**). The **F-SubPCs** were characterized by NMR, MALDI-TOF MS, UV/vis absorbance and fluorescence spectroscopy, FT-IR, and elemental analysis. The low solubility of **F-SubPC-1** in deuterated solvents prevented the acquisition of NMR characterization.



**Scheme 3.3** Unsuccessful alternative synthetic scheme to obtain **F-SubPC-1** in an  $\text{S}_{\text{N}}\text{Ar}$  reaction installing the fluoroalkyl thiols on halogenated subphthalocyanines.

### 3.3.4 Properties of F-SubPCs

The **F-SubPCs** are consistently more soluble than their **F-PCs** counterparts despite possessing near identical wt% F, perhaps due to their nonplanar molecular geometry. **F-SubPC-1** was insoluble in common organic solvents but was readily soluble in fluorous solvents such as perfluoro(methylcyclohexane) (PFMCH), HFE-7500, and FC-770 ( $> 1\text{ mg/mL}$ ). **F-SubPC-2** and **F-SubPC-3** displayed moderate solubility ( $\sim 1\text{ mg/mL}$ ) in organic solvents such as chloroform and toluene (PhMe), as well as the mentioned fluorous solvents. We determined the fluorous partition coefficient ( $P$ ) of **F-SubPCs** by subjecting each compound to a 1:1 mixture of PFMCH and PhMe and quantifying the amount in each layer by UV/vis absorbance spectroscopy (**Figure 3.3a–c**). **F-SubPC-1**, **F-SubPC-2**, and **F-SubPC-3** had a  $P$  value of 36 (97:3 in PFMCH/PhMe), 1.1 (53:47 in PFMCH/PhMe), and 0.044 (4:96 in PFMCH/PhMe), respectively. From these results, we confirm a trend that higher wt% F leads to superior partitioning into fluorous solvents. The low  $P$  of **F-SubPC-3** may also be reflective of the fact that it is a regioisomeric mixture, and therefore possesses an asymmetric molecular structure.

**Table 3.2** Summary of photophysical properties of **F-SubPCs**

Compound	Fluorous Partition Coefficient (PFMCH/PhMe) ( <i>P</i> )	$\lambda_{\text{abs}}$ (nm)	Molar Extinction Coefficient at $\lambda_{\text{abs}}$ ( $10^4 \text{ L} \cdot \text{mol}^{-1} \cdot \text{cm}^{-1}$ )	$\lambda_{\text{em}}$ (nm) <sup>a</sup>	Quantum Yield $\phi$ (%) <sup>b</sup>	Fluorescence Lifetime $\tau_1$ (ns) <sup>c</sup>
<b>F-SubPC-1</b>	36	595 (PhMe)	– (PhMe) <sup>d</sup>	606 (PhMe)	– (PhMe) <sup>d</sup>	– (PhMe) <sup>d</sup>
		580 (PFMCH)	1.46 (PFMCH)	587 (PFMCH)	– (PFMCH) <sup>e</sup>	– (PFMCH) <sup>e</sup>
<b>F-SubPC-2</b>	1.1	595 (PhMe)	5.23 (PhMe)	605 (PhMe)	25.1 (PhMe)	2.72 (PhMe)
		586 (PFMCH)	2.00 (PFMCH)	588 (PFMCH)	– (PFMCH) <sup>e</sup>	– (PFMCH) <sup>e</sup>
<b>F-SubPC-3</b>	0.044	581 (PhMe)	6.27 (PhMe)	594 (PhMe)	35.2 (PhMe)	2.87 (PhMe)
		567 (PFMCH)	– (PFMCH) <sup>d</sup>	573 (PFMCH)	– (PFMCH) <sup>e</sup>	– (PFMCH) <sup>e</sup>

<sup>a</sup>Excited at 500 nm. <sup>b</sup>Measured with an integrating sphere excited at 500 nm. <sup>c</sup>Referenced to 1,4-bis(5-phenyloxazol-2-yl)benzene ( $\tau_1 = 1.32$  ns, MeOH). <sup>d</sup>Not measured due to low solubility. <sup>e</sup>Not measured due to weak fluorescence.

The photophysical properties of **F-SubPCs** are summarized **Table 3.2** and **Figure 3.3d–f**. In PhMe, **F-SubPC-2** and **F-SubPC-3** exhibited fluorescence with quantum yields of 25.1% and 35.2%, respectively. The limited solubility of **F-SubPC-1** in PhMe hindered the determination of the quantum yield in PhMe. **The F-SubPCs** dissolved in PFMCH also displayed a broad absorbance in the visible region, with a small hypsochromic shift. **The F-SubPCs** were only weakly fluorescent in PFMCH (**Figure 3.3a–c**), and the quantum yields in PFMCH could not be determined.

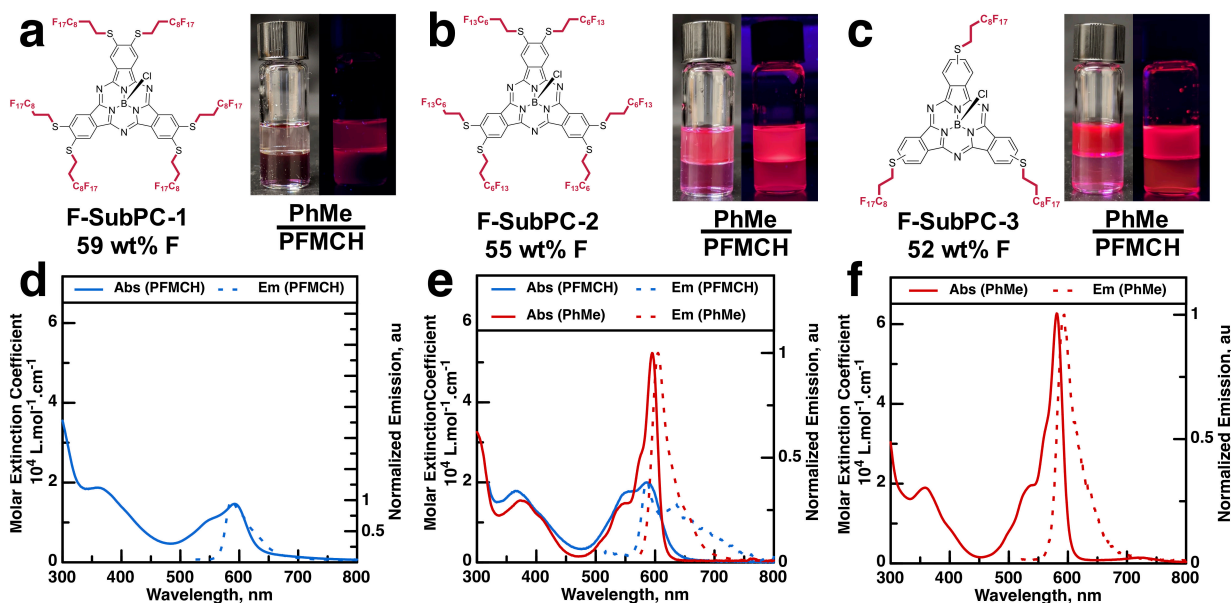


**Figure 3.3** Chemical structure and fluoros partition of (a) **F-SubPC-1**, (b) **F-SubPC-2**, and (c) **F-SubPC-3**. Absorbance and emission spectra of (d) **F-SubPC-1**, (e) **F-SubPC-2**, and (f) **F-SubPC-3**. Scheme adapted with permission.<sup>77</sup> Copyright © 2020, World Scientific Publishing.

**F-SubPC-2** displayed solubility in both organic and fluoros phases to allow for comparisons, and in fluoros solvent the intensity of Q-band ( $\lambda_{\text{abs}} \approx 590$  nm) decreases with a small increase in the absorbance at  $\sim 540$  nm. This is indicative of H-aggregation in fluoros solvents, which is also likely the cause of fluorescence quenching.<sup>81</sup> However, the **F-SubPCs** can display fluorescence in fluoros solvents. For instance, **F-SubPC-1** is fluorescent in HFE-7500 and shows excellent partition in HFE-7500 over DEB (**Figure 3.7**).

### 3.3.5 Faraday Rotation Properties of F-PCs and F-SubPCs

The Faraday effect, discovered by Michael Faraday nearly two centuries ago, is a ubiquitous magneto-optical phenomenon, describing the rotation of plane-polarized light traveling through a material along the axis of an applied magnetic field.<sup>82</sup> This effect is quantified by a constant of proportionality intrinsic to each material called the Verdet constant (**V**), which is wavelength dependent, and linearly correlated to the applied magnetic field and the thickness of



the material (**Figure 3.4**). Recent emergence of organic materials possessing high Verdet constants such as semiconducting polymers,<sup>83,84</sup> mesogenic organic molecules<sup>85,86</sup>, small-molecule chromophores such as phthalocyanines,<sup>87,88</sup> and radical-containing polymers<sup>89,90</sup> holds promises in utilizing these materials in processable devices. We have recently discovered that the role of polymer conformation and supramolecular organization affects the electronic delocalization and electromagnetic interactions and thereby modulate the sign and magnitude of the Faraday effect.<sup>83,89</sup> Because we observed H-aggregation of **F-PCs** and **F-SubPCs** in fluoruous solvents, we hypothesized that the intermolecular organization in fluoruous solvents may influence the Faraday rotation properties in such fluoruous molecules. We sought to investigate the Faraday rotation properties of **F-PCs** and **F-SubPCs** in fluoruous solvents.

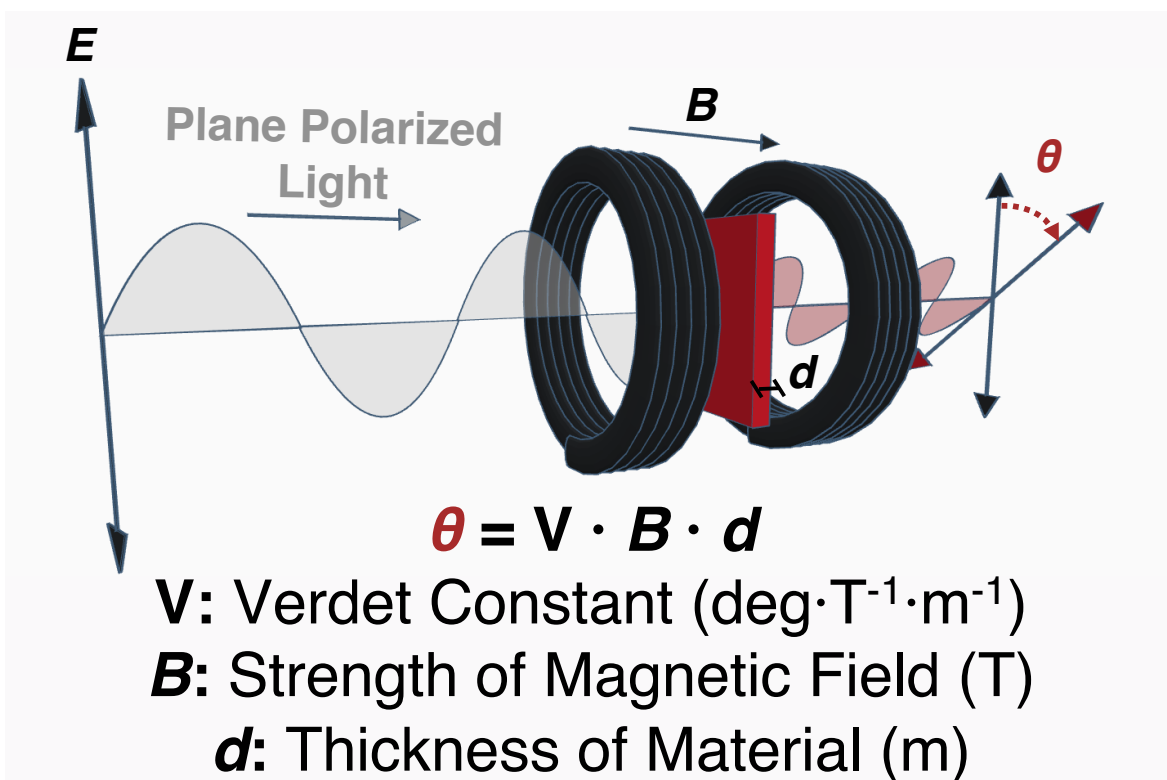


**Figure 3.4** Schematic image of magneto-optical material displaying a Faraday rotation. The degree of rotation ( $\theta$ ) is governed by the materials' Verdet Constant ( $V$ ), strength of magnetic field ( $B$ ), and the thickness of the material ( $d$ ). Scheme adapted with permission.<sup>77</sup> Copyright © 2020, World Scientific Publishing.

**Figure 3.5** summarizes the Faraday rotation properties of **F-PCs** and **F-SubPCs** in various solvents (also see **Figure 3.9** for experimental setup). An analog property of the Verdet constant, the molar specific magnetic rotation ( $\text{deg}\cdot\text{L}\cdot\text{mol}^{-1}\cdot\text{T}^{-1}\cdot\text{m}^{-1}$ ), was used to quantify magneto-optical effects to accommodate for the solution-phase nature of the samples. Because **F-PCs** displayed limited solubility in fluoruous solvents, the rotation spectra could not be obtained. Instead, rotation spectra for **F-PC-2** and **F-PC-3** were obtained in THF, displaying their largest molar specific magnetic rotations of  $-3.6 \times 10^6 \text{ deg}\cdot\text{L}\cdot\text{mol}^{-1}\cdot\text{T}^{-1}\cdot\text{m}^{-1}$  (observed at 700 nm) and  $-8.8 \times 10^5 \text{ deg}\cdot\text{L}\cdot\text{mol}^{-1}\cdot\text{T}^{-1}\cdot\text{m}^{-1}$  (observed at 700 nm), respectively. The measurement of **F-PC-2** was conducted at elevated temperatures due to its low solubility. For **F-SubPCs**, rotation spectra were obtained in fluoruous solvent PFMCH for **F-SubPC-1** and **F-SubPC-2**, and in organic solvent PhMe for **F-SubPC-2** and **F-SubPC-3**. The comparison of the spectra for **F-SubPC-2** enables the study of the effect of organic and fluoruous solvents on Faraday rotation properties. While we observe Faraday rotation in fluoruous solvent PFMCH (largest molar specific magnetic rotation of  $-1.1 \times 10^5 \text{ deg}\cdot\text{L}\cdot\text{mol}^{-1}\cdot\text{T}^{-1}\cdot\text{m}^{-1}$  observed at 560 nm), it is lower in intensity than that in organic solvent PhMe (largest molar specific magnetic rotation of  $-2.4 \times 10^5 \text{ deg}\cdot\text{L}\cdot\text{mol}^{-1}\cdot\text{T}^{-1}\cdot\text{m}^{-1}$  observed at 600 nm). Contrary to our expectations, these results confirm that H-aggregation in fluoruous solvents was detrimental to the Faraday effect. One of the reasons for this result could simply be because of the lowered extinction coefficient due to H-aggregation.<sup>91</sup> We remain uncertain about the effect of the fluoruous environment on the materials' Faraday rotating properties. Nonetheless, Faraday rotation properties measured in fluoruous solvents is unprecedented and these entries enrich the library of Faraday rotating materials.

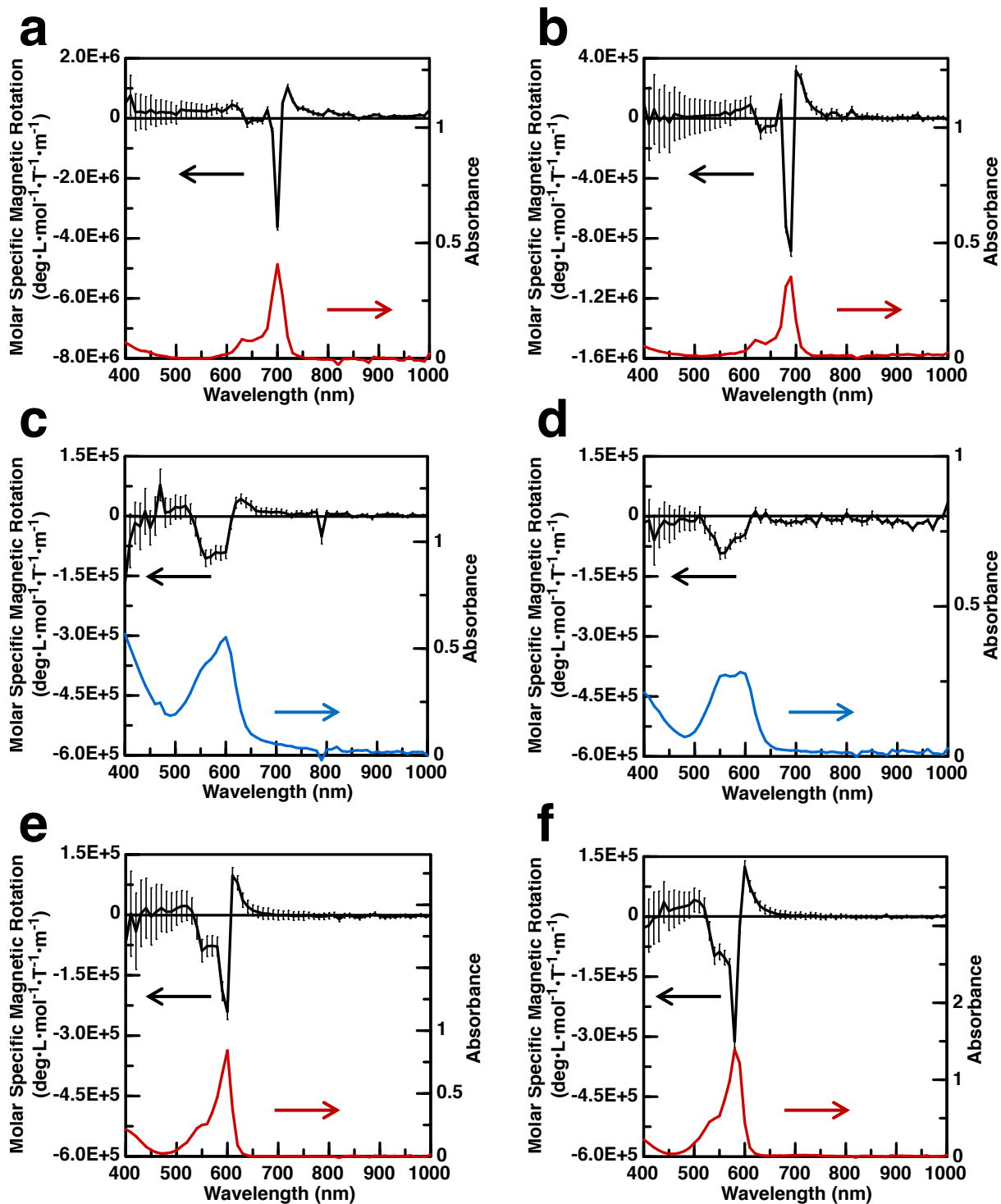


**Figure 3.5** Faraday rotation properties of F-PCs and F-SubPCs. Molar specific magnetic rotation of (a) F-PC-2 and (b) F-PC-3 in THF. Molar specific magnetic rotation of (c) F-SubPC-1 and (d) F-SubPC-2 in PFMCH. Molar specific magnetic rotation of (e) F-SubPC-2 and (f) F-SubPC-3 in PhMe. Spectra for F-PC-1 obtained by heating the solution to its boiling temperature (66 °C). Scheme adapted with permission.<sup>77</sup> Copyright © 2020, World Scientific Publishing.

### 3.4 Conclusions

In summary, we have described the synthesis and characterization of fluorinated phthalocyanines and subphthalocyanines. **F-PC-1** and **F-PC-2** displayed limited solubility in both organic and fluorinated solvents, whereas **F-PC-3** was more soluble in fluorinated solvents. The absorbance spectra of **F-PCs** in organic and fluorinated solvents showed different trends, suggestive of H-aggregation in fluorinated solvents. On the other hand, the nonplanar **F-SubPCs** demonstrated improved solubility in fluorinated solvents and followed the trend of higher wt% F displaying higher fluorinated solubility. The **F-SubPCs** were fluorescent in organic solvents and HFE-7500, but were only weakly fluorescent in PFMCH, which is also suggestive of H-aggregation. We have also studied the Faraday rotation properties of **F-PCs** and **F-SubPCs** in fluorinated and organic solvents. The compounds described in this report pave the way for the discovery and development of functional fluorinated soluble phthalocyanines and subphthalocyanines. Further characterization of the properties of **F-PCs** and **F-SubPCs** is underway, and we anticipate these compounds will find applications as new fluorinated soluble/dispersible materials.

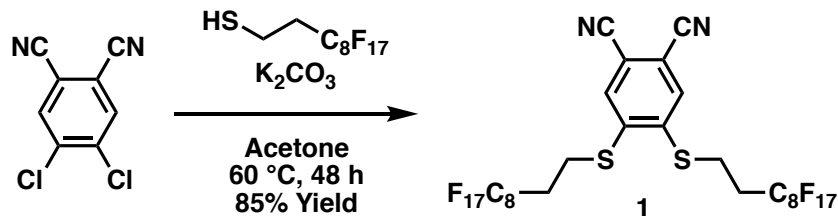
### 3.5 Experimental

#### 3.5.1 General

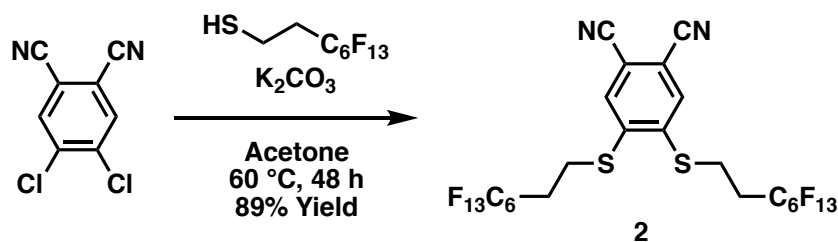
All chemical reagents were purchased from Sigma-Aldrich, Synquest Laboratories, Oakwood Chemicals, Fluorox Labs, or TCI, and used without purification unless noted otherwise. Thin layer chromatography was performed with Baker-flex Silica Gel 1B-F plates (JT Baker). Flash chromatography was performed using technical grade silica gel with 60 Å pores and 230–400 mesh particle size (Sigma-Aldrich, 717185).

$^1\text{H}$ ,  $^{13}\text{C}$ , and  $^{19}\text{F}$  nuclear magnetic resonance (NMR) spectra were recorded on a JEOL model JNM-ECZ500R/S1 spectrometer operating at 500, 126, and 471 MHz, respectively. For  $^1\text{H}$ ,  $^{13}\text{C}$  NMR spectra, deuterated solvent references were used as internal standards ( $^1\text{H}$ : 7.26 ppm for  $\text{CDCl}_3$ , 2.05 ppm for acetone- $d_6$ ;  $^{13}\text{C}$ : 77.16 ppm for  $\text{CDCl}_3$ , 206.26 ppm for acetone- $d_6$ ). Multiplicities are abbreviated as singlet (s), doublet (d), triplet (t), multiplet (m). Direct Analysis in Real Time (DART) mass spectra and matrix-assisted laser desorption/ionization time-of-flight (MALDI-TOF) mass spectra were obtained at the MIT Department of Chemistry Instrumentation Facility. Elemental analysis data were obtained at Robertson Microlit Laboratories. Fourier-transform infrared spectra were obtained on a Thermo Scientific Nicolet 6700 FT-IR spectrometer. UV/Vis absorbance spectra were obtained on a Cary 4000 UV/Vis spectrophotometer (Agilent Technologies) with a scan rate of  $600 \text{ nm} \cdot \text{min}^{-1}$ . The instrument was blanked on the solvent prior to obtaining a spectrum. Fluorescence spectra were obtained on a Horiba Jobin Yvon SPEX Fluorolog- $\tau 3$  fluorimeter (model FL-321, 450 W Xenon lamp). Quantum yields were determined by using Horiba Quanta- $\phi$  integrating sphere. Absorbance and fluorescence data were collected in a quartz cuvette (1 cm path length). Magneto-optical (MO) measurements were performed using our custom Faraday rotation apparatus (see **Figure 3.9** for experimental setup). Preparation of thin films was unsuccessful, so various solutions of **F-PCs** and **F-SubPCs** in organic and fluoruous solvents were measured in a quartz cuvette (0.05 cm path length). An analog property of the Verdet constant, the molar specific magnetic rotation ( $\text{deg} \cdot \text{L} \cdot \text{mol}^{-1} \cdot \text{T}^{-1} \cdot \text{m}^{-1}$ ), was used to quantify MO effects to accommodate for the solution-phase nature of the samples.

### 3.5.2 Synthetic Procedures

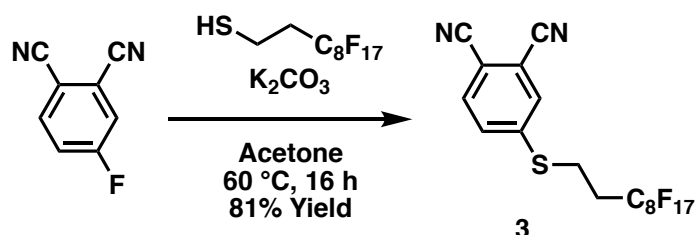


**Compound 1.** A mixture of 4,5-dichlorophthalonitrile (98.5 mg, 0.500 mmol), 1*H*,1*H*,2*H*,2*H*-perfluorodecanethiol (504 mg, 1.05 mmol), and anhydrous  $\text{K}_2\text{CO}_3$  (400 mg, 2.89 mmol) in acetone (5 mL) was stirred at  $60\text{ }^\circ\text{C}$  for 48 h. Then, 1M HCl aq (10 mL) was added and the product precipitated. The precipitate was filtered and collected and was recrystallized from chloroform to provide colorless crystals **1** (462 mg, 0.426 mmol, 85% yield).  $^1\text{H}$  NMR (500 MHz; acetone- $d_6$ ):  $\delta$  (ppm) 8.06 (s, 2H), 3.59 (t,  $J = 7.6$  Hz, 4H), 2.68–2.84 (m, 4H).  $^{13}\text{C}$  NMR (126 MHz; acetone- $d_6$ ):  $\delta$  (ppm) 143.70, 131.54, 116.43, 113.43, 31.10 (t,  $J = 22$  Hz), 24.35.  $^{19}\text{F}$  NMR (471 MHz; acetone- $d_6$ ):  $\delta$  (ppm) -81.56 (t,  $J = 9.8$  Hz, 6F), -114.23 (m, 4F), -122.14 (m, 4F), -122.37 (m, 8F), -123.19 (m, 4F), -123.67 (m, 4F), -126.66 (m, 4F). DART MS:  $m/z$  calcd. for  $[\text{C}_{28}\text{H}_{10}\text{F}_{34}\text{N}_2\text{S}_2]^+$ : 1083.9742. Found: 1083.9742.

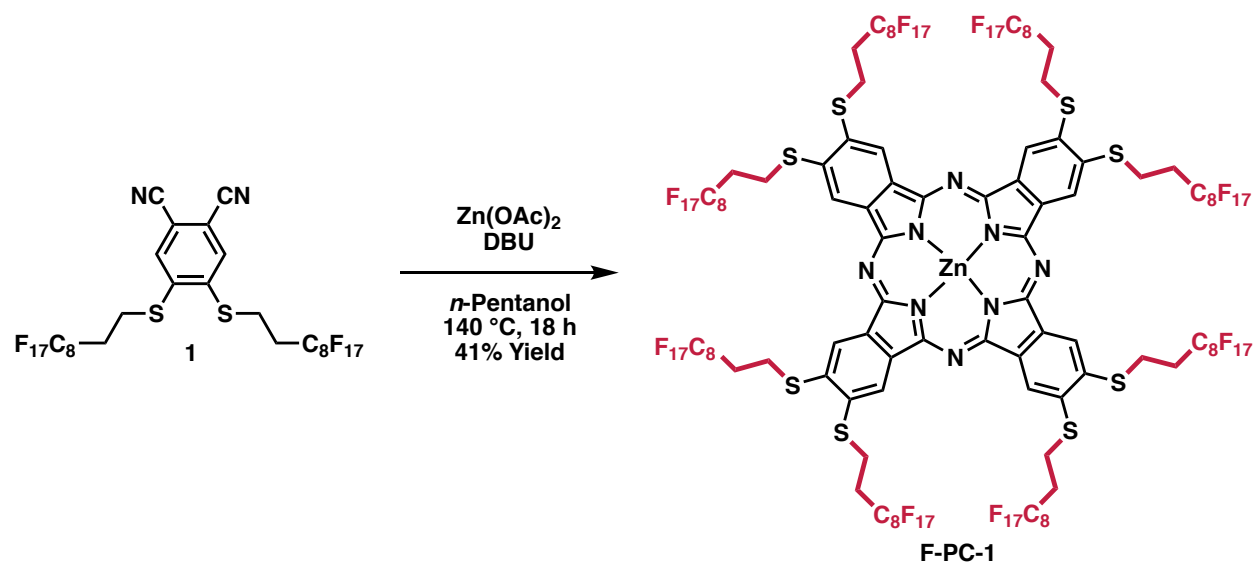


**Compound 2.** Compound **2** was prepared by following a previous literature report.<sup>75</sup> A mixture of 4,5-dichlorophthalonitrile (197 mg, 1.00 mmol), 1*H*,1*H*,2*H*,2*H*-perfluorooctanethiol (849 mg, 2.23 mmol), and anhydrous  $\text{K}_2\text{CO}_3$  (412 mg, 2.98 mmol) in acetone (5 mL) was stirred at  $60\text{ }^\circ\text{C}$  for 48 h. Then, 1M HCl aq (10 mL) was added and the product precipitated. The precipitate was

filtered and collected and was recrystallized from chloroform to provide colorless crystals **2** (789 mg, 0.892 mmol, 89% yield).  $^1\text{H}$  NMR (500 MHz; acetone- $d_6$ ):  $\delta$  (ppm) 8.04 (s, 2H), 3.58 (t,  $J$  = 7.6 Hz, 4H), 2.86–2.62 (m, 4H).  $^{19}\text{F}$  NMR (471 MHz, acetone- $d_6$ , 25 °C):  $\delta$  (ppm) -81.62 (t,  $J$  = 9.8 Hz, 6F), -114.26 (m, 4F), -122.39 (m, 4F), -123.39 (m, 4F), -123.74 (m, 4F), -126.73 (m, 4F). The characterization is consistent with the previous literature report.<sup>75</sup>

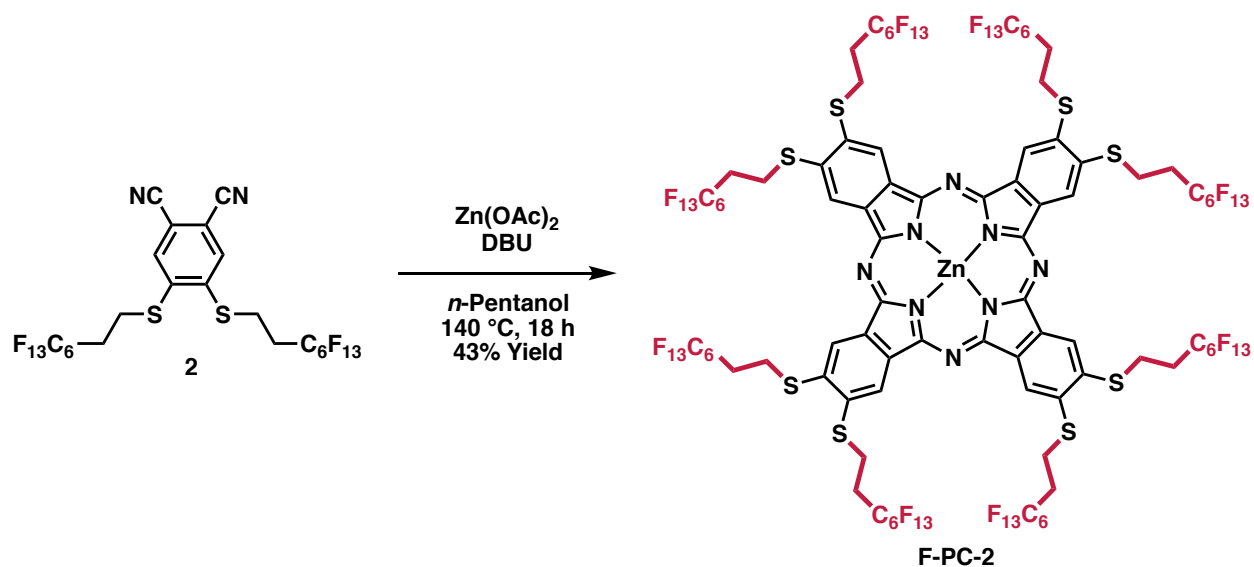


**Compound 3.** A mixture of 4-fluorophthalonitrile (294 mg, 2.01 mmol), 1*H*,1*H*,2*H*,2*H*-perfluorodecanethiol (985 mg, 2.05 mmol), and anhydrous  $\text{K}_2\text{CO}_3$  (400 mg, 2.89 mmol) in acetone (5 mL) was stirred at 60 °C for 16 h. Then, 1M HCl aq (10 mL) was added and the product precipitated. The precipitate was filtered and collected and dissolved in acetone. The acetone solution was precipitated in excess hexanes, and the precipitate was filtered and collected to provide **3** as a white solid (980 mg, 1.62 mmol, 81% yield).  $^1\text{H}$  NMR (500 MHz; acetone- $d_6$ ):  $\delta$  (ppm) 8.06 (s, 1H), 7.98 (d,  $J$  = 8.4 Hz, 1H), 7.88 (d,  $J$  = 8.4 Hz, 1H), 3.56 (t,  $J$  = 7.8 Hz, 2H), 2.70–2.79 (m, 2H).  $^{13}\text{C}$  NMR (126 MHz; acetone- $d_6$ ):  $\delta$  (ppm) 146.08, 134.79, 131.94, 131.85, 117.15, 116.55, 116.20, 112.42, 31.22 (t,  $J$  = 22 Hz), 23.42.  $^{19}\text{F}$  NMR (471 MHz; acetone- $d_6$ ):  $\delta$  (ppm) -81.56 (t,  $J$  = 9.8 Hz, 3F), -114.36 (m, 2F), -122.14 (m, 2F), -122.35 (m, 4F), -123.18 (m, 2F), -123.67 (m, 2F), -126.65 (m, 2F). DART MS:  $m/z$  calcd. for  $\text{C}_{18}\text{H}_7\text{F}_{17}\text{N}_2\text{S}$   $[\text{M}]^+$ : 606.0058. Found: 606.0071, 607.0155  $[\text{M} + \text{H}]^+$ , 624.0422  $[\text{M} + \text{NH}_4]^+$ , 665.0584  $[\text{M} + \text{acetone} + \text{H}]^+$ .

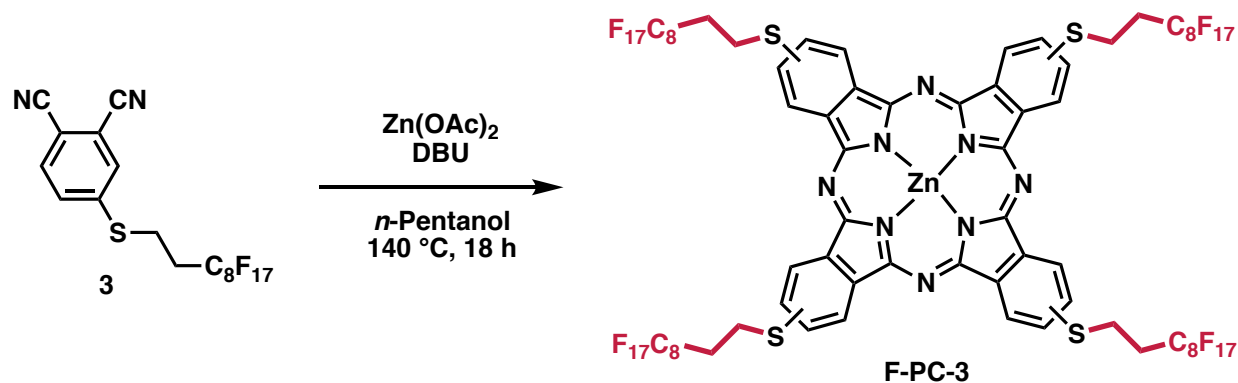


**F-PC-1.** A mixture of compound **1** (271 mg, 0.250 mmol),  $\text{Zn(OAc)}_2$  (12.8 mg, 0.0698 mmol), and 1,8-diazabicyclo[5.4.0]undec-7-ene (DBU, 50  $\mu\text{L}$ ) in *n*-pentanol (5 mL) was stirred at 140 °C for 18 h. The reaction mixture was cooled to room temperature and filtered. Further purification was carried out by Soxhlet extraction with MeOH,  $\text{CH}_2\text{Cl}_2$ , and AcOEt for 24 h each to obtain **F-PC-1** as a dark green solid (114 mg, 0.0625 mmol, 41% yield). NMR and MALDI-TOF MS spectra could not be obtained due to low solubility and aggregation. Elemental Anal. calcd. for  $\text{C}_{112}\text{H}_{40}\text{F}_{136}\text{N}_8\text{S}_8\text{Zn}$  (%): C, 30.55; H, 0.92; N, 2.54. Found: C, 30.53; H, 1.03; N, 3.23. UV-vis (THF):  $\lambda_{\text{abs}}$  ( $\log \epsilon$ ) = 369 (4.9), 629 (4.7), 698 (5.2).



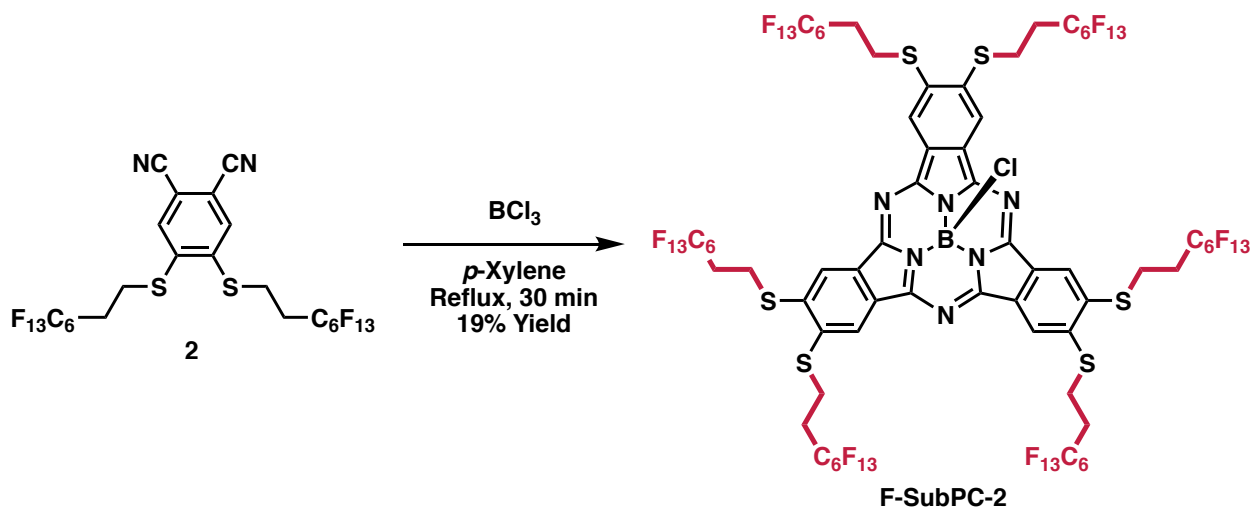


**F-PC-2.** **F-PC-2** was synthesized by following a previous literature report.<sup>75</sup> A mixture of compound **2** (221 mg, 0.250 mmol),  $\text{Zn(OAc)}_2$  (12.8 mg, 0.0698 mmol), and 1,8-diazabicyclo[5.4.0]undec-7-ene (DBU, 50  $\mu\text{L}$ ) in *n*-pentanol (5 mL) was stirred at 140 °C for 18 h. The reaction mixture was cooled to room temperature and filtered. Further purification was carried out by Soxhlet extraction with MeOH,  $\text{CH}_2\text{Cl}_2$ , and AcOEt for 24 h each to obtain **F-PC-2** as a green solid (97.0 mg, 0.0269 mmol, 43% yield). NMR spectra could not be obtained due to low solubility and aggregation. MALDI-TOF MS:  $m/z$  calcd. for  $\text{C}_{96}\text{H}_{40}\text{F}_{104}\text{N}_8\text{S}_8\text{Zn}$   $[\text{M}]^+$ : 3599.8772. Found: 3599.8692. UV-vis (THF):  $\lambda_{\text{abs}}$  (log  $\epsilon$ ) = 366 (5.0), 627 (4.7), 697 (5.4). The characterization is consistent with the previous literature report.<sup>75</sup>



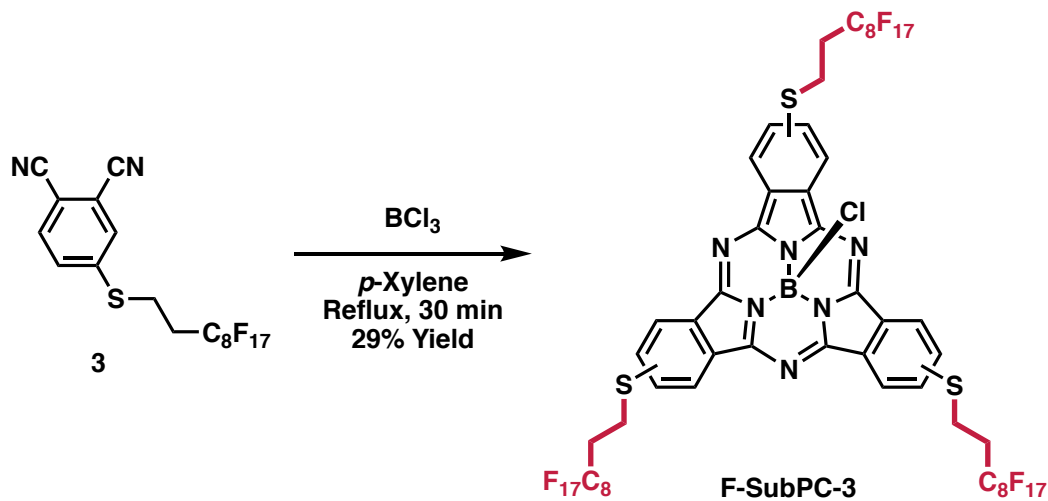


under reduced pressure. Further purification was carried out by Soxhlet extraction with acetone for 72 h to obtain **F-SubPC-1** as a dark purple solid (63.2 mg, 0.0191 mmol, 13% yield). NMR spectra could not be obtained due to low solubility and aggregation. MALDI-TOF MS:  $m/z$  calcd. for  $C_{84}H_{30}BClF_{102}N_6S_6$   $[M]^+$ : 3297.9009. Found: 3297.9106. UV-vis (HFE-7500):  $\lambda_{abs}$  ( $\log \epsilon$ ) = 359 (4.3), 592 (4.2).



**F-SubPC-2.** Compound **2** (265 mg, 0.300 mmol) was added to a dried flask, and  $BCl_3$  (1.0 M in *p*-xylene, 0.300 mL) was added dropwisely. Then, the reaction mixture was stirred at 160 °C in a pre-heated oil bath for 30 min. Upon cooling the reaction mixture to room temperature, it was diluted with FC-770 (5 mL) and transferred to a separation funnel. The fluorous layer was washed with chloroform (10 mL), acetone (10 mL), water, (10 mL), brine (10 mL), dried with  $MgSO_4$ , and evaporated to dryness under reduced pressure. The residue was chromatographed on silica gel using  $CHCl_3$  as an eluent, and the fraction containing **F-SubPC-2** ( $R_f = 0.60$ ) was collected and evaporated to dryness to provide a dark purple solid (50.2 mg, 0.0185 mmol, 19% yield).  $^1H$  NMR (500 MHz;  $CDCl_3$ ):  $\delta$  (ppm) 8.76 (s, 6H), 3.38–3.49 (m, 12H), 2.49–2.64 (m, 12H).  $^{19}F$  NMR (471 MHz;  $CDCl_3$ ):  $\delta$  (ppm) -80.79 (t,  $J = 9.8$  Hz, 18F), -113.94 (m, 12F), -121.87 (m, 12F), -122.87

(m, 12F), -123.19 (m, 12F), -126.17 (m, 12F). MALDI-TOF MS:  $m/z$  calcd. for  $C_{72}H_{30}BClF_{78}N_6S_6$   $[M + H]^+$ : 2698.9471. Found: 2698.9707. Elemental Anal. calcd. for  $C_{72}H_{30}BClF_{78}N_6S_6$  (%): C, 32.03; H, 1.12; N, 3.11. Found: C, 32.49; H, 1.03; N, 2.89. UV-vis (PhMe):  $\lambda_{abs}$  ( $\log \epsilon$ ) = 373 (4.2), 595 (4.7).



**F-SubPC-3.** Compound **3** (300 mg, 0.495 mmol) was added to a dried flask, and  $BCl_3$  (1.0 M in *p*-xylene, 0.500 mL) was added dropwisely. Then, the reaction mixture was stirred at 160 °C in a pre-heated oil bath for 30 min. Upon cooling the reaction mixture to room temperature, it was diluted with FC-770 (5 mL) and transferred to a separation funnel. The fluorous layer was washed with chloroform (10 mL), acetone (10 mL), water, (10 mL), brine (10 mL), dried with  $MgSO_4$ , and evaporated to dryness under reduced pressure. The residue was chromatographed on silica gel using  $CHCl_3$  as an eluent, and the fraction containing **F-SubPC-3** ( $R_f = 0.60$ ) was collected and evaporated to dryness to provide a dark purple solid (90.0 mg, 0.0483 mmol, 29% yield). HPLC separation was unsuccessful.  $^1H$  NMR (500 MHz;  $CDCl_3$ ):  $\delta$  (ppm) 8.76–8.83 (m, 6H), 7.85–7.89 (m, 3H), 3.35–3.48 (m, 6H), 2.48–2.59 (m, 6H).  $^{19}F$  NMR (471 MHz;  $CDCl_3$ ):  $\delta$  (ppm) -80.78–80.51 (m, 9F), -113.60 (m, 2F), -113.99 (m, 4F), -121.59 (m, 6F), -121.82 (m, 12F), -122.62 (m,

6F), -123.15 (m, 6F), -126.01 (m, 6F). MALDI-TOF MS:  $m/z$  calcd. for  $C_{54}H_{21}BClF_{51}N_6S_3 [M]^+$ :  
1863.9957. Found:1863.9942. UV/Vis absorbance (PhMe):  $\lambda_{abs}$  ( $\log \epsilon$ ) = 358 (4.3), 581 (4.8).

### 3.6 Appendix for CHAPTER 3

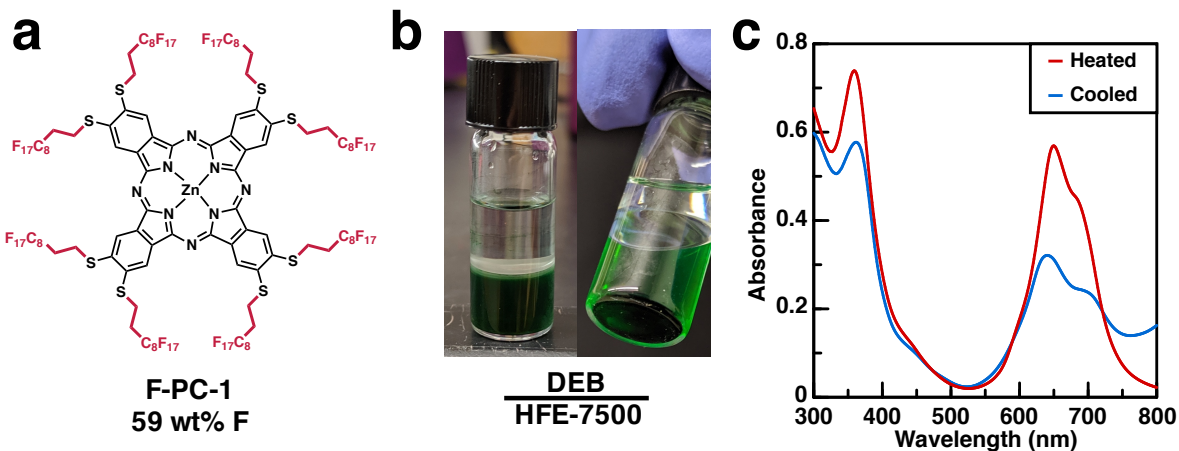


**Figure 3.6** (a) Chemical structure of **F-PC-1**. (b) Fluorous partition of **F-PC-1** in DEB and HFE-7500 (left), and observation of precipitates after a few hours (right). (c) UV/Vis absorbance spectra of a heated solution of **F-PC-1** in HFE-7500 (red) and the same cooled solution (blue).

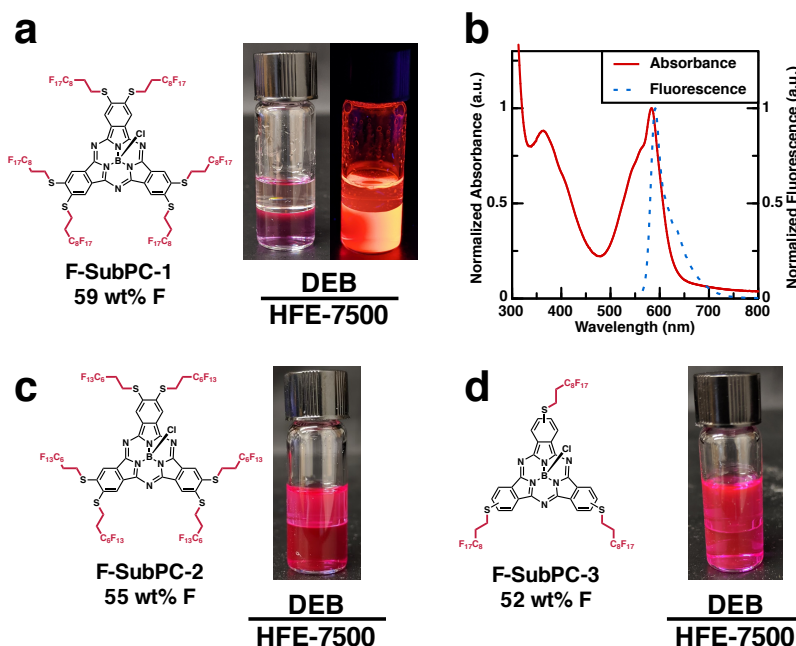


**Figure 3.7** (a) Chemical structure of **F-SubPC-1** and its fluorous partition in diethylbenzene (DEB) and HFE-7500. (b) UV/Vis absorbance and fluorescence spectra of **F-SubPC-1** (solvent: HFE-7500). (c) Chemical structure of **F-SubPC-2** and its fluorous partition in DEB and HFE-7500. (d) Chemical structure of **F-SubPC-3** and its fluorous partition in DEB and HFE-7500.

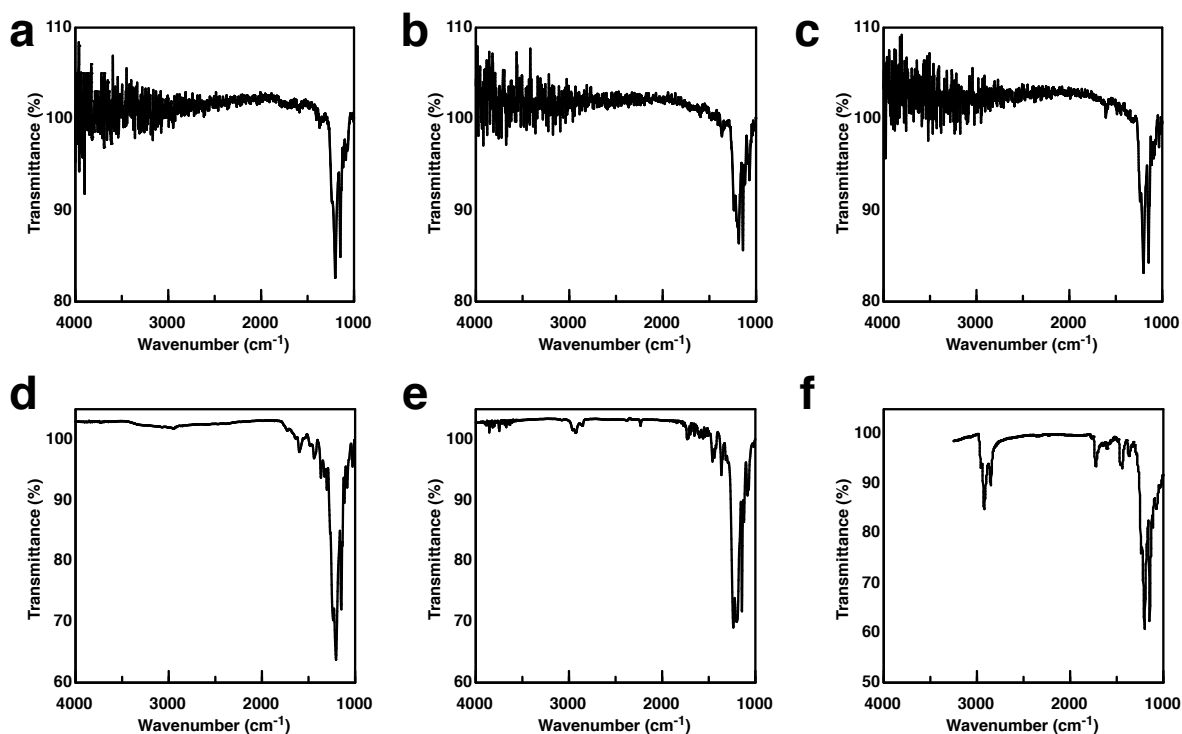


**Figure 3.8** FT-IR spectra of (a) F-PC-1, (b) F-PC-2, (c) F-PC-3, (d) F-SubPC-1, (e) F-SubPC-2, and (f) F-SubPC-3. F-SubPCs were deposited on KBr pellets.

### 3.6.1 Instrumental Setup for Faraday Rotation Measurement

The Faraday rotation instrument is depicted in **Figure 3.9**. The light source used is a 300W Newport TLS260-300X xenon lamp coupled via a condenser lens assembly to a filter wheel and then a Cornerstone 260 (0.25 meter) monochromator. The beam is focused on a mechanical chopper wheel (frequency of 1 kHz), which ensures clean modulation and consistent and uniform measurements. It is then prepared in a linear polarization ( $45^\circ$ ) by a wire-grid polarizer then passed through a series of lenses to focus the beam directly on the sample. The sample is a high-precision quartz cuvette (0.5 mm path, Starna Quartz Spectrophotometer cell) containing a solution of the targeted compound. The sample is fixed to a cuvette-holder mounted on a ramp such that it can be moved at the center of the magnet directly perpendicular to the beam propagation direction. The

sample is in the gap of an electromagnet (GMW 3470) which is powered by a Crown DC-300A Series II amplifier. The beam then passes through a Wollaston prism (Thorlabs WPA10) which produces two divergent beams of orthogonal polarization. These beams are then passed through one large (2 inch diameter) lens, and then individually through short-focal length lenses onto the photodiodes. The photodetector (PDB210A) features two 4 mm photodiode arrays (PDAs). The PDAs are balanced in performance and are used to measure the polarization change as a function of magnetic field. We initially polarized the light at about  $45^\circ$ . The Wollaston prism (set at  $0^\circ$ ) splits this polarized light into its two orthogonal components ( $0^\circ$  and  $90^\circ$ ), which have equal intensity. Any change of polarization from the sample, when the magnetic field is applied, will lead to a detectable signal. The arrows below the polarizer and the analyzer show the relative orientations of their optical axes. Green lines show light propagation.

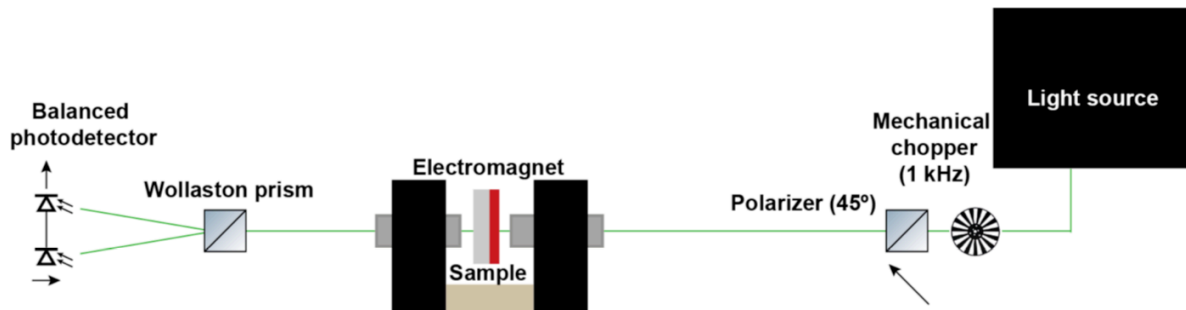


**Figure 3.9** Schematic of the instrument for Faraday rotation measurement.



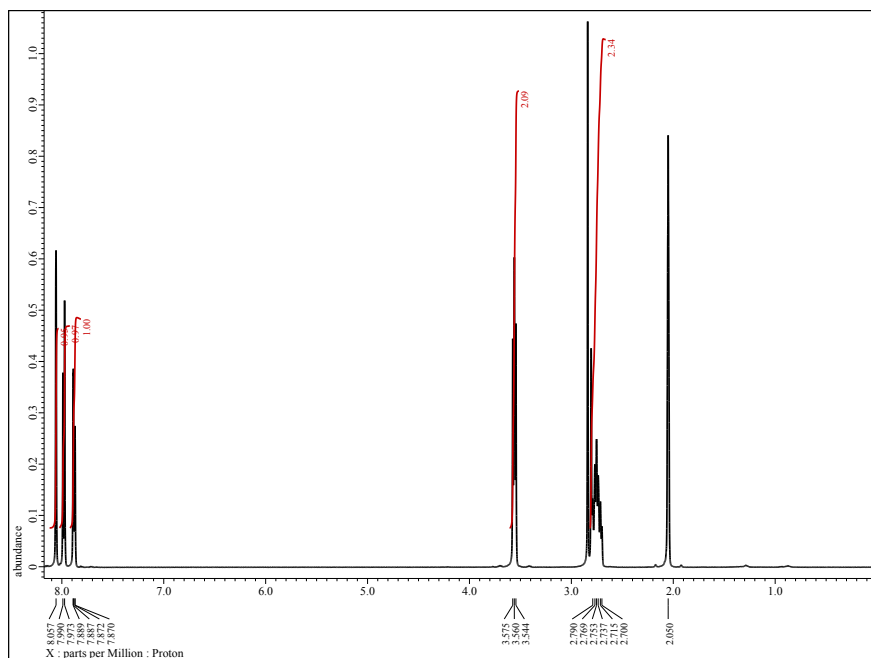


Figure 3.10 Compound 3  $^1\text{H}$  NMR (500 MHz, acetone- $d_6$ , 25 °C)

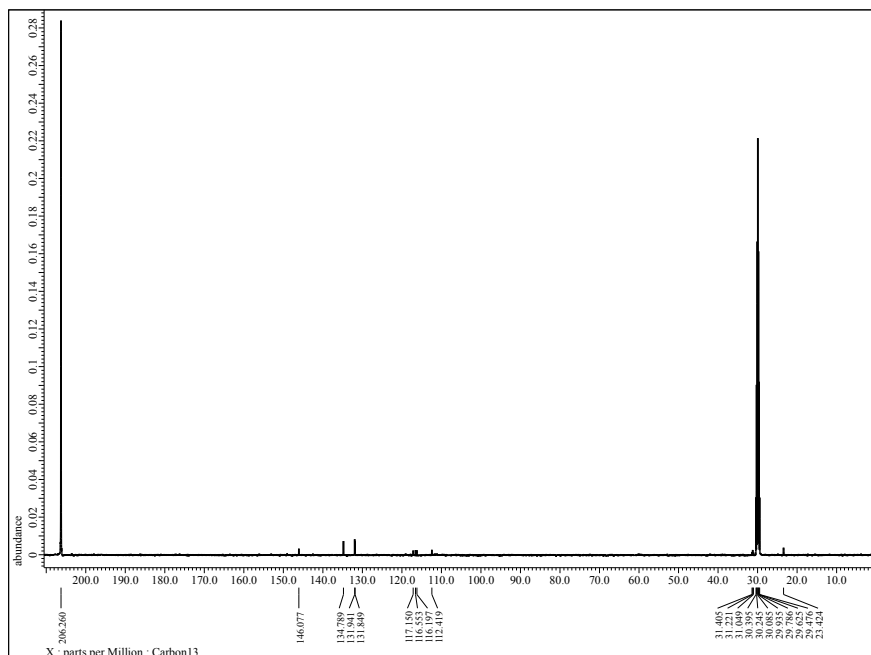


Figure 3.11 Compound 3  $^{13}\text{C}$  NMR (126 MHz, acetone- $d_6$ , 25 °C)

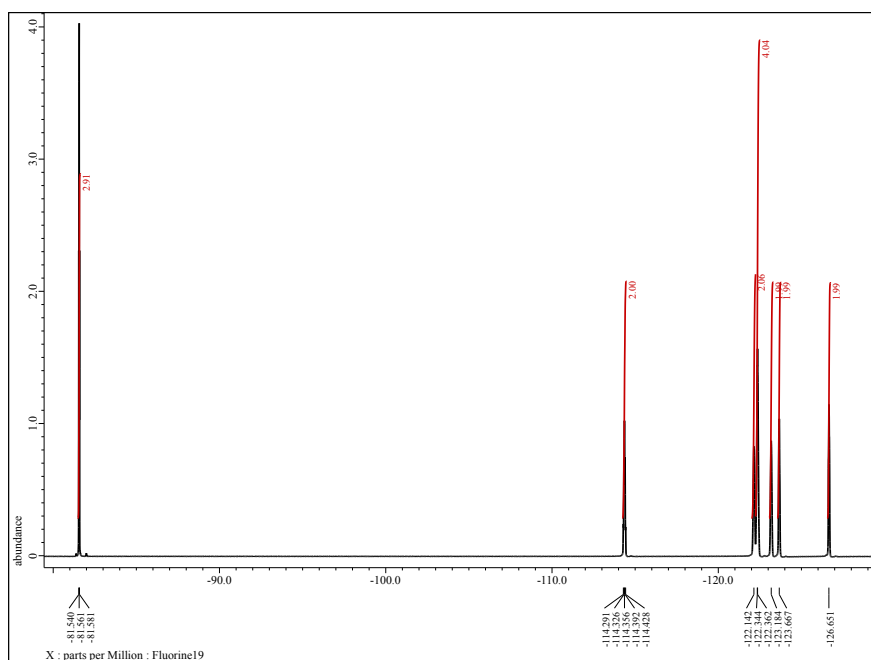


Figure 3.12 Compound 3  $^{19}\text{F}$  NMR (471 MHz, acetone- $d_6$ , 25 °C)

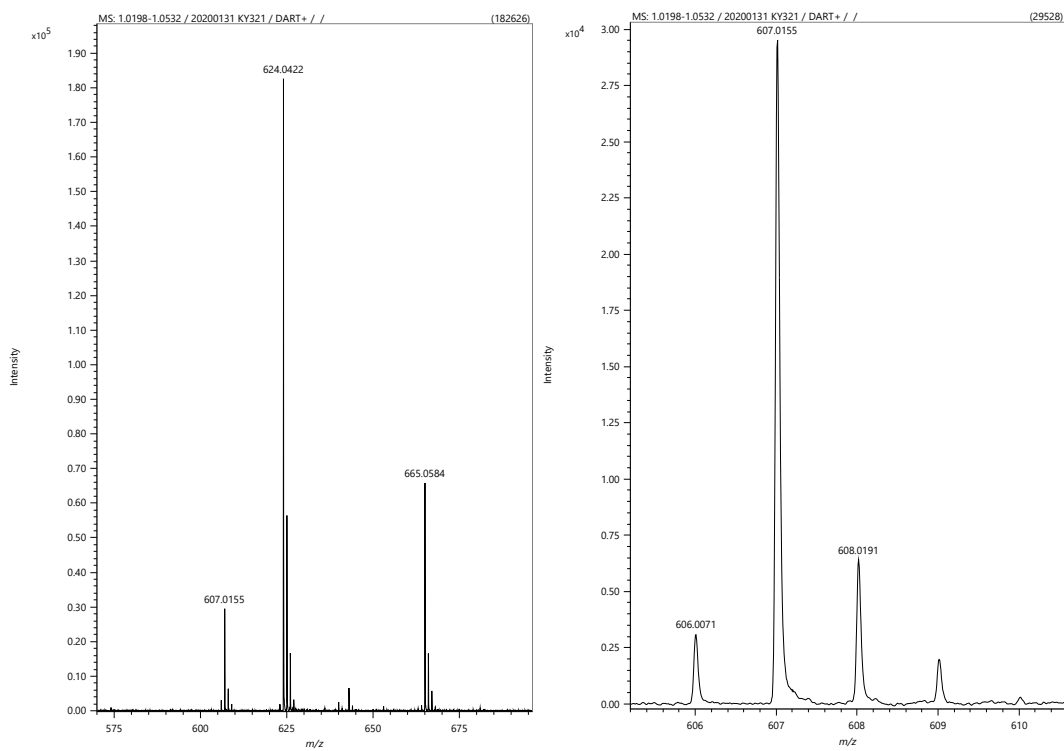
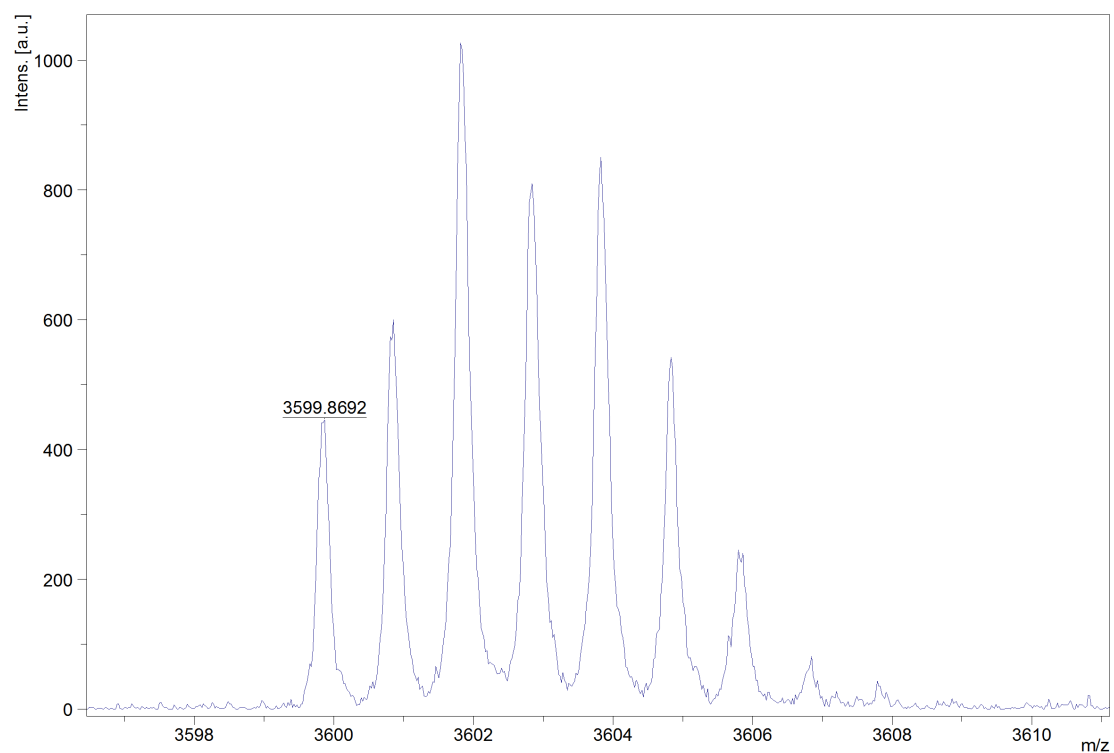
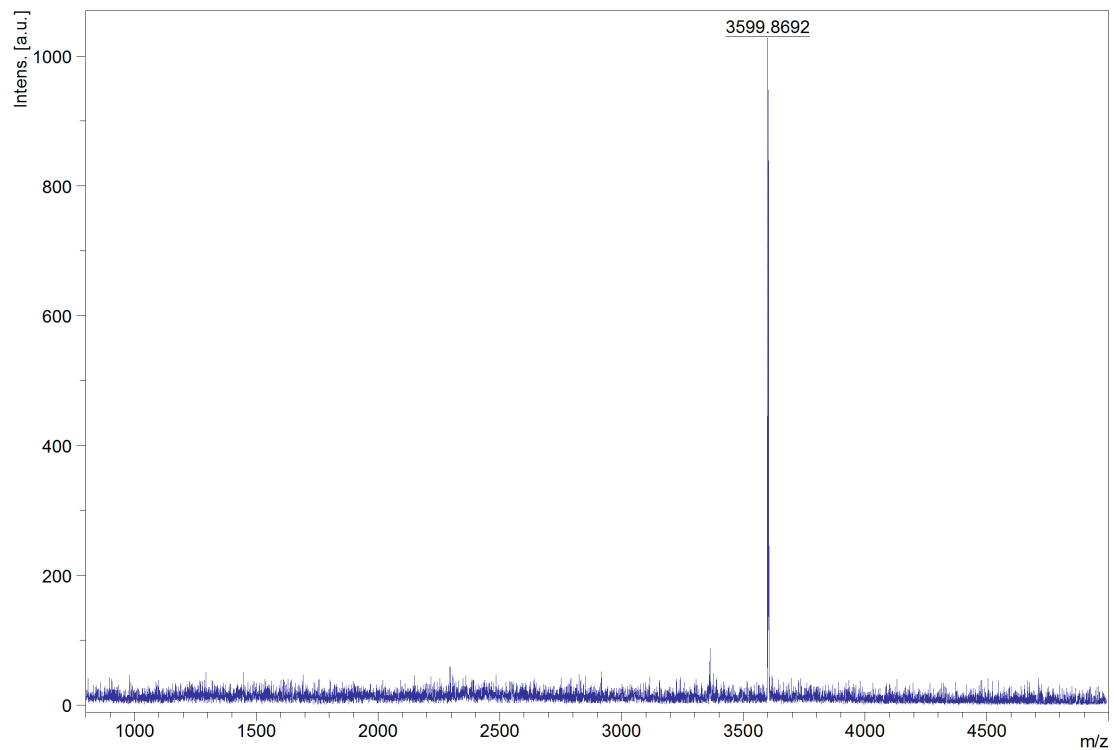
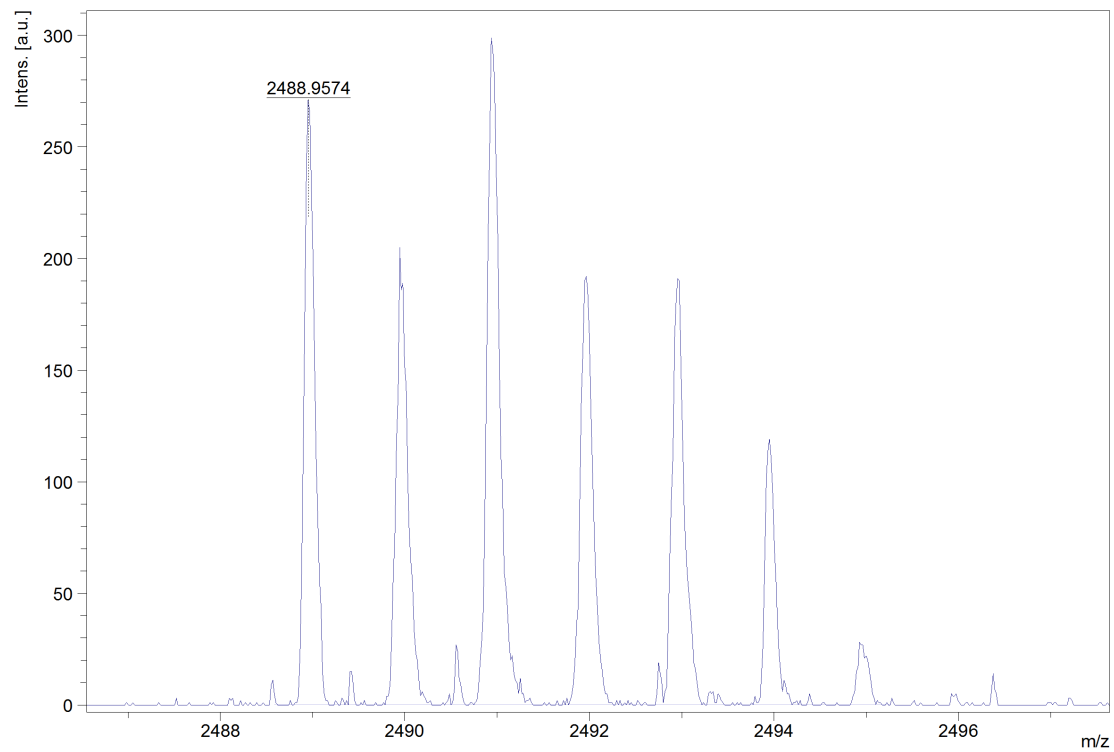
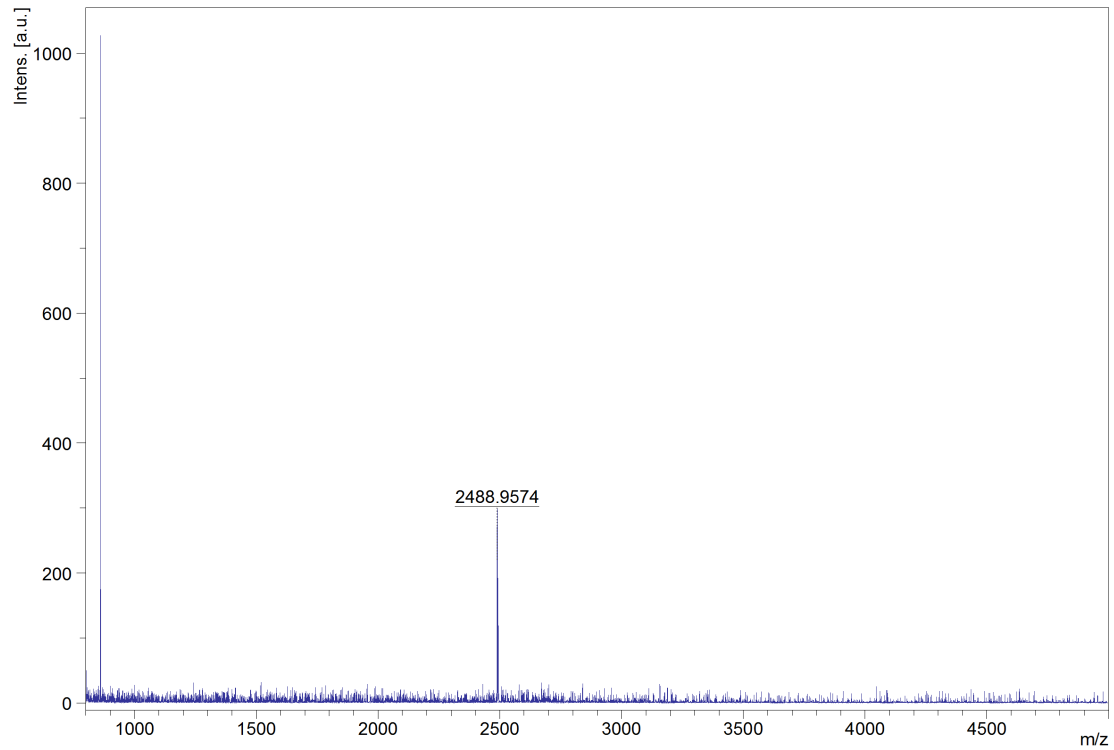


Figure 3.13 Compound 3 DART MS



**Figure 3.14 F-PC-2 MALDI TOF-MS spectra**



**Figure 3.15 F-PC-3 MALDI TOF-MS spectra**

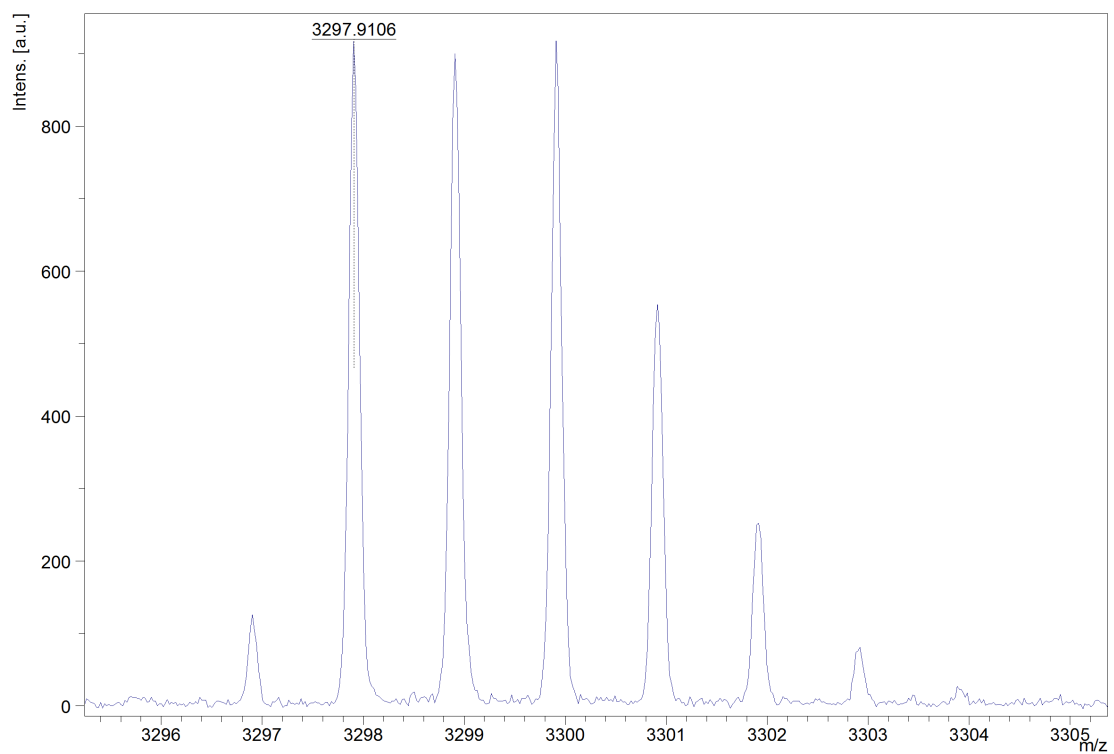
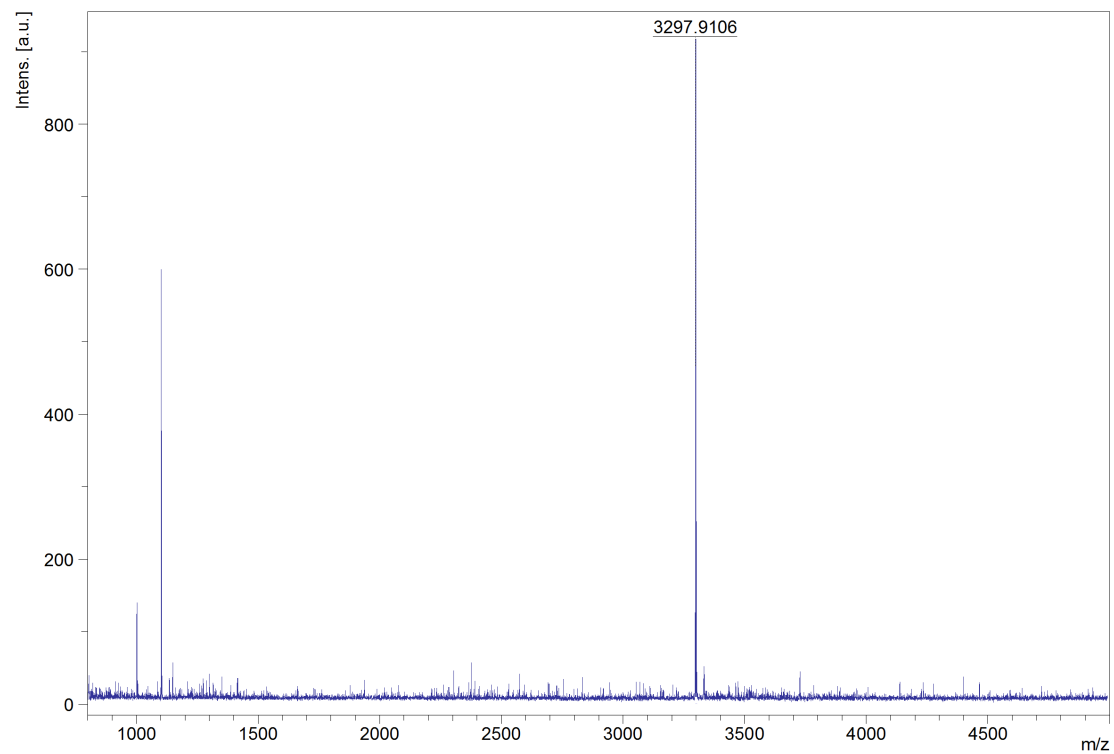


**Figure 3.16 F-SubPC-I MALDI TOF-MS spectra**

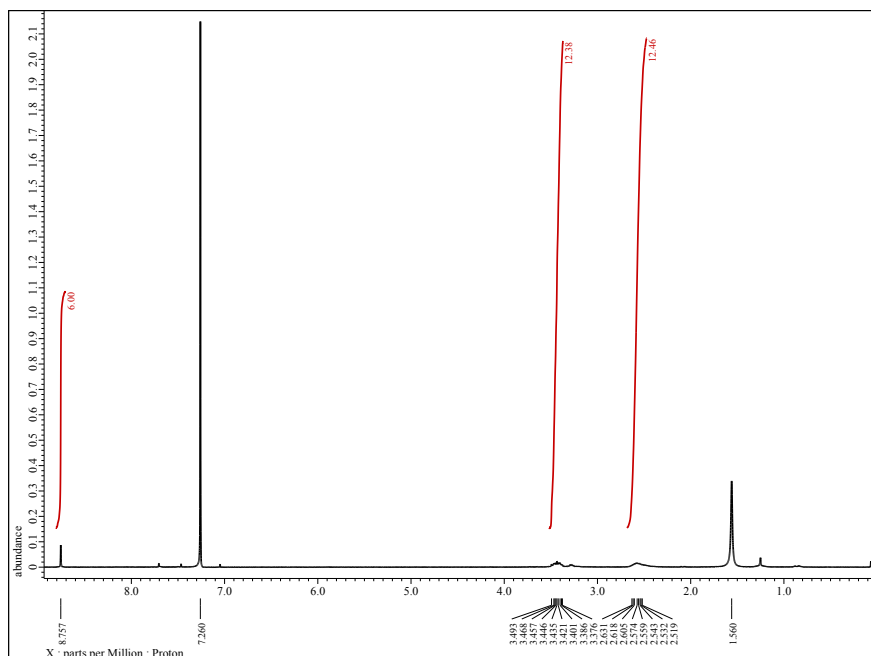


Figure 3.17 F-SubPC-2  $^1\text{H}$  NMR (500 MHz,  $\text{CDCl}_3$ , 25  $^\circ\text{C}$ )

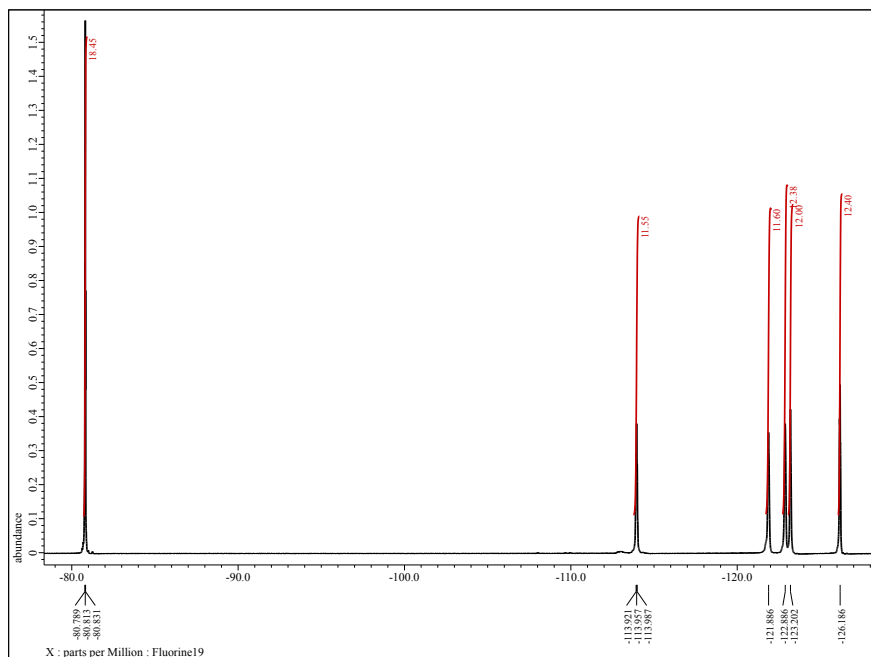
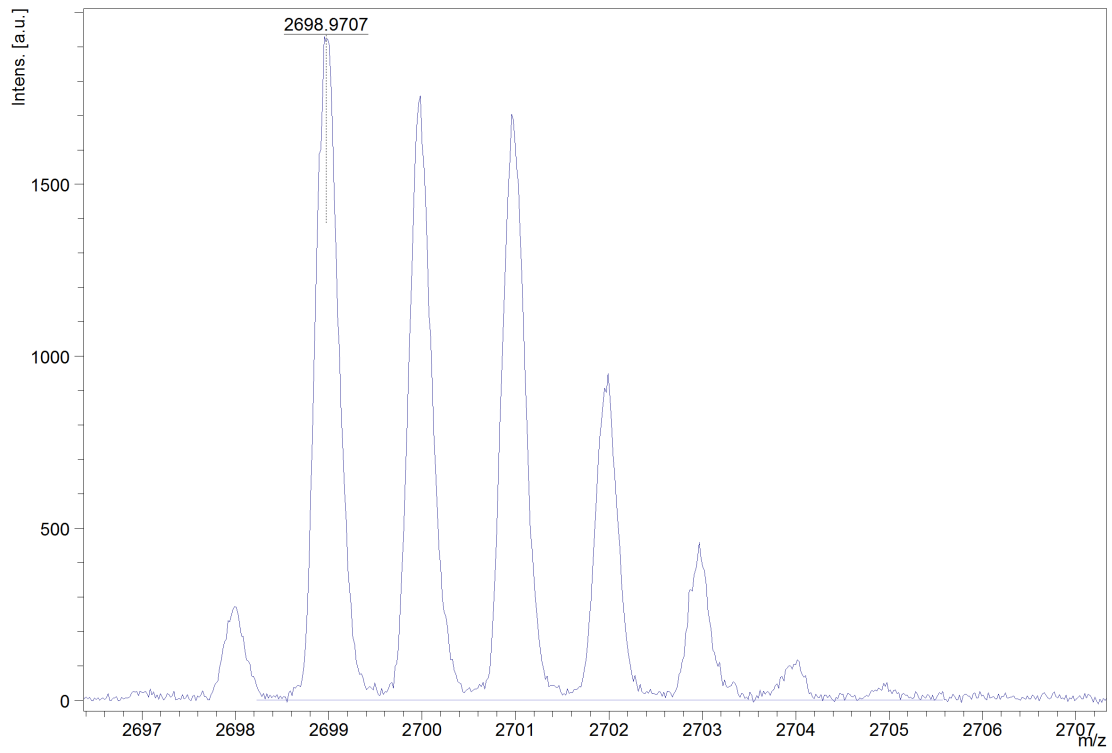
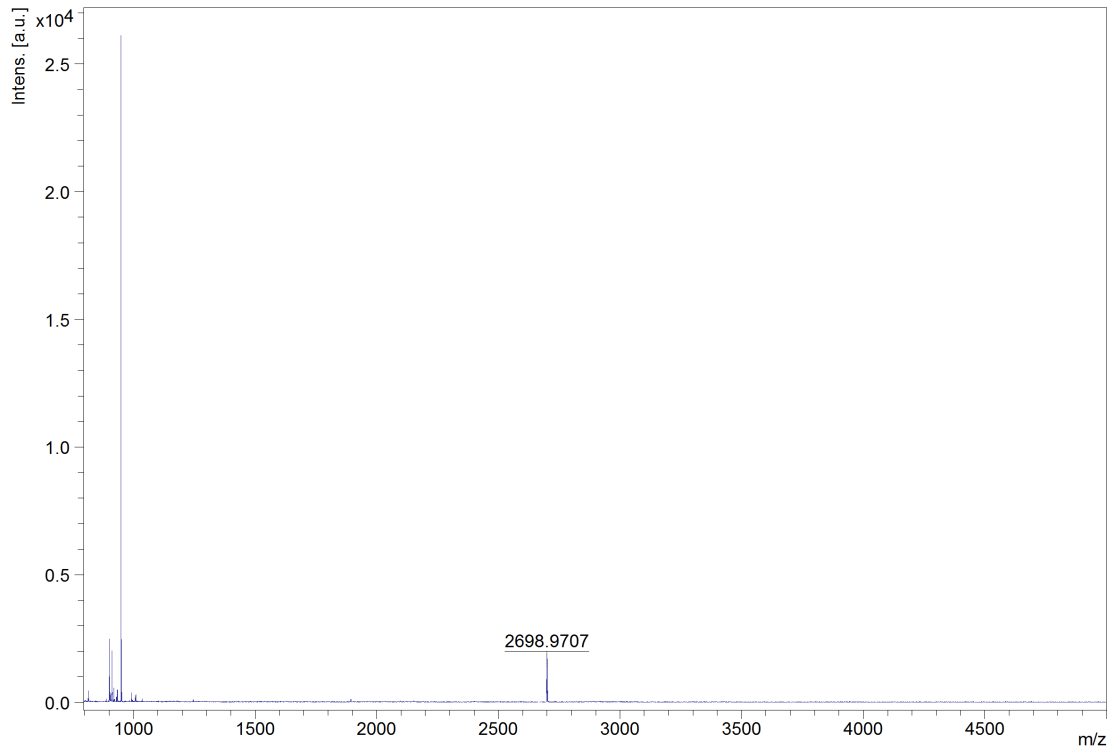


Figure 3.18 F-SubPC-2  $^{19}\text{F}$  NMR (476 MHz,  $\text{CDCl}_3$ , 25  $^\circ\text{C}$ )



**Figure 3.19 F-SubPC-2 MALDI TOF-MS spectra**

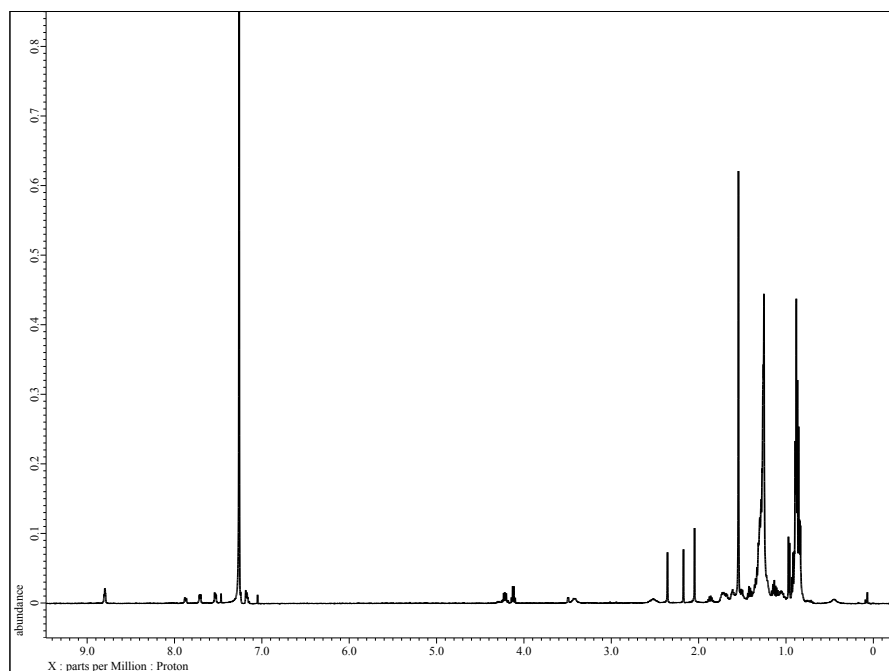


Figure 3.20 F-SubPC-3  $^1\text{H}$  NMR (500 MHz,  $\text{CDCl}_3$ , 25  $^\circ\text{C}$ )

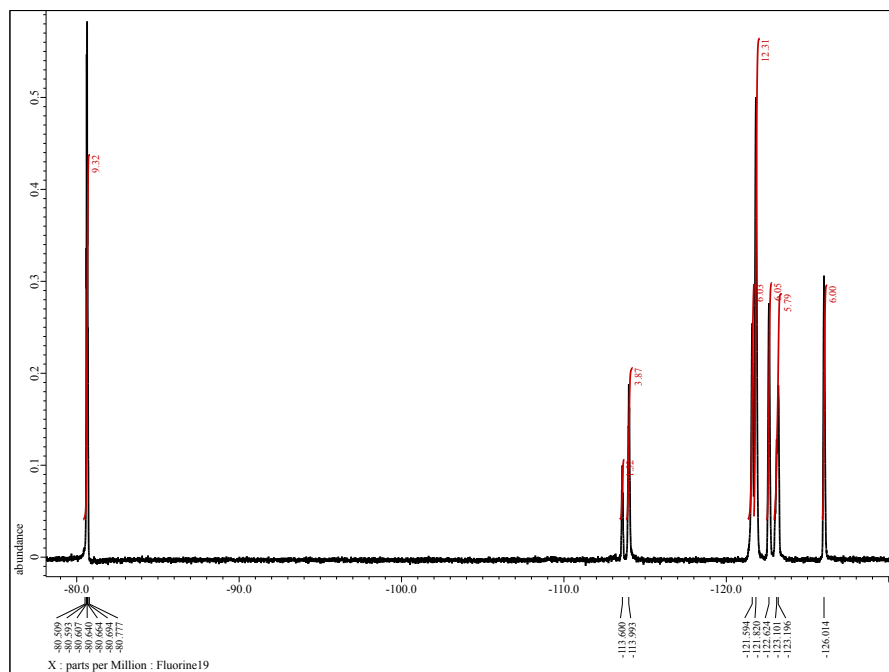
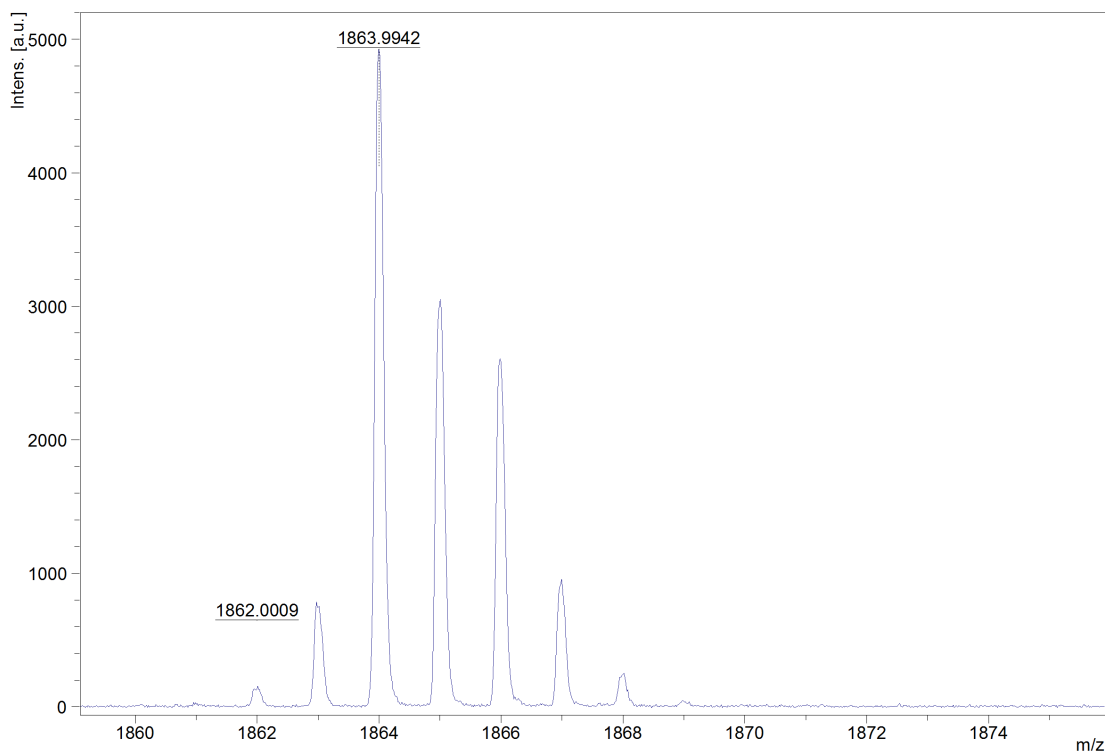
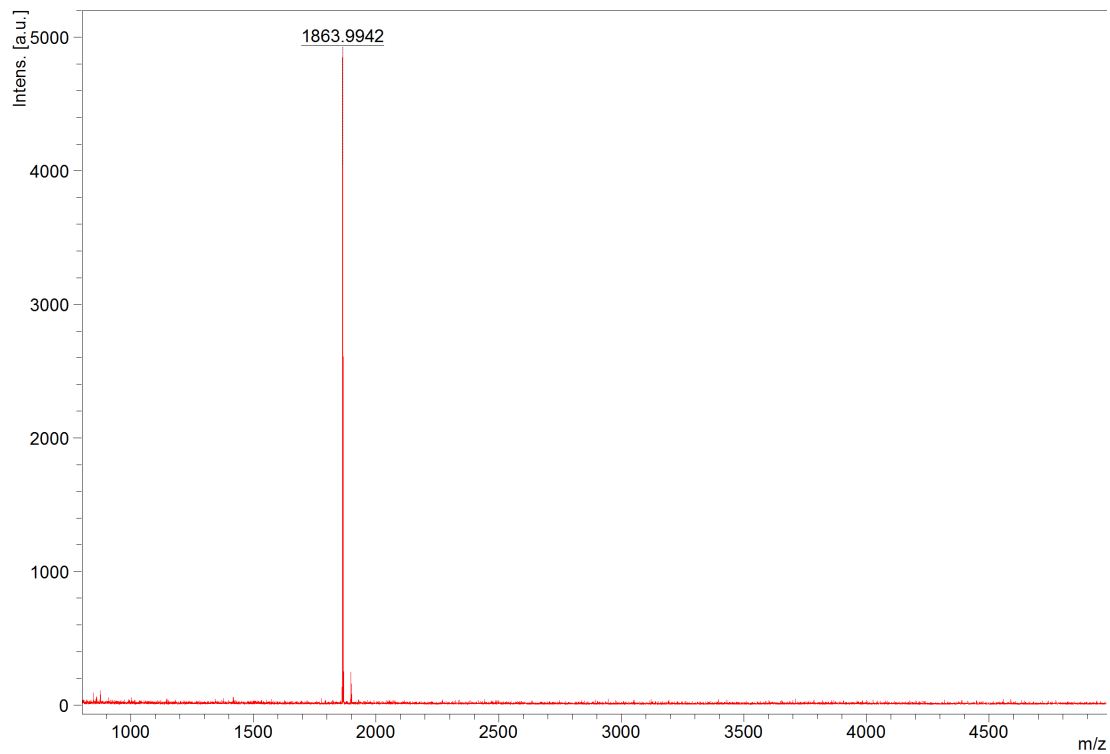
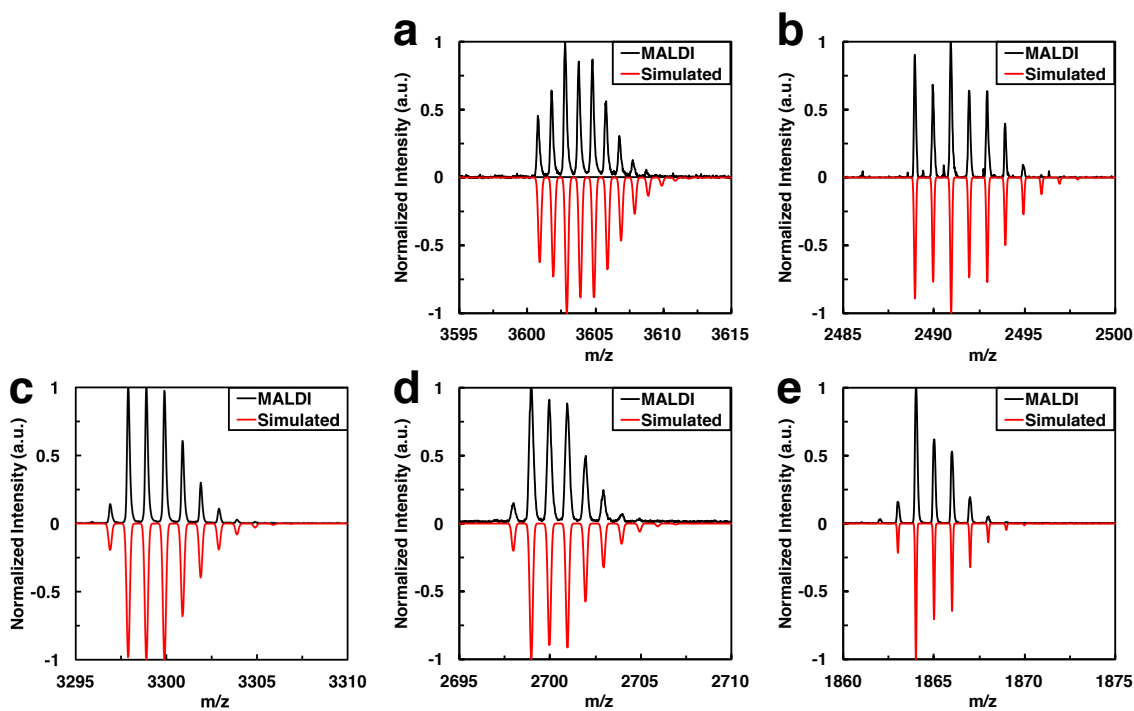


Figure 3.21 F-SubPC-3  $^{19}\text{F}$  NMR (476 MHz,  $\text{CDCl}_3$ , 25  $^\circ\text{C}$ )





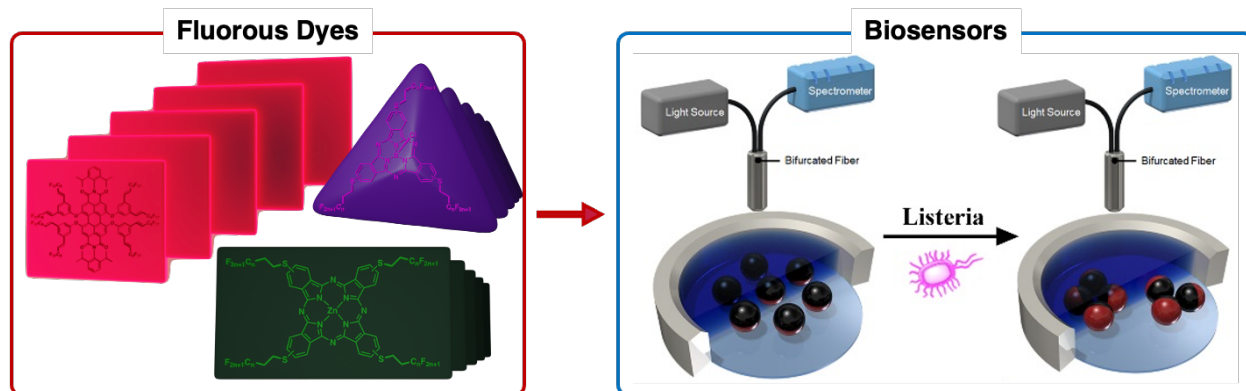
**Figure 3.22 F-SubPC-3 MALDI TOF-MS spectra**



**Figure 3.23** MALDI TOF-MS isotope distribution comparisons of (a) **F-PC-2**, (b) **F-PC-3**, (c) **F-SubPC-1**, (d) **F-SubPC-2**, and (e) **F-SubPC-3**, with their respective simulated mass spectra. MALDI TOF-MS spectra could not be obtained for **F-PC-1**, presumably due to aggregation.

## CHAPTER 4:

### Adding Color to Dynamically Reconfigurable Complex Emulsions



Parts of this chapter were adapted and reprinted with permission from:

Zhang, Q.; Zeininger, L.; Sung, K. J.; Miller, E. A.; Yoshinaga, K.; Sikes, H. D.; Swager, T. M. Emulsion Agglutination Assay for the Detection of Protein-Protein Interactions: An Optical Sensor for Zika Virus. *ACS Sensors* **2019**, *4*, 180. Copyright © 2019, American Chemical Society. Q.Z., L.Z., H.D.S., and T.M.S. designed research; Q.Z., L.Z., K.J.S., E.A.M., and K.Y. performed research; K.J.S., E.A.M., and K.Y. contributed new reagents/analytic tools; Q.Z., L.Z., H.D.S., and T.M.S. analyzed data; all authors contributed to the writing of the paper.

Zeininger, L.; Nagelberg, S.; Harvey, K.; Savagatrup, S.; Herbert, M.; Yoshinaga, K.; Capobianco, J.; Kolle, M.; Swager, T. Rapid Detection of *Salmonella Enterica* via Directional Emission from Carbohydrate-Functionalized Dynamic Double Emulsions. *ACS Cent. Sci.* **2019**, *5*, 789. Copyright © 2019, American Chemical Society. L.Z., S. N., M.K., and T.M.S. designed research; L.Z., S.N., K.H., S.S., M.H., and K.Y. performed research; L.Z., S.N., M.K., and T.M.S. analyzed data; all authors contributed to the writing of the paper.

Li, J.; Savagatrup, S.; Nelson, Z.; Yoshinaga, K.; Swager, T. M. Fluorescent Janus Emulsions for Biosensing of *Listeria Monocytogenes*. *Proc. Natl. Acad. Sci.* **2020**, *117*, 11923. Copyright © 2020, National Academy of Sciences. J.L. and T.M.S. designed research; J.L., S.S., Z.N., and K.Y. performed research; Z.N. and K.Y. contributed new reagents/analytic tools; J.L., S.S., and T.M.S. analyzed data; all authors contributed to the writing of the paper.

Li, J.; Concellón, A.; Yoshinaga, K.; Nelson, Z.; He, Q.; Swager, T. M. Janus Emulsion Biosensors for Anti-SARS-CoV-2 Spike Antibody. *ACS Cent. Sci.* **2021**, *7*, 1166. Copyright © 2021, American Chemical Society. J.L. and T.M.S. designed research; J.L., A.C., K.Y., Z.N., and Q.H. performed research; K.Y. and Z. N. contributed new reagents/analytic tools; J.L., A.C., and T.M.S. analyzed data; all authors contributed to the writing of the paper.

## 4.1 Abstract

This chapter summarizes our efforts in utilizing dynamically reconfigurable complex emulsions for the detection of various analytes. The complex emulsions consist of hydrocarbon and fluorocarbon oils, and they can undergo morphology changes due to external stimuli. The morphology change in the emulsions can be translated into various signals, including opacity, which has enabled the detection of Concanavalin A. To improve the sensitivity of this sensor, we sought to “add color” to the emulsions by incorporating emissive dyes into the emulsions and construct a fluorescence-based sensing mechanism of analytes. This chapter will demonstrate iterations of dye combinations incorporated in the hydrocarbon and fluorocarbon phases, and we disclose our efforts in improving the sensitivity of the emulsion-based sensor.

## 4.2 Introduction

In the broadest definition, a sensor is a device, module, machine, or subsystem whose purpose is to detect events or changes in its environment and send the information to other devices. Chemical sensing relies on detecting changes in environment such as chemical transformation or molecular recognition. Requirements for a sensor ready for general use includes selectivity, high sensitivity, simplicity, and quick readout. To highlight successful examples of chemical sensors that fulfill those, glucose meter and home pregnancy tests are widely used. The chemical sensing field is withholding unlimited potential and discovery of new disruptive technologies awaits.<sup>92</sup>

This project was initiated when we realized the necessity of quickly identifying foodborne pathogens in the food industry. Conventional methods used for bacterial detection requires cell culturing and a multiday enrichment step.<sup>93</sup> Tragedies caused by foodborne pathogens could have been avoided if inexpensive and fast devices to test large amounts of food and water for pathogenic

bacteria prior to consumption were available. Modern methods based on surface plasmon resonance (SPR),<sup>94</sup> the polymerase chain reaction (PCR),<sup>95,96</sup> and immunoassays<sup>97</sup> are much more rapid but require expensive equipment and complicated procedures that has to be operated by trained technicians. These drawbacks of the current methods surrender the possibility of food testing before consumption. As a result, an on-site detection method that is rapid, inexpensive, and user-friendly is urgently needed.

This chapter focuses on the development of a biosensor using a novel class of complex emulsions that dynamically reconfigure in response to external stimuli.<sup>16</sup> The emulsions, nominally double emulsions comprising equal volumes of two immiscible oils (e.g. hydrocarbon (H) and fluorocarbon (F) oils), change morphologies from encapsulated to Janus configurations by tuning interfacial tensions at the H/W and F/W interfaces (**Figure 4.1a**). For example, changing the surfactant mass balance can reversibly change the morphology of these emulsions (**Figure 4.1c**). Because these emulsions show a response to the environment very quickly (within minutes), we envisioned to develop a sensing scheme so that these emulsions respond to stimuli of interest. The advantage of these emulsions is the fact that the oils have different refractive indices to produce directional optical properties that are very sensitive to interfacial bioconjugation, molecular binding, and enzyme modification.

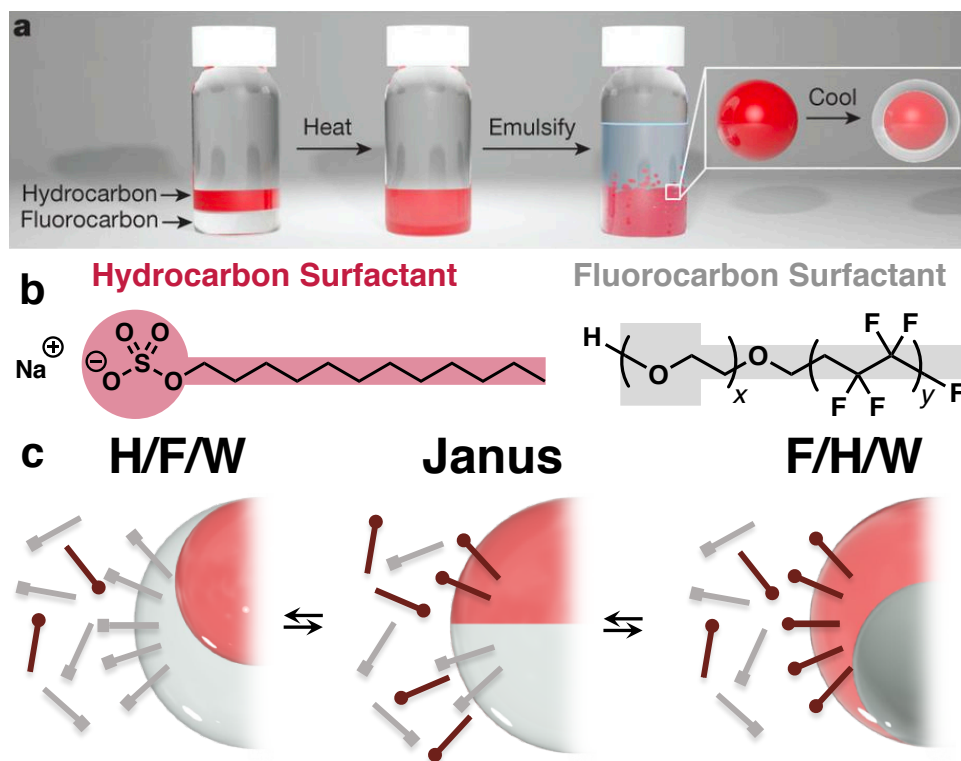


**Figure 4.1** (a) Fabrication of the complex emulsion. The hydrocarbon phase contains Nile Red. Figure adapted with permission.<sup>16</sup> Copyright © 2015, Springer Nature. (b) Chemical structures of typical hydrocarbon and fluorocarbon surfactants. (c) Schematic image of the emulsions undergoing reversible morphology change.

Previous work from the group pioneered by Zhang *et al.* has enabled the detection of Concanavalin A (ConA), an *E. coli* mimic. In this work, the emulsions were fabricated with a mannose-functionalized surfactant that selectively localizes at the H/W interface (**Figure 4.2a**).<sup>98</sup> When these emulsions were exposed to ConA, a carbohydrate-binding protein, the emulsions showed an interesting agglutination phenomenon. This agglutination behavior can be observed in the microscope images where the emulsions are tilted (**Figure 4.2b**). The degree of agglutination, hence the concentration of ConA, could be computationally quantified by image analysis. This detection can also be demonstrated by reading of a QR code (**Figure 4.2c**). Because the Janus emulsions can act as a lens, the QR code is readable when it is in its initial state. Upon agglutination, the emulsions are forced out of their natural orientation, which is aligned by gravity with the

fluorocarbon phase being denser, thereby leading to scattering and render the image opaque and unreadable.

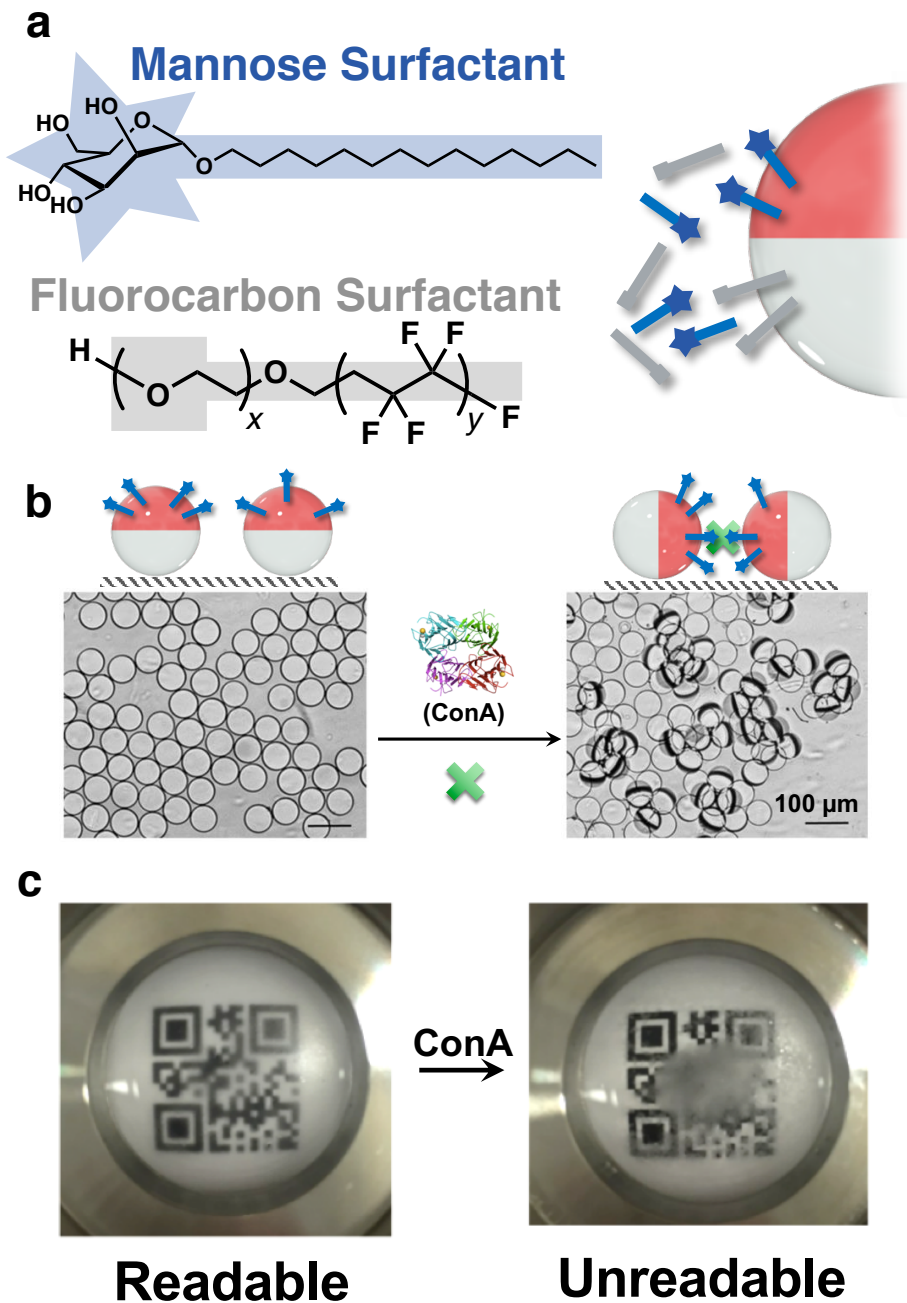


**Figure 4.2** Janus emulsions for the detection of ConA. (a) Chemical structure of the surfactants to fabricate the Janus emulsions and an illustration of the emulsion. (b) Cartoon and top-view microscope images of the emulsions before and after addition of ConA. (c) QR code placed under the sample for the agglutination detection scheme. The sample becomes opaque upon agglutination, rendering the QR code to be unreadable. Figure adapted with permission.<sup>98</sup> Copyright © 2017, American Chemical Society.

To further expand the scope and utility of this sensor, we turned to the utilization of fluorescence as an optical read-out for a sensor with a higher sensitivity. Our recent efforts has enabled the detection of analytes such as the Zika virus,<sup>99</sup> *Salmonella*,<sup>100</sup> *Listeria*,<sup>101</sup> and anti-SARS-CoV-2 spike antibody.<sup>102</sup> This chapter focuses on the optical aspect of the sensor and its iterations, since the sensing analyte is interchangeable when there is a mechanism for an interaction. The biosensors discussed in this chapter does not require technical equipment, gives results within 2 hours, as well as they are simple, specific, and sensitive. All these features highlight the sensor's potential for widespread use.

### **4.3 Results and Discussion**

Among the many unique features of the dynamically reconfigurable complex emulsions, we had not yet utilized them to incorporate functionality in the fluoruous phase. One of the reasons is the limited number of materials that can partition in the fluoruous phase, as mentioned in previous chapters of this thesis. The discovery of fluoruous dyes opens the possibility of incorporating them into the fluoruous phase of these emulsions, thereby enabling fluorescence analysis of them. The chemical structures of the dyes discussed in this chapter is summarized in **Figure 4.3**.



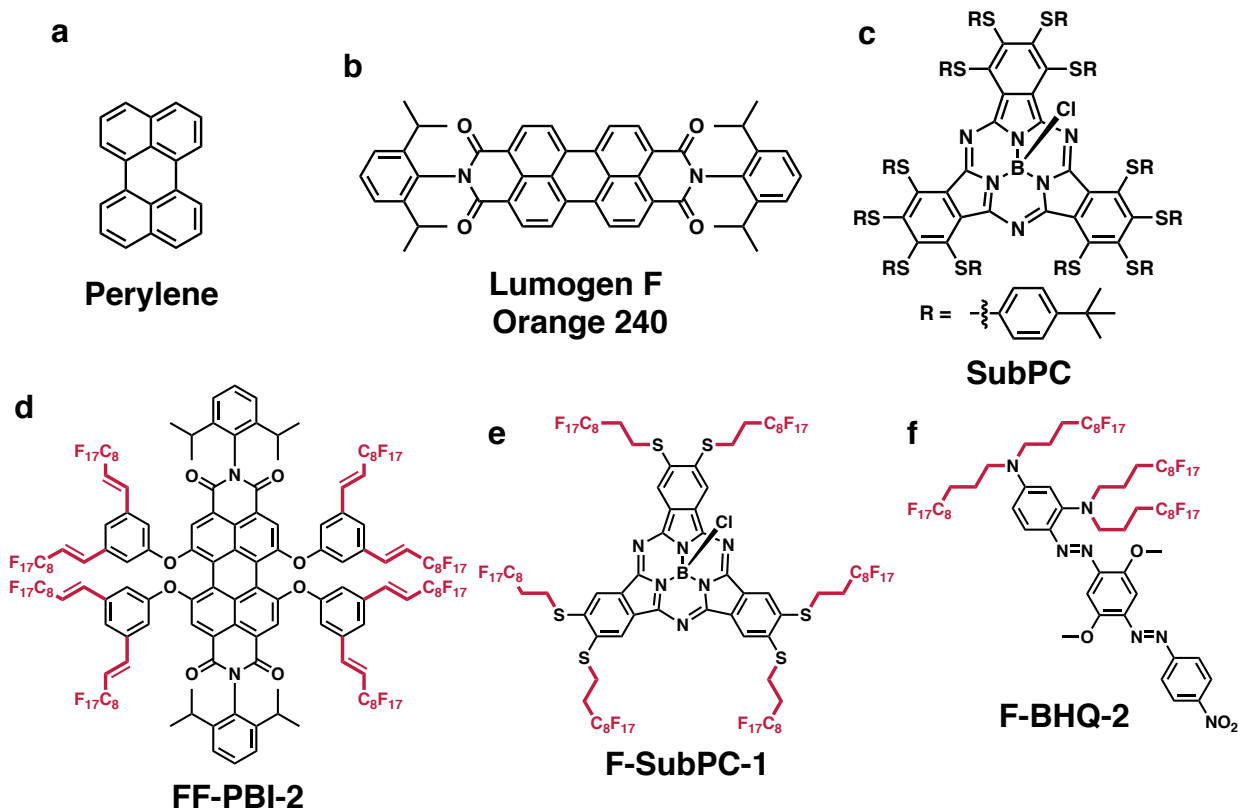


**Figure 4.3** Chemical structures of dyes discussed in this chapter.

### 4.3.1 Combination of Perylene and FF-PBI-2 in Emulsions

We first attempted to incorporate a perylene dye in the hydrocarbon phase and **FF-PBI-2** in the fluorocarbon phase. Perylene was chosen because it possesses a high quantum yield, and the emission overlaps with the absorption of **FF-PBI-2**, so that the inner filter effect can take place. We envisioned that by monitoring the wavelengths of the emission of the two dyes, we could develop a ratiometric sensor for the detection of agglutination, with potential for multiplexing. The overall emission of the emulsions will be dominated by **FF-PBI-2** if the emulsions are arranged in their gravity aligned fashion because the emitted light from perylene collected by the optical fiber must pass through the fluorocarbon phase with **FF-PBI-2** before exiting the emulsion (**Figure 4.4a**). The degree of agglutination is accompanied by a continuous increase of the emission of the perylene dye, because of the decreased path length through the absorbing fluorocarbon phase

(**Figure 4.4b**). In this example, we utilized tetravalent streptavidin as our analyte, and attempted agglutination with emulsions with the recognition protein rcSso7d immobilized on the surface via surfactant functionalization. The detection of the ratio of perylene ( $I_H$ ) and **FF-PBI-2** ( $I_F$ ) emission provide for precise correlation with the level of agglutination, which can be used to quantify analyte concentration. Higher concentrations of analyte produced saturation of the light intensity ratio (**Figure 4.4c**).

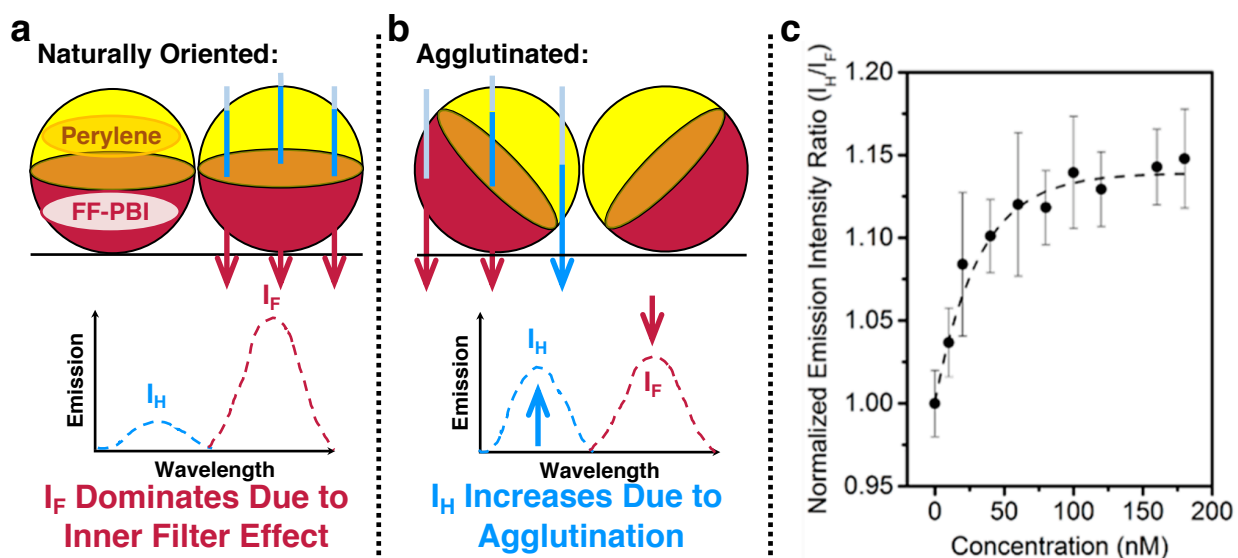


**Figure 4.4** Schematic diagram of the emulsions using the inner filter effect. (a) Diagram of naturally oriented emulsions and its optical path. (b) Diagram of agglutinated emulsions and its optical path. (c) Normalized emission intensity ratio  $I_H/I_F$  in correlation with the concentration of streptavidin. Figure adapted with permission.<sup>99</sup> Copyright © 2019, American Chemical Society.

In another scheme with this dye combination, we utilized the emulsions' morphology change for the analyte detection. In a raytracing simulation shown in **Figure 4.5**,<sup>100</sup> we found that when light is shone on the emulsion from above a H/F/W morphology emulsion, light travels through the H/F interface due to total internal reflection originating from the low refractive index of the fluororous phase. In addition, the simulation suggests that when the morphology is between H/F/W and the Janus state, the light intensity becomes the highest. The proposed detection strategy relies on reversible reactions between boronic acid surfactants and carbohydrates at the

hydrocarbon/water interface leading to a dynamic reconfiguration of the droplet morphology, which alters the angular distribution of the droplet's fluorescent light emission. We exploited this unique chemical–morphological–optical coupling to detect *Salmonella enterica*, a species of bacteria with a well-known binding affinity for mannose.<sup>100</sup>

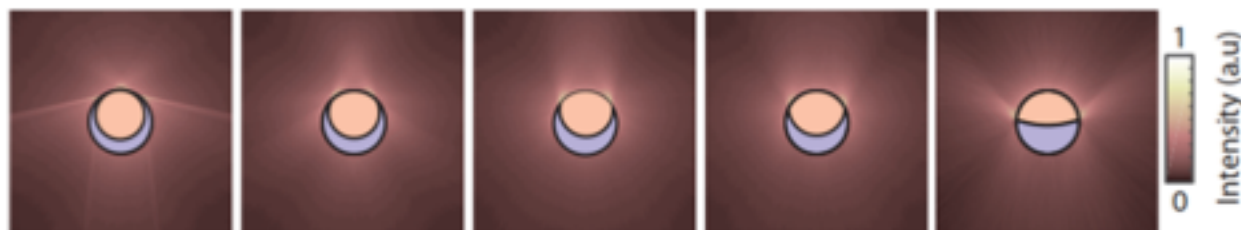


**Figure 4.5** Intensity distribution around the droplet determined by 2D raytracing for varying emulsion morphologies. Figure adapted with permission.<sup>100</sup> Copyright © 2019, American Chemical Society.

To invoke a dynamic reconfiguration of the emulsions' morphology in response to the presence of microorganisms, we employed boronic acid surfactants that reversibly bind mono- and polysaccharides, as well as N-glycans present in IgG antibodies (**Figure 4.6a**). Changes in the H/W interfacial tension associated with reversible interfacial reactions between the boronic acids and these recognition groups are detected optically. **Figure 4.6b** shows a schematic image of the light-curve (L-curve) developed in this work. Boronic acid-functionalized emulsions are adjusted to yield the highest emission intensity (**Figure 4.6b**, (1)). Upon reversible binding to carbohydrates or antibodies the emission intensity decreases by up to 60% resulting from the reconfiguration to the near-Janus morphology (**Figure 4.6b**, (2)); the emission intensity transitions back to the high original state upon removal of the carbohydrates or antibodies by *Salmonella* cells (**Figure 4.6b**, (3)).

**Figure 4.6c** shows the normalized emission intensities of emulsions containing perylene in the hydrocarbon phase, **FF-PBI-2** in the fluorocarbon phase, and the ratiometric read-out of the two emissions. A ratiometric read-out has advantages for allowing a calibration-free detection by fulfilling the needs for on-site sensing platforms such as simplicity, stability, and modularity, as

well as negates any reproducibility issues arising from the polydispersity of the emulsions. The results confirm that the ratiometric read-out can reach a highest normalized intensity ratio greater than 2.0, whereas a single read-out reaches to about 1.6.

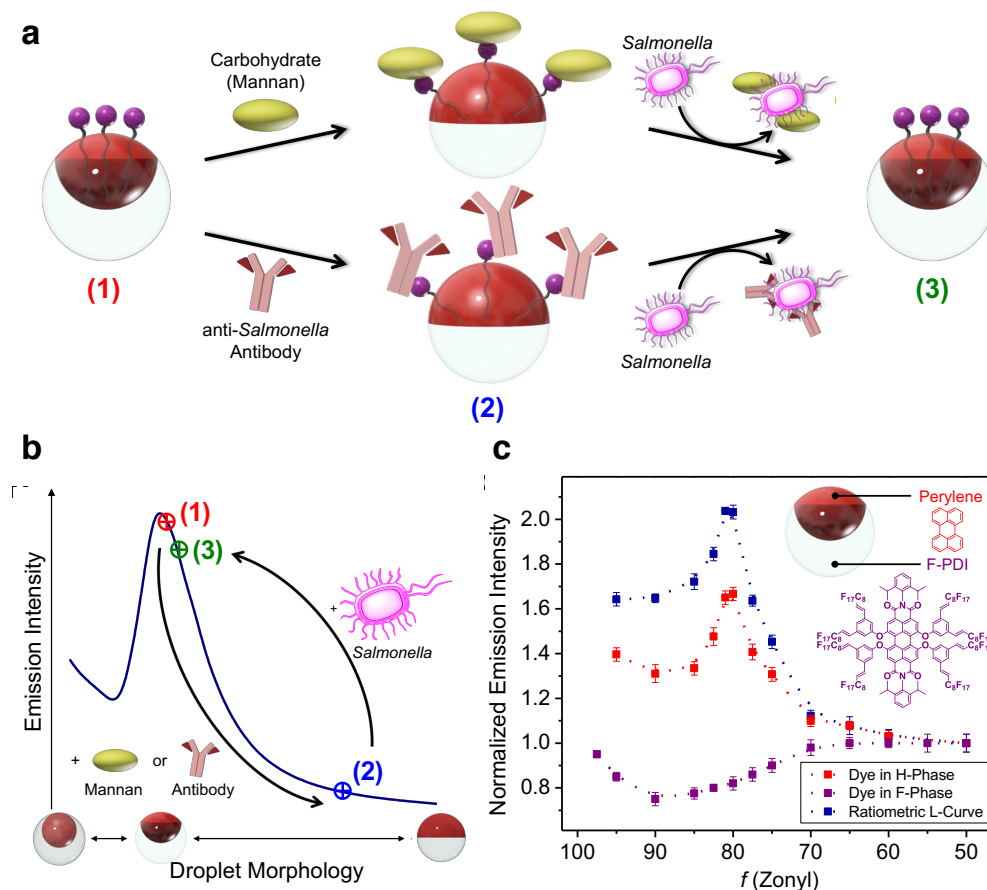


**Figure 4.6** Conceptual sketch of the mechanism for the detection of *Salmonella enterica* cells using boronic acid-functionalized complex emulsions with reversible assembly of carbohydrate or IgG antibody. (a) Changes in the droplet morphology, induced by reversible assembly of carbohydrates or IgG antibodies at the hydrocarbon (HC, red) water (W) interface and upon removal by competitive binding to *Salmonella* cells. (b) Light-curve: Boronic acid-functionalized emulsions are initialized to yield the highest emission intensity (1); upon reversible binding to carbohydrates or antibodies the emission intensity decreases by up to 60% resulting from the reconfiguration to the Janus morphology (2); the emission intensity transitions back to the high original state upon removal of the carbohydrates or antibodies by *Salmonella* cells (3). (c) Normalized emission intensities of polydisperse droplets containing perylene dye in the hydrocarbon phase ( $\lambda = 475$  nm) and **FF-PBI-2** in the fluorocarbon phase ( $\lambda = 580$  nm). The ratio between the two emissions was used as a ratiometric read-out for the detection of live *Salmonella* bacteria. Figures adapted with permission.<sup>100</sup> Copyright © 2019, American Chemical Society.

### 4.3.2 Combination of SubPC and FF-PBI-2 in Emulsions

Although employing perylene as the hydrocarbon soluble dye was successful, perylene was only chosen for its commercial availability and high quantum yield. In parallel, we also sought to discover new dye combinations that may help improve the sensitivity, for example, a dye that has a higher molar extinction coefficient or a better spectral overlap with **FF-PBI-2**. We turned to utilize a non-emissive blocker dye and developed a fluorescence blocking mechanism. We synthesized a new subphthalocyanine (**SubPC**) for the hydrocarbon phase and used the same **FF-PBI-2** for the fluorocarbon phase. The subphthalocyanine has 2 features: (1) it has a high molar extinction coefficient at the excitation wavelength, and (2) it also has a high molar extinction coefficient at the emission wavelength being monitored. This double fluorescence blocking mechanism has an advantage over the inner filter mechanism discussed in the previous section **4.3.1** that in order to detect the fluorescence by the optical fiber placed on top of the sample, the light must travel through the hydrocarbon phase containing the subphthalocyanine twice, which would increase the signal-to-noise ratio of our sensor. **Figure 4.7b** summarizes the photophysical properties of the two dyes. The absorbance spectra of **SubPC** shows a higher absorbance over **FF-PBI-2** in the near UV region, as well as a good spectral overlap with high molar extinction coefficient with the emission of **FF-PBI-2**. **Figure 4.7c** compares the molar extinction coefficient of **SubPC** ( $\epsilon_H$ ) and **FF-PBI-2** ( $\epsilon_F$ ), and from this graph we find blocking of the excitation light to be most efficient at 361 nm. The data showing the filter effect are illustrated in **Figure 4.7d** wherein the addition of the **SubPC** dye reduces the **FF-PBI-2** emission by 17-fold (from 8,000 to 450 arbitrary units).

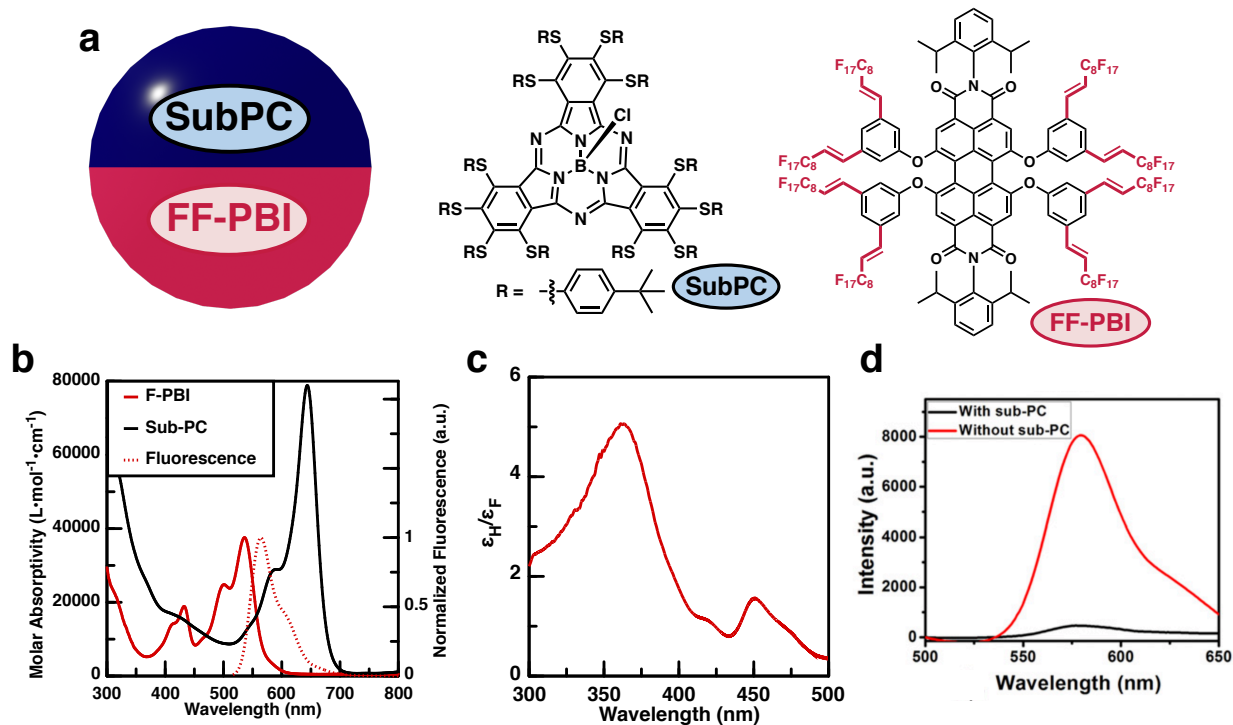


**Figure 4.7** Photophysical properties of the dyes in solution and in emulsions. (a) Schematic image of the emulsions and the chemical structure of the dyes incorporated in the emulsions. (b) Normalized absorbance and fluorescence spectra of **FF-PBI-2** in HFE-7500, overlaid with absorbance spectra of **SubPC** in DEB. (c) Molar extinction coefficient ratio of **SubPC** ( $\epsilon_H$ ) and **FF-PBI-2** ( $\epsilon_F$ ) plotted against the wavelength. (d) Fluorescence spectra of emulsions containing **FF-PBI-2** in the fluorocarbon phase with and without **SubPC** in the hydrocarbon phase. Figures adapted with permission.<sup>101</sup> Copyright © 2020, National Academy of Sciences.

Agglutination of functionalized dye containing droplets results in a tilting and creates a path between the bifurcated optical fiber for excitation light and emitted light that does not need to pass through the **SubPC** filter layer. Hence, the action of tilting the dyes from their surface normal orientation by agglutination produces an emission signal that can be monitored using a bifurcated optical fiber assembly as shown in **Figure 4.8a**. We employed a polymeric H/W surfactant block copolymer containing a hydrophobic polystyrene block with a high affinity for the hydrocarbon phase, a hydrophilic polyacrylic acid block, and a polyacrylic acid block that is partially conjugated with transcyclooctene (Poly-TCO). *Listeria* antibodies were functionalized through their free amines by reaction with tetrazine-N-hydroxysuccinimide (NHS) ester. Janus

emulsions prepared in phosphate buffered saline (PBS) buffer have Poly-TCO localized at the H/W interface, and the tetrazine and transcyclooctene bioorthogonal reaction is performed *in situ*. Detection was accomplished when the droplet immobilized antibodies bind multivalently to *Listeria* to cause clusters of tilted droplets, also called agglutinations.

The responses of emulsions functionalized with antibodies and containing dyes were determined as a function of different concentrations of heat-killed *Listeria* with mixing for 2 h. **Figure 4.8b** and **c** shows the top-view microscope image of the emulsions before and after adding 100 CFU/mL of *Listeria*, respectively. Before addition, only the top hydrocarbon phase could be observed due to blocking by **SubPC**, whereas after addition, we observe agglutination of the emulsions which exposes the bottom fluorocarbon phase containing **FF-PBI-2** due to tilting. **Figure 4.8d** illustrates a schematic diagram of agglutination, revealing the fluorescent fluorocarbon phase upon agglutination. **Figure 4.8e** shows the emission spectra taken using the scheme in **Figure 4.8a**. The calibration curve in **Figure 4.8f** reveals a limit of detection less than 100 CFU/mL. As expected, the emission at 580 nm increases with greater amounts of *Listeria*.

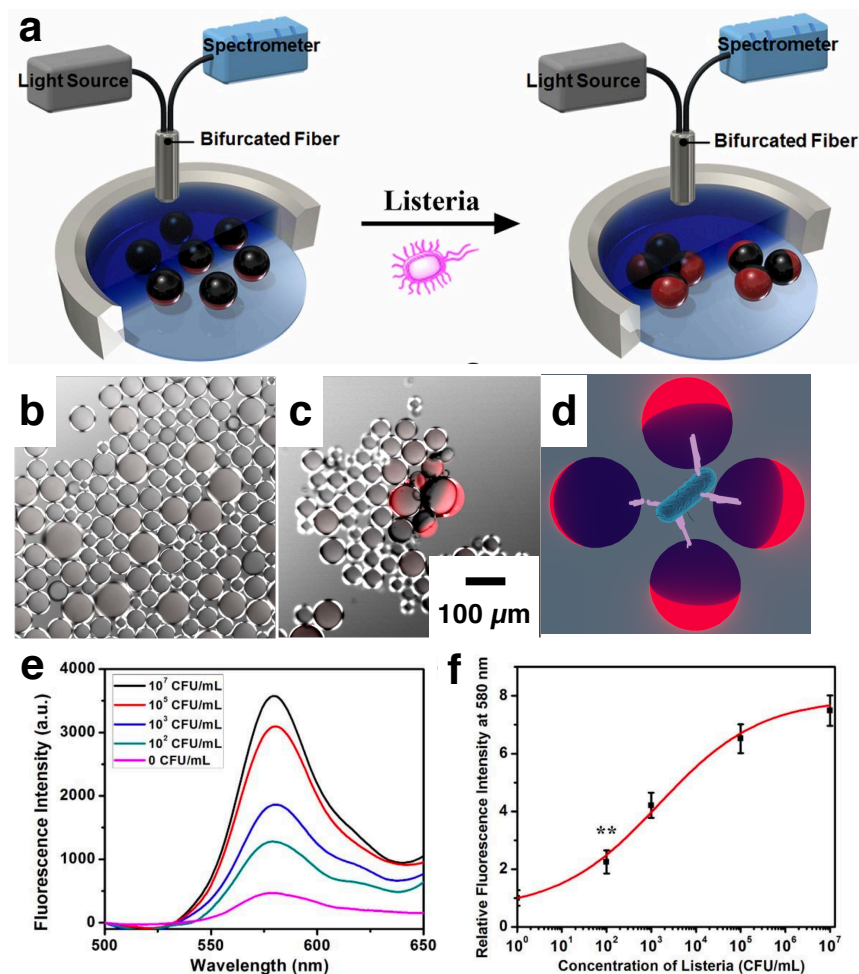


**Figure 4.8** (a) Measurement scheme showing excitation and monitoring of the fluorescence coming from the dyed emulsions. (b and c) Confocal microscope image of (b) nonagglutinated emulsion (without addition of *Listeria*) and (c) agglutinated emulsions (with the addition of *Listeria* at 100 CFU/mL), with sub-PC dye in the hydrocarbon phase and F-PBI dye in the fluorocarbon phase. (d) Schematic illustration of agglutinated emulsions. (e) Fluorescence spectra ( $\lambda_{\text{ex}} = 361 \text{ nm}$ ) of droplet containing Poly-TCO and sub-PC dye in the hydrocarbon phase and F-PBI dye in the fluorocarbon phase after addition of heat-killed *Listeria* at different concentrations. (f) Correlation of concentration of heat-killed *Listeria* and relative fluorescence intensity at 580 nm (three replicate measurements were performed for the error bars,  $**p \leq 0.01$ ). Figures adapted with permission.<sup>101</sup> Copyright © 2020, National Academy of Sciences.

Emulsions using a dye combination of **SubPC** and **FF-PBI-2** was also found useful in detecting anti-SARS-CoV-2 (severe acute respiratory syndrome coronavirus 2) antibody, the antibody that binds to the novel coronavirus responsible for the global COVID-19 pandemic that began in 2019.<sup>102</sup> Effective vaccination, which could prevent continuous or repeated pandemic has begun, however there will be a continuing need for methods to evaluate immunity. As a result,



rapid methods to detect the anti-SARS-CoV-2 antibody will be a key component of combating the pandemic. In this work, the H/W interfaces were functionalized with a secondary antibody of IgG protein and SARS-CoV-2 spike receptor binding domain (RBD), to produce two different Janus emulsions. Mixtures of these Janus emulsions enabled the detection of the anti-SARS-CoV-2 spike IgG antibody in an agglutination assay caused by the antibody's binding to both the secondary antibody of IgG antibody and SARS-CoV-2 spike protein RBD (**Figure 4.9a**). **Figure 4.9b** details the fluorescence spectra of an assay using emulsions containing dyes that were incubated with anti-SARS-CoV-2 spike antibody at different concentrations. **Figure 4.9c** shows the correlation of the relative fluorescence intensity at 580 nm and the concentration of anti-SARS-CoV-2 spike antibody. The results are consistent with the optical images and with increasing agglutination, the emission intensity grows. As revealed in **Figure 4.9b** and **c**, the limit of detection of anti-SARS-CoV-2 spike antibody is 0.2  $\mu\text{g/mL}$ . The detection results of clinical human serum samples using this agglutination assay confirm that this method is applicable to clinical samples with good sensitivity and specificity. Compared to conventional detection methods, our sensor has an order of magnitude lower detection limit (typically 20  $\mu\text{g/mL}$ ), as well as an order of magnitude shorter time to obtain results, providing a more robust testing method to combat the COVID-19 pandemic.

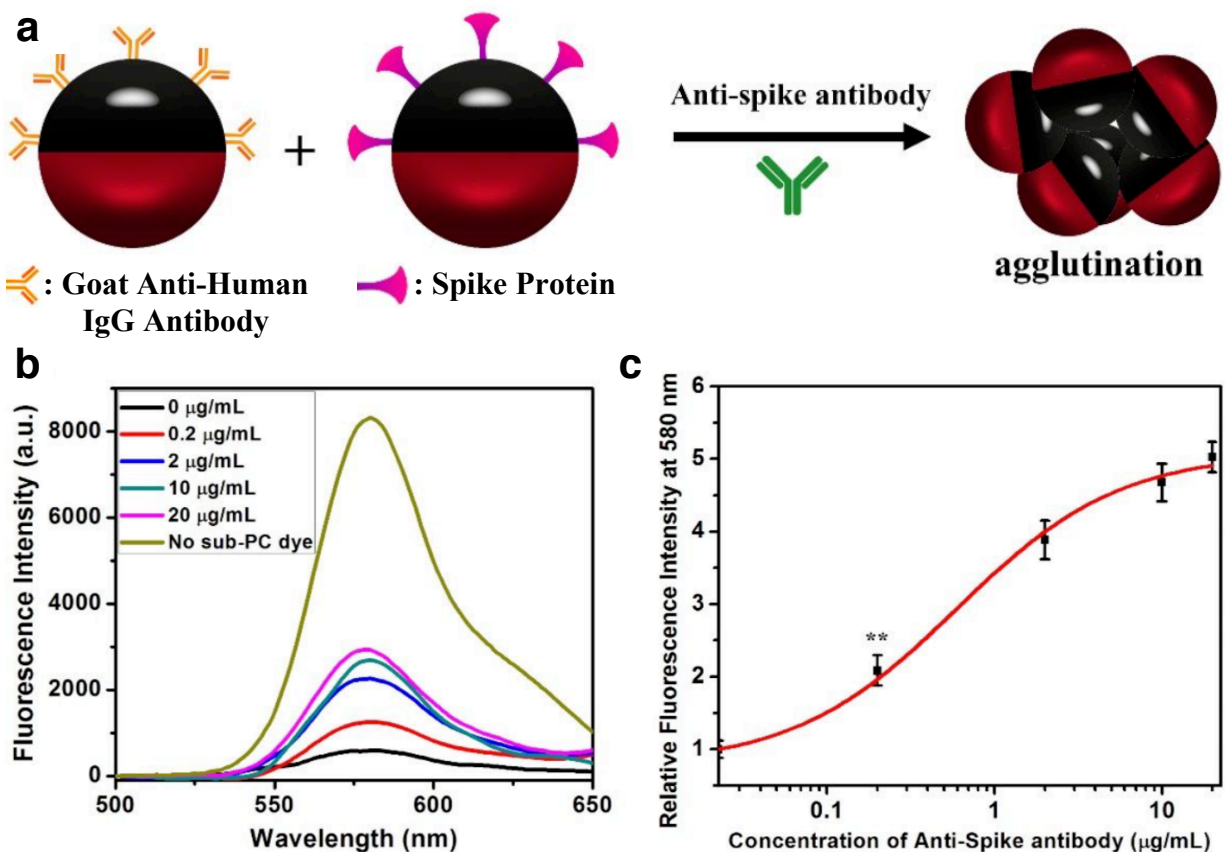


**Figure 4.9** Detection of anti-SARS-CoV-2 spike antibody. (a) Agglutination scheme of emulsions functionalized with SARS-CoV-2 spike receptor binding domain and Goat Anti-Human IgG antibody. (b) Fluorescence spectra ( $\lambda_{\text{ex}} = 361 \text{ nm}$ ) of 1:1 mixture of dye containing fully bioconjugated Janus emulsions with addition of anti-SARS-CoV-2 spike antibody at different concentrations. Note that the fluorescence intensity increases with concentration. (c) Correlation of concentration of anti-SARS-CoV-2 spike antibody and relative fluorescence intensity at 580 nm. All error bars are calculated from three independent experiments ( $n = 3$ ), and \*\* represent statistical significance (\*\* $p \leq 0.01$ ). Figures adapted with permission.<sup>102</sup> Copyright © 2021, American Chemical Society.

### 4.3.3 Combination of Lumogen F Orange 240 and F-SubPC-1 in Emulsions

Although we have focused on tracking the emission of **FF-PBI-2** in the fluorocarbon phase thus far, the arrangement of the dyes in the emulsions need not be in form given in **Figure 4.7a**, and in some cases an inverted arrangement of the blocking and emitting dyes has advantages. For example, in a highly scattering sample, such as human serum, the emission could alternatively be detected from the bottom directly through a glass support, thereby eliminating the path length through the solution. This situation is accomplished as shown in **Figure 4.10a**, wherein the

perylene dye Lumogen F Orange 240 is exclusively soluble in the hydrocarbon phase. We utilized **F-SubPC-1** as the blocking dye which is exclusively soluble in the fluorocarbon phase. Because the synthesis of **F-SubPC-1** could be accomplished in two steps, and Lumogen Orange is commercially available, this combination offers a significant synthetic accessibility as well as cost effectiveness over the **SubPC** and **FF-PBI-2** combination. The molar extinction coefficient of the two dyes and the fluorescence property of Lumogen Orange is summarized in **Figure 4.10b**. The plot of ratio of the molar extinction coefficient of **F-SubPC-1** ( $\epsilon_F$ ) and Lumogen F Orange 240 ( $\epsilon_H$ ) indicates that blocking of the excitation light to be most efficient at 398 nm (**Figure 4.10c**), so that we excite the inverted two-dye system at 398 nm. **F-SubPC-1** absorbs both the 398-nm excitation and the Lumogen F Orange 240 emission at 535 nm. The assay for the detection of *Listeria* was attempted with this dye combination. As shown in **Figure 4.10d**, *Listeria* triggers an increased emission at 535 nm. The calibration curve suggests similar limit of detection to the previous dye combination, of less than 100 CFU/mL (**Figure 4.10e**).

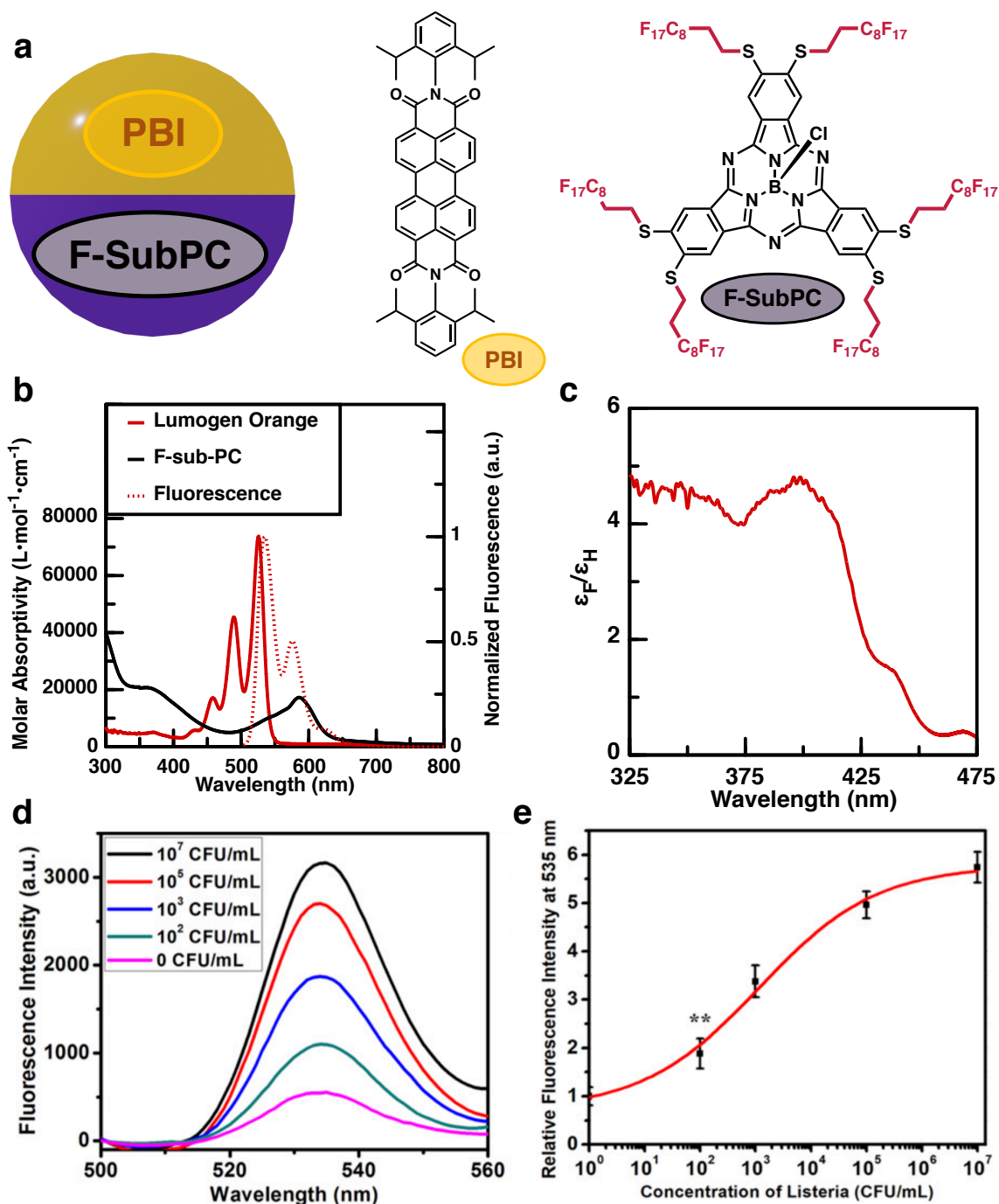


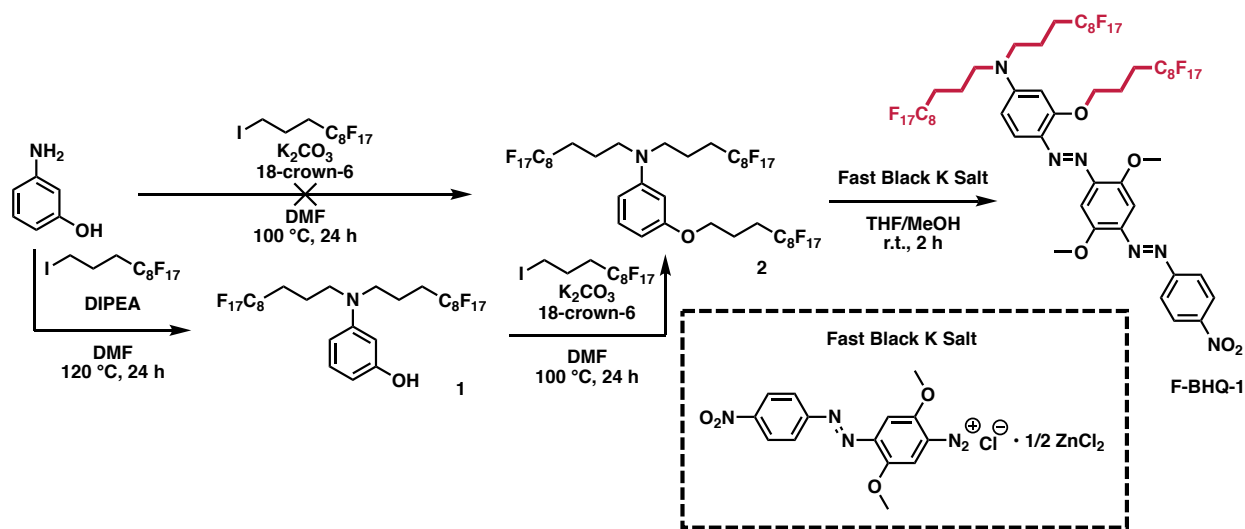
**Figure 4.10** (a) Schematic image of the emulsions and the chemical structure of the dyes incorporated in the emulsions. (b) Normalized absorbance and fluorescence spectra of Lumogen Orange in DEB, overlaid with absorbance spectra of **F-SubPC-1** in HFE-7500. (c) Molar extinction coefficient ratio of **F-SubPC-1** ( $\epsilon_F$ ) and Lumogen Orange ( $\epsilon_H$ ) plotted against the wavelength. (d) Fluorescence spectra ( $\lambda_{ex} = 398$  nm) of emulsions containing Poly-TCO and Lumogen Orange in the hydrocarbon phase and **F-SubPC-1** in the fluorocarbon phase after addition of *Listeria* at different concentrations. (e) Correlation of concentration of *Listeria* and relative fluorescence intensity at 535 nm (three replicate measurements were performed for the error bars, \*\* $p \leq 0.01$ ). Figures adapted with permission.<sup>101</sup> Copyright © 2020, National Academy of Sciences.

Although we were successful in employing these dyes in emulsions, there were a few drawbacks in the system comprising of Lumogen Orange and **F-SubPC-1**. Due to the H-aggregation of **F-SubPC-1** in fluoruous solvents, the molar extinction coefficient was only 20,000 L·mol<sup>-1</sup>·cm<sup>-1</sup>, whereas that of the organic soluble **SubPC** was 80,000 L·mol<sup>-1</sup>·cm<sup>-1</sup>. This significant decrease in the molar extinction coefficient does not enhance the sensitivity of the emulsion sensor that utilizes **F-SubPC-1** in the fluorocarbon phase, though we were able to see similar sensitivity. In addition, while our intent was that **F-SubPC-1** would be non-fluorescent like the organic **SubPC**, it was weakly fluorescent in HFE-7500. Because the emission of Lumogen F Orange 240 is monitored at 535 nm, the fluorescence from **F-SubPC-1** does not affect the sensory response but adds undesirable signal to the sensing setup. This led us to search for fluoruous dye structures that are completely non-emissive and has a higher molar extinction coefficient than **F-SubPC-1**.

#### 4.3.4 Synthesis of F-BHQs

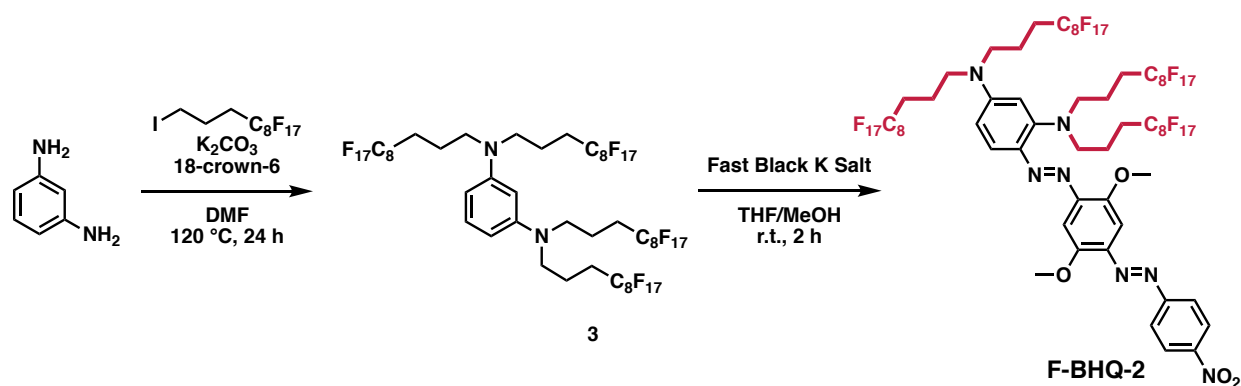
The combination of Lumogen F Orange 240 and **F-SubPC-1** showed a slightly lower sensitivity than the **SubPC** and **FF-PBI-2** combination, partially due to the low extinction coefficient of **F-SubPC-1**. We turned to the black hole quencher (BHQ) dyes, a common dye motif used in quantitative PCR probes and other Förster resonance energy transfer applications due to their broad absorption with no native emission. Since there were no precedence for fluoruous soluble BHQs, we newly designed two structures of fluoruous BHQs (**F-BHQs**) for our emulsion assay. Our first target structure, **F-BHQ-1**, was designed by following a previous report,<sup>103,104</sup> and was synthesized following **Scheme 4.1**. We attempted a three-fold alkylation of 3-aminophenol by modifying the procedures reported by Sletten and Swager.<sup>15</sup> However, the reaction led to a complicated mixture, not containing the desired product. Therefore, we took a two-step alkylation

approach, where we alkylated the amine first, then the phenol. This approach was successful in yielding the alkylated product **2** in 42% in two steps. Compound **2** was then reacted with Fast Black K salt to obtain the desired **F-BHQ-1**, though this compound could not be isolated in pure form.



**Scheme 4.1** Synthesis of **F-BHQ-1**

In parallel, **F-BHQ-2** was synthesized in a similar manner, starting from the alkylation of *m*-phenylenediamine. The synthetic scheme of **F-BHQ-2** shown in **Scheme 4.2** has multiple advantages in that it eliminates the necessity of the two-step alkylation due to the symmetry of *m*-phenylenediamine, the electron-donating nature of the two amines should further bathochromically shift the absorbance spectra, and it increases the wt% F of the final product, therefore enhancing fluorous partition. **F-BHQ-2** was obtained in 13% isolated yield over two steps, while efforts to optimize the reaction conditions to increase the reaction yields are ongoing.



**Scheme 4.2** Synthesis of F-BHQ-2

As shown in **Figure 4.11a** and **b**, both F-BHQs showed reasonable fluorous partition. Although F-BHQ-2 showed low solubility in perfluorinated solvents, it showed good partition in HFE-7500 over DEB ( $\log(P) = 0.64$ , 81:19 in HFE-7500/DEB). The absorbance spectra of F-BHQ-1 and F-BHQ-2 was overlaid in **Figure 4.11c** for comparison. As expected, the absorbance maximum of F-BHQ-2 ( $\lambda_{\text{max}} = 537\text{ nm}$ ) showed a slight bathochromic shift than F-BHQ-1 ( $\lambda_{\text{max}} = 532\text{ nm}$ ). The extinction coefficient of F-BHQ-2 was calculated to be  $30,000\text{ L}\cdot\text{mol}^{-1}\cdot\text{cm}^{-1}$ , which was higher than F-SubPC-1. F-BHQ-2 showed no aggregation in both organic and fluorous solvents, presumably because the molecule has no driving force for aggregation owing to its low symmetry. The synthetic accessibility and the photophysical observations imply the F-BHQ-2 being a more viable dye to incorporate in the fluorescent Janus emulsions.

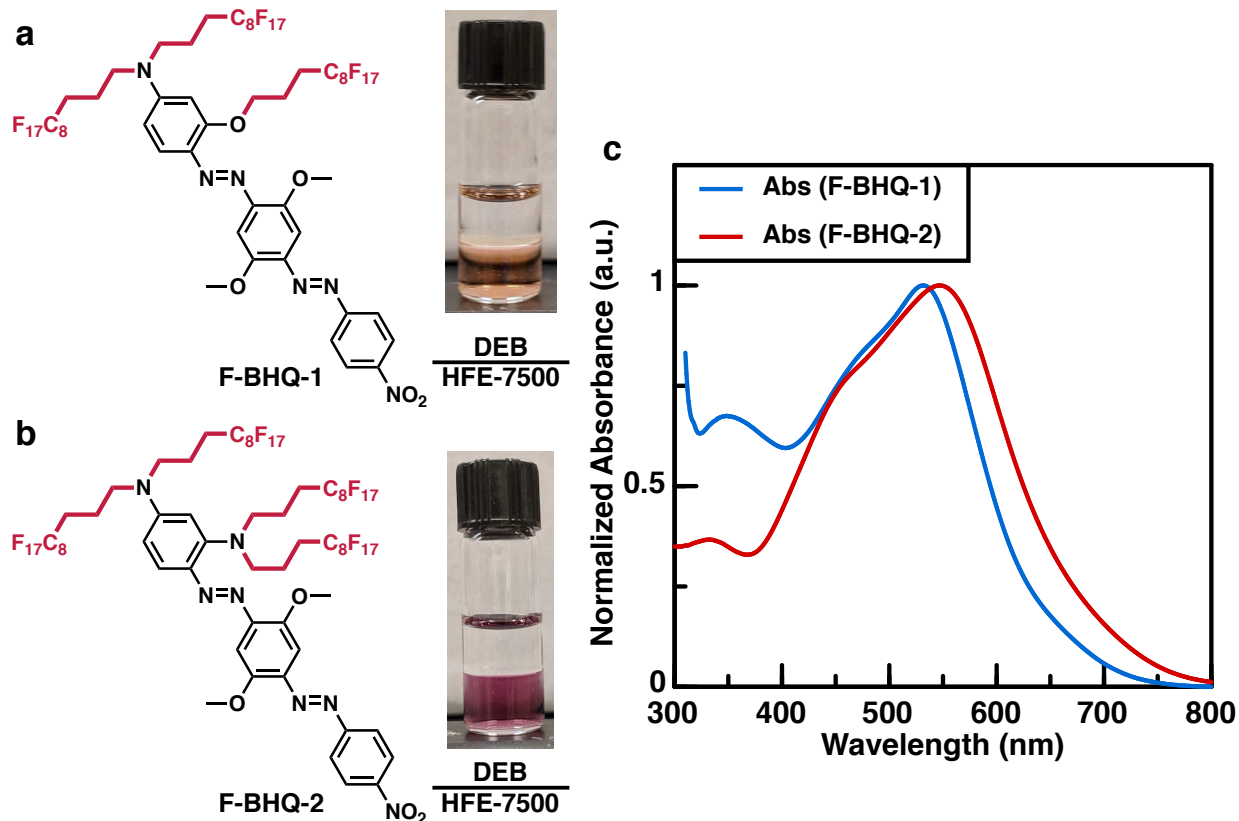


**Figure 4.11** (a) Chemical structure and picture showing fluororous partitioning of F-BHQ-1. (b) Chemical structure and picture showing fluororous partitioning of F-BHQ-2. (c) Normalized absorbance spectra of F-BHQ-1 and F-BHQ-2 in HFE-7500.

#### 4.3.5 Combination of Lumogen F Orange 240 and F-BHQ-2 in Emulsions

**Figure 4.13b** summarizes the photophysical properties of the two dyes Lumogen F Orange 240 and F-BHQ-2. The emission maximum wavelength of Lumogen Orange in DEB was 535 nm, where F-BHQ-2 has a near-max absorbance. By plotting the molar extinction coefficient ratio of Lumogen Orange and F-BHQ-2, we identified 400 nm to be the most efficient for F-BHQ-2 to block the excitation light (**Figure 4.13c**).



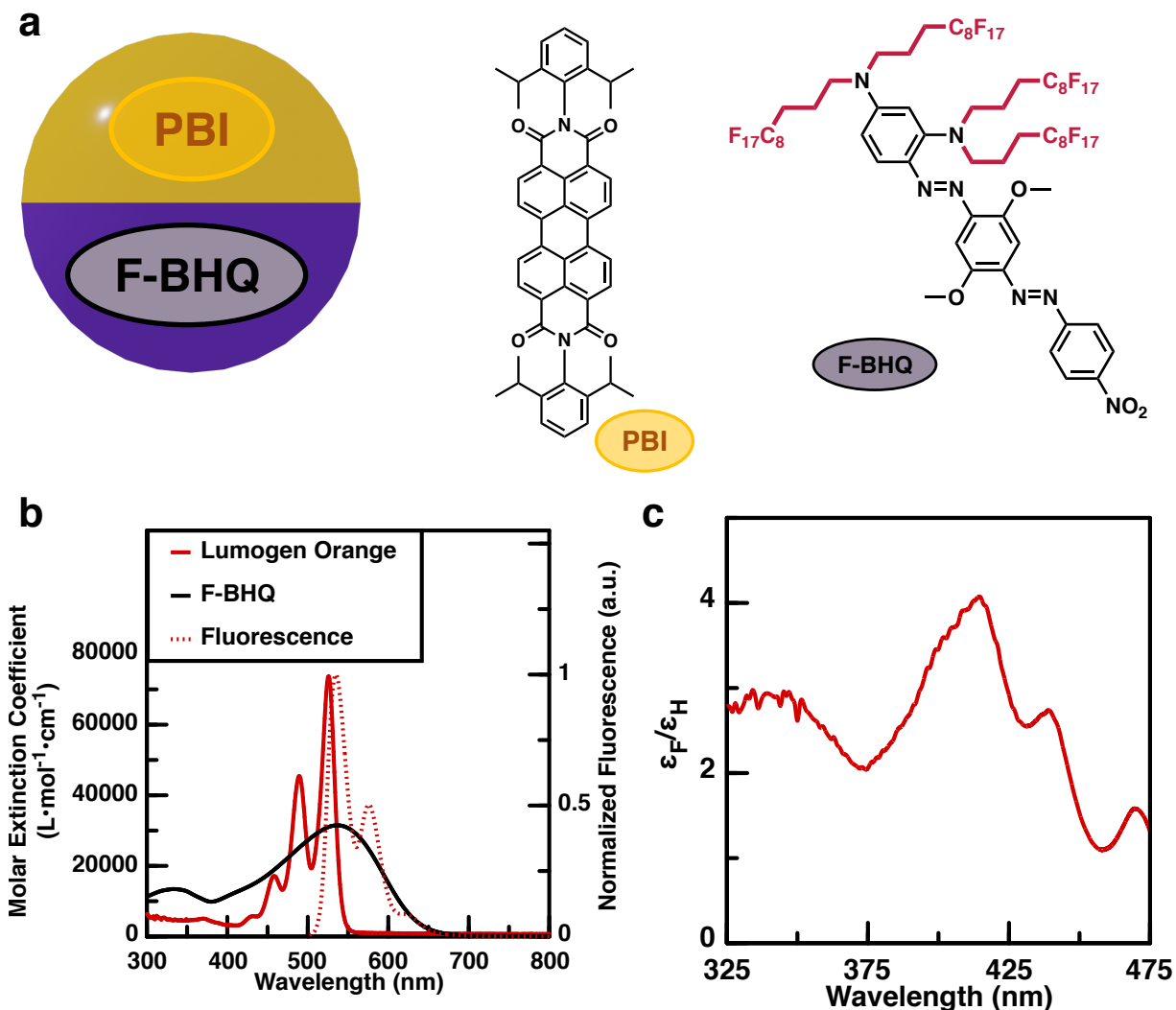


**Figure 4.12** (a) Schematic image of the emulsions and the chemical structure of the dyes incorporated in the emulsions. (b) Normalized absorbance and fluorescence spectra of Lumogen Orange in DEB, overlaid with absorbance spectra of **F-BHQ-2** in HFE-7500. (c) Molar extinction coefficient ratio of **F-BHQ-2** ( $\epsilon_F$ ) and Lumogen Orange ( $\epsilon_H$ ) plotted against the wavelength. Figures adapted with permission.<sup>102</sup> Copyright © 2021, American Chemical Society.

With these analyses in hand, we fabricated complex emulsions containing Lumogen F Orange 240 and **F-BHQ-2** in the hydrocarbon and fluorocarbon phase, respectively. As mentioned before, in the emulsions' equilibrium configuration the denser fluorocarbon will normally be located at the bottom. As a result, in the non-agglutinated state the blocker dye **F-BHQ-2** will be at the bottom and the emissive dye Lumogen F Orange 240 will be on the top. A schematic illustration of the sensing device is shown in **Figure 4.13a**. Locating the detector and light source

(the bifurcated optical fiber) at the bottom of a glass analysis dish, reveals minimal emission with 400 nm excitation in the absence of the analyte. Agglutination with the addition of the analyte causes droplet tilting and the hydrocarbon phase containing emissive dye is exposed to the light source and increased emissive signals are detected. Using this dye combination, we performed the detection of anti-SARS-CoV-2 spike IgG antibody described in section 4.3.2,<sup>102</sup> with the detector and light source located at the bottom of the sample. **Figure 4.13b** shows the fluorescence spectra of the 1:1 mixture of the bioconjugated Janus emulsions with this dye pair after being treated with different concentrations of anti-SARS-CoV-2 spike IgG antibody. With higher concentration of anti-SARS-CoV-2 spike antibody, the emissive signal at 535 nm increases. The correlation of concentration of anti-SARS-CoV-2 spike antibody and relative fluorescence intensity at 535 nm indicates a similar limit of detection of 0.2  $\mu\text{g/mL}$  (**Figure 4.13c**).

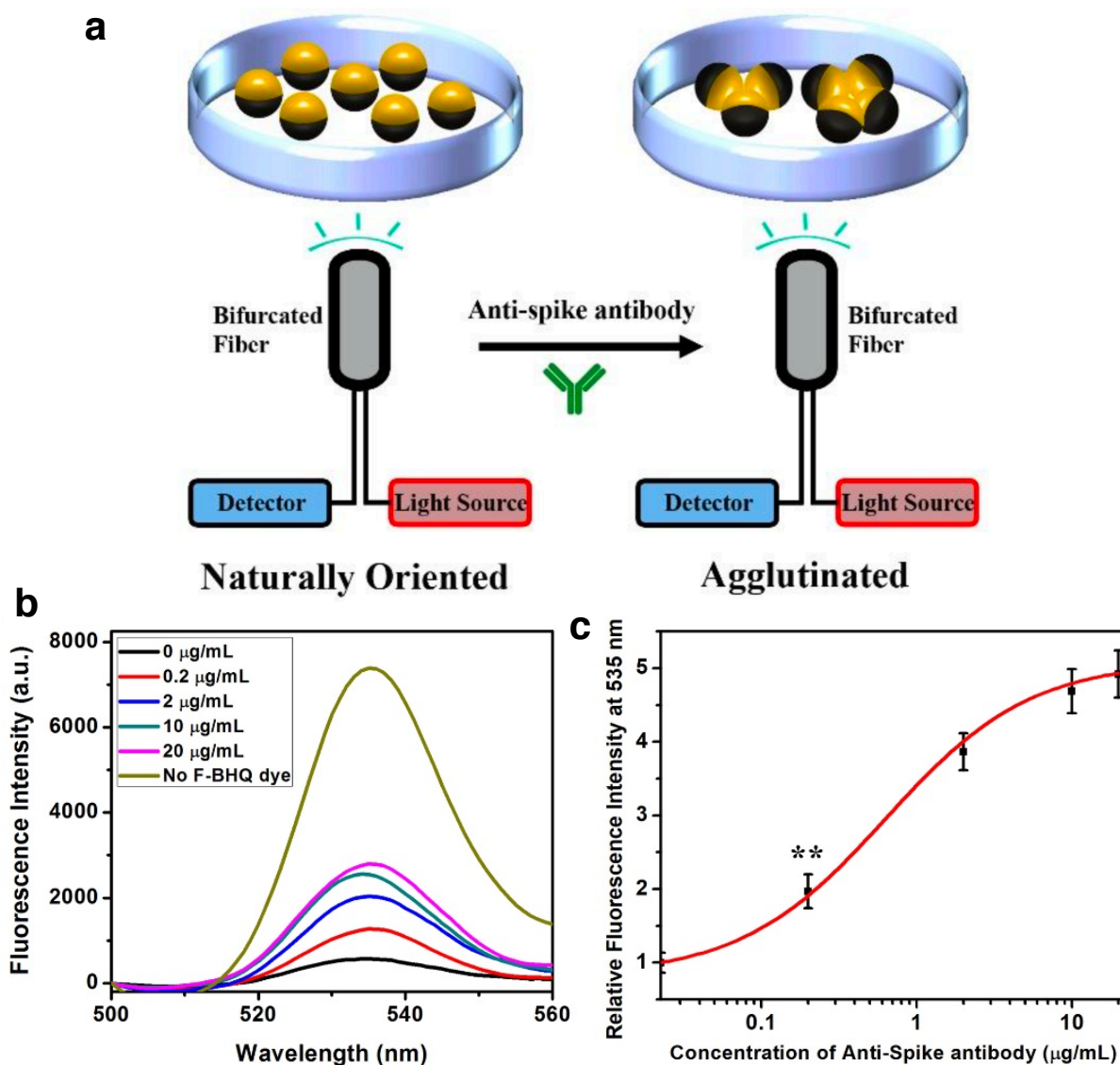


**Figure 4.13** (a) Schematic illustrations of the sensing device using the emulsions containing the two dyes. (b) Fluorescence spectra ( $\lambda_{\text{ex}} = 400 \text{ nm}$ ) of 1:1 mixture of bioconjugated Janus droplets containing of F-BHQ dye in the fluorocarbon phase, P-TCO and Lumogen Orange dye in the hydrocarbon phase, after addition of anti-SARS-CoV-2 spike antibody at different concentrations. (c) Correlation of concentration of anti-SARS-CoV-2 spike antibody and relative fluorescence intensity at 535 nm. All error bars are calculated from three independent experiments ( $n = 3$ ), and \*\* represent statistical significance (\*\* $p \leq 0.01$ ). Figures adapted with permission.<sup>102</sup> Copyright © 2021, American Chemical Society.

## 4.4 Conclusions

In this chapter, the utilization of fluorescent complex emulsions in sensing was discussed in the context of optics and absorbance/fluorescence spectroscopy. Owing to the orthogonal

solubility of organic and fluoruous dyes, detection of the fluorescence from the emulsions could be developed. This chapter exhibited the iterations of the sensors and how we were able to incrementally improve our detection scheme. Our first iteration was based on perylene and **FF-PBI-2**, where we took the ratio of the fluorescence to assess the morphology or the degree of agglutination of the emulsions. The second iteration featured a **SubPC** dye, which is organic soluble and possess a high extinction coefficient. For the third iteration, we flipped the dye combination by having Lumogen F Orange 240 in the hydrocarbon phase and **F-SubPC-1** in the fluorocarbon phase. This setup enables the detector to be placed at the bottom of the sample to minimize path lengths of the sample and the detector so that optical scattering from the continuous phase could be minimized. For the final iteration discussed in this thesis concerns the use of a newly synthesized black hole quencher **F-BHQ-2** dye, which possessed a high molar extinction coefficient with no native emission. Our sensors have proven effective in the detection of Zika virus, *Salmonella*, *Listeria*, and anti-SARS-CoV-2 spike antibody within only 2 hours, demonstrating the versatility and the variety of our sensing platform.

## 4.5 Experimental

### 4.5.1 General

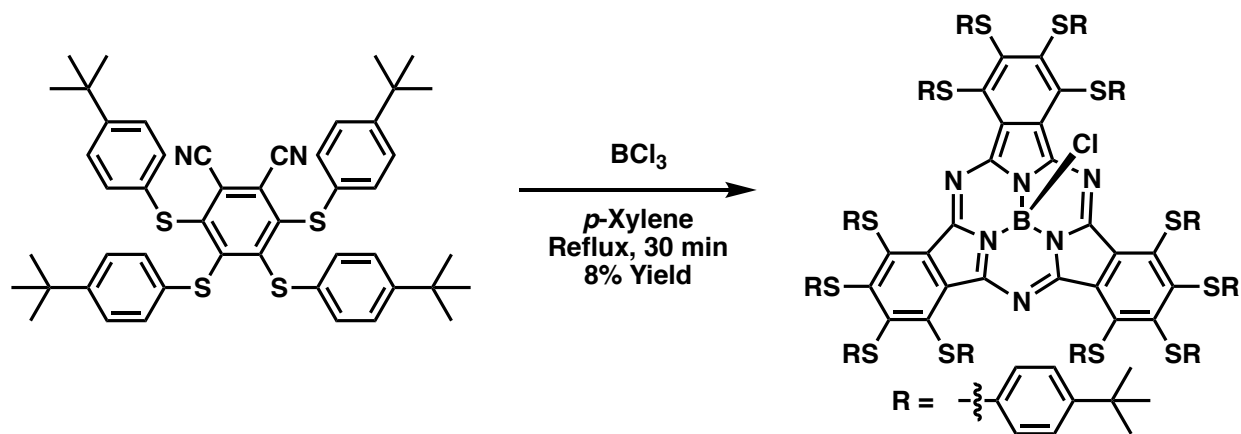
All the chemical reagents used were purchased from Fisher Scientific, Sigma-Aldrich, Click Chemistry Tools, Alfa Aesar, Acros Organics, Combi-Blocks, TCI, Synquest, Abcam or BroadPharm. Custom DNA oligonucleotides were synthesized by Integrated DNA Technologies (San Jose, CA, USA). DL-dithiothreitol and tris(2-carboxyethyl)phosphine hydrochloride were purchased from VWR (Radnor, PA, USA). All reagents and solvents were used as received without further purification unless otherwise noted.

NMR spectra were recorded with a Bruker Ascend-400 (400 MHz), JEOL model JNM-ECZ500R/S1 (500 MHz), or Bruker Ascend-600 (600 MHz) spectrometer. Chemical shifts  $\delta$  are reported in ppm downfield from tetramethylsilane using the residual solvent signals ( $\text{CDCl}_3$ :  $\delta_{\text{H}}$  7.26 ppm,  $\delta_{\text{C}}$  77.16 ppm; acetone- $d_6$ :  $\delta_{\text{H}}$  2.05 ppm,  $\delta_{\text{C}}$  206.26 ppm) as an internal reference. For  $^1\text{H}$  NMR, coupling constants  $J$  are given in Hz and the resonance multiplicity is described as s (singlet), d (doublet), t (triplet), p (quintet), and m (multiplet). Mass spectra were recorded with a high-resolution JEOL AccuTOF 4G LC-plus equipped with an ionSense Direct Analysis in Real Time source, and a Bruker Autoflex Speed MALDI-TOF (Matrix-Assisted Laser Desorption/Ionization Time-of-Flight Mass Spectrometer) in Reflectron Detection mode. Mass spectra were calibrated using either poly(ethylene glycol) of the appropriate mass range as external standards, or reserpine as an internal standard. ATR-FTIR spectra were obtained using a Thermo Scientific Nicolet 6700 FTIR with a Ge crystal for ATR. UV-Vis absorbance spectra were recorded on a Cary 4000 UV-Vis spectrophotometer using a quartz cuvette. Fluorescence spectra were obtained at room temperature using a bifurcated fiber on a Horiba Jobin Yvon SPEX Fluorolog- $\tau$ 3 fluorimeter (model FL-321, 450 W Xenon lamp). Optical images of emulsions were obtained by an inverted microscope equipped with an AmScope camera.

Details of the fabrication of emulsions can be found in the respective publications.<sup>99-102</sup> In brief, emulsification was conducted by a temperature-induced phase separation method. Emulsions were fabricated using either bulk emulsification or a microfluidic device, which generates polydisperse or monodisperse droplets, respectively. Both procedures allow for the formation of droplets with highly uniform morphology and composition. In a typical bulk emulsification preparation, the disperse phase was heated above their upper critical temperature ( $T_c$ ) to form a homogeneous mixture. 25  $\mu\text{L}$  of the heated H/F mixture was added to 500  $\mu\text{L}$  of continuous phase

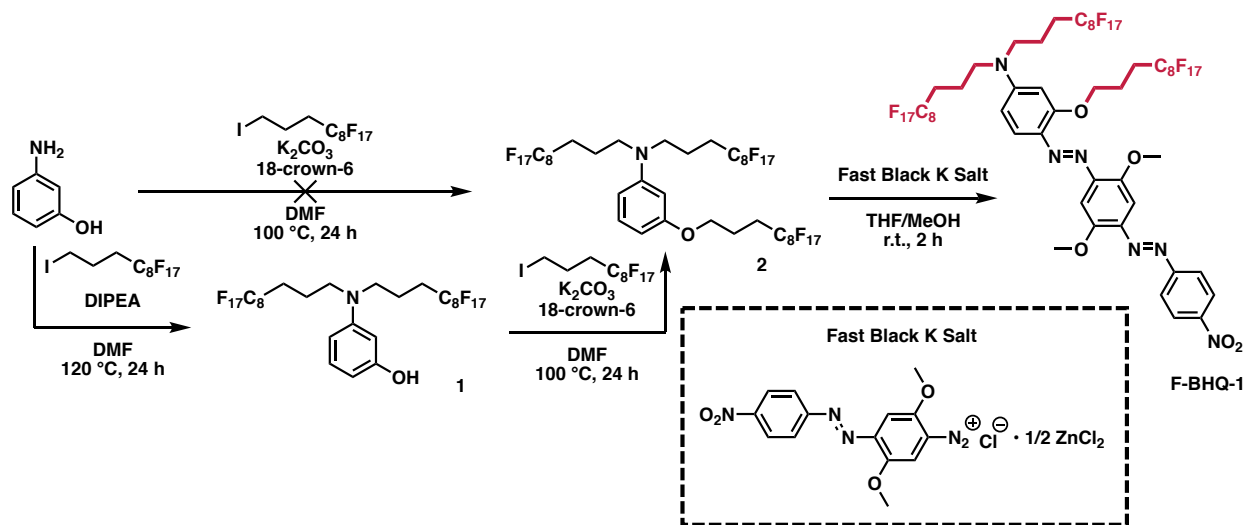
and vortexed for 10 s to emulsify. Double emulsions were obtained upon cooling using an ice bath. This bulk emulsification method generated polydispersed droplets with diameters ranging from 10 to 200  $\mu\text{m}$  as observed by an optical microscopy. Emulsions were also fabricated using a microfluidic device purchased from Dolomite Microfluidic, which generates emulsion droplets with well-controlled sizes. A Telos 2 Reagent Chip (50  $\mu\text{m}$ ) was used, and two Mitos P pressure pumps, one for the dispersed phase and one for the continuous phase, were used for controlling the flow rate. After heating the disperse phase above its upper critical temperature ( $T_c$ ), the fluids were driven by pressurizing the two individual dispersed and continuous chambers with  $\text{N}_2$  providing a pulseless, stable flow to the flow focusing chip (pressures: dispersed phase: 200 mbar; continuous phase: 800 mbar). The dispersed phase was split into two crinkled adjacent flow resistors which provide additional flow stability and mixing. The average diameter of the monodispersed droplets generated from this setup were  $50 \pm 5 \mu\text{m}$  as observed by optical microscopy.

#### 4.5.2 Synthetic Procedures



**Synthesis of SubPC.** Procedure adapted from a previous work.<sup>105</sup>  $\text{BCl}_3$  (1.0 mL, 1 M solution in  $p\text{-xylene}$ ) was added to the phthalonitrile precursor (785 mg, 1 mmol) and stirrer under argon in a

25 mL two-necked round-bottomed flask fitted with a condenser and septum. The septum was replaced with a glass stopper, and the apparatus was placed in a pre-heated oil bath at 160 °C and stirred for 30 minutes. After cooling to room temperature, the solution was concentrated under reduced pressure. The resulting blue solid was subjected to silica gel column chromatography with toluene/hexanes (2:3, v/v) as eluent, yielding **SubPC** as a dark blue solid (62 mg, 8%). <sup>1</sup>H NMR (600 MHz, Chloroform-*d*, 20 °C):  $\delta$  (ppm) 7.32 (d,  $J = 8.7$  Hz, 12H), 7.11 (d,  $J = 8.7$  Hz, 12H), 7.06 (d,  $J = 8.7$  Hz, 12H), 6.92 (d,  $J = 8.7$  Hz, 12H), 1.21 (s, 54H), 1.15 (s, 54H). <sup>13</sup>C NMR (151 MHz, Chloroform-*d*, 20 °C):  $\delta$  (ppm) 149.45, 149.36, 149.31, 147.73, 139.80, 134.72, 134.60, 133.69, 129.42, 128.63, 125.95, 125.92, 34.54, 34.49, 31.42, 31.35. MALDI-TOF  $m/z$  calculated for C<sub>144</sub>H<sub>156</sub>BClN<sub>6</sub>S<sub>12</sub> [M]<sup>+</sup>: 2397.886, found 2397.920. UV/Vis (PhMe):  $\lambda_{\text{max}}$  (log  $\epsilon$ ) = 310 (4.78), 645 (4.91).



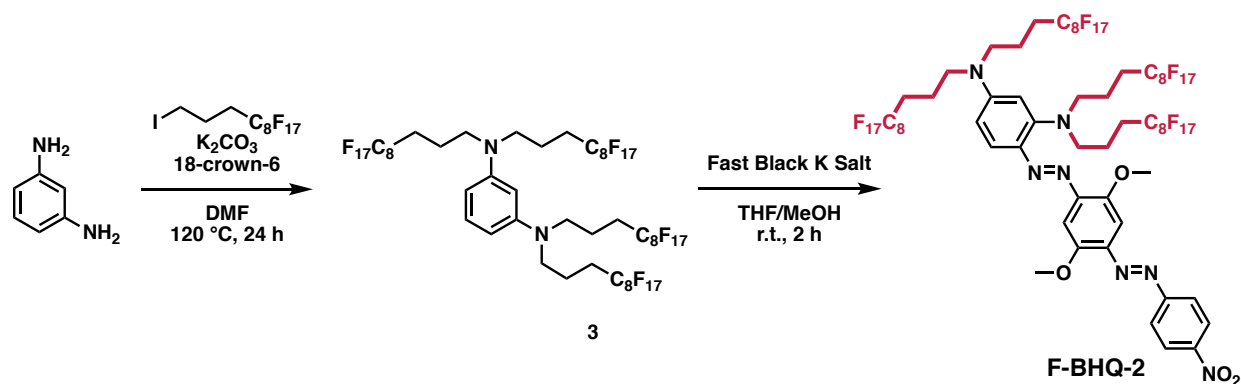
**Synthesis of Compound 1.** Compound 1 was synthesized in 71% yield following a previous literature.<sup>15</sup>

**Synthesis of Compound 2.** A mixture of Compound 1 (366 mg, 0.356 mmol), 3-(perfluorooctyl)propyl iodide (235 mg, 0.400 mmol), and anhydrous K<sub>2</sub>CO<sub>3</sub> (55 mg, 0.398 mmol)

in DMF (1 mL) was stirred at 100 °C for 24 h. Upon cooling the reaction mixture to room temperature, the residue was dissolved in AcOEt (30 mL) and water (30 mL). The organic layer was separated, washed with water (30 mL × 3) and brine (30 mL), dried with MgSO<sub>4</sub>, and evaporated to dryness under reduced pressure. The residue was chromatographed on silica gel using chloroform as eluent, and the fraction containing compound **2** (R<sub>f</sub> = 0.80 in chloroform) was collected and evaporated to dryness to provide a white solid (313 mg, 0.210 mmol, 53% yield). <sup>1</sup>H NMR (500 MHz, CDCl<sub>3</sub>, 20 °C): δ (ppm) 7.16 (t, *J* = 8.2 Hz, 1H), 6.29-6.33 (m, 2H), 6.22 (t, *J* = 2.3 Hz, 1H), 4.03 (t, *J* = 5.9 Hz, 2H), 3.35 (t, *J* = 7.4 Hz, 4H), 2.25-2.35 (m, 2H), 2.06-2.17 (m, 6H), 1.88-1.94 (m, 4H). <sup>13</sup>C NMR (126 MHz, CDCl<sub>3</sub>, 20 °C): δ (ppm) 160.14, 149.04, 130.46, 106.51, 102.65, 100.48, 66.35, 50.61, 29.86, 28.60-27.87 (m, 2C), 20.72, 18.48. <sup>19</sup>F NMR (471 MHz, CDCl<sub>3</sub>, 20 °C): δ (ppm) -80.84 (t, *J* = 9.8 Hz, 9F), -113.88 (m, 4F), -114.45 (m, 2F), -121.74 (m, 6F), -121.97 (m, 12F), -122.78 (m, 6F), -123.41 (m, 4F), -123.54 (m, 2F), -126.18 (m, 6F). DART MS: *m/z* calcd. for [C<sub>39</sub>H<sub>22</sub>F<sub>51</sub>NO + H]<sup>+</sup>: 1490.0960, found: 1490.0876.

**Synthesis of F-BHQ-1 (not isolated).** Compound **2** (61 mg, 0.0411 mmol) was added to a dried flask, and dissolved in acetone (2 mL). Fast Black K salt (50 mg, 0.120 mmol) was added in portions, followed by MeOH (0.4 mL). The reaction mixture immediately turned purple. The reaction mixture was monitored by TLC and stirred at room temperature for 2 h. Then, the reaction was filtered through a short pad of silica gel with AcOEt as eluent and evaporated to dryness. The residue was triturated twice with hot MeOH (10 mL × 2) to provide **F-BHQ-1** as a dark purple solid.





**Synthesis of Compound 3.** A mixture of *m*-phenylenediamine (54 mg, 0.500 mmol), 3-(perfluorooctyl)propyl iodide (1.30 g, 2.21 mmol), and anhydrous  $K_2CO_3$  (304 mg, 2.20 mmol) in DMF (5 mL) was stirred at 100 °C for 24 h. Upon cooling the reaction mixture to room temperature, the residue was dissolved in AcOEt (50 mL) and water (50 mL). The organic layer was separated, washed with water (50 mL  $\times$  3) and brine (50 mL), dried with  $MgSO_4$ , and evaporated to dryness under reduced pressure. The residue was chromatographed on silica gel using hexanes with a gradient of 1%  $\rightarrow$  10% AcOEt as eluent, and the fraction containing compound **3** ( $R_f$  = 0.30 in hexanes, 5% AcOEt) was collected and evaporated to dryness to provide a white solid (190 mg, 0.0975 mmol, 20% yield).  $^1H$  NMR (500 MHz, acetone- $d_6$ , 20 °C):  $\delta$  (ppm) 7.04 (t,  $J$  = 8.2 Hz, 1H), 6.26 (dd,  $J$  = 8.2, 2.1 Hz, 2H), 6.21 (s, 1H), 3.51 (t,  $J$  = 7.2 Hz, 8H), 2.29–2.37 (m, 8H), 1.91–1.97 (m, 8H).  $^{13}C$  NMR spectra could not be obtained due to low solubility.  $^{19}F$  NMR (471 MHz, acetone- $d_6$ , 20 °C):  $\delta$  (ppm) -81.66 (t,  $J$  = 9.8 Hz, 3F), -114.47 (m, 2F), -122.25 (m, 2F), -122.48 (m, 4F), -123.29 (m, 2F), -123.95 (m, 2F), -126.76 (m, 2F). DART MS:  $m/z$  calcd. for  $[C_{50}H_{28}N_2F_{68} + H]^+$ : 1949.1239, found: 1949.1227.

**Synthesis of F-BHQ-2.** Compound **3** (80 mg, 0.0411 mmol) was added to a dried flask, and dissolved in acetone (2 mL). Fast Black K salt (50 mg, 0.120 mmol) was added in portions, followed by MeOH (0.4 mL). The reaction mixture immediately turns purple. The reaction mixture

was monitored by TLC and stirred at room temperature for 2 h. Then, the reaction was filtered through a short pad of silica gel with AcOEt as eluent and evaporated to dryness. The residue was triturated twice with hot MeOH (10 mL  $\times$  2) to provide **F-BHQ-2** as a dark purple solid (59 mg, 0.0261 mmol, 65% yield).  $^1\text{H}$  NMR (500 MHz, acetone- $d_6$ , 20  $^\circ\text{C}$ ):  $\delta$  (ppm) 8.46 (d,  $J$  = 8.8 Hz, 2H), 8.12 (d,  $J$  = 8.8 Hz, 2H), 7.82 (d,  $J$  = 9.5 Hz, 1H), 7.56 (s, 1H), 7.40 (s, 1H), 6.68 (dd,  $J$  = 9.5, 2.3 Hz, 1H), 6.55 (d,  $J$  = 2.3 Hz, 1H), 4.03 (s, 3H), 3.99 (s, 3H), 3.70–3.82 (m, 8H), 2.29–2.46 (m, 8H), 1.96–2.04 (m, 8H).  $^{13}\text{C}$  NMR spectra could not be obtained due to low solubility.  $^{19}\text{F}$  NMR (471 MHz, acetone- $d_6$ , 20  $^\circ\text{C}$ ):  $\delta$  (ppm) -81.65 (m, 12F), -114.40 (m, 8F), -122.25 (m, 8F), -122.47 (m, 16F), -123.29 (m, 8F), -123.88 (m, 8F), -126.77 (m, 8F). MALDI TOF-MS:  $m/z$  calcd. for  $[\text{C}_{64}\text{H}_{39}\text{F}_{68}\text{N}_7\text{O}_4 - \text{H}]^+$ : 2260.1905; found: 2260.1954. Elemental Analysis calcd. for  $\text{C}_{64}\text{H}_{39}\text{F}_{68}\text{N}_7\text{O}_4$  (%): C, 33.98; H, 1.74; N, 4.33. Found: C, 34.32; H, 1.73; N, 4.41. UV/Vis (HFE7500):  $\lambda_{\text{max}}$  ( $\log \epsilon$ ) = 333 (4.13), 537 (4.50).

## 4.6 Appendix for CHAPTER 4

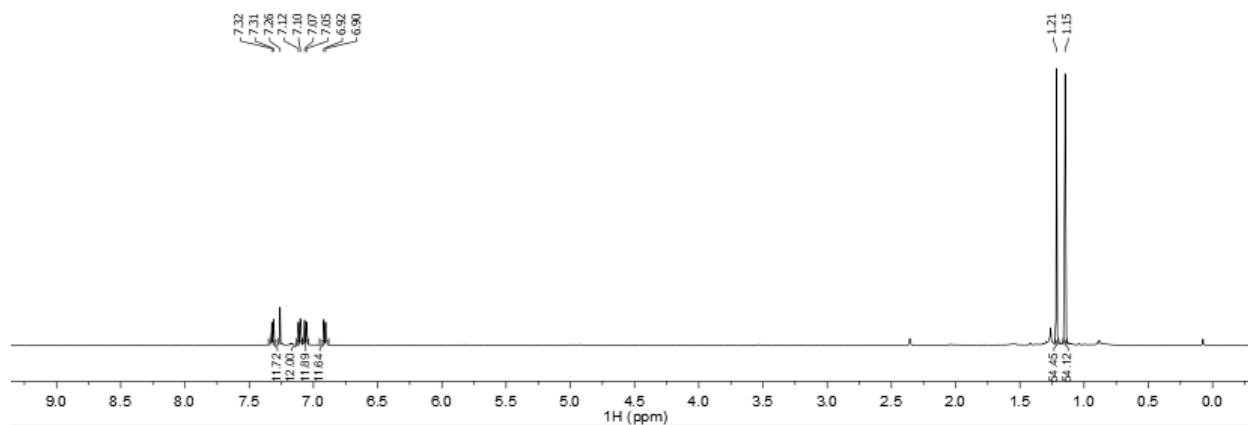


**Figure 4.14** Compound SubPC <sup>1</sup>H NMR (600 MHz, chloroform-*d*, 20 °C)

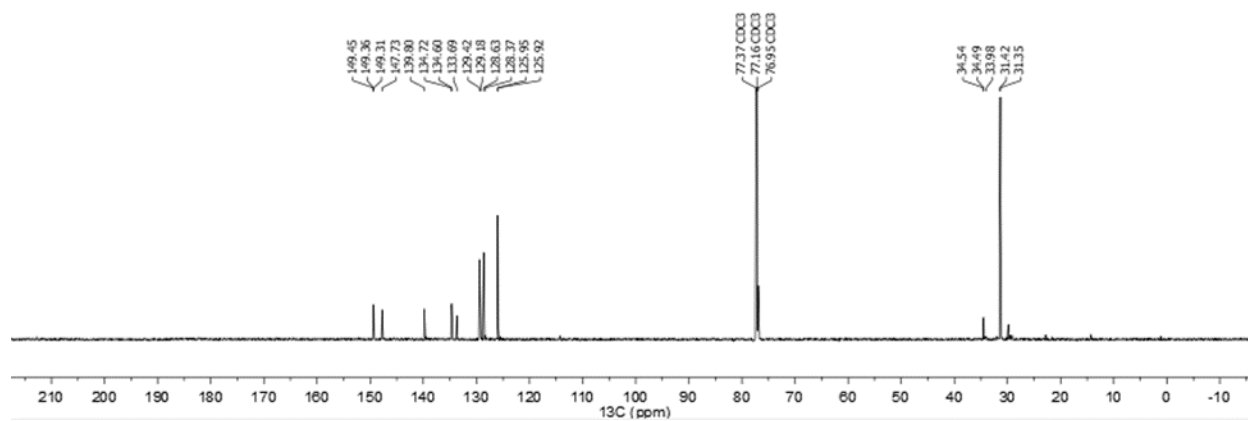


**Figure 4.15** Compound SubPC <sup>13</sup>C NMR (151 MHz, chloroform-*d*, 20 °C)

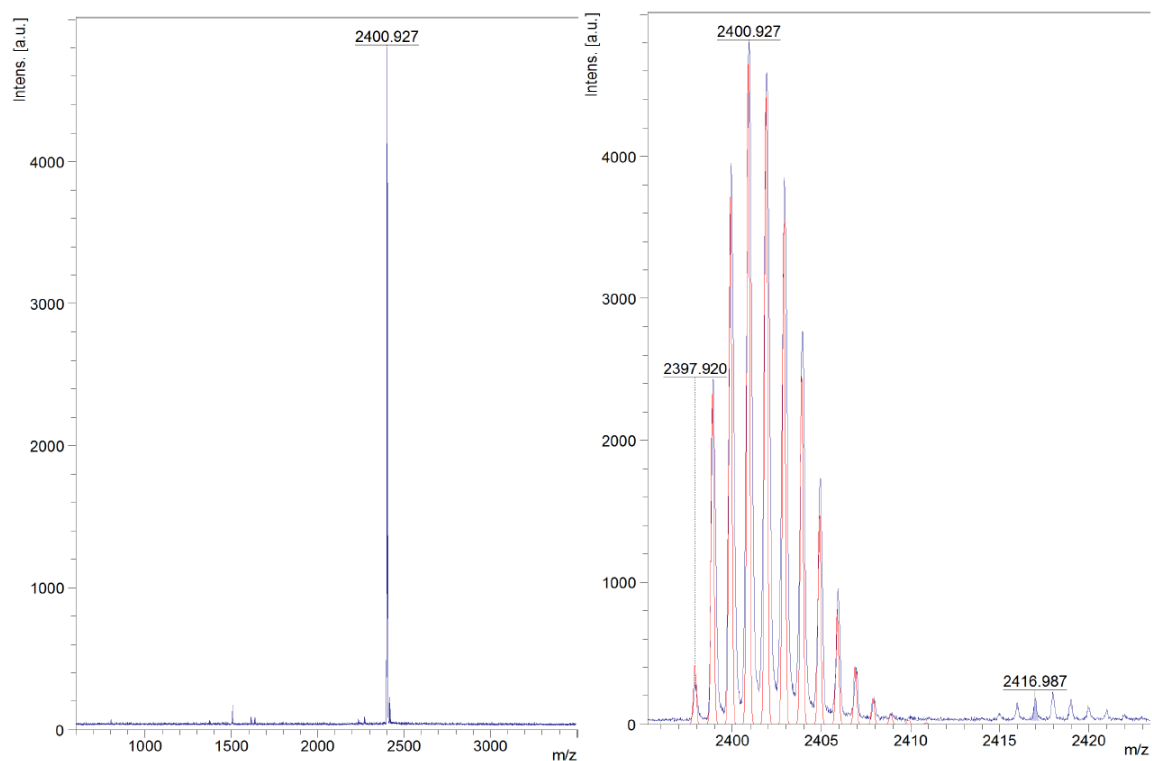


**Figure 4.16** MALDI-TOF mass spectrometry spectrum of **SubPC** shown in blue. Simulated isotopic distribution for  $C_{144}H_{156}BCIN_6S_{12}$  shown in red.

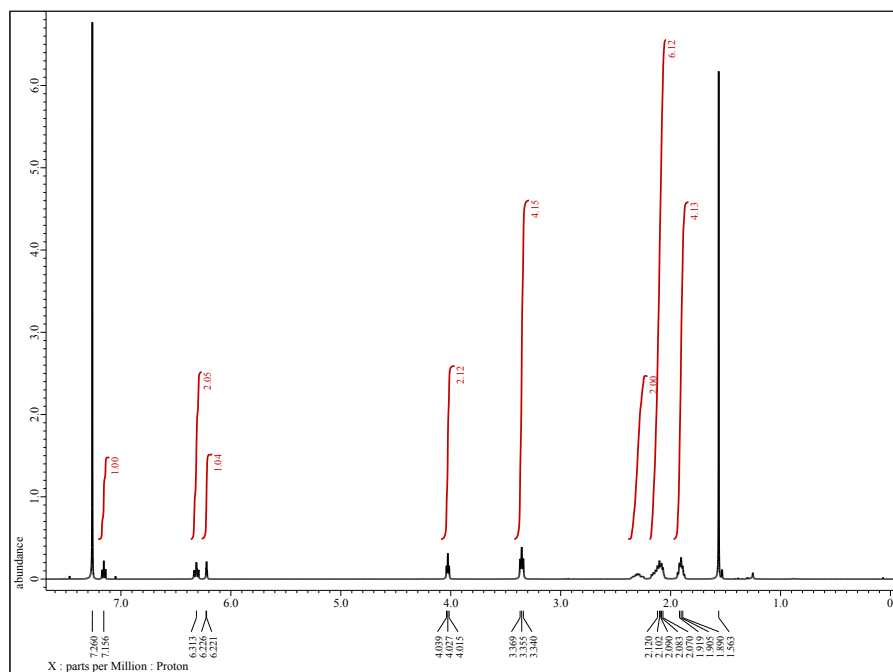


**Figure 4.17** Compound **2**  $^1H$  NMR (500 MHz,  $CDCl_3$ , 20 °C)

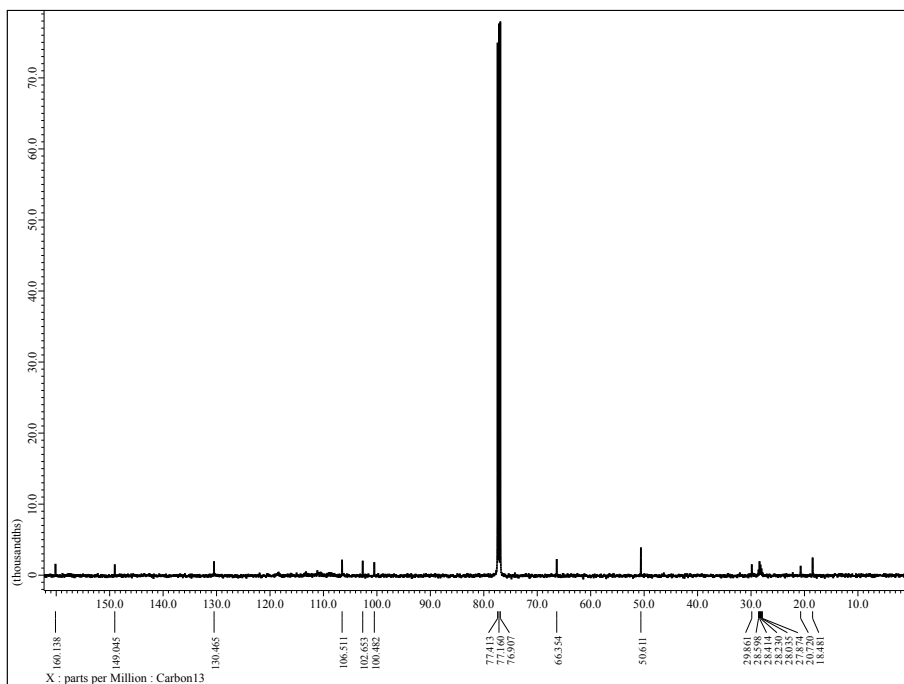


Figure 4.18 Compound 2 <sup>13</sup>C NMR (126 MHz, CDCl<sub>3</sub>, 20 °C)

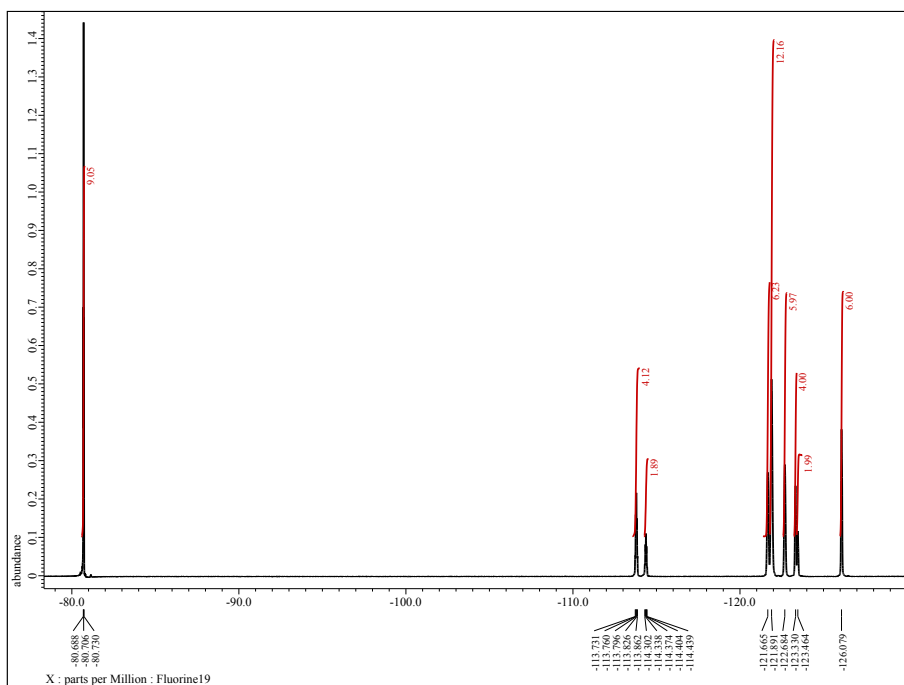
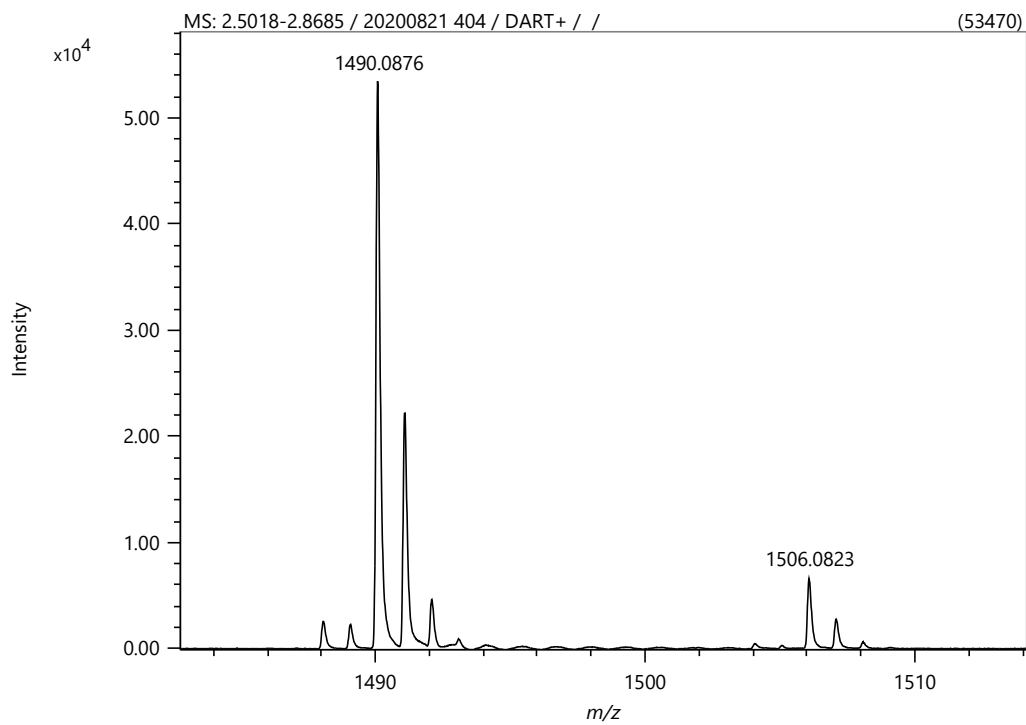
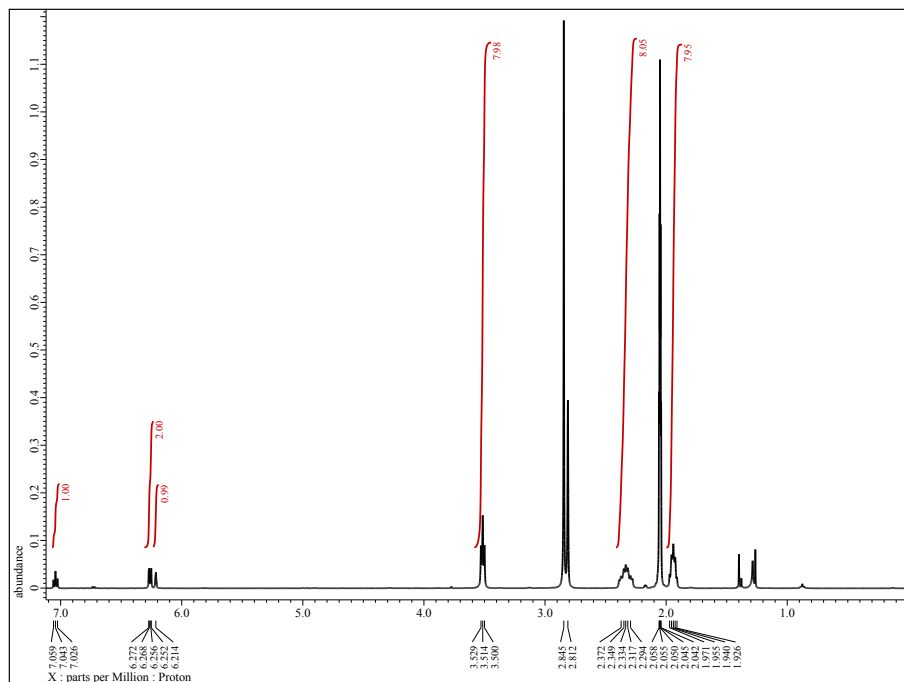


Figure 4.19 Compound 2 <sup>19</sup>F NMR (471 MHz, CDCl<sub>3</sub>, 20 °C)



**Figure 4.20** Compound 2 DART MS



**Figure 4.21** Compound 3  $^1\text{H}$  NMR (500 MHz, acetone- $d_6$ , 20 °C)

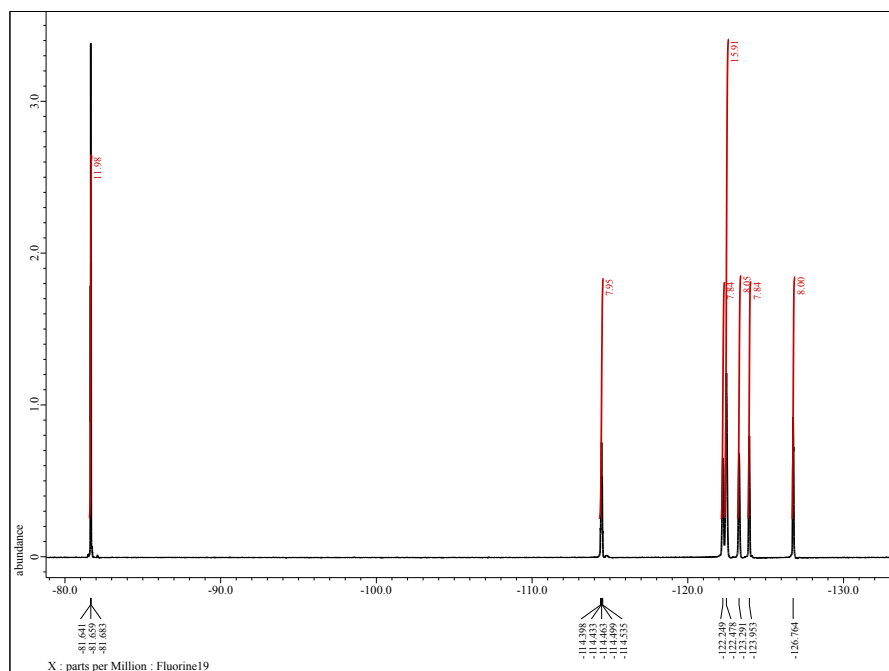


**Figure 4.22** Compound 3  $^{19}\text{F}$  NMR (471 MHz, acetone- $d_6$ , 20 °C)

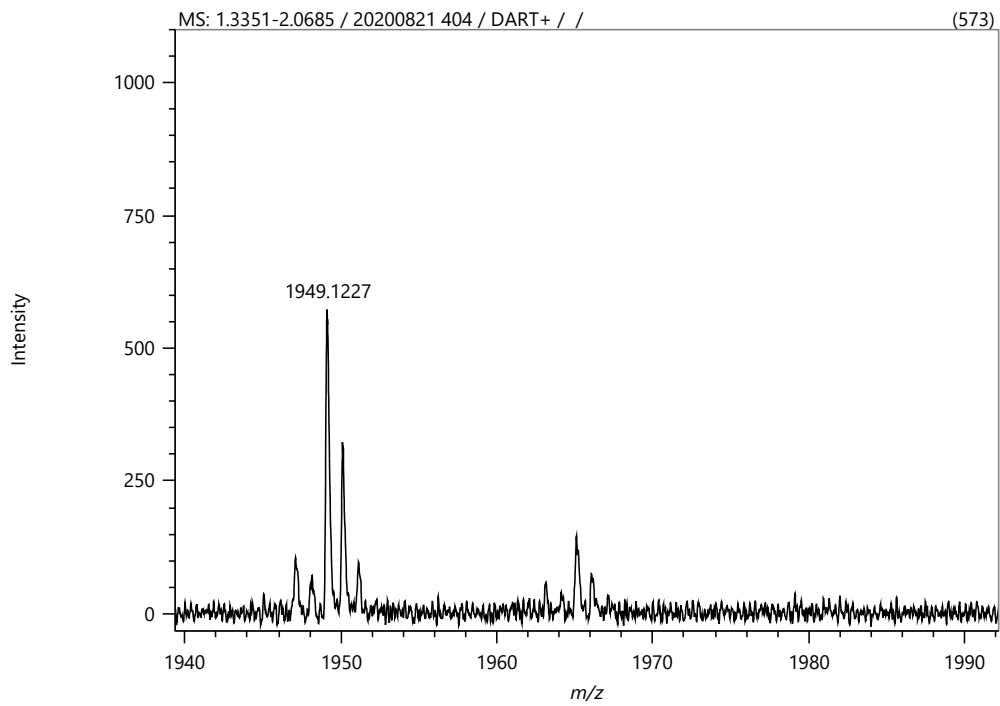


**Figure 4.23** Compound 3 DART MS

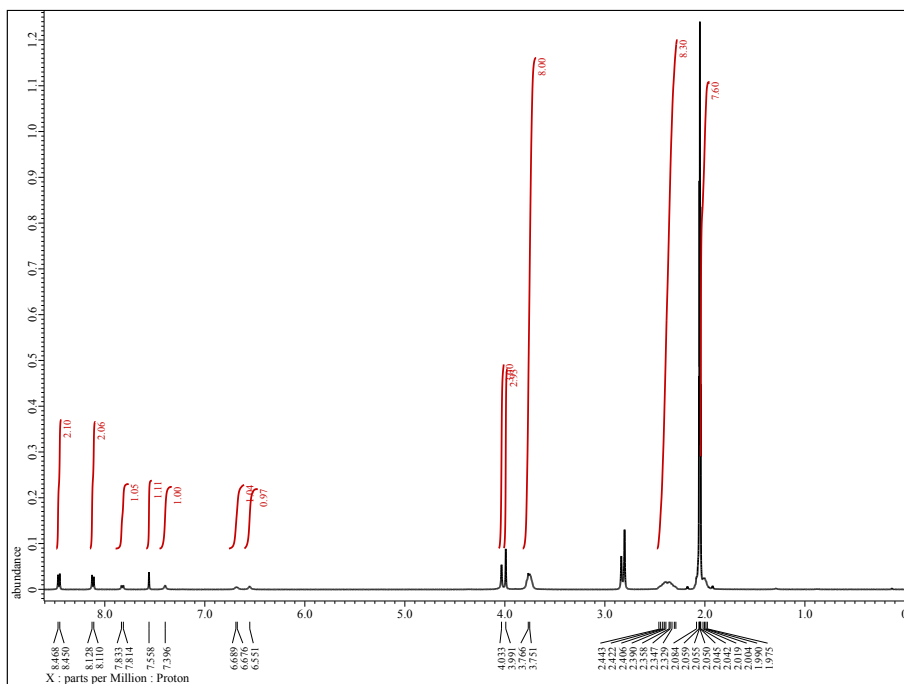


Figure 4.24 Compound F-BHQ-2  $^1\text{H}$  NMR (500 MHz, acetone- $d_6$ , 20 °C)

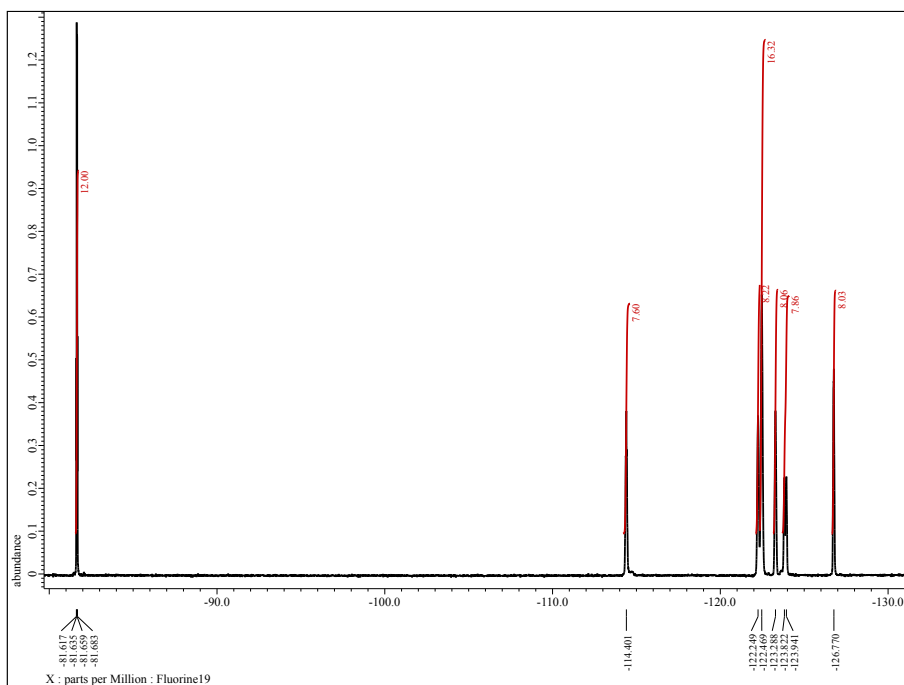


Figure 4.25 Compound F-BHQ-2  $^{19}\text{F}$  NMR (471 MHz, acetone- $d_6$ , 20 °C)



Comment 1  
Comment 2

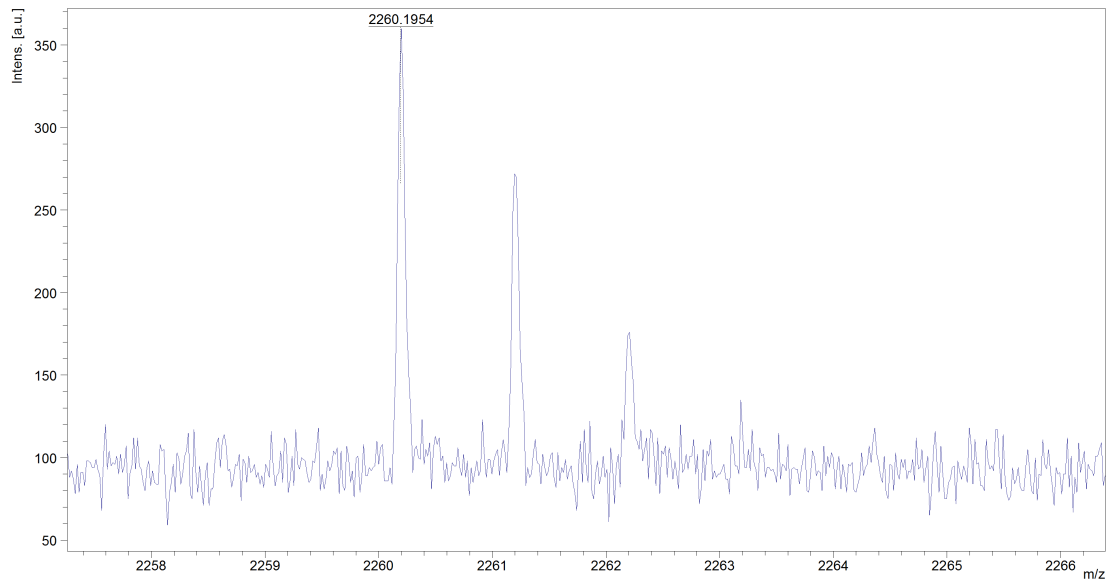


Figure 4.26 Compound F-BHQ-2 MALDI TOF-MS (Matrix: DCTB)

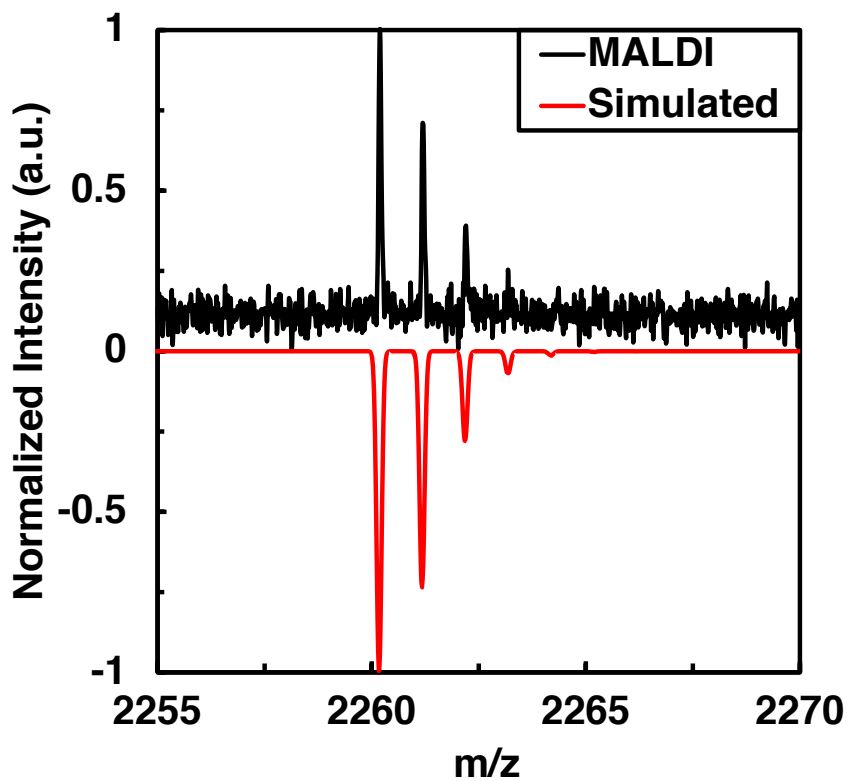
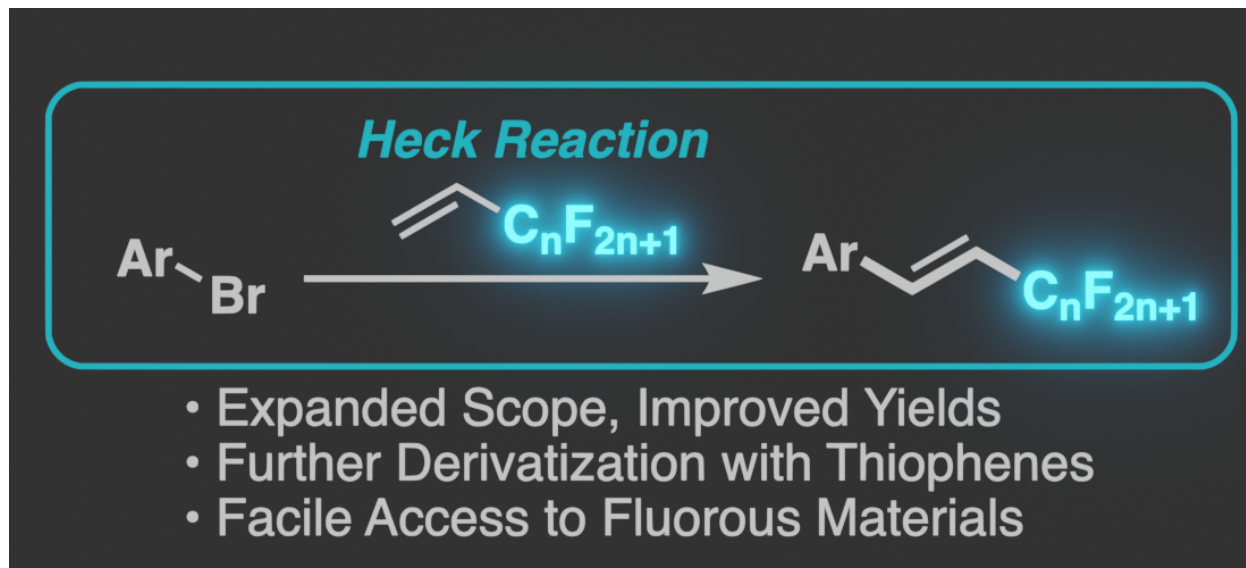


Figure 4.27 MALDI TOF-MS isotope distribution comparison of F-BHQ-2.



## CHAPTER 5:

### Revisiting the Heck Reaction for Fluorous Materials Applications



Parts of this chapter were adapted and reprinted with permission from:

Yoshinaga, K. and Swager, T. M. Revisiting the Fluorous Heck Reaction for Materials Applications. *Synlett* **2021**, *Accepted*. Copyright © 2021, Georg Thieme Verlag KG.

Swager, T. M.; Gallant, B. M.; Yoshinaga, K.; Gao, H. Electrochemical Reduction of Halogenated Compounds. *Patent Filed*. K.Y. and T.M.S. designed research; K.Y. performed the synthesis of compounds; H.G. performed the discharge experiments; all authors analyzed data; all authors contributed to the writing of the patent.

## 5.1 Abstract

Installing fluoroalkyl chains on a molecule can drastically transform its properties that enable unique materials applications. Compared to other methods, the installation of fluoroalkyl chains by the Heck reaction is a cost-effective and versatile method. Although previous reports utilizing this fluorinated Heck reaction have been mostly limited to simple phenyl derivatives, this work further expands the scope of this reaction to thiophenes, a versatile building block in materials chemistry. We show that microwave heating conditions can improve the yields of this reaction. The thiophene products were able to undergo further functionalization and polymerization, highlighting the potential incorporation of these molecules in conjugated organic materials. The molecules described in this work accelerates the discovery of a variety of novel fluorinated conjugated materials and provides opportunities for new applications.

## 5.2 Introduction

Fluorine has become an important component to incorporate into organic semiconducting materials to enhance device performance through improved stability and organization.<sup>5,11,66,106–108</sup> In particular, semifluoroalkyl chains, which possess an alkyl spacer between the molecule and fluoroalkyl chains, are known to induce self-packing with minimal influence on the molecule's electronic properties.<sup>11,109,110</sup> A convenient strategy to attach semifluoroalkyl chains to molecules has been to utilize semifluoroalkyl iodides<sup>15,35,36</sup> and semifluoroalkyl thiols<sup>75</sup> (**Figure 5.1a**). These reagents are generally utilized in  $S_N2$  or  $S_NAr$  reactions, however, they are relatively expensive and thus become cost ineffective for large scale synthesis. Miller and Sletten recently reported the synthesis of a branched fluorinated tag and rendered porphyrins to be soluble in fluorinated solvents (**Figure 5.1b**).<sup>69</sup> Although the branched fluorinated tag is broadly applicable and the fluoroalkyl

iodide precursor is inexpensive, it requires multiple synthetic steps to obtain the functional group precursor of interest. Fluoroalkyl alkenes (FAAs) are affordable and accessible precursors, providing an impressive potential of fluorinated material discovery (**Figure 5.1c**). These alkenes can undergo Pd-catalyzed Heck reactions with aryl halides,<sup>49,111–114</sup> aryl diazonium salts,<sup>115,116</sup> and aryl boronic acids.<sup>117</sup> However, the substrate scope in these reports are mostly limited to phenyl groups, with a few exceptions including naphthyl groups,<sup>116</sup> binaphthyl groups,<sup>49,112,118</sup> and perylene bisimides.<sup>36</sup> In addition, no reports have explored the chemical reactivity of the synthesized molecules, thus the application of this reaction to create functional molecules and materials remains unexplored.

In this report, we exploit the fluorous Heck reaction on thiophenes to explore their potential utility in conjugated materials applications (**Figure 5.1d**). We find that the reaction is compatible with microwave heating conditions and yields can be improved under these protocols. The thiophenes synthesized by this method can then be brominated for further derivatization. As a demonstration, we synthesized terthiophenes and polythiophenes and studied their properties. We have found that the incorporation of FAA groups into conjugated polymers such as polythiophenes has several benefits including the lower energy levels of highest occupied molecular orbital/lowest unoccupied molecular orbital (HOMO/LUMO) as a result of the cross-conjugation of the alkene and the electron-withdrawing nature of the fluorine, and these properties also endow materials with increased photochemical stability.

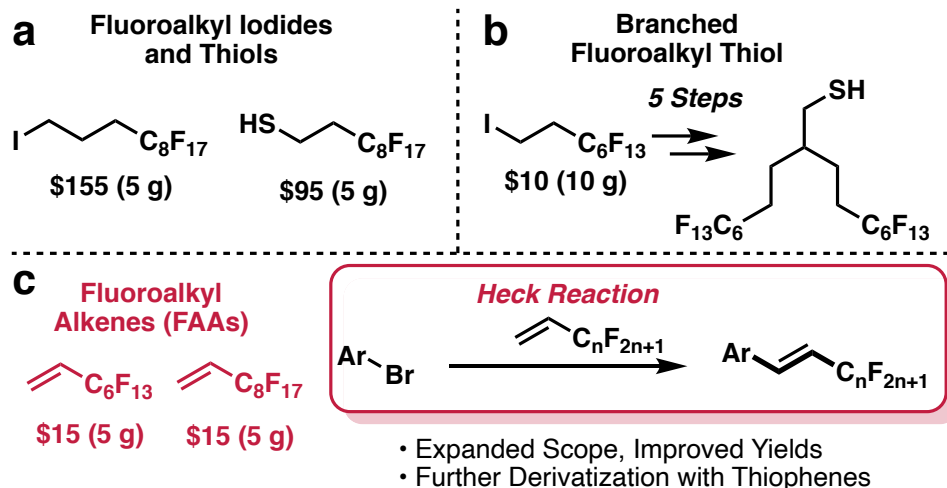


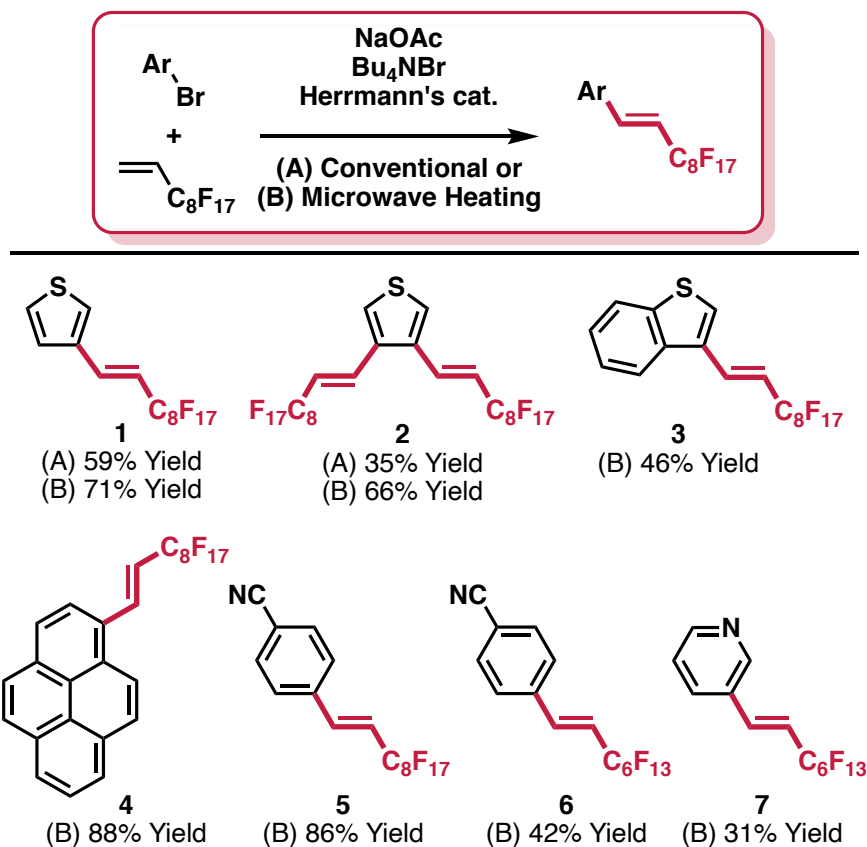
**Figure 5.1** Summary of perfluoroalkyl precursor installation. (a) Commercially available iodides and thiols. (b) Recent 5-step synthesis of branched perfluoroalkyl chains from perfluorohexyl ethyl iodide.<sup>69</sup> Functional groups besides thiol could be obtained in fewer steps. (c) Commercially available perfluoroalkyl alkenes. The listed prices are obtained from a June 15, 2021 web search.<sup>119</sup> Scheme of the fluororous Heck reaction described in this work. Figure adapted with permission.<sup>120</sup> Copyright © 2021, Georg Thieme Verlag KG.

## 5.3 Results and Discussion

### 5.3.1 Heck Reaction: Substrate Scope

**Scheme 5.1** shows the Heck reaction scheme and the substrate scope described in this work. The precursor aryl bromide, 1*H*,1*H*,2*H*-perfluoro-1-decene, tetrabutylammonium bromide (*n*-Bu<sub>4</sub>NBr), sodium acetate (NaOAc), and Herrmann's catalyst<sup>47</sup> were dissolved in *N,N*-dimethylformamide (DMF), and the reaction mixture was stirred and heated for either 24 hours at 125 °C (**Condition A**)<sup>113</sup> or 1 hour at 200 °C in a microwave reactor (**Condition B**). **Condition A** proceeded to smoothly provide thiophene **1** in reasonable yield. However, we quickly found this reaction condition was not applicable to all substrates. When we endeavored to synthesize compound **2** under similar conditions, we found the reaction would not proceed to completion. The reaction yield plateaued after 96 h and yielded only 35% the desired compound **2**. In parallel we utilized the microwave reactor for the fluororous Heck reaction to reach higher temperatures and

shorten the reaction times (**Condition B**). We found that **Condition B** gave higher yields relative to **Condition A**, providing 71% and 66% yields of compounds **1** and **2**, using the different respective conditions. There is precedence for synthesizing fluoroalkyl thiophenes in multiple synthetic steps,<sup>11,109,121</sup> however our work provides access to these substrates in one step. Benzothiophene **3** and pyrene **4** analogues were also synthesized in 46% and 88% yields, respectively. Slow evaporation of a toluene solution of compound **4** resulted in crystals suitable for single crystal X-ray diffraction, although the quality of the crystal was low as a result of twinning (See **Figure 5.9** and **Table 5.1** Crystal data and structure refinement for compound **4**.for details). Nonetheless, the atom connectivity could be assessed to confirm the successful functionalization and a coplanar orientation of the FAA group with aromatic rings. As a further comparison, we synthesized compound **5** in 86% isolated yield using the microwave, and obtained a higher yield than 76%, reported by Su *et al.*<sup>113</sup> **Condition B** was also shown to be compatible with the installation of C<sub>6</sub>F<sub>13</sub> chains (Compound **6**, 42% yield), and to tolerate pyridine groups (Compound **7**, 31% yield), although the yields with the shorter fluorocarbons were slightly lower than the C<sub>8</sub>F<sub>17</sub> chain analogues.



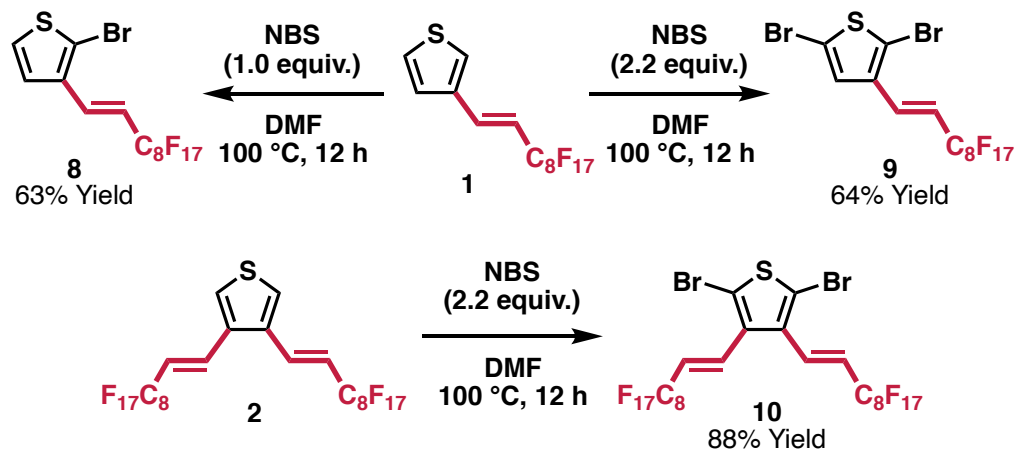
**Scheme 5.1** Fluorous Heck Reaction for the Synthesis of FAA-Functionalized Thiophenes. Scheme adapted with permission.<sup>120</sup> Copyright © 2021, Georg Thieme Verlag KG.

### 5.3.2 Brominations of FAA-Functionalized Thiophenes

We then explored the bromination of the thiophenes as shown in **Scheme 5.2**, to explore the utility of these molecules as building blocks for the synthesis of fluorinated conjugated materials. When compound **1** was treated with 1.0 equivalent of NBS, regioselective monobromination was observed at the 2-position to produce compound **8** in 63% yield. This regioselectivity is the same with the bromination of 3-alkylthiophenes.<sup>122</sup> When compound **1** was treated with 2.2 equivalent of NBS, it led to clean dibromination at 2- and 5-positions, giving compound **9** in 64% yield. When compound **2** was treated with >2 equivalents of NBS, dibromination proceeded to give compound **10** in 88% yield. Although it is known that these alkenes can undergo hydrogenation,<sup>49,111–113,115,116</sup> it is noteworthy that the alkenes remain intact



under these bromination conditions. The clean regiochemistry for the monobromination is surprising when it is considered that the FAA groups appear to have somewhat electron withdrawing character.

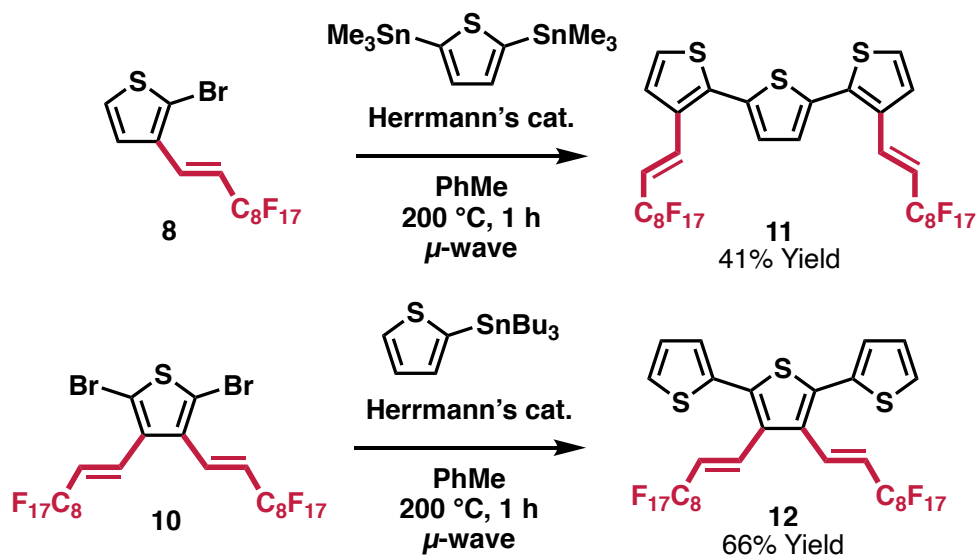


**Scheme 5.2** Brominations of FAA-Functionalized Thiophenes. Scheme adapted with permission.<sup>120</sup> Copyright © 2021, Georg Thieme Verlag KG.

### 5.3.3 Synthesis and Properties of FAA-Functionalized Terthiophenes

With the brominated thiophenes in hand, we synthesized terthiophene molecular building blocks. **Scheme 5.3** shows two model terthiophene compounds synthesized from precursors **8** and **10**. Compounds **11** and **12** were obtained by a Stille coupling reaction. We initially utilized Pd(PPh<sub>3</sub>)<sub>4</sub> as the catalyst for the reaction, although the reaction could not reach full conversion. Alternatively, we found the Herrmann's catalyst was more efficient in this reaction, giving products **11** and **12** in 41% and 66% yields, respectively. Compounds **11** and **12** are compositional regioisomers differing only by the position of the FAA group, and we find that compound **11** was more emissive than compound **12**, as well as emissive in the solid state. For comparison, **3T-C<sub>12</sub>**, an alkyl analogue of compound **11**, was prepared by following literature procedure.<sup>123</sup> The absorbance/fluorescence properties of **11**, **12**, **3T-C<sub>12</sub>**, and a commercially available 2,2':5',2''-terthiophene (**3T**) are summarized in **Figure 5.2** and **Table 5.2**. Both compounds **11** and **12**

exhibited a bathochromic shift in absorption and emission maximum with an increased Stokes shift compared to **3T-C<sub>12</sub>**. These characteristics are likely derived from the extended conjugation from the adjacent alkene. The emission quantum yield ( $\Phi_F$ ) of compound **11** was 0.0654, like the value of that of **3T-C<sub>12</sub>** (0.0651). In contrast,  $\Phi_F$  of compound **12** was much lower (0.0063).



**Scheme 5.3** Synthesis of FAA-Functionalized Terthiophenes. Scheme adapted with permission.<sup>120</sup> Copyright © 2021, Georg Thieme Verlag KG.

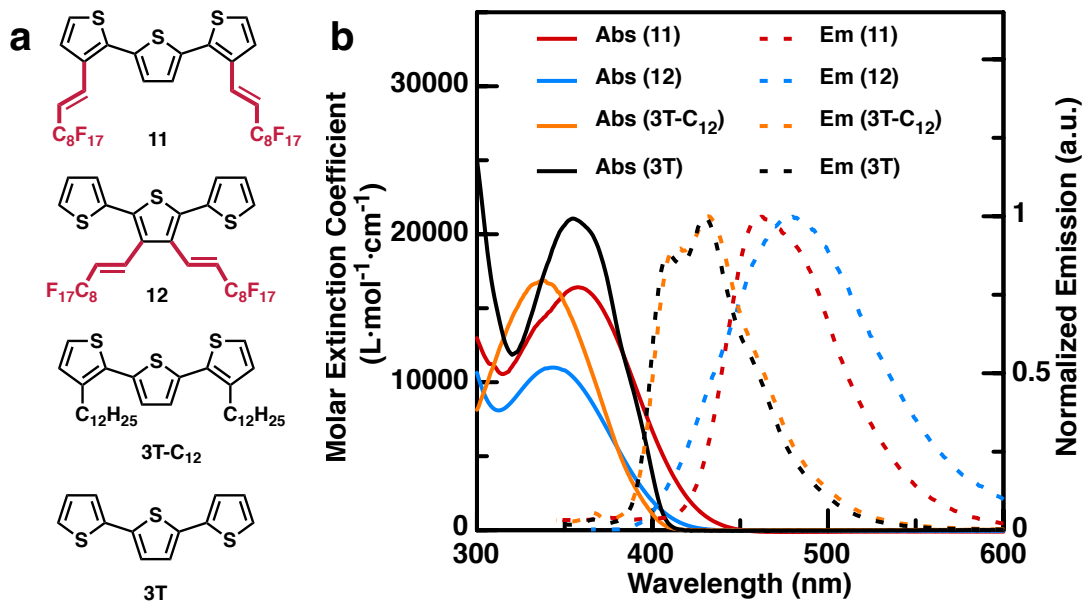
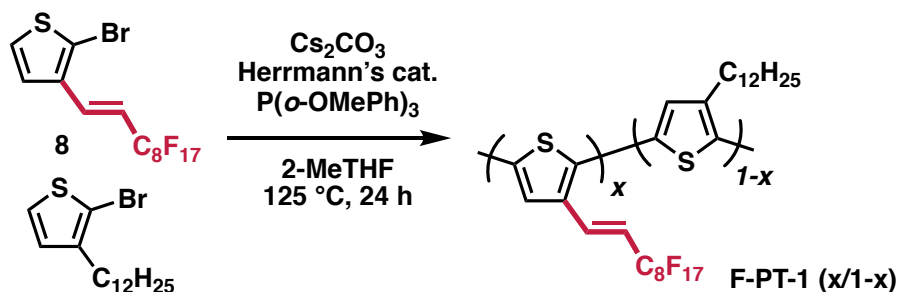


**Figure 5.2** (a) Chemical structure and (b) UV/vis absorbance and fluorescence spectra of compounds **11**, **12**, **3T-C<sub>12</sub>**, and **3T** in toluene solution. Excitation wavelength = 330 nm. Figure adapted with permission.<sup>120</sup> Copyright © 2021, Georg Thieme Verlag KG.

### 5.3.4 Synthesis and Properties of FAA-Functionalized Polythiophenes

We have also proceeded to synthesize conjugated polythiophenes from the FAA-functionalized thiophenes. Following procedures reported by Wane *et al.*,<sup>124</sup> we attempted to synthesize statistical copolymers with monomer **8** and 2-bromo-3-dodecylthiophene using direct arylation polymerization (DARp). DARp is an attractive polymerization method because it reduces the multi-step functional group conversion required for other polymerization methods such as the Stille polymerization or the Suzuki polymerization, though the latter are reliable and have been widely used to make materials for photovoltaic applications.<sup>125,126</sup> The polymerization is outlined in **Scheme 5.4** and the properties of the obtained polymers are summarized in **Table 5.3**. We obtained polymers with >10 kDa molecular weight determined by gel permeation chromatography. The proton nuclear magnetic resonance spectra roughly confirmed the correspondence of the initial feed ratio of the monomers and the ratio of the monomers in the obtained polymer. A broadened fluorine NMR spectra suggests the successful incorporation of compound **8** into the polymer

structure. The energy level of the HOMO (ionization energy) was estimated from cyclic voltammetry measurements (**Figure 5.12**). Both polymers had a value of -5.30 eV, which was lower than P3HT.<sup>127</sup> Thin films could be readily obtained by dropcasting a 5 mg/mL chloroform of polymer solution onto a glass slide. Using the onset of the film absorption, the optical bandgap was estimated to be 1.90 eV for **F-PT-1 (25/75)** and 1.85 eV for **F-PT-1 (50/50)** (**Figure 5.13**). Both values are smaller than the reported bandgap for P3HT.<sup>127</sup> The lower HOMO and narrower bandgap compared to P3HT can both be rationalized by the extended conjugation of the alkene side chains and the electron-withdrawing nature of the fluorine.<sup>128</sup> A continuous 2 h irradiation of a chloroform solution of **F-PT-1 (50/50)** using the fluorimeter showed no decay in fluorescence intensity, although a chloroform solution of P3HT showed a gradual decay in fluorescence intensity (**Figure 5.15**). This result highlights the increased photostability of the reported polymer, which is likely derived from fluorine incorporation.<sup>5,108</sup>

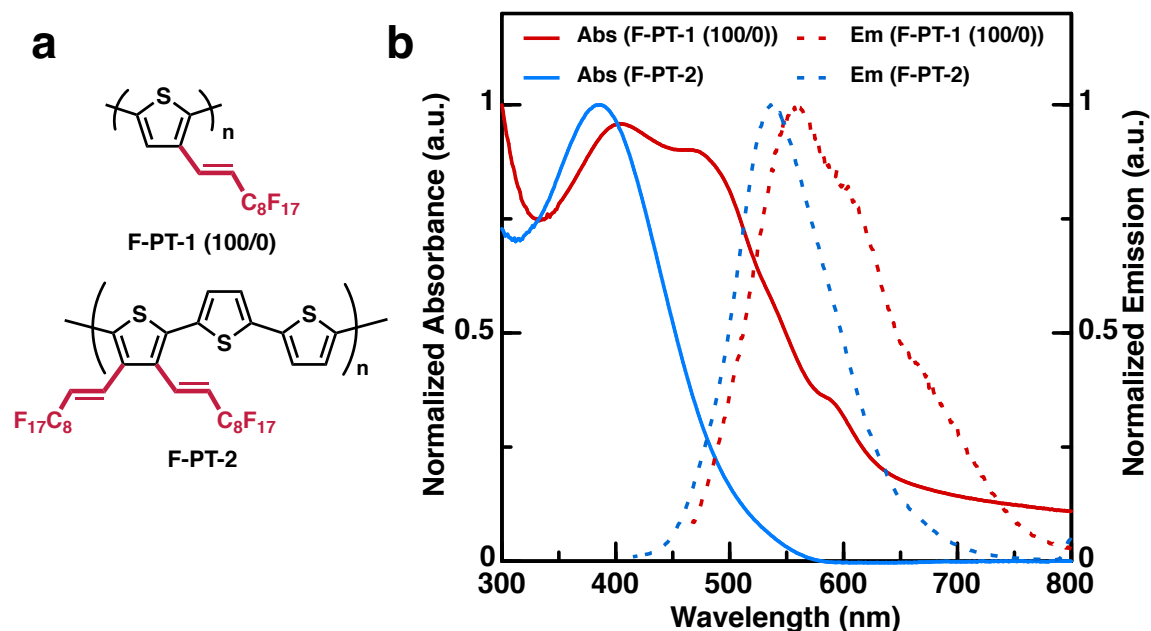
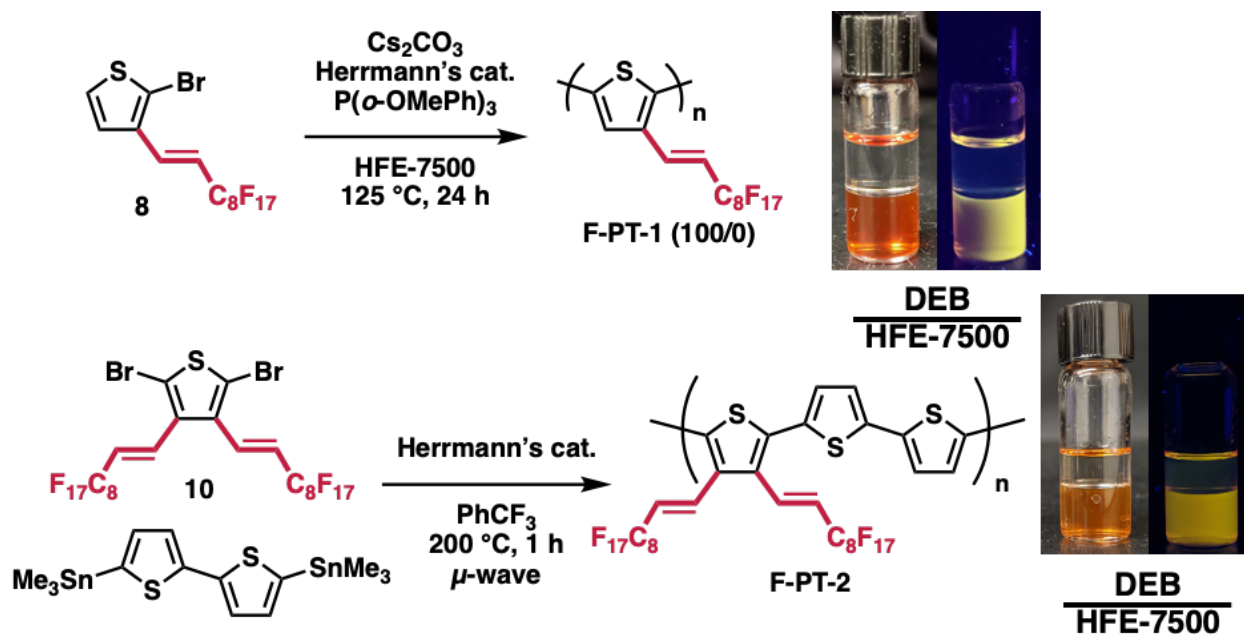


**Scheme 5.4** Synthesis of **F-PT-1 (x/1-x)**. Scheme adapted with permission.<sup>120</sup> Copyright © 2021, Georg Thieme Verlag KG.

### 5.3.5 Synthesis and Properties of Fluorous-Soluble Polythiophenes

We also attempted to synthesize a homopolymer from compound **8** using DArP to give polymer **F-PT-1 (100/0)** as shown in **Scheme 5.5**. The homopolymer was a red-brown solid and was only moderately soluble in hydrofluoroethers such as methoxyperfluorobutane and 2-(trifluoromethyl)-3-ethoxydodecafluorohexane (HFE-7500). Alternatively, a conventional Stille

polymerization using compound **10** and a commercially available stannylated bithiophene gave **F-PT-2** in 72% yield. Like **F-PT-1 (100/0)**, **F-PT-2** was again a red-brown solid and was only moderately soluble in hydrofluoroethers such as methoxyperfluorobutane and HFE-7500. As a result, we were unable to obtain molecular weight data for these polymers. We studied the fluorous partition behavior of these polymers with solvents diethylbenzene (DEB) and HFE-7500, which were chosen as a result of their low interfacial tension and low upper critical mixing temperature.<sup>77,101</sup> Both polymers showed good partition in HFE-7500 over DEB (**Scheme 5.5**, right) and were emissive in HFE-7500 solution (**Figure 5.3b**). Interestingly, although compounds **11**, **12**, and **F-PT-2** all possess similar weight percent fluorine, they had distinct fluorous partition properties: compound **11** and **12** showed partition in both DEB and HFE-7500, and **F-PT-2** showed exclusive partition in HFE-7500 (**Figure 5.10**). This result hints at the relationship between the position of the fluoroalkyl chains and the molecule's fluorous solubility. Further characterization of these fluorous soluble polymers and study of structure-property relationship of a molecule's fluorous solubility is in progress.



### 5.3.6 Fluorous Aromatics in Lithium Primary Batteries

Lithium (Li) is the lightest metal and has the greatest electrochemical potential, making it one of the most reactive metals. These features give lithium the opportunity to achieve high energy and power density to batteries and endow multiple battery applications.<sup>129–131</sup> Lithium primary batteries, with their outstanding performance and characteristics, are being used in increasing quantities in a variety of applications, including cameras, memory backup circuits, security devices, calculators, watches, etc.<sup>132</sup> Nevertheless, lithium primary batteries have not attained a major share of the market as was anticipated, because of their high initial cost, concerns with safety, the advances made with competitive systems, and the cost-effectiveness of the alkaline/manganese battery.<sup>133</sup> Conventional commercialized primary batteries, for example, such as Li-SOCl<sub>2</sub> and Li-CF<sub>x</sub> batteries, deliver good electrochemical performance but face various challenges. Li-SOCl<sub>2</sub> primary batteries, for example, deliver high cell-level energy densities (i.e., 500 Wh/kg or 1200 Wh/L), but the liquid SOCl<sub>2</sub>, which functions as both cathode and electrolyte, which is highly toxic and corrosive, making such batteries unsuitable for civil applications and/or transportation.<sup>134,135</sup> Li-CF<sub>x</sub> batteries have the highest theoretical specific energy (i.e., 2180 Wh/kg) among all Li primary battery chemistries, but the solid CF<sub>x</sub> particles are highly insulating, thus the Li-CF<sub>x</sub> batteries are only suitable for low-to-medium rate applications.<sup>136,137</sup>

Li-perfluorinated gas batteries based on sulfur hexafluoride (SF<sub>6</sub>)<sup>138,139</sup> and nitrogen trifluoride (NF<sub>3</sub>)<sup>140</sup> have been reported to defluorinate perfluorinated compounds in a single electrochemical cell setup at room temperature (RT). The full defluorination enable estimation of the theoretical energy density (e.g., 3900–5100 Wh/kg), which is ~6–9x higher than traditional Li-ion batteries (~590 Wh/kg<sub>reactant</sub>).<sup>141</sup> However, the limited kinetics and low solubilities (e.g., less than 5 mM) achieved by the dissolved gas nature of the SF<sub>6</sub> and NF<sub>3</sub> cathodes results in large

overpotentials during cell discharge, which severely hinders the attainable energy densities of these systems.

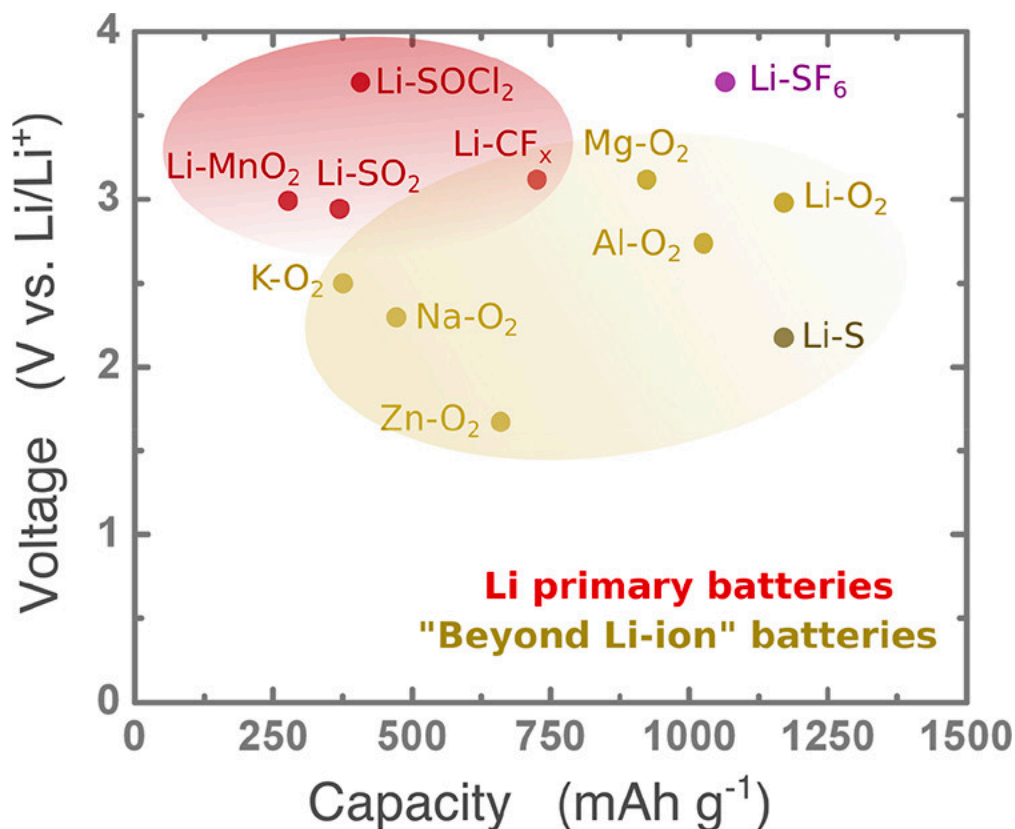


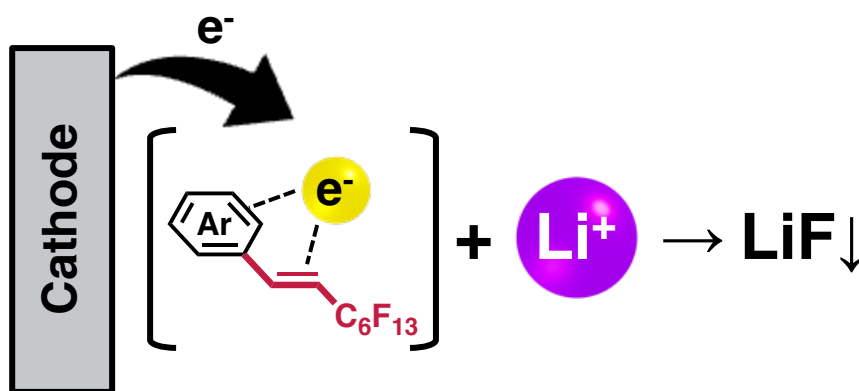
**Figure 5.4** Theoretical voltages and cell capacities of Li primary batteries and metal-O<sub>2</sub> and Li-S batteries. Reprinted with permission.<sup>138</sup> Copyright © 2018, American Chemical Society.

In this regard, we hypothesized that the FAA-functionalized aromatic molecules could provide opportunities as novel cathode materials. Since these molecules are noncorrosive, batteries based on FAA-functionalized aromatics are suitable for civil applications and/or transportation. In addition, because these molecules are either solids or liquids, they can exhibit high electrolyte solubility and therefore high cell-level energy density compared to the gas cathodic materials. The tunability of the molecular structure enables strategic design of electrochemical performance improvement of the fabricated Li primary batteries.

Our preliminary findings suggest a close-to-full dehalogenation of the FAA-functionalized compounds can be achieved at practical discharge conditions (0.3 mA/cm<sup>2</sup>), yielding 8 to 15 e<sup>-</sup>



transfer per molecule and relatively high discharge potentials ( $\sim 2.6$  V). As a result, high achievable specific energies (up to  $2190 \text{ Wh/kg}_{\text{reactant}}$ ) are attainable, making the FAA-functionalized molecules a strong competitor as electrodes in high-energy primary batteries. Furthermore, we investigate the structure-property relationship by synthesizing a variety of derivatives and comparing their discharge properties. The synthetic flexibility offered by this class of molecules offer great opportunity for electrochemical performance improvement, but also serves as a new platform to further investigate the mechanism of this halide ion reduction.

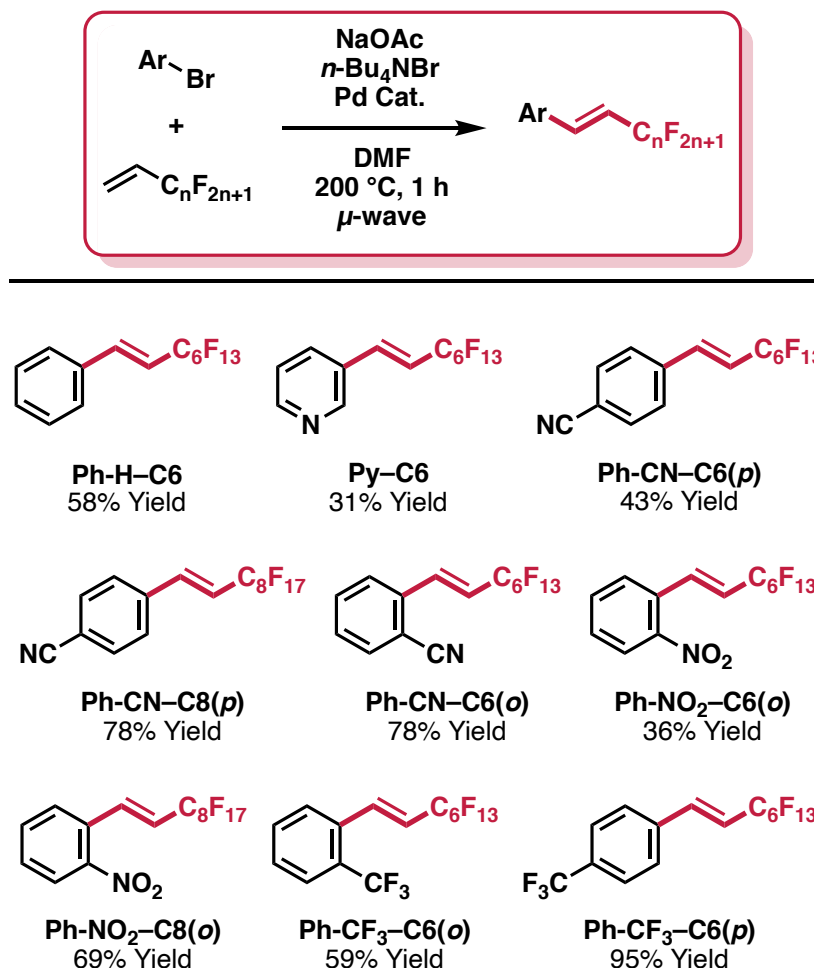


**Scheme 5.6** Hypothetical mechanism of fluoride reduction of the FAA-functionalized molecules

### 5.3.7 Synthesis of Fluorous Aromatics

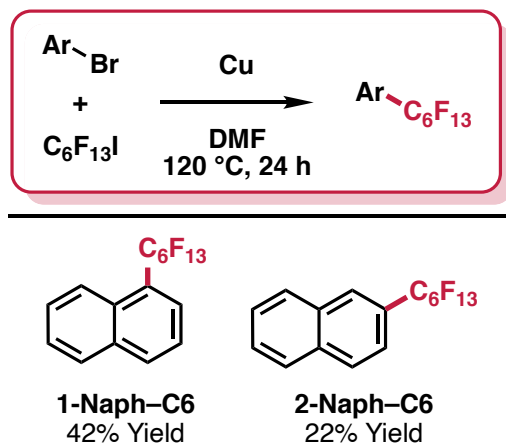
The fluorous aromatics synthesized by the fluorous Heck reaction is described in **Scheme 5.7**. In general, the fluorous Heck reaction condition was adopted from previous literature,<sup>113</sup> and the fluorous aromatics shown were generally obtained in good yields. For the synthesis of **Py-C6**, using Herrmann's catalyst as the palladium (Pd) catalyst gave no conversion, therefore palladium acetate ( $\text{Pd}(\text{OAc})_2$ ) was utilized. Nonetheless, **Py-C6** was obtained in only 31% yield, presumably due to the instability of the reaction intermediate or the coordination of pyridine to Pd leading to complicated byproducts. For the synthesis of **Ph-NO<sub>2</sub>-C6(o)** and **Ph-NO<sub>2</sub>-C8(o)**, using  $\text{Pd}(\text{OAc})_2$  gave better yields than Herrmann's catalyst. Lower yields were observed for **Ph-CN-C6(o)** and

**Ph-CF<sub>3</sub>-C6(*o*)** than their para counterparts because of the steric hindrance derived from the functional groups. In general, C8 products were obtained in better yields due to the high melting point and higher crystallinity from the longer fluoroalkyl chain, providing the products as solids.



**Scheme 5.7** Synthesis of FAA-functionalized molecules described in this work

Perfluoroalkyl naphthalenes were synthesized by Ullmann coupling of perfluoroalkyl iodides and the respective bromonaphthalene (**Scheme 5.7b**).<sup>142</sup> The naphthalenes were synthesized by an Ullmann-type coupling, giving **1-Naph-C6** and **2-Naph-C6** in 42% and 22% yields, respectively.



Scheme 5.8 Synthesis of perfluoroalkyl naphthalenes

### 5.3.8 Discharge Profiles of Fluorous Aromatics in Lithium Primary Batteries

It was first demonstrated how the FAA-group reduction properties can be manipulated by molecular structure design. Note that even for those reactants that are in the liquid state at RT (others are solids), no common lithium salt (i.e., LiClO<sub>4</sub>, LiPF<sub>6</sub>, LiTFSI) can be dissolved in the neat form, making it necessary to use a co-solvent to help with the salt solvation. Therefore, as a proof of concept, we chose dimethyl sulfoxide (DMSO, without any optimization) as the co-solvent for all the cells tested. Due to the limited solubility of **Ph-CN-C8(p)** at RT, the cells were measured at 50 °C with 0.1 M reactants in DMSO electrolyte to form fair comparisons. The discharge performances shown in **Figure 5.5** reveals that **Ph-CN-C8(p)** is electrochemically active and can be discharged at a high voltage of ~2.5 V (vs. Li/Li<sup>+</sup>). Scanning electron microscope images of the discharged electrode reveals the formation of a cubic lithium fluoride (LiF) salt, likely generated from the defluorination of the reactant (**Figure 5.5b**). Powder X-ray diffraction of the discharged electrode shows sharp peak patterns that overlaps perfectly with the reference LiF powder pattern (LiF: Space Group: Fm-3m, JCPDS: 00-004-0857), again confirming the formation of LiF on the electrode (**Figure 5.5c**). Key control discharge experiments were performed to validate the importance of the chemical identity of the cathode material. A

commercially available (perfluorohexyl)benzene showed negligible discharge behavior (**Figure 5.16a**). This result highlights the importance of the alkene between the phenyl ring and the perfluoroalkyl chain in the molecules electrochemical activity. *1H,1H,2H*-perfluoro-1-octene was also electrochemically inactive, suggesting the need of the phenyl group and the alkene (**Figure 5.16b**). Finally, we also failed to discharge a mixture of benzonitrile and *1H,1H,2H*-perfluoro-1-octene, suggesting the necessity of covalent bonding between the alkene and the phenyl ring (**Figure 5.16c**).

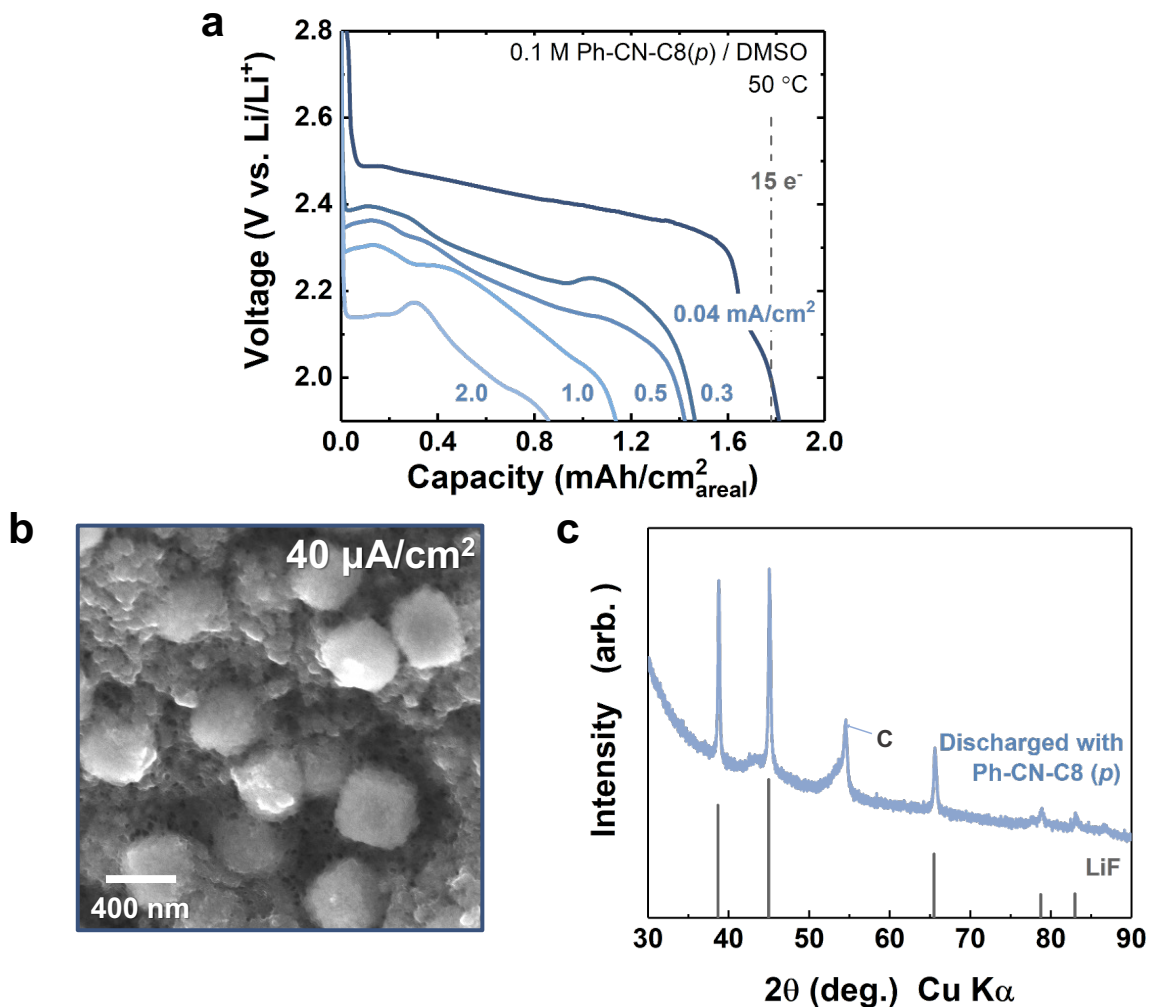


**Figure 5.5** Galvanostatic discharge properties of **Ph-CN-C8(*p*)**. (a) Galvanostatic discharge profile of **Ph-CN-C8(*p*)** at 50 °C with varying discharge rate. (b) Scanning electron microscope image of the discharged carbon cathode. (c) Powder X-ray diffraction pattern of the discharged carbon cathode.

We then investigated how the molecular structure affects the discharge performances of these molecules. We hypothesized that the discharge voltage, i.e., the reduction potential of the molecule, should correlate with the electron withdrawing strength of the functional groups. Other comparisons of our interest were *ortho* vs. *para* isomers, length of the perfluoroalkyl chain ( $-\text{C}_6\text{F}_{13}$  vs.  $-\text{C}_8\text{F}_{17}$ ), and heterocycles vs. phenyl ring. To this end, we synthesized the relevant FAA-functionalized molecules and studied their discharge properties. The molecular structures discharged for comparison is summarized in **Figure 5.6a**. As shown in **Figure 5.6b**, up to  $11\text{ e}^-$  or  $15\text{ e}^-$  transfer per molecule (calculated based on capacities) can be obtained during discharge for C6 or C8 containing reactants, respectively. Considering that there are only 13 or 17 C–F bonds in the C6 or C8 groups, respectively, the discharge profiles indicate that, assuming all the  $\text{e}^-$  transfer are induced by C–F bond reduction, nearly full defluorination of the FAA groups can be achieved, with only two C–F bonds remaining unreacted. **Ph-NO<sub>2</sub>-C6(*o*)** and **Ph-NO<sub>2</sub>-C8(*o*)** discharged at the highest voltage of  $\sim 2.6\text{ V}$ . **Ph-CN-C6(*p*)** and **Ph-CN-C6(*o*)** displayed nearly identical discharge profiles, suggesting the minimal influence of the position (*para* vs. *ortho*) of the functional group. To understand the effect of the chain length of the FAA group, we compared the discharge profiles of **Ph-NO<sub>2</sub>-C6(*o*)** and **Ph-NO<sub>2</sub>-C8(*o*)**, as well as **Ph-CN-C6(*p*)** and **Ph-CN-C8(*p*)**. Although longer fluoroalkyl chains tend to exhibit better F utilization (11 of 13 vs. 15 of 17 fluorine reduction), they also tend to decrease the solubility of the reactants in DMSO. For example, **Ph-CN-C6(*p*)** is a liquid and is miscible with DMSO at RT, but its C8 counterpart is a solid at RT and is only soluble at elevated temperatures ( $50\text{ }^\circ\text{C}$ ). **Py-C6** showed a higher discharge voltage than **Ph-H-C6**. This could be explained by the fact that pyridine is an electron-deficient aromatic molecule and has a higher reduction potential. The discharge voltage and the computed

LUMO values show a strong correlation as shown in **Figure 5.6c**. **Ph-CF<sub>3</sub>-C6(o)** and **Ph-CF<sub>3</sub>-C6(p)** were immiscible with DMSO and thus did not have good discharge performance.

The naphthalenes shown in **Scheme 5.8** were also discharged in a similar manner. **1-Naph-C6** was more electrochemically active than **2-Naph-C6**, though much less active than the FAA-functionalized molecules (see **Figure 5.17**). The discharged voltage and the computed LUMO of **1-Naph-C6** (~2.0 V and -1.46 eV, respectively) are in good agreement with the correlation plot shown in **Figure 5.6c**.

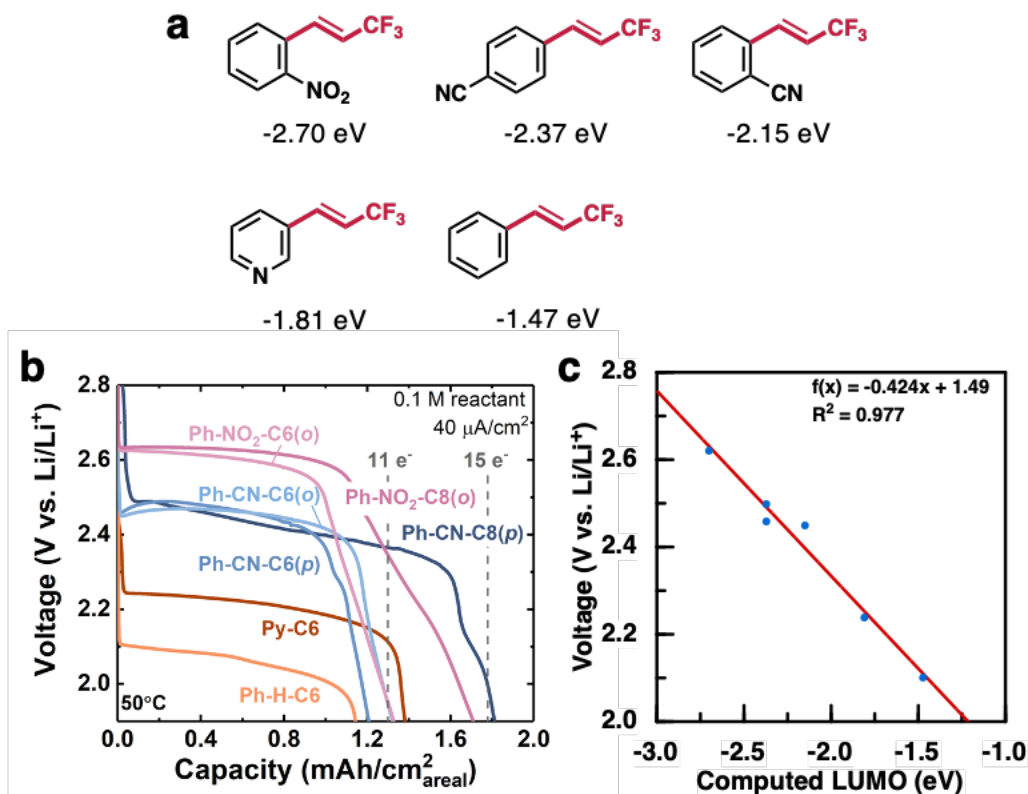


**Figure 5.6** Discharge performance of the synthesized molecules. (a) Chemical structures and the respective computed LUMO values. (b) Galvanostatic discharge profiles of the synthesized molecules. All discharge experiments were performed at 50 °C. (c) Correlation plot of the discharge voltage and the computed LUMO values of the molecules.

With these preliminary results in hand, we took **Ph-NO<sub>2</sub>-C6(o)** and attempted to investigate the rate capability and the effect of temperature on the performance of the battery discharge. While the *ortho* and *para* isomers displayed similar performance, the *ortho* isomer is

advantageous because it is more soluble and has a lower melting point due to its nonsymmetrical molecular structure. **Figure 5.7** compares the discharge performance of **Ph-NO<sub>2</sub>-C6(o)** at either 50 °C or RT. Both temperatures showed stable discharge at rates as high as 1.0 mA/cm<sup>2</sup>. Improved rate capability could be observed at 50 °C when compared to RT. Up to 11 e<sup>-</sup> per molecule can be obtained, resulting in a capacity of 642 mAh/g<sub>reactant</sub>.

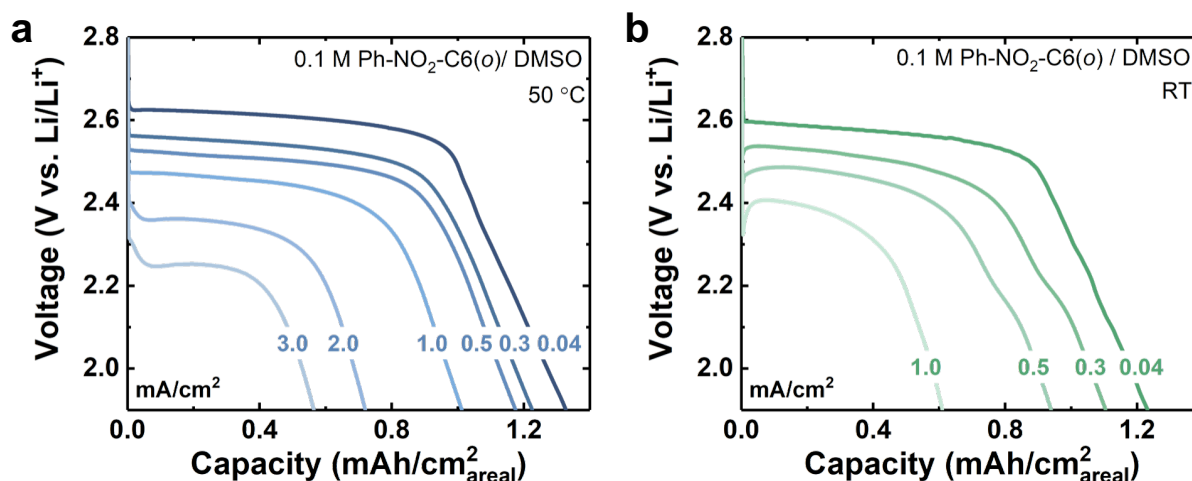


**Figure 5.7** Galvanostatic discharge profile of 0.1 M **Ph-NO<sub>2</sub>-C6(o)** performed at 50 °C. Galvanostatic discharge profile of 1 M **Ph-NO<sub>2</sub>-C6(o)** performed at RT.

Finally, to evaluate the potentials of the disclosed system, the high concentration performances were compared with the state-of-the-art Li-CF<sub>x</sub> batteries. The discharge performance of Li-CF<sub>x</sub> cells were measured at 50 °C with purchased CF<sub>x</sub> powder (coating on Toray paper substrate). Since the laboratory scale cells need excess amount of electrolyte, and the electrolyte weight are typically not reported for commercialized Li-CF<sub>x</sub> batteries, a CF<sub>x</sub>-to-electrolyte weight ratio of 1:1 was assumed, and the obtained gravimetric energy densities (based on CF<sub>x</sub> weight) were normalized to the weight of electrolyte+CF<sub>x</sub> for fair comparisons. It is worth noting that this electrolyte/CF<sub>x</sub> weight ratio is a typical value reported in CF<sub>x</sub> batteries,<sup>143,144</sup> and thus is a reasonable assumption to represent commercial CF<sub>x</sub> cells. As is shown in **Figure 5.8a**, with a **Ph-NO<sub>2</sub>-C6(o)** or a **Ph-NO<sub>2</sub>-C8(o)** concentration of 2 M, the cell will exhibit energy

densities of  $\sim 1100 \text{ Wh/kg}_{\text{electrolyte+cathode}}$ , comparable to or better than that of the  $\text{Li-CF}_x$  batteries. Experimentally, a higher concentration of  $1 \text{ M Ph-NO}_2\text{-C6(o)}$  at  $50 \text{ }^\circ\text{C}$  was demonstrated to attempt to achieve higher energy density. Our preliminary measurements shown in **Figure 5.8b** revealed a high areal capacity of  $\sim 8 \text{ mAh/cm}^2$  can be attained, which roughly equals to  $\sim 7 \text{ e}^-$  per molecule can be obtained, resulting in a capacity of  $\sim 400 \text{ mAh/g}_{\text{reactant}}$ . The lower values can probably be attributed to the limited surface area of the electrode. We hypothesize that the  $\text{LiF}$  formed during discharge passivated the electrode surface, resulting in the “sudden death” of the cell, which is also observed in other  $\text{Li}$  cells such as  $\text{Li-O}_2$ <sup>145,146</sup> and  $\text{Li-SF}_6$  cells.<sup>138,139</sup> Current work focuses on further increasing the carbon loading on the electrode in order to get higher capacities.

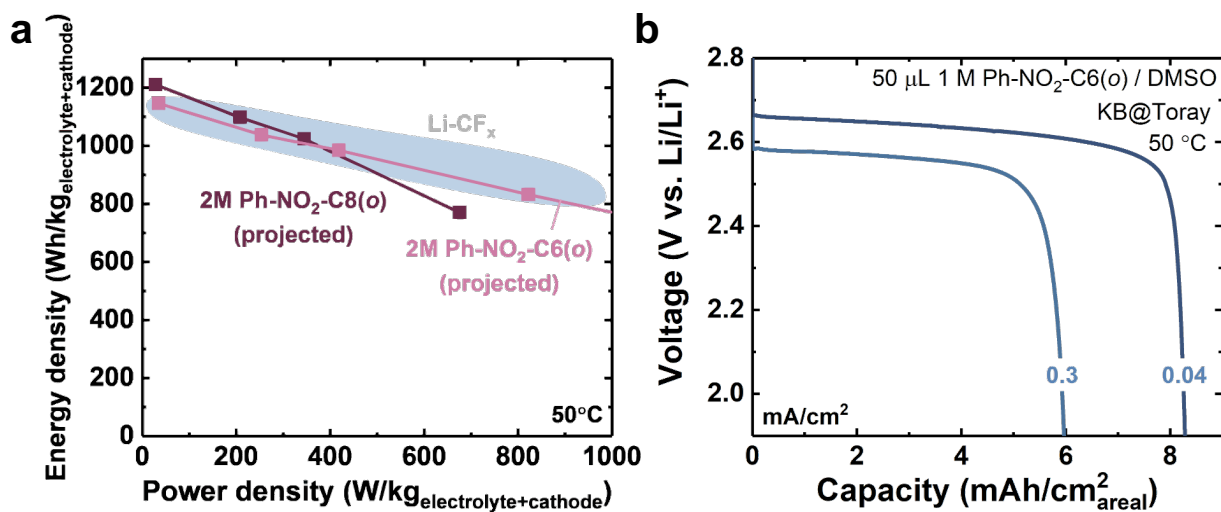


**Figure 5.8** (a) A Ragone plot comparing the projected discharge performances of  $\text{Li}$ -fluoro-aromatic cells and  $\text{Li-CF}_x$  cells at  $50 \text{ }^\circ\text{C}$ . (b) Galvanostatic discharge profile of  $1 \text{ M Ph-NO}_2\text{-C6(o)}$  performed at  $50 \text{ }^\circ\text{C}$ .

## 5.4 Conclusions

In summary, we have expanded the scope of the fluorinated Heck reaction and showcase its utility in synthesizing fluorinated conjugated materials. We found that the utilization of microwave heating conditions increases the yield as well as enables the incorporation of  $\text{C}_6\text{F}_{13}$  chains to an



aromatic molecule. NBS bromination of thiophenes was selectively achieved in the presence of the alkene. The brominated thiophenes underwent Stille coupling as well as direct arylation polymerization to obtain terthiophenes and polythiophenes. Access to these fluorinated molecular building blocks enable their incorporation into existing materials, as well as discovery of new functional fluorinated conjugated materials. In the latter part of this chapter, we expanded the substrate scope of the FAA-functionalized aromatic molecules to study their performance in lithium primary batteries. The synthetic flexibility offered by this class of molecules offer great opportunity for electrochemical performance improvement, but also serves as a new platform to further investigate the mechanism of this halide ion reduction. Ongoing efforts are focused on the structural diversification of the fluorinated conjugated materials and their applications.

## 5.5 Experimental

### 5.5.1 General

All chemical reagents were purchased from Sigma-Aldrich, Synquest Laboratories, Oakwood Chemicals, Fluoryx Labs, or TCI, and used without purification unless noted otherwise. Thin layer chromatography was performed with Baker-flex Silica Gel 1B-F plates (JT Baker). Flash chromatography was performed using technical grade silica gel with 60 Å pores and 230–400 mesh particle size (Sigma-Aldrich, 717185). Compound **3T-C<sub>12</sub>** was synthesized by reproducing the work by Grand et al.<sup>123</sup>

<sup>1</sup>H, <sup>13</sup>C, and <sup>19</sup>F nuclear magnetic resonance (NMR) spectra were recorded on a JEOL model JNM-ECZ500R/S1 spectrometer operating at 500, 126, and 471 MHz, respectively. For <sup>1</sup>H, <sup>13</sup>C NMR spectra, deuterated solvent references were used as internal standards (<sup>1</sup>H: 7.26 ppm, <sup>13</sup>C: 77.16 ppm for CDCl<sub>3</sub>). Multiplicities are abbreviated as singlet (s), doublet (d), triplet (t), multiplet

(m). Direct Analysis in Real Time (DART) mass spectra were obtained at the MIT Department of Chemistry Instrumentation Facility. Single crystal X-ray diffraction data were obtained at MIT Department of Chemistry's X-Ray Diffraction Facility. Single crystal X-ray structure of compound **4** is deposited to Cambridge Crystallographic Data Centre (CCDC). CCDC 2090155 contains all crystallographic details of this publication and is available free of charge at [www.ccdc.cam.ac.uk/conts/retrieving.html](http://www.ccdc.cam.ac.uk/conts/retrieving.html). Wide angle X-ray scattering data were obtained at MIT Materials Research Laboratory. UV/Vis absorbance spectra were obtained on a Cary 4000 UV/Vis spectrophotometer (Agilent Technologies) with a scan rate of 600 nm/min. The instrument was blanked on the solvent prior to obtaining a spectrum. Fluorescence spectra were obtained on a Horiba Jobin Yvon SPEX Fluorolog- $\tau$ 3 fluorimeter (model FL-321, 450 W Xenon lamp). Quantum yields were measured using 9,10-diphenylanthracene as a standard ( $\Phi_F = 0.90$  in cyclohexane, excited at 350 nm). Absorbance and fluorescence data were collected in a quartz cuvette (1 cm path length). THF gel permeation chromatography (GPC) was performed with a concentration of 0.5 mg/mL on an Agilent 1260 Infinity system equipped with three PL gel columns (103, 104, 105 Å) in series, calibrated with monodisperse polystyrene standards. Cyclic voltammetry was performed by dropcasting an analyte solution onto ITO glass (working electrode). 0.1 M Bu<sub>4</sub>NPF<sub>6</sub> in CH<sub>3</sub>CN was used as the electrolyte, Pt wire as the counter electrode, and Ag/AgNO<sub>3</sub> as the reference electrode at 100 mV/s. Ferrocene ( $E_{1/2} = 0.10$  V) was used as external standard. LUMO value calculations of the described molecules were obtained from the Spartan '18 software with a basis set of B3LYP/6-31G.

### ***Electrochemical Cell Testing***

*Chemicals and Materials:* All electrodes and cell-making materials were stored in an argon-filled glovebox (H<sub>2</sub>O content <1 ppm, O<sub>2</sub> content <1 ppm, MBRAUN) after dried. LiClO<sub>4</sub> (99.99%

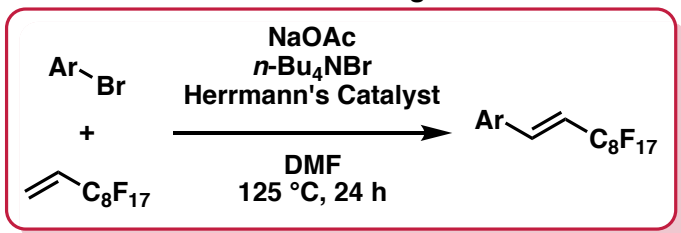
trace metals basis, Sigma-Aldrich), stainless steel mesh (316 stainless steel, McMaster) and the Whatman filter paper (Grade QM-A, 2.2  $\mu\text{m}$  pore size, 450  $\mu\text{m}$  in thickness, Sigma Aldrich) were dried in a Buchi glass oven under active vacuum for 24 hours at 120  $^{\circ}\text{C}$ . DMSO (anhydrous, > 99.9%, Sigma-Aldrich) and 4-Nitrophenylsulfur pentafluoride ( $\text{Ph-NO}_2\text{-SF}_5$  (*p*), 97%, Synquest) were stored inside the glovebox at room temperature.

*Carbon electrode Preparation:* The Kejten black (KB) electrodes were fabricated in-house by uniformly coating sonicated inks composed of KB (AzkoNobel) powder, N-Methyl-2-pyrrolidone (NMP), and polyvinylidene difluoride (PVDF) (with a weight ratio of KB: PVDF =80: 20) onto a sheet of Toray paper (TGP-H-030, Fuel cell earth). After being air-dried at room temperature, the obtained KB coated Toray paper was punched into circular disks (12 mm diameter) and then dried under active vacuum in a glass oven (Buchi) overnight at 90  $^{\circ}\text{C}$ .

*Galvanostatic Discharge:* Two-electrode Swagelok-type Li cells were constructed in an argon glovebox, with the dried KB cathode and a 9 mm diameter disk of Li metal as anode (0.75 mm thick, 99.9% metals basis, Alfa Aesar), which was pre-stabilized by soaking in pure  $\text{C}_6\text{F}_{13}\text{I}$  (99%, Sigma-Aldrich) for at least three days prior to use. The separator (13 mm diameter glass fiber filter paper) was impregnated with 50  $\mu\text{L}$  electrolyte solution (as indicated in text). The cells were rested at open circuit voltage (OCV) for 5 h before the galvanostatic discharge tests, which were carried out (BioLogic VMP3 potentiostat or MPG2 workstation) at the specified current density with a voltage window ranging from OCV to a lower cutoff voltage of 1.9 V vs Li/Li<sup>+</sup>. For galvanostatic discharge conducted at 50  $^{\circ}\text{C}$ , the cells were placed in an incubator (Memmert GmbH + Co. KG) after assembling.

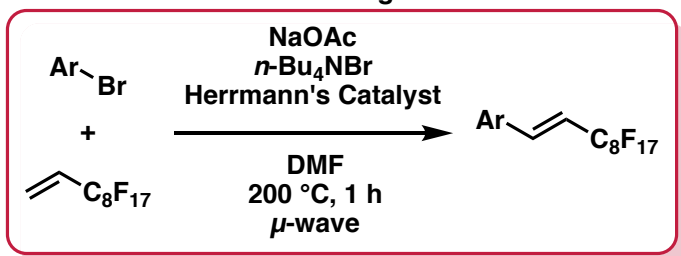
## 5.5.2 Synthetic Procedures

### Condition A: Conventional Heating



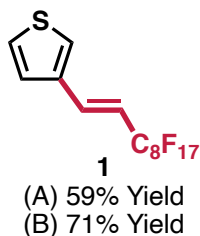
A mixture of aryl bromide (1.0 equiv), 1H,1H,2H-perfluoro-1-decene (1.5 equiv/Ar-Br bond), *n*-Bu<sub>4</sub>NBr (0.85 equiv/Ar-Br bond), NaOAc (1.5 equiv/Ar-Br bond), and Herrmann's catalyst (4 mol%/Ar-Br bond) were dissolved in DMF in a Schlenk flask. The reaction mixture was stirred for 24 h at 125 °C. Upon cooling the reaction mixture to room temperature, the residue was dissolved in AcOEt and HCl (1 M). The organic layer was separated, washed three times with water and once with brine, dried with MgSO<sub>4</sub>, and evaporated to dryness under reduced pressure. The residue was chromatographed on silica gel, and the fraction containing the product was collected and evaporated to dryness.

### Condition B: Microwave Heating



A mixture of aryl bromide (1.0 equiv), 1H,1H,2H-perfluoro-1-decene (1.5 equiv/Ar-Br bond), *n*-Bu<sub>4</sub>NBr (0.85 equiv/Ar-Br bond), NaOAc (1.5 equiv/Ar-Br bond), and Herrmann's catalyst (4 mol%/Ar-Br bond) were dissolved in DMF in a microwave vial. The reaction mixture was stirred for 1 h at 200 °C in a microwave. Upon cooling the reaction mixture to room temperature, the residue was dissolved in AcOEt and HCl (1 M). The organic layer was separated, washed three

times with water and once with brine, dried with MgSO<sub>4</sub>, and evaporated to dryness under reduced pressure. The residue was chromatographed on silica gel, and the fraction containing the product was collected and evaporated to dryness.



**Compound 1. Condition A** was followed using 3-bromothiophene (159 mg, 0.976 mmol), 1*H*,1*H*,2*H*-perfluoro-1-decene (669 mg, 1.50 mmol), *n*-Bu<sub>4</sub>NBr (285 mg, 0.884 mmol), NaOAc (122 mg, 1.49 mmol), and Herrmann's catalyst (37 mg, 0.0395 mmol) dissolved in DMF (1 mL). Isolation by silica gel column chromatography (hexanes, R<sub>f</sub> = 0.50) yielded compound **1** as a yellow oil (310 mg, 0.586 mmol, 59% yield).

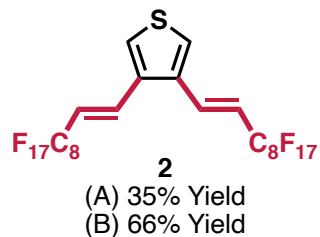
**Condition B** was followed to yield compound **1** as a yellow oil (373 mg, 0.706 mmol, 71% yield).

<sup>1</sup>H NMR (500 MHz, CDCl<sub>3</sub>, 20 °C): δ (ppm) 7.45 (s, 1H), 7.36–7.38 (m, 1H), 7.27 (d, *J* = 5.0 Hz, 1H), 7.16 (d, *J* = 16.0 Hz, 1H), 5.99–6.07 (m, 1H).

<sup>13</sup>C NMR (126 MHz, CDCl<sub>3</sub>, 20 °C): δ (ppm) 136.60, 133.53 (t, *J* = 10.1 Hz), 127.54, 127.32, 124.93, 114.03 (t, *J* = 10.1 Hz).

<sup>19</sup>F NMR (471 MHz, CDCl<sub>3</sub>, 20 °C): δ (ppm) -80.66 (t, *J* = 9.8 Hz, 3F), -110.96 (q, *J* = 12.2 Hz, 2F), -121.28 (m, 2F), -121.82 (m, 4F), -122.62 (m, 2F), -123.06 (m, 2F), -126.01 (m, 2F).

DART MS: *m/z* calcd. for [C<sub>14</sub>H<sub>5</sub>F<sub>17</sub>S]<sup>+</sup>: 527.9841; found: 527.9862.



**Compound 2. Condition A** was followed using 3,4-dibromothiophene (122 mg, 0.504 mmol), 1*H*,1*H*,2*H*-perfluoro-1-decene (687 mg, 1.54 mmol), *n*-Bu<sub>4</sub>NBr (286 mg, 0.887 mmol), NaOAc (126 mg, 1.54 mmol), and Herrmann's catalyst (95 mg, 0.101 mmol) dissolved in DMF (1 mL), and heated to 125 °C for 96 h. Isolation by silica gel column chromatography (hexanes, *R<sub>f</sub>* = 0.50) yielded compound **2** as a white solid (170 mg, 0.175 mmol, 35% yield).

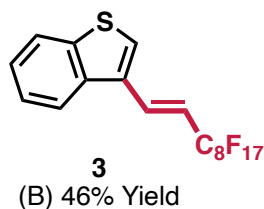
**Condition B** was followed to yield compound **2** as a white solid (322 mg, 0.331 mmol, 66% yield).

<sup>1</sup>H NMR (500 MHz, CDCl<sub>3</sub>, 20 °C): δ (ppm) 7.52 (s, 2H), 7.18 (d, *J* = 16.0 Hz, 2H), 5.99–6.07 (m, 2H).

<sup>13</sup>C NMR (126 MHz, CDCl<sub>3</sub>, 20 °C): δ (ppm) 134.93, 132.23 (t, *J* = 10.1 Hz), 126.74, 117.70 (t, *J* = 10.6 Hz).

<sup>19</sup>F NMR (471 MHz, CDCl<sub>3</sub>, 20 °C): δ (ppm) -80.80 (t, *J* = 11.2 Hz, 6F), -111.51 (q, *J* = 12.2 Hz, 4F), -121.31 (m, 4F), -121.93 (m, 8F), -122.74 (m, 4F), -123.36 (m, 4F), -126.14 (m, 4F).

DART MS: *m/z* calcd. for [C<sub>24</sub>H<sub>6</sub>F<sub>34</sub>S]<sup>+</sup>: 971.9647; found: 971.9674.



**Compound 3. Condition B** was followed using 3-bromobenzo[b]thiophene (430 mg, 2.02 mmol), 1*H*,1*H*,2*H*-perfluoro-1-decene (1.32 g, 2.96 mmol), *n*-Bu<sub>4</sub>NBr (278 mg, 1.71 mmol), NaOAc (239

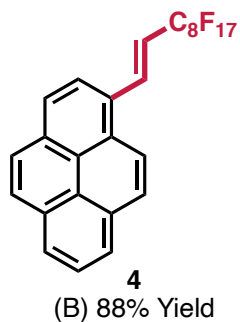
mg, 2.91 mmol), and Herrmann's catalyst (93 mg, 0.992 mmol) dissolved in DMF (10 mL). Isolation by silica gel column chromatography (hexanes,  $R_f = 0.50$ ) yielded compound **6** as a white solid (530 mg, 0.917 mmol, 46% yield).

$^1\text{H}$  NMR (500 MHz,  $\text{CDCl}_3$ , 20 °C):  $\delta$  (ppm) 7.93 (d,  $J = 8.0$  Hz, 1H), 7.90 (d,  $J = 8.0$  Hz, 1H), 7.66 (s, 1H), 7.42–7.50 (m, 3H), 6.29–6.37 (m, 1H).

$^{13}\text{C}$  NMR (126 MHz,  $\text{CDCl}_3$ , 20 °C):  $\delta$  (ppm) 140.72, 137.08, 131.96 (t,  $J = 10.1$  Hz), 130.74, 127.32, 125.27, 125.14, 123.23, 121.83, 115.42 (t,  $J = 23.2$  Hz).

$^{19}\text{F}$  NMR (471 MHz,  $\text{CDCl}_3$ , 20 °C):  $\delta$  (ppm) -81.02 (t,  $J = 9.8$  Hz, 3F), -111.26 (q,  $J = 12.2$  Hz, 2F), -121.36 (m, 2F), -121.96 (m, 4F), -122.81 (m, 2F), -123.05 (m, 2F), -126.26 (m, 2F).

DART MS:  $m/z$  calcd. for  $[\text{C}_{18}\text{H}_7\text{F}_{17}\text{S}]^+$ : 577.9997; found: 578.0017.



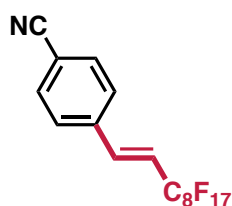
**Compound 4. Condition B** was followed using 1-bromopyrene (281 mg, 1.00 mmol), 1*H*,1*H*,2*H*-perfluoro-1-decene (669 mg, 1.50 mmol), *n*- $\text{Bu}_4\text{NBr}$  (274 mg, 0.850 mmol), NaOAc (123 mg, 1.50 mmol), and Herrmann's catalyst (38 mg, 0.0400 mmol) dissolved in DMF (1 mL). Isolation by silica gel column chromatography (hexanes/ $\text{CHCl}_3$ : 1:1,  $R_f = 0.40$ ) yielded compound **4** as a white solid (570 mg, 0.881 mmol, 88% yield).

$^1\text{H}$  NMR (500 MHz,  $\text{CDCl}_3$ , 20 °C):  $\delta$  (ppm) 8.35 (d,  $J = 9.2$  Hz, 1H), 8.30 (d,  $J = 15.6$  Hz, 1H), 8.24–8.25 (m, 2H), 8.20–8.22 (m, 3H), 8.14 (d,  $J = 8.8$  Hz, 1H), 8.04–8.10 (m, 2H), 6.38–6.47 (m, 1H).

$^{13}\text{C}$  NMR (126 MHz,  $\text{CDCl}_3$ , 20 °C):  $\delta$  (ppm) 137.16 (t,  $J = 9.5$  Hz), 132.61, 131.38, 130.72, 129.29, 128.75, 128.60, 127.54, 127.35, 126.42, 126.14, 125.92, 125.09, 124.84, 124.63, 124.16, 122.15, 116.82 (t,  $J = 22.7$  Hz).

$^{19}\text{F}$  NMR (471 MHz,  $\text{CDCl}_3$ , 20 °C):  $\delta$  (ppm) -80.66 (t,  $J = 9.8$  Hz, 3F), -110.50 (q,  $J = 12.2$  Hz, 2F), -121.14 (m, 2F), -121.75 (m, 4F), -122.58 (m, 2F), -122.80 (m, 2F), -126.00 (m, 2F).

DART MS:  $m/z$  calcd. for  $\text{C}_{26}\text{H}_{11}\text{F}_{17}$   $[\text{M}+\text{H}]^+$ : 647.0662; found: 647. 0721.



(B) 86% Yield

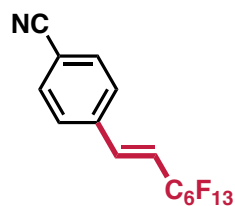
**Compound 5. Condition B** was followed using 4-bromobenzonitrile (184 mg, 1.01 mmol), 1H,1H,2H-perfluoro-1-decene (720 mg, 1.61 mmol), *n*-Bu<sub>4</sub>NBr (283 mg, 0.878 mmol), NaOAc (133 mg, 1.62 mmol), and Herrmann's catalyst (36 mg, 0.0384 mmol) dissolved in DMF (1 mL). Isolation by silica gel column chromatography ( $\text{CHCl}_3$ ,  $R_f = 0.70$ ) yielded compound **5** as a light brown solid (470 mg, 0.859 mmol, 86% yield).

$^1\text{H}$  NMR (500 MHz,  $\text{CDCl}_3$ , 20 °C):  $\delta$  (ppm) 7.70 (d,  $J = 8.0$  Hz, 2H), 7.58 (d,  $J = 8.4$  Hz, 2H), 7.19 (d,  $J = 16.4$  Hz, 1H), 6.28-6.36 (m, 1H).

$^{19}\text{F}$  NMR (471 MHz,  $\text{CDCl}_3$ , 20 °C):  $\delta$  (ppm) -80.79 (t,  $J = 9.1$  Hz, 3F), -111.70 (q,  $J = 12.2$  Hz, 2F), -121.35 (m, 2F), -121.89 (m, 4F), -122.71 (m, 2F), -123.03 (m, 2F), -126.12 (m, 2F).

Characterization is consistent with the previous work.<sup>113</sup>





**6**

(B) 42% Yield

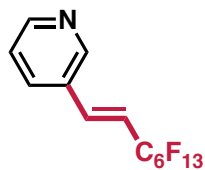
**Compound 6.** Condition **B** was followed using 4-bromobenzonitrile (362 mg, 1.99 mmol), 1*H*,1*H*,2*H*-perfluoro-1-octene (1.04 g, 3.00 mmol), NaOAc (246 mg, 3.00 mmol), *n*-Bu<sub>4</sub>NBr (540 mg, 1.68 mmol), and Herrmann's catalyst (75 mg, 0.080 mmol) dissolved in DMF (10 mL). Isolation by silica gel column chromatography (hexanes with a gradient of 1% → 5% CH<sub>2</sub>Cl<sub>2</sub>) yielded compound **6** as a beige solid (380 mg, 0.850 mmol, 43% yield).

<sup>1</sup>H NMR (500 MHz, CDCl<sub>3</sub>, 20 °C): δ (ppm) 7.71 (d, *J* = 8.4 Hz, 2H), 7.59 (d, *J* = 8.4 Hz, 2H), 7.20 (dt, *J* = 16.2, 2.1 Hz, 1H), 6.28-6.36 (m, 1H)

<sup>13</sup>C NMR (126 MHz, CDCl<sub>3</sub>, 20 °C): δ (ppm) 138.06 (t, *J* = 8.7 Hz), 137.79, 132.91, 128.31, 118.33, 118.21(t, *J* = 22.7 Hz), 113.78.

<sup>19</sup>F NMR (471 MHz, CDCl<sub>3</sub>, 20 °C): δ (ppm) -80.66 (t, *J* = 9.1 Hz, 3F), -111.62 (q, *J* = 12.2 Hz, 2F), -121.50 (m, 2F), -122.75 (m, 2F), -122.98 (m, 2F), -126.04 (m, 2F).

DART MS: *m/z* calcd. for [C<sub>15</sub>H<sub>6</sub>F<sub>13</sub>N + H]<sup>+</sup>: 448.0371, [C<sub>15</sub>H<sub>6</sub>F<sub>13</sub>N + NH<sub>4</sub>]<sup>+</sup>: 465.0636; found: 448.0384, 465.0636.



**7**

(B) 31% Yield

**Compound 7.** Condition **B** was followed using 3-bromopyridine (316 mg, 2.00 mmol), 1*H*,1*H*,2*H*-perfluoro-1-octene (1.06 g, 3.06 mmol), NaOAc (254 mg, 3.10 mmol), *n*-Bu<sub>4</sub>NBr (548

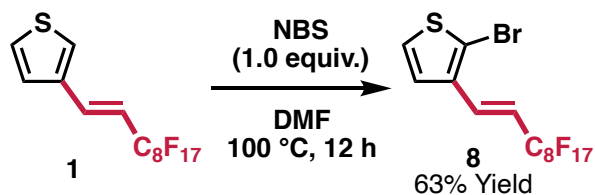
mg, 1.70 mmol), and Pd(OAc)<sub>2</sub> (23 mg, 0.102 mmol) dissolved in DMF (10 mL). Isolation by silica gel column chromatography (CH<sub>2</sub>Cl<sub>2</sub>, R<sub>f</sub> = 0.45) yielded compound **7** as a colorless oil (260 mg, 0.614 mmol, 31% yield).

<sup>1</sup>H NMR (500 MHz, CDCl<sub>3</sub>, 20 °C): δ (ppm) 8.71 (d, *J* = 2.3 Hz, 1H), 8.63 (dd, *J* = 4.8, 1.3 Hz, 1H), 7.81 (dt, *J* = 7.9, 1.8 Hz, 1H), 7.36 (dd, *J* = 7.8, 4.8 Hz, 1H), 7.19 (dt, *J* = 16.0, 2.1 Hz, 1H), 6.25-6.33 (m, 1H).

<sup>13</sup>C NMR (126 MHz, CDCl<sub>3</sub>, 20 °C) δ (ppm) 151.27, 149.50, 136.60 (t, *J* = 10.1 Hz), 134.07, 129.36, 123.91, 116.77 (t, *J* = 22.7 Hz).

<sup>19</sup>F NMR (471 MHz, CDCl<sub>3</sub>, 20 °C) δ (ppm) -80.69 (t, *J* = 9.8 Hz, 3F), -111.50 (q, *J* = 13.1 Hz, 2F), -121.52 (m, 2F), -122.77 (m, 2F), -123.04 (m, 2F), -126.06 (m, 2F).

DART MS: *m/z* calcd. for [C<sub>13</sub>H<sub>6</sub>F<sub>13</sub>N + H]<sup>+</sup>: 424.0371; found: 424.0378.



**Compound 8.** A mixture of compound **1** (531 mg, 1.01 mmol) and N-bromosuccinimide (173 mg, 0.972 mmol) were dissolved in DMF (10 mL) in a round bottom flask. The reaction mixture was stirred for 12 h at 100 °C. Upon cooling the reaction mixture to room temperature, 10 wt% Na<sub>2</sub>S<sub>2</sub>O<sub>3</sub> aq (50 mL) was added, and the mixture was extracted with Et<sub>2</sub>O (50 mL × 3). The organic layer was collected, washed with water (50 mL × 3) and brine (50 mL), dried with MgSO<sub>4</sub>, and evaporated to dryness under reduced pressure. The residue was chromatographed on silica gel using hexanes as an eluent, and the fraction containing compound **8** (R<sub>f</sub> = 0.60) was collected and

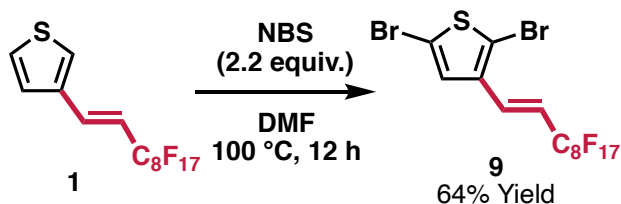
evaporated to dryness under reduced pressure to provide white solid (380 mg, 0.625 mmol, 63% yield).

$^1\text{H}$  NMR (500 MHz,  $\text{CDCl}_3$ , 20 °C):  $\delta$  (ppm) 7.31 (d,  $J = 6.1$  Hz, 1H), 7.17 (d,  $J = 16.0$  Hz, 1H), 7.13 (d,  $J = 5.7$  Hz, 1H), 6.05-6.14 (m, 1H).

$^{13}\text{C}$  NMR (126 MHz,  $\text{CDCl}_3$ , 20 °C):  $\delta$  (ppm) 135.83, 130.75 (t,  $J = 10.1$  Hz), 127.50, 116.75 (t,  $J = 23.9$  Hz), 115.84, 113.21.

$^{19}\text{F}$  NMR (471 MHz,  $\text{CDCl}_3$ , 20 °C):  $\delta$  (ppm) -80.61 (t,  $J = 9.8$  Hz, 3F), -111.15 (q,  $J = 12.2$  Hz, 2F), -121.24 (m, 2F), -121.78 (m, 4F), -122.59 (m, 2F), -122.92 (m, 2F), -125.98 (m, 2F).

DART MS:  $m/z$  calcd. for  $[\text{C}_{14}\text{H}_4\text{BrF}_{17}\text{S}]^+$ : 605.8946; found: 605.8949.



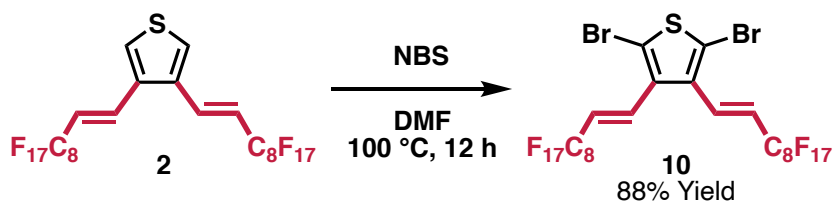
**Compound 9.** A mixture of compound **1** (1.49 g, 2.82 mmol) and N-bromosuccinimide (1.02 g, 5.73 mmol) were dissolved in DMF (10 mL) in a round bottom flask. The reaction mixture was stirred for 12 h at 100 °C. Upon cooling the reaction mixture to room temperature, 10 wt%  $\text{Na}_2\text{S}_2\text{O}_3$  aq (50 mL) was added, and the mixture was extracted with  $\text{Et}_2\text{O}$  (50 mL  $\times$  3). The organic layer was collected, washed with water (50 mL  $\times$  3) and brine (50 mL), dried with  $\text{MgSO}_4$ , and evaporated to dryness under reduced pressure. The residue was chromatographed on silica gel using hexanes as an eluent, and the fraction containing compound **9** ( $R_f = 0.60$ ) was collected and evaporated to dryness under reduced pressure to provide a white solid (1.49 g, 2.17 mmol, 64% yield).

$^1\text{H}$  NMR (500 MHz,  $\text{CDCl}_3$ , 20 °C):  $\delta$  (ppm) 7.13 (s, 1H), 7.07 (d,  $J = 16.0$  Hz, 1H), 6.00-6.08 (m, 1H).

$^{13}\text{C}$  NMR (126 MHz,  $\text{CDCl}_3$ , 20 °C):  $\delta$  (ppm) 135.83, 130.75 (t,  $J = 10.1$  Hz), 127.50, 116.75 (t,  $J = 23.9$  Hz), 115.84, 113.21.

$^{19}\text{F}$  NMR (471 MHz,  $\text{CDCl}_3$ , 20 °C):  $\delta$  (ppm) -80.61 (t,  $J = 9.1$  Hz, 3F), -111.36 (q,  $J = 12.2$  Hz, 2F), -121.23 (m, 2F), -121.79 (m, 4F), -122.59 (m, 2F), -122.92 (m, 2F), -125.98 (m, 2F).

DART MS:  $m/z$  calcd. for  $[\text{C}_{14}\text{H}_3\text{Br}_2\text{F}_{17}\text{S}]^+$ : 683.8051; found: 683.8079.



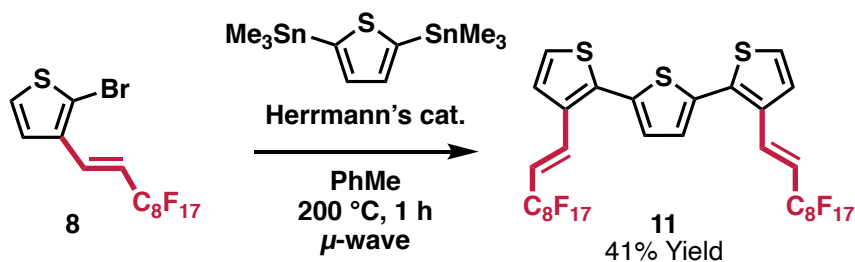
**Compound 10.** A mixture of compound **2** (807 mg, 0.830 mmol) and N-bromosuccinimide (596 mg, 3.35 mmol) were dissolved in DMF (3 mL) in a round bottom flask. The reaction mixture was stirred for 12 h at 100 °C. Upon cooling the reaction mixture to room temperature, 10 wt%  $\text{Na}_2\text{S}_2\text{O}_3$  aq (50 mL) was added, and the mixture was extracted with  $\text{Et}_2\text{O}$  (50 mL  $\times$  3). The organic layer was collected, washed with water (50 mL  $\times$  3) and brine (50 mL), dried with  $\text{MgSO}_4$ , and evaporated to dryness under reduced pressure. The residue was chromatographed on silica gel using hexanes as an eluent, and the fraction containing compound **10** ( $R_f = 0.60$ ) was collected and evaporated to dryness under reduced pressure to provide a white solid (830 mg, 0.734 mmol, 88% yield).

$^1\text{H}$  NMR (500 MHz,  $\text{CDCl}_3$ , 20 °C):  $\delta$  (ppm) 6.98 (d,  $J = 16.4$  Hz, 2H), 6.12-6.20 (m, 2H).

$^{13}\text{C}$  NMR (126 MHz,  $\text{CDCl}_3$ , 20 °C):  $\delta$  (ppm) 133.75, 131.13 (t,  $J = 10.1$  Hz), 121.71 (t,  $J = 23.1$  Hz), 114.61.

$^{19}\text{F}$  NMR (471 MHz,  $\text{CDCl}_3$ , 20 °C):  $\delta$  (ppm) -80.81 (t,  $J = 9.8$  Hz, 3F), -112.36 (q,  $J = 12.2$  Hz, 2F), -121.31 (m, 2F), -121.96 (m, 4F), -122.76 (m, 2F), -123.21 (m, 2F), -126.17 (m, 2F).

DART MS:  $m/z$  calcd. for  $[\text{C}_{24}\text{H}_4\text{Br}_2\text{F}_{34}\text{S}]^+$ : 1127.7858; found: 1127.7913.



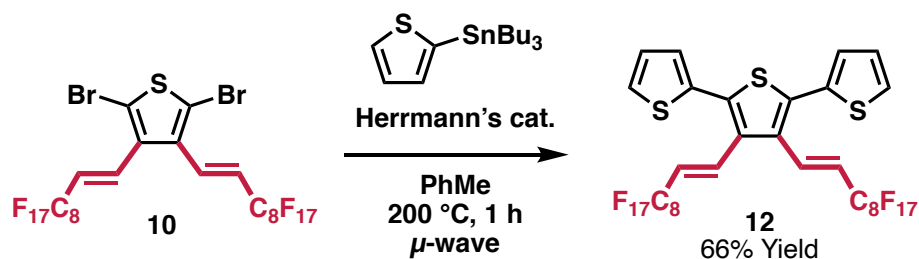
**Compound 11.** A mixture of compound **8** (120 mg, 0.198 mmol), 2,5-bis(trimethylstannyl)thiophene (41 mg, 0.100 mmol) were dissolved in PhMe (1 mL) in a microwave vial. The reaction mixture was stirred for 1 h at 200 °C in a microwave. Upon cooling the reaction mixture to room temperature, it was diluted with hexanes and filtered through a silica plug. The solution is evaporated under reduced pressure and dissolved in chloroform. The chloroform solution was precipitated in excess methanol, and the precipitate was filtered and collected to provide compound **11** as a yellow fluorescent solid (47 mg, 0.0414 mmol, 41% yield).

$^1\text{H}$  NMR (500 MHz,  $\text{CDCl}_3$ , 20 °C):  $\delta$  (ppm) 7.45 (dt,  $J = 16.2, 2.3$  Hz, 2H), 7.32 (d,  $J = 5.4$  Hz, 2H), 7.29 (d,  $J = 5.4$  Hz, 2H), 7.13 (s, 2H), 6.13 (td,  $J = 16.0, 12.1$  Hz, 2H).

$^{13}\text{C}$  NMR (126 MHz,  $\text{CDCl}_3$ , 20 °C):  $\delta$  (ppm) 136.90, 135.99, 132.65, 132.27 (t,  $J = 10.1$  Hz), 128.62, 126.41, 126.23, 115.82 (t,  $J = 23.3$  Hz).

$^{19}\text{F}$  NMR (471 MHz,  $\text{CDCl}_3$ , 20 °C):  $\delta$  (ppm) -80.72 (t,  $J = 10.6$  Hz), -111.04 (q,  $J = 13.1$  Hz), -121.31 (m, 4F), -121.86 (m, 8F), -122.67 (m, 4F), -122.96 (m, 4F), -126.08 (m, 4F).

DART MS: calcd. for  $[\text{C}_{32}\text{H}_{10}\text{F}_{34}\text{S}_3]^+$ : 1135.9402; found: 1135.9422.



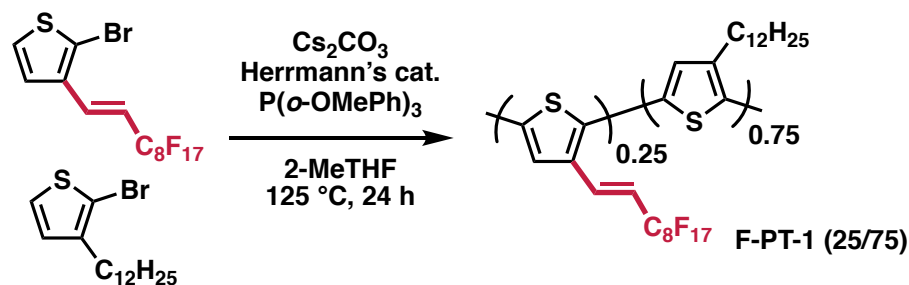
**Compound 12.** A mixture of compound **10** (110 mg, 0.0973 mmol), 2-(tributylstannyl)thiophene (82 mg, 0.218 mmol) were dissolved in PhMe (1 mL) in a microwave vial. The reaction mixture was stirred for 1 h at 200 °C in the microwave. Upon cooling the reaction mixture to room temperature, it was diluted with hexanes and filtered through a silica plug. The solution is evaporated under reduced pressure and dissolved in chloroform. The chloroform solution was precipitated in excess methanol, and the precipitate was filtered and collected to provide compound **12** as a white solid (75 mg, 0.0660 mmol, 66% yield).

$^1\text{H NMR}$  (500 MHz,  $\text{CDCl}_3$ , 20 °C):  $\delta$  (ppm) 7.44 (d,  $J = 5.0$  Hz, 2H), 7.22 (d,  $J = 16.0$  Hz, 2H), 7.16 (d,  $J = 3.1$  Hz, 2H), 7.11 (m, 2H), 5.89–5.97 (m, 2H).

$^{13}\text{C NMR}$  (126 MHz,  $\text{CDCl}_3$ , 20 °C):  $\delta$  (ppm) 135.94, 133.23, 132.70 (t,  $J = 10.1$  Hz), 131.42, 128.54, 128.08, 128.02, 120.88 (t,  $J = 23.1$  Hz).

$^{19}\text{F NMR}$  (471 MHz,  $\text{CDCl}_3$ , 20 °C):  $\delta$  (ppm) -80.83 (t,  $J = 9.8$  Hz, 6F), -112.25 (q,  $J = 11.2$  Hz, 4F), -121.44 (m, 4F), -121.97 (m, 8F), -122.77 (m, 4F), -123.09 (m, 4F), -126.18 (m, 4F).

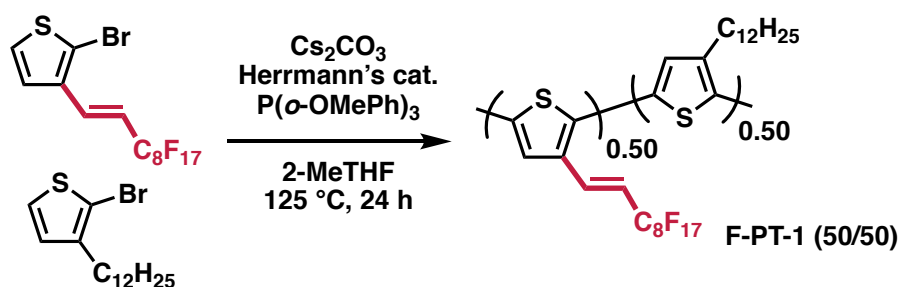
DART MS: calcd. for  $[\text{C}_{32}\text{H}_{10}\text{F}_{34}\text{S}_3]^+$ : 1135.9402; found: 1135.9417.



**F-PT-1(25/75).** Compound **8** (76 mg, 0.125 mmol), 2-bromo-3-dodecylthiophene (124 mg, 0.374 mmol),  $P(o\text{-OMePh})_3$  (18 mg, 0.051 mmol), Herrmann's catalyst (23 mg, 0.025 mmol),  $\text{Cs}_2\text{CO}_3$  (326 mg, 1.00 mmol), and 2-methyltetrahydrofuran (2 mL) were added to a 15 mL ChemGlass microwave vial with a magnetic stir bar. The reaction vessel was sealed, and the mixture was stirred for 24 h at 125 °C. Upon cooling the reaction mixture to room temperature, it was precipitated in excess methanol, and the precipitate was filtered and collected. The solid was transferred to a Soxhlet thimble, and Soxhlet extraction was performed using hexanes for 6 h. The hexanes extract was evaporated under reduced pressure and dissolved in chloroform. The chloroform solution was precipitated in excess methanol, and the precipitate was filtered and collected to provide **F-PT-1(25/75)** as a brown solid (150 mg, >99% yield).

$^1\text{H}$  NMR (500 MHz,  $\text{CDCl}_3$ , 20 °C):  $\delta$  (ppm) 7.35–7.51 (m, 1H), 6.92–7.03 (m, 4H), 6.02–6.27 (m, 1H), 2.78–2.82 (m, 6H), 1.68–1.72 (m, 6H), 1.02–1.48 (m, 54H), 0.83–0.91 (m, 9H).

$^{19}\text{F}$  NMR (471 MHz,  $\text{CDCl}_3$ , 20 °C):  $\delta$  (ppm) -80.41–-81.26 (m, 3F), -110.29–-111.82 (m, 2F), -120.92–-121.56 (m, 2F), -121.56–-122.21 (m, 4F), -122.35–-123.56 (m, 4F), -125.72–-126.77 (m, 2F).

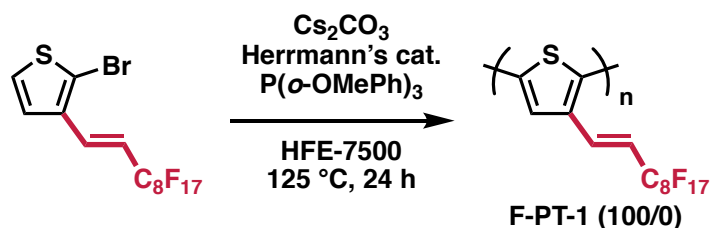


**F-PT-1(50/50).** Compound **8** (152 mg, 0.250 mmol), 2-bromo-3-dodecylthiophene (83 mg, 0.250 mmol),  $P(o\text{-OMePh})_3$  (18 mg, 0.051 mmol), Herrmann's catalyst (23 mg, 0.025 mmol),  $\text{Cs}_2\text{CO}_3$  (326 mg, 1.00 mmol), and 2-methyltetrahydrofuran (2 mL) were added to a 15 mL ChemGlass

microwave vial with a magnetic stir bar. The reaction vessel was sealed, and the mixture was stirred for 24 h at 125 °C. Upon cooling the reaction mixture to room temperature, it was precipitated in excess methanol, and the precipitate was filtered and collected. The solid was transferred to a Soxhlet thimble, and Soxhlet extraction was performed using hexanes for 6 h. The hexanes extract was evaporated under reduced pressure and dissolved in chloroform. The chloroform solution was precipitated in excess methanol, and the precipitate was filtered and collected to provide **F-PT-1(50/50)** as a brown solid (80 mg, 41% yield).

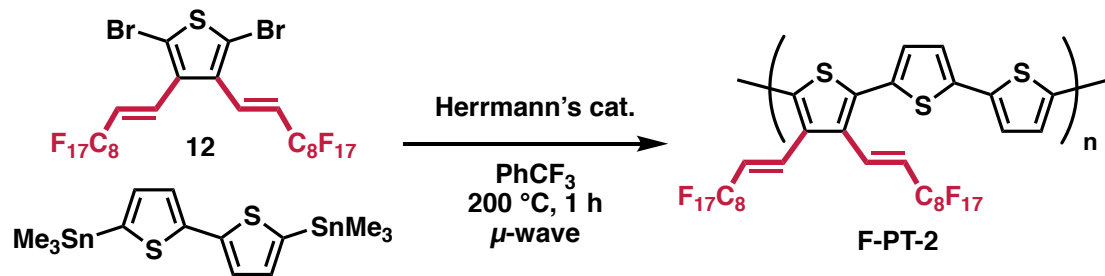
<sup>1</sup>H NMR (500 MHz, CDCl<sub>3</sub>, 20 °C): δ (ppm) 7.34–7.52 (m, 1H), 6.87–7.10 (m, 2H), 6.00–6.29 (m, 1H), 2.71–2.89 (m, 2H), 1.65–1.77 (m, 2H), 1.21–1.28 (m, 18H), 0.83–0.87 (m, 3H).

<sup>19</sup>F NMR (471 MHz, CDCl<sub>3</sub>, 20 °C): δ (ppm) -80.54–80.98 (m, 3F), -110.44–111.56 (m, 2F), -121.03–121.60 (m, 2F), -121.60–122.41 (m, 4F), -122.41–123.42 (m, 4F), -125.88–126.39 (m, 2F).

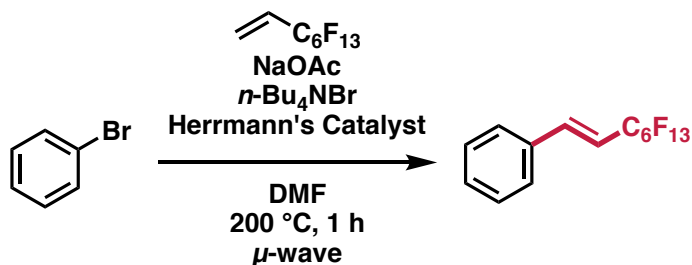


**F-PT-1(100/0)**. Compound **8** (122 mg, 0.201 mmol),  $\text{P}(o\text{-OMePh})_3$  (3 mg, 0.00851 mmol), Herrmann's catalyst (9 mg, 0.00960 mmol),  $\text{Cs}_2\text{CO}_3$  (66 mg, 0.203 mmol), and HFE-7500 (1 mL) were added to a 15 mL ChemGlass microwave vial with a magnetic stir bar. The reaction vessel was sealed, and the mixture was stirred for 24 h at 125 °C. Upon cooling the reaction mixture to room temperature, it was diluted with HFE-7500 and was precipitated in excess methanol. The precipitate was filtered and collected to provide **F-PT-1(100/0)** as a brown solid (100 mg, 94% yield). NMR could not be taken due to low solubility.





**F-PT-2.** A mixture of compound **12** (113 mg, 0.100 mmol), 5,5'-bis(trimethylstannyl)-2,2'-bithiophene (46 mg, 0.0935 mmol) were dissolved in PhCF<sub>3</sub> (1 mL) in a microwave vial. The reaction mixture was stirred for 1 h at 200 °C in the microwave. Upon cooling the reaction mixture to room temperature, it was diluted with PhCF<sub>3</sub> and was precipitated in excess methanol. The precipitate was filtered and collected to provide **F-PT-2** as a brown solid (82 mg, 72% yield). NMR could not be taken due to low solubility.



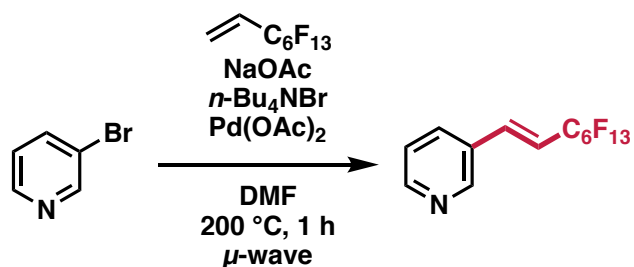
**Synthesis of Compound Ph-H-C6.** A mixture of bromobenzene (313 mg, 1.99 mmol), 1*H*,1*H*,2*H*-perfluoro-1-octene (1.04 g, 2.99 mmol), NaOAc (255 mg, 3.11 mmol), *n*-Bu<sub>4</sub>NBr (553 mg, 1.72 mmol), and Herrmann's catalyst (98 mg, 0.105 mmol) was dissolved in DMF (10 mL), and the reaction mixture was stirred for 1 h at 200 °C in a microwave reactor. Upon cooling the reaction mixture to room temperature, the residue was dissolved in AcOEt (50 mL) and 1M HCl (50 mL). The organic layer was separated, washed with water (50 mL × 3) and brine (50 mL), dried with MgSO<sub>4</sub>, and evaporated to dryness under reduced pressure. The residue was chromatographed on silica gel using hexanes as eluent, and the fraction containing compound **Ph-**

**H-C6** ( $R_f = 0.50$  in hexanes) was collected and evaporated to dryness to provide a colorless oil (490 mg, 1.16 mmol, 58% yield).

$^1\text{H}$  NMR (500 MHz,  $\text{CDCl}_3$ , 20 °C):  $\delta$  (ppm) 7.47-7.50 (m, 2H), 7.39-7.42 (m, 3H), 7.18 (dt,  $J = 16.4, 2.3$  Hz, 1H), 6.17-6.25 (m, 1H).

$^{19}\text{F}$  NMR (471 MHz,  $\text{CDCl}_3$ , 20 °C):  $\delta$  (ppm) -80.66 (t,  $J = 9.8$  Hz, 3F), -110.99 (q,  $J = 12.2$  Hz, 2F), -121.49 (m, 2F), -122.75 (m, 2F), -123.12 (m, 2F), -126.03 (m, 2F).

The characterization is consistent with the previous literature report.<sup>114</sup>



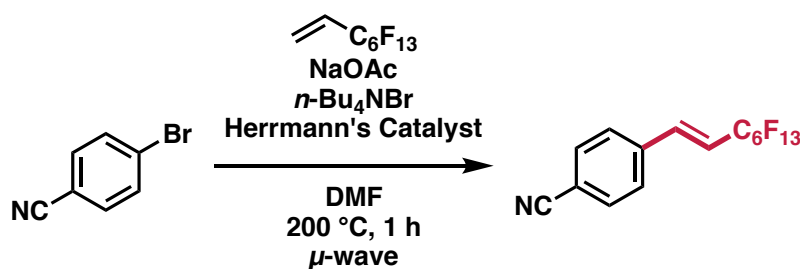
**Synthesis of Compound Py-C6.** A mixture of 3-bromopyridine (316 mg, 2.00 mmol), 1H,1H,2H-perfluoro-1-octene (1.06 g, 3.06 mmol), NaOAc (254 mg, 3.10 mmol), *n*-Bu<sub>4</sub>NBr (548 mg, 1.70 mmol), and Pd(OAc)<sub>2</sub> (23 mg, 0.102 mmol) was dissolved in DMF (10 mL), and the reaction mixture was stirred for 1 h at 200 °C in a microwave reactor. Upon cooling the reaction mixture to room temperature, the residue was dissolved in AcOEt (50 mL) and H<sub>2</sub>O (50 mL). The organic layer was separated, washed with water (50 mL  $\times$  3) and brine (50 mL), dried with MgSO<sub>4</sub>, and evaporated to dryness under reduced pressure. The residue was chromatographed on silica gel using CH<sub>2</sub>Cl<sub>2</sub> as eluent, and the fraction containing compound **Py-C6** ( $R_f = 0.45$  in CH<sub>2</sub>Cl<sub>2</sub>) was collected and evaporated to dryness to provide a colorless oil (260 mg, 0.614 mmol, 31% yield).

$^1\text{H}$  NMR (500 MHz,  $\text{CDCl}_3$ , 20 °C):  $\delta$  (ppm) 8.71 (d,  $J = 2.3$  Hz, 1H), 8.63 (dd,  $J = 4.8, 1.3$  Hz, 1H), 7.81 (dt,  $J = 7.9, 1.8$  Hz, 1H), 7.36 (dd,  $J = 7.8, 4.8$  Hz, 1H), 7.19 (dt,  $J = 16.0, 2.1$  Hz, 1H), 6.25-6.33 (m, 1H).

$^{19}\text{F}$  NMR (471 MHz,  $\text{CDCl}_3$ , 20 °C)  $\delta$  (ppm) -80.69 (t,  $J = 9.8$  Hz, 3F), -111.50 (q,  $J = 13.1$  Hz, 2F), -121.52 (m, 2F), -122.77 (m, 2F), -123.04 (m, 2F), -126.06 (m, 2F).

$^{13}\text{C}$  NMR (126 MHz,  $\text{CDCl}_3$ , 20 °C)  $\delta$  (ppm) 151.27, 149.50, 136.60, 134.07, 129.36, 123.91, 116.77.

DART MS:  $m/z$  calcd. for  $[\text{C}_{13}\text{H}_6\text{F}_{13}\text{N} + \text{H}]^+$ : 424.0371; found: 424.0378.



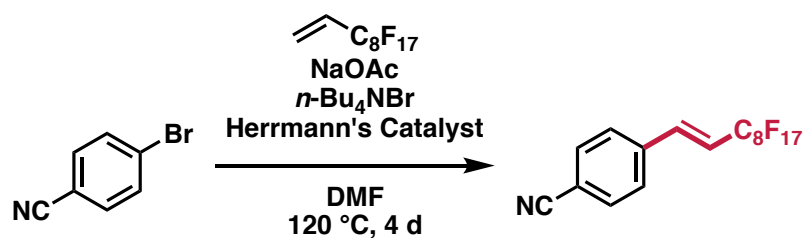
**Synthesis of Compound Ph-CN-C6(p).** A mixture of 4-bromobenzonitrile (362 mg, 1.99 mmol),  $1H,1H,2H$ -perfluoro-1-octene (1.04 g, 3.00 mmol), NaOAc (246 mg, 3.00 mmol),  $n\text{-Bu}_4\text{NBr}$  (540 mg, 1.68 mmol), and Herrmann's catalyst (75 mg, 0.080 mmol) was dissolved in DMF (10 mL), and the reaction mixture was stirred for 1 h at 200 °C in a microwave reactor. Upon cooling the reaction mixture to room temperature, the residue was dissolved in AcOEt (50 mL) and 1M HCl (50 mL). The organic layer was separated, washed with water (50 mL  $\times$  3) and brine (50 mL), dried with  $\text{MgSO}_4$ , and evaporated to dryness under reduced pressure. The residue was chromatographed on silica gel using hexanes with a gradient of 1%  $\rightarrow$  5%  $\text{CH}_2\text{Cl}_2$  as eluent, and the fraction containing compound **Ph-CN-C6(p)** ( $R_f = 0.35$  in hexanes, 33%  $\text{CH}_2\text{Cl}_2$ ) was collected and evaporated to dryness to provide a beige solid (380 mg, 0.850 mmol, 43% yield).

$^1\text{H}$  NMR (500 MHz,  $\text{CDCl}_3$ , 20 °C):  $\delta$  (ppm) 7.71 (d,  $J = 8.4$  Hz, 2H), 7.59 (d,  $J = 8.4$  Hz, 2H), 7.20 (dt,  $J = 16.2, 2.1$  Hz, 1H), 6.28-6.36 (m, 1H).

$^{19}\text{F}$  NMR (471 MHz,  $\text{CDCl}_3$ , 20 °C):  $\delta$  (ppm) -80.66 (t,  $J = 9.1$  Hz, 3F), -111.62 (q,  $J = 12.2$  Hz, 2F), -121.50 (m, 2F), -122.75 (m, 2F), -122.98 (m, 2F), -126.04 (m, 2F).

$^{13}\text{C}$  NMR (126 MHz,  $\text{CDCl}_3$ , 20 °C):  $\delta$  (ppm) 138.06 (t,  $J = 8.7$  Hz), 137.79, 132.91, 128.31, 118.33, 118.21(t,  $J = 23$  Hz), 113.78.

DART MS:  $m/z$  calcd. for  $[\text{C}_{15}\text{H}_6\text{F}_{13}\text{N} + \text{H}]^+$ : 448.0371,  $[\text{C}_{15}\text{H}_6\text{F}_{13}\text{N} + \text{NH}_4]^+$ : 465.0636; found: 448.0384, 465.0636.

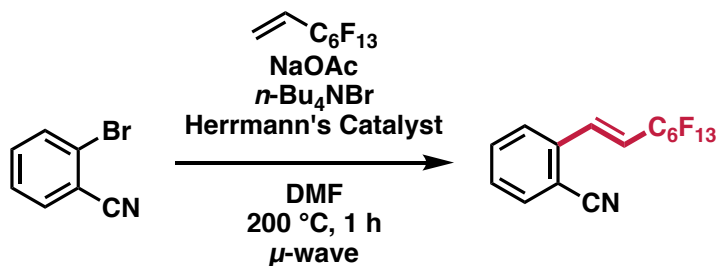


**Synthesis of Compound Ph-CN-C8(p).** A mixture of 4-bromobenzonitrile (364 mg, 2.00 mmol), 1*H*,1*H*,2*H*-perfluoro-1-decene (1.34 g, 3.00 mmol), NaOAc (246 mg, 3.00 mmol), *n*-Bu<sub>4</sub>NBr (548 mg, 1.70 mmol), and Herrmann's catalyst (94 mg, 0.100 mmol) was dissolved in DMF (10 mL), and the reaction mixture was stirred for 4 d at 120 °C. Upon cooling the reaction mixture to room temperature, the residue was dissolved in AcOEt (50 mL) and 1M HCl (50 mL). The organic layer was separated, washed with water (50 mL  $\times$  3) and brine (50 mL), dried with MgSO<sub>4</sub>, and evaporated to dryness under reduced pressure. The residue was chromatographed on silica gel using hexanes, 33% CH<sub>2</sub>Cl<sub>2</sub> as eluent, and the fraction containing compound **Ph-CN-C8(p)** ( $R_f = 0.30$  in hexanes, 33% CH<sub>2</sub>Cl<sub>2</sub>) was collected and evaporated to dryness to provide a white solid (850 mg, 1.55 mmol, 78% yield).

$^1\text{H}$  NMR (500 MHz,  $\text{CDCl}_3$ , 20 °C):  $\delta$  (ppm) 7.70 (d,  $J = 8.0$  Hz, 2H), 7.58 (d,  $J = 8.4$  Hz, 2H), 7.19 (d,  $J = 16.4$  Hz, 1H), 6.28-6.36 (m, 1H).

$^{19}\text{F}$  NMR (471 MHz,  $\text{CDCl}_3$ , 20 °C):  $\delta$  (ppm) -80.79 (t,  $J = 9.1$  Hz, 3F), -111.70 (q,  $J = 12.2$  Hz, 2F), -121.35 (m, 2F), -121.89 (m, 4F), -122.71 (m, 2F), -123.03 (m, 2F), -126.12 (m, 2F).

The characterization is also consistent with the previous report.<sup>113</sup>



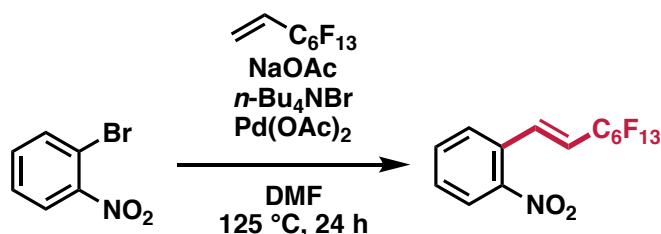
**Synthesis of Compound Ph-CN-C6(o).** A mixture of 2-bromobenzonitrile (364 mg, 2.00 mmol), 1*H*,1*H*,2*H*-perfluoro-1-octene (1.04 g, 3.00 mmol), NaOAc (246 mg, 3.00 mmol), *n*-Bu<sub>4</sub>NBr (548 mg, 1.70 mmol), and Herrmann's catalyst (94 mg, 0.100 mmol) was dissolved in DMF (10 mL), and the reaction mixture was stirred for 1 h at 200 °C in a microwave reactor. Upon cooling the reaction mixture to room temperature, the residue was dissolved in AcOEt (50 mL) and 1M HCl (50 mL). The organic layer was separated, washed with water (50 mL  $\times$  3) and brine (50 mL), dried with MgSO<sub>4</sub>, and evaporated to dryness under reduced pressure. The residue was chromatographed on silica gel using hexanes, 33% CH<sub>2</sub>Cl<sub>2</sub> as eluent, and the fraction containing compound **Ph-CN-C6(o)** ( $R_f = 0.30$  in hexanes, 33% CH<sub>2</sub>Cl<sub>2</sub>) was collected and evaporated to dryness to provide a colorless oil (700 mg, 1.57 mmol, 78% yield).

$^1\text{H}$  NMR (500 MHz,  $\text{CDCl}_3$ , 20 °C):  $\delta$  (ppm) 7.73 (d,  $J = 8.4$  Hz, 1H), 7.71 (d,  $J = 7.6$  Hz, 1H), 7.66 (t,  $J = 7.6$  Hz, 1H), 7.50-7.54 (m, 2H), 6.39-6.47 (m, 1H).

$^{19}\text{F}$  NMR (471 MHz,  $\text{CDCl}_3$ , 20 °C):  $\delta$  (ppm) -80.70 (t,  $J = 11.2$  Hz, 3F), -111.75 (q,  $J = 13.1$  Hz, 2F), -121.48 (m, 2F), -122.76 (m, 2F), -122.92 (m, 2F), -126.07 (m, 2F).

$^{13}\text{C}$  NMR (126 MHz,  $\text{CDCl}_3$ , 20 °C):  $\delta$  (ppm) 136.42, 135.61 (t,  $J = 9.5$  Hz), 133.67, 133.29, 130.41, 127.00, 119.48 (t,  $J = 23$  Hz), 116.97, 112.76.

DART MS:  $m/z$  calcd. for  $[\text{C}_{15}\text{H}_6\text{F}_{13}\text{N} + \text{H}]^+$ : 448.0371,  $[\text{C}_{15}\text{H}_6\text{F}_{13}\text{N} + \text{NH}_4]^+$ : 465.0636; found: 448.0379, 465.0629.



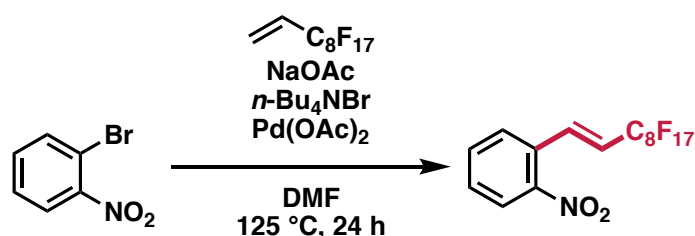
**Synthesis of Compound Ph-NO<sub>2</sub>-C<sub>6</sub>(o).** A mixture of 1-bromo-2-nitrobenzene (2.02 g, 10.0 mmol), 1*H*,1*H*,2*H*-perfluoro-1-octene (5.19 g, 15.0 mmol), NaOAc (1.23 g, 15.0 mmol), *n*-Bu<sub>4</sub>NBr (2.74 g, 8.50 mmol), and Pd(OAc)<sub>2</sub> (112 mg, 0.499 mmol) was dissolved in DMF (10 mL), and the reaction mixture was stirred for 24 h at 125 °C. Upon cooling the reaction mixture to room temperature, the residue was dissolved in AcOEt (50 mL) and 1M HCl (50 mL). The organic layer was separated, washed with water (50 mL × 3) and brine (50 mL), dried with MgSO<sub>4</sub>, and evaporated to dryness under reduced pressure. The residue was chromatographed on silica gel using hexanes with a gradient of 1% → 5% CH<sub>2</sub>Cl<sub>2</sub> as eluent, and the fraction containing compound **Ph-NO<sub>2</sub>-C<sub>6</sub>(o)** ( $R_f = 0.55$  in hexanes, 33% CH<sub>2</sub>Cl<sub>2</sub>) was collected and evaporated to dryness to provide a colorless oil (1.70 g, 3.64 mmol, 36% yield).

$^1\text{H}$  NMR (500 MHz,  $\text{CDCl}_3$ , 20 °C):  $\delta$  (ppm) 8.11-8.13 (m, 1H), 7.68-7.76 (m, 2H), 7.56-7.62 (m, 2H), 6.10-6.18 (m, 1H).

$^{19}\text{F}$  NMR (471 MHz,  $\text{CDCl}_3$ , 20 °C):  $\delta$  (ppm) -80.74 (t,  $J = 9.8$  Hz, 3F), -111.74 (q,  $J = 12.2$  Hz, 2F), -121.52 (m, 2F), -122.79 (m, 2F), -123.15 (m, 2F), -126.10 (m, 2F).

$^{13}\text{C}$  NMR (126 MHz,  $\text{CDCl}_3$ , 20 °C):  $\delta$  (ppm) 147.98, 136.93, 136.85, 136.77, 134.05, 130.66, 130.21, 129.52, 125.26, 119.59, 119.41, 119.22, 77.42, 77.16, 76.91.

DART MS:  $m/z$  calcd. for  $[\text{C}_{14}\text{H}_6\text{F}_{13}\text{NO}_2 + \text{H}]^+$ : 468.0264,  $[\text{C}_{14}\text{H}_6\text{F}_{13}\text{NO}_2 + \text{NH}_4]^+$ : 485.0529; found: 468.0287, 485.0548.

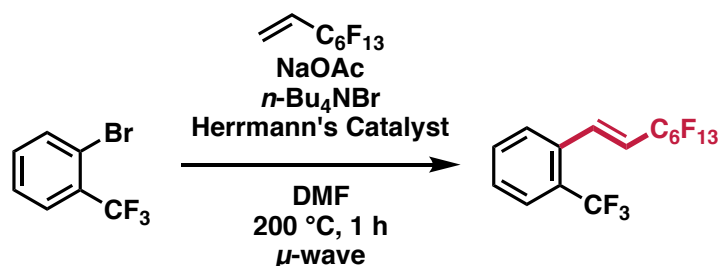


**Synthesis of Compound Ph-NO<sub>2</sub>-C8(o).** A mixture of 1-bromo-2-nitrobenzene (2.02 g, 10.0 mmol), 1*H*,1*H*,2*H*-perfluoro-1-octene (5.19 g, 15.0 mmol), NaOAc (1.23 g, 15.0 mmol), *n*-Bu<sub>4</sub>NBr (2.74 g, 8.50 mmol), and Pd(OAc)<sub>2</sub> (112 mg, 0.499 mmol) was dissolved in DMF (10 mL), and the reaction mixture was stirred for 24 h at 125 °C. Upon cooling the reaction mixture to room temperature, the residue was dissolved in AcOEt (50 mL) and 1M HCl (50 mL). The organic layer was separated, washed with water (50 mL × 3) and brine (50 mL), dried with MgSO<sub>4</sub>, and evaporated to dryness under reduced pressure. The residue was chromatographed on silica gel using hexanes with a gradient of 1% → 5% CH<sub>2</sub>Cl<sub>2</sub> as eluent, and the fraction containing compound **Ph-NO<sub>2</sub>-C8(o)** ( $R_f = 0.55$  in hexanes, 33% CH<sub>2</sub>Cl<sub>2</sub>) was collected and evaporated to dryness to provide a white solid (3.92 g, 6.95 mmol, 69% yield).

$^1\text{H}$  NMR (500 MHz,  $\text{CDCl}_3$ , 20 °C):  $\delta$  (ppm) 8.13 (d,  $J = 8.4$  Hz, 1H), 7.74 (d,  $J = 16.0$  Hz, 1H), 7.70 (t,  $J = 7.4$  Hz, 1H), 7.57-7.60 (m, 2H), 6.10-6.18 (m, 1H).

$^{19}\text{F}$  NMR (471 MHz,  $\text{CDCl}_3$ , 20 °C):  $\delta$  (ppm) -80.62 (t,  $J = 9.8$  Hz, 3F), -111.65 (q,  $J = 12.2$  Hz, 2F), -121.23 (m, 2F), -121.77 (m, 4F), -122.59 (m, 2F), -123.02 (m, 2F), -125.98 (m, 2F).

The characterization is also consistent with the previous report.<sup>113</sup>



**Synthesis of Compound Ph-CF<sub>3</sub>-C6(o).** A mixture of 2-bromobenzotrifluoride (450 mg, 2.00 mmol),  $1H,1H,2H$ -perfluoro-1-octene (1.01 g, 2.92 mmol), NaOAc (250 mg, 3.05 mmol),  $n\text{-Bu}_4\text{NBr}$  (540 mg, 1.68 mmol), and Herrmann's catalyst (94 mg, 0.100 mmol) was dissolved in DMF (10 mL), and the reaction mixture was stirred for 1 h at 200 °C in a microwave reactor. Upon cooling the reaction mixture to room temperature, the residue was dissolved in AcOEt (50 mL) and 1M HCl (50 mL). The organic layer was separated, washed with water (50 mL  $\times$  3) and brine (50 mL), dried with  $\text{MgSO}_4$ , and evaporated to dryness under reduced pressure. The residue was chromatographed on silica gel using hexanes as eluent, and the fraction containing compound **Ph-CF<sub>3</sub>-C6(o)** ( $R_f = 0.50$  in hexanes) was collected and evaporated to dryness to provide a colorless oil (574 mg, 1.17 mmol, 59% yield).

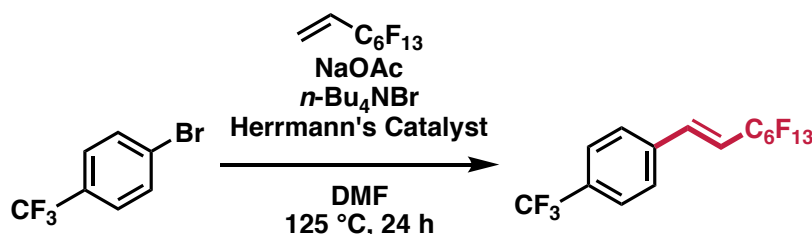
$^1\text{H}$  NMR (500 MHz,  $\text{CDCl}_3$ , 20 °C):  $\delta$  (ppm) 7.72 (d,  $J = 7.6$  Hz, 1H), 7.57-7.64 (m, 3H), 7.51 (t,  $J = 7.4$  Hz, 1H), 6.13-6.21 (m, 1H).

$^{19}\text{F}$  NMR (471 MHz,  $\text{CDCl}_3$ , 20 °C):  $\delta$  (ppm) -59.43 (s, 3F), -80.87 (t,  $J = 9.8$  Hz, 3F), -111.83 (q,  $J = 12.2$  Hz, 2F), -121.63 (m, 2F), -122.89 (m, 2F), -123.37 (m, 2F), -126.20 (m, 2F).



$^{13}\text{C}$  NMR (126 MHz,  $\text{CDCl}_3$ , 20 °C):  $\delta$  (ppm) 136.52 (t,  $J = 10$  Hz), 132.86, 132.41, 129.81, 128.90 (q,  $J = 32$  Hz), 128.15, 126.34 (q,  $J = 5.7$  Hz), 123.99 (q,  $J = 274$  Hz), 119.12 (t,  $J = 23$  Hz).

DART MS:  $m/z$  calcd. for  $[\text{C}_{15}\text{H}_6\text{F}_{16}]^+$ : 490.0214; found: 490.0234.



**Synthesis of Compound Ph- $\text{CF}_3$ - $\text{C}_6(p)$ .** A mixture of 4-bromobenzotrifluoride (450 mg, 2.00 mmol), 1*H*,1*H*,2*H*-perfluoro-1-octene (1.04 g, 3.00 mmol), NaOAc (246 mg, 3.00 mmol), *n*- $\text{Bu}_4\text{NBr}$  (540 mg, 1.68 mmol), and Herrmann's catalyst (94 mg, 0.100 mmol) was dissolved in DMF (10 mL), and the reaction mixture was stirred for 24 h at 125 °C. Upon cooling the reaction mixture to room temperature, the residue was dissolved in AcOEt (50 mL) and 1M HCl (50 mL). The organic layer was separated, washed with water (50 mL  $\times$  3) and brine (50 mL), dried with  $\text{MgSO}_4$ , and evaporated to dryness under reduced pressure. The residue was chromatographed on silica gel using hexanes as eluent, and the fraction containing compound **Ph- $\text{CF}_3$ - $\text{C}_6(p)$**  ( $R_f = 0.50$  in hexanes) was collected and evaporated to dryness to provide a colorless oil (930 mg, 1.90 mmol, 95% yield).

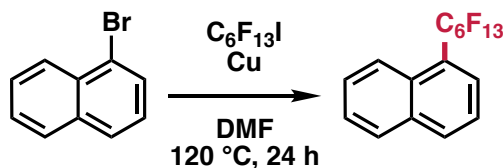
$^1\text{H}$  NMR (500 MHz,  $\text{CDCl}_3$ , 20 °C):  $\delta$  (ppm) 7.67 (d,  $J = 8.4$  Hz, 2H), 7.59 (d,  $J = 8.0$  Hz, 2H), 7.22 (dt,  $J = 16.2, 2.1$  Hz, 1H), 6.26-6.34 (m, 1H).

$^{19}\text{F}$  NMR (471 MHz,  $\text{CDCl}_3$ , 20 °C):  $\delta$  (ppm) -62.92 (s, 3F), -80.80 (t,  $J = 11.2$  Hz, 3F), -111.58 (q,  $J = 12.2$  Hz, 2F), -121.57 (m, 2F), -122.83 (m, 2F), -123.12 (m, 2F), -126.14 (m, 2F).

$^{13}\text{C}$  NMR (126 MHz,  $\text{CDCl}_3$ , 20 °C):  $\delta$  (ppm) 138.48 (t,  $J = 10$  Hz), 137.00, 132.12 (q,  $J = 33$  Hz), 128.05, 126.14 (q,  $J = 2.9$  Hz), 123.92 (q,  $J = 272$  Hz), 117.19 (t,  $J = 25$  Hz).

DART MS:  $m/z$  calcd. for  $[C_{15}H_6F_{16}]^+$ : 490.0214; found: 490.0237.

The characterization is also consistent with the previous literature report.<sup>114</sup>



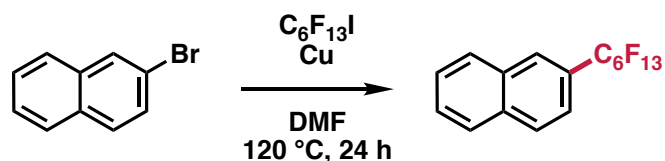
**Synthesis of Compound 1-Naph-C6.** A mixture of 1-bromonaphthalene (1.24 g, 6.00 mmol), perfluorohexyl iodide (3.48 g, 7.80 mmol), and copper (powder,  $<75\text{ }\mu m$ , 1.00 g, 15.6 mmol) was dissolved in  $DMF$  (10 mL), and the reaction mixture was stirred for 24 h at  $120\text{ }^\circ C$ . Upon cooling the reaction mixture to room temperature, the residue was dissolved in  $AcOEt$  (50 mL) and 1M  $HCl$  (50 mL). The organic layer was separated, washed with water ( $50\text{ mL} \times 3$ ) and brine (50 mL), dried with  $MgSO_4$ , and evaporated to dryness under reduced pressure. The residue was chromatographed on silica gel using hexanes as eluent, and the fraction containing compound **1-Naph-C6** ( $R_f = 0.55$  in hexanes) was collected and evaporated to dryness to provide a colorless oil (1.12 g, 2.51 mmol, 42% yield).

$^1H$  NMR (500 MHz,  $CDCl_3$ ,  $20\text{ }^\circ C$ ):  $\delta$  (ppm) 8.24 (d,  $J = 8.4\text{ Hz}$ , 1H), 8.06 (d,  $J = 8.0\text{ Hz}$ , 1H), 7.93 (d,  $J = 7.6\text{ Hz}$ , 1H), 7.84 (d,  $J = 7.2\text{ Hz}$ , 1H), 7.55-7.65 (m, 3H).

$^{19}F$  NMR (471 MHz,  $CDCl_3$ ,  $20\text{ }^\circ C$ ):  $\delta$  (ppm) -80.69 (t,  $J = 9.8\text{ Hz}$ , 3F), -104.37 (t,  $J = 16.8\text{ Hz}$ , 2F), -120.14 (m, 2F), -121.42 (m, 2F), -122.62 (m, 2F), -126.02 (m, 2F).

$^{13}C$  NMR (126 MHz,  $CDCl_3$ ,  $20\text{ }^\circ C$ ):  $\delta$  (ppm) 134.24, 133.59, 130.43, 129.16, 128.18 (t,  $J = 10\text{ Hz}$ ), 127.80, 126.53, 124.98, 124.73 (t,  $J = 22\text{ Hz}$ ), 124.40.

DART MS:  $m/z$  calcd. for  $[C_{16}H_7F_{13}]^+$ : 446.0340; found: 446.0339.



**Synthesis of Compound 2-Naph-C6.** A mixture of 2-bromonaphthalene (1.24 g, 6.00 mmol), perfluorohexyl iodide (3.48 g, 7.80 mmol), and copper (powder, <75  $\mu\text{m}$ , 1.00 g, 15.6 mmol) was dissolved in DMF (10 mL), and the reaction mixture was stirred for 24 h at 120  $^\circ\text{C}$ . Upon cooling the reaction mixture to room temperature, the residue was dissolved in AcOEt (50 mL) and 1M HCl (50 mL). The organic layer was separated, washed with water (50 mL  $\times$  3) and brine (50 mL), dried with  $\text{MgSO}_4$ , and evaporated to dryness under reduced pressure. The residue was chromatographed on silica gel using hexanes as eluent, and the fraction containing compound **1-Naph-C6** ( $R_f = 0.55$  in hexanes) was collected and evaporated to dryness to provide a white solid (600 mg, 1.34 mmol, 22% yield).

$^1\text{H}$  NMR (500 MHz,  $\text{CDCl}_3$ , 20  $^\circ\text{C}$ ):  $\delta$  (ppm) 8.13 (s, 1H), 7.97 (d,  $J = 5.0$  Hz, 1H), 7.95 (d,  $J = 4.2$  Hz, 1H), 7.92 (d,  $J = 8.0$  Hz, 1H), 7.60-7.64 (m, 3H).

$^{19}\text{F}$  NMR (471 MHz,  $\text{CDCl}_3$ , 20  $^\circ\text{C}$ ):  $\delta$  (ppm) -80.65 (t,  $J = 9.8$  Hz, 3F), -110.05 (t,  $J = 14.0$  Hz, 2F), -121.33 (m, 2F), -121.50 (m, 2F), -122.69 (m, 2F), -126.01 (m, 2F).

$^{13}\text{C}$  NMR (126 MHz,  $\text{CDCl}_3$ , 20  $^\circ\text{C}$ ):  $\delta$  (ppm) 134.81, 132.41, 129.05, 128.85, 128.42, 127.98, 127.98 (t,  $J = 8.6$  Hz), 127.32, 126.35 (t,  $J = 24$  Hz), 122.74.

DART MS:  $m/z$  calcd. for  $[\text{C}_{16}\text{H}_7\text{F}_{13}]^+$ : 446.0340; found: 446.0342.

## 5.6 Appendix for CHAPTER 5

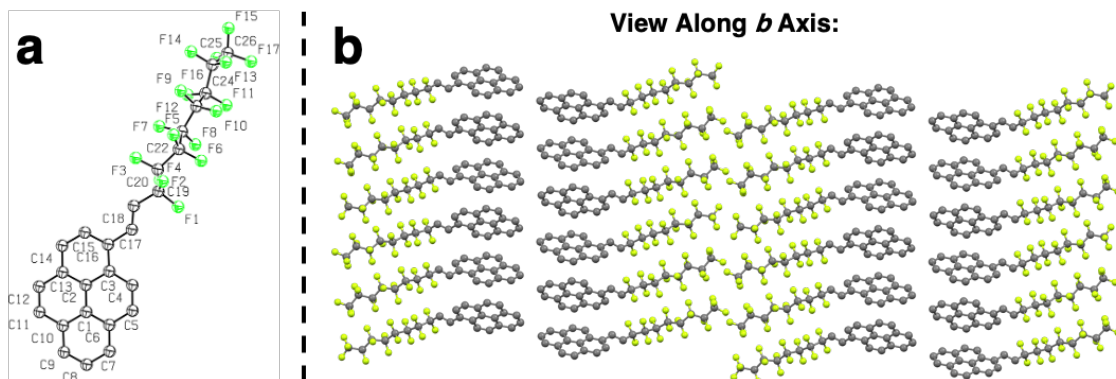


**Figure 5.9** Single crystal X-ray structure and packing of compound **4**. (a) ORTEP diagram of compound **4**, shown at 50% ellipticity. (b) View along the *b* axis of the crystal packing. Hydrogen atoms are omitted for clarity.

**Table 5.1** Crystal data and structure refinement for compound **4**.

Empirical formula	C <sub>26</sub> H <sub>11</sub> F <sub>17</sub>
Formula weight	646.35
Temperature	100(2) K
Wavelength	1.54178 Å
Crystal system	monoclinic
Space group	C 2/c
Lattice parameters	
<i>a</i>	83.568(8) Å
<i>b</i>	5.6972(7) Å
<i>c</i>	30.011(4) Å
$\alpha$	90°
$\beta$	92.937(6)°
$\gamma$	90°
Volume	14269(3)
<i>Z</i>	24
$2\theta_{\max}$	74.40°
Number of reflections	12650
Independent reflections	12650
Number of parameters	1164
$R_{\text{int}}$	0.1671
Completeness to $\theta$	0.937
$R_1 [I > 2\sigma(I)]$	0.1299
$wR_2$ (all data)	0.3151
Largest diff. peak	0.936 e.Å <sup>3</sup>
Largest diff. hole	-0.488 e.Å <sup>3</sup>
Goodness-of-fit	1.316

**Table 5.2** Photophysical summary of compounds **11**, **12**, **3T-C<sub>12</sub>**, and **3T** in toluene solution.

Entry	$\lambda_{\text{abs}}$ (nm)	$\epsilon$ (M <sup>-1</sup> cm <sup>-1</sup> ) <sup>a</sup>	$\lambda_{\text{em}}$ (nm) <sup>b</sup>	$\Phi_{\text{F}}$ <sup>c</sup>
<b>11</b>	358	16416	460	0.0654
<b>12</b>	343	10991	478	0.0063
<b>3T-C<sub>12</sub></b>	337	16876	432	0.0651
<b>3T</b>	355	21059	430	0.0784

<sup>a</sup>Molar extinction coefficient at  $\lambda_{\text{abs}}$ . <sup>b</sup>Excited at 330 nm. <sup>c</sup> $\Phi_{\text{F}}$  were measured using 9,10-diphenylanthracene as a standard, excited at 350 nm ( $\Phi_{\text{F}} = 0.90$  in cyclohexane).

**Table 5.3** Property summary of **F-PT(x/1-x)**.

Entry	Yield	$M_n$ (kDa) <sup>a</sup>	PDI <sup>a</sup>	$\lambda_{\text{abs, sol}}$ (nm) <sup>b</sup>	$\lambda_{\text{em, sol}}$ (nm) <sup>b,c</sup>	$\lambda_{\text{abs, film}}$ (nm) <sup>d</sup>	$E_{\text{HOMO}}$ (eV) <sup>e</sup>	$E_{\text{LUMO}}$ (eV)	$E_g$ (eV) <sup>f</sup>
<b>F-PT-1 (25/75)</b>	>99%	13.4	1.46	435	577	510	-5.30	-3.40	1.90
<b>F-PT-1 (50/50)</b>	41%	11.9	1.49	437	576	504	-5.30	-3.45	1.85

<sup>a</sup>Determined by gel permeation chromatography by using polystyrene as standard. <sup>b</sup>Spectra taken in chloroform. <sup>c</sup>Excited at 400 nm. <sup>d</sup>Films were prepared by dropcasting chloroform solutions onto a glass slide. <sup>e</sup>Calculated from the onset of the oxidation potential. <sup>f</sup>Calculated from the onset of film absorption.

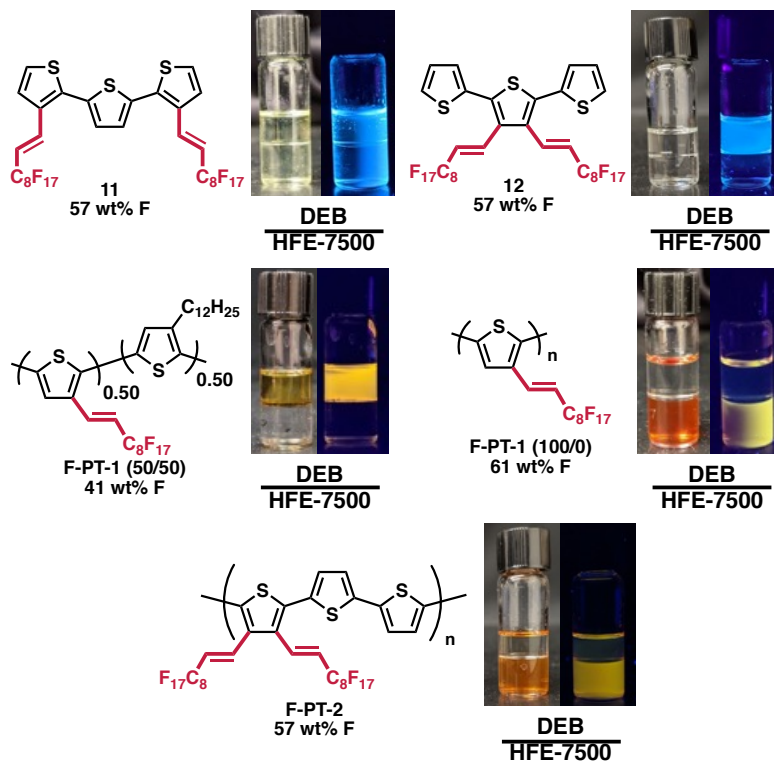


**Figure 5.10** Fluorous Partition of compounds. Solvents diethylbenzene (DEB) and 2-(trifluoromethyl)-3-ethoxydodecafluorohexane (HFE-7500) were chosen as a result of their low interfacial tension and low upper critical mixing temperature.

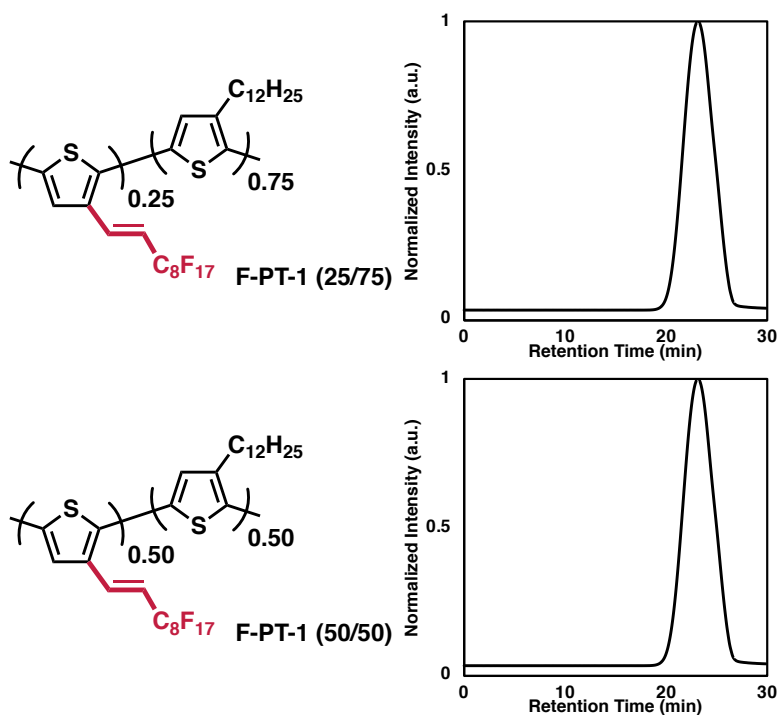


**Figure 5.11** Gel Permeation Chromatogram of F-PT-1(25/75) and F-PT-1(50/50).

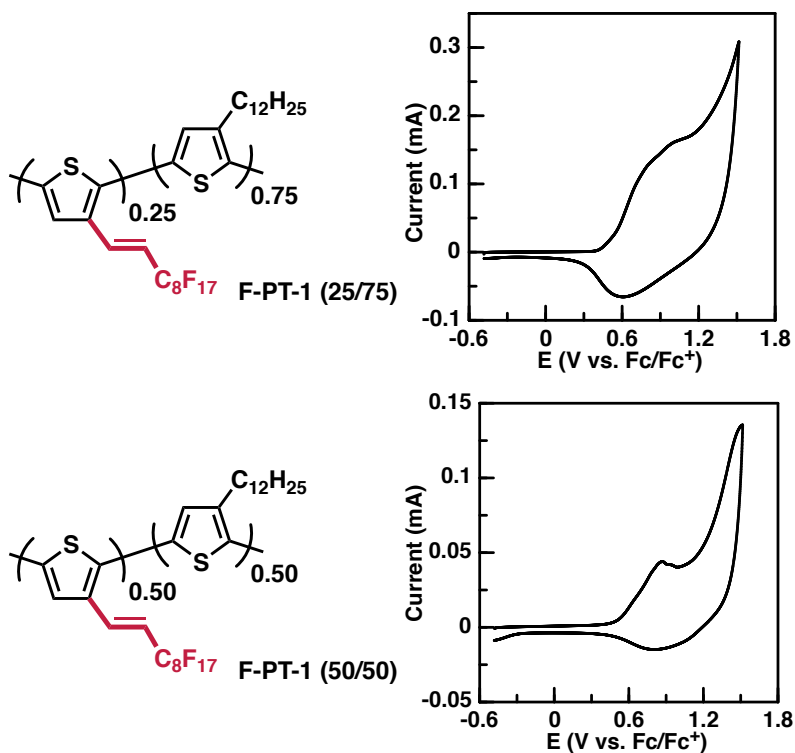


Figure 5.12 Cyclic voltammetry of F-PT-1(25/75) and F-PT-1(50/50).

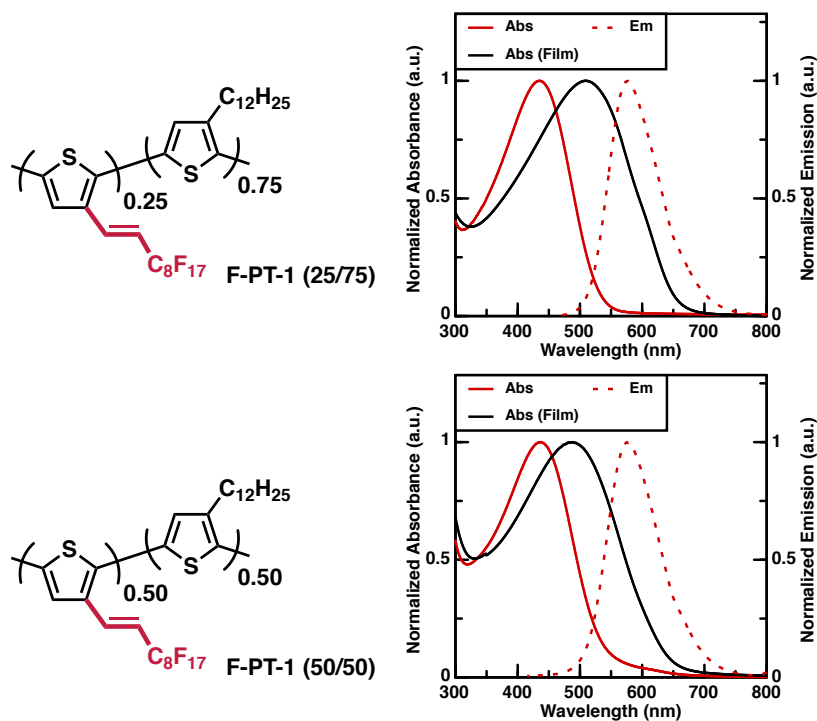


Figure 5.13 UV/vis absorption and fluorescence spectra of F-PT-1(25/75) and F-PT-1(50/50) in chloroform solution and in film. Films were prepared by dropcasting a chloroform solution of the polymers onto a glass slide.

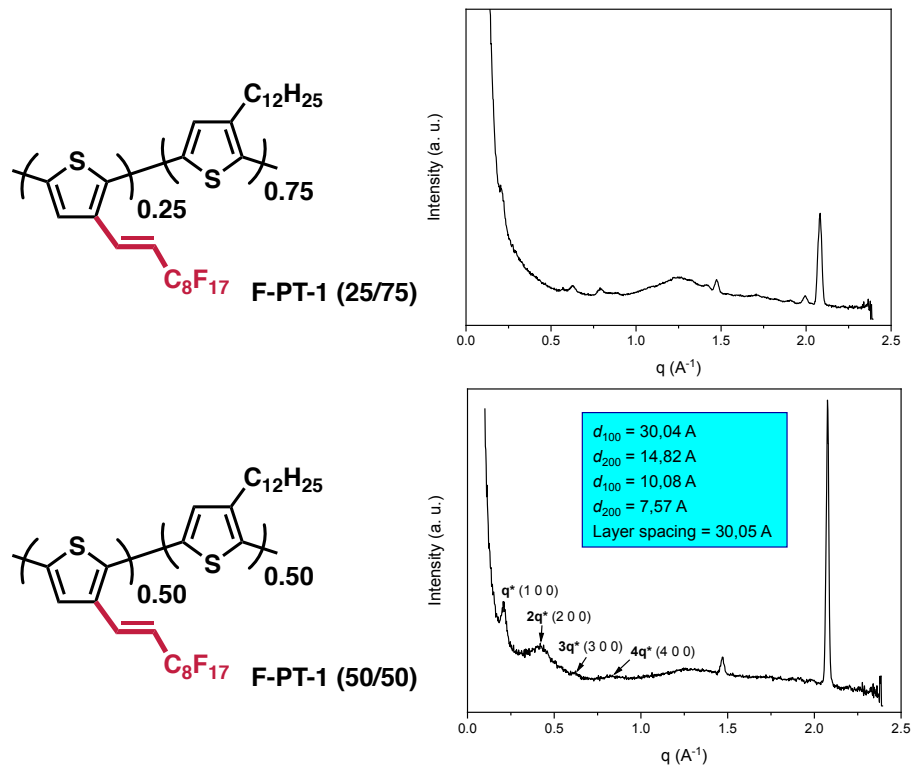


Figure 5.14 Wide angle X-ray scattering of F-PT-1(25/75) and F-PT-1(50/50).

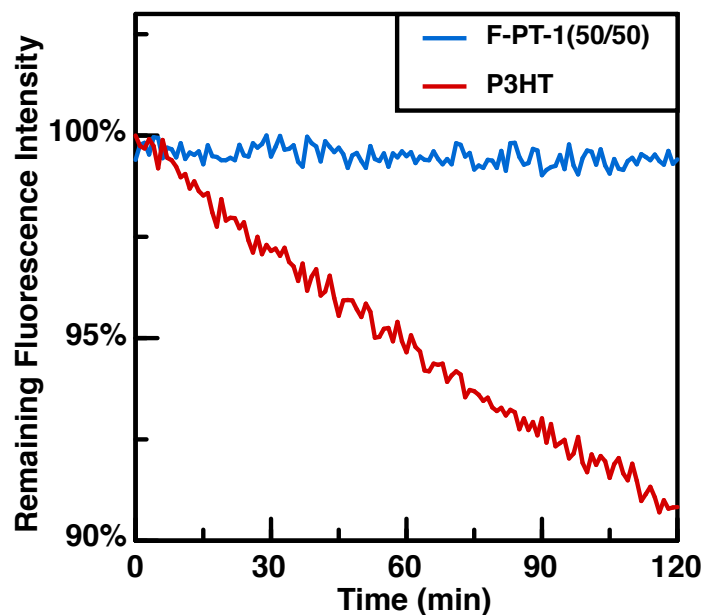
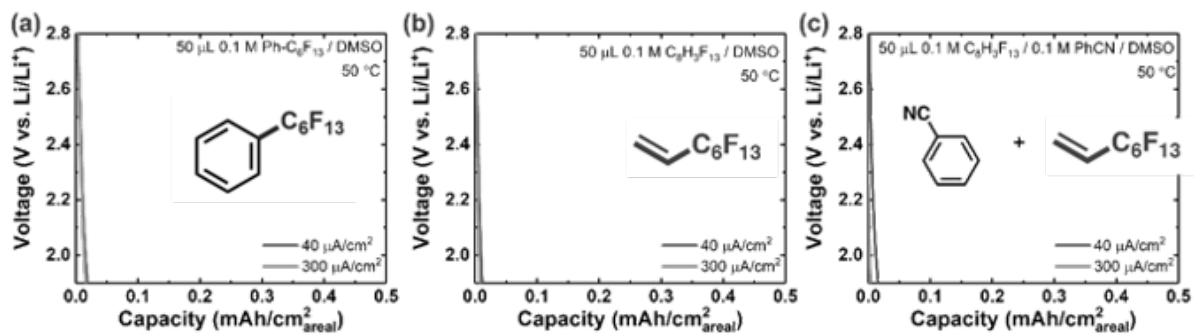
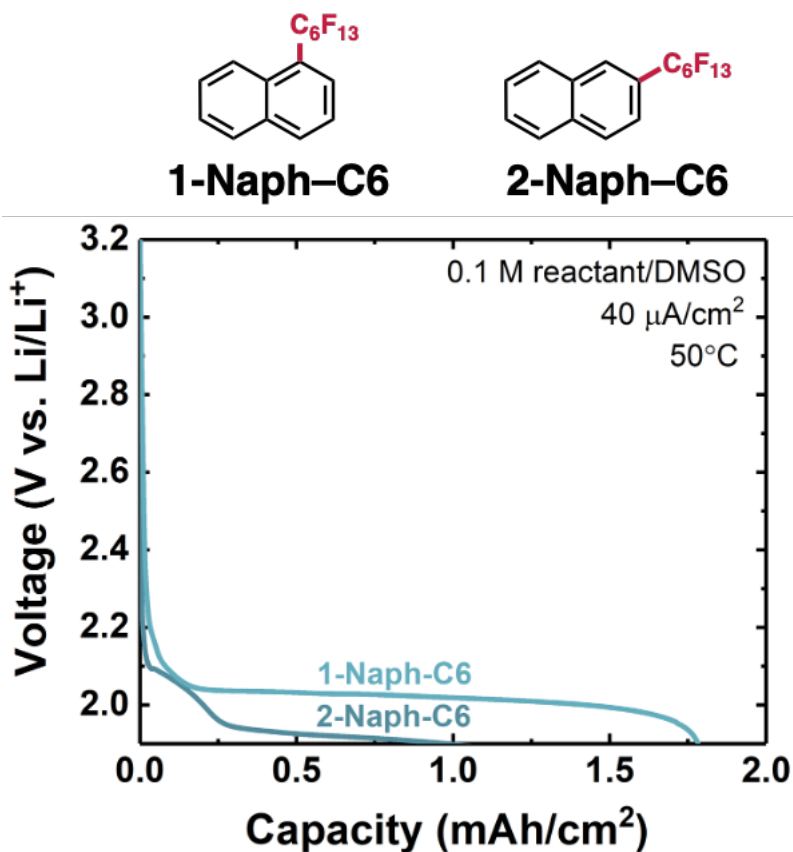


Figure 5.15 Study of photostability of fluororous thiophenes by using fluorescence spectra. Samples were continuously irradiated in the fluorimeter for 120 minutes and the intensity was recorded every 1 minute. Excitation slit width: 14 nm; Emission slit width: 1 nm.





**Figure 5.16** Galvanostatic discharge of control compounds. (a) Galvanostatic discharge profile of (perfluorohexyl)benzene. (b) Galvanostatic discharge profile of 1H,1H,2H-perfluoro-1-octene. (c) Galvanostatic discharge profile of a mixture of benzonitrile and 1H,1H,2H-perfluoro-1-octene. All discharges were performed at 50 °C.



**Figure 5.17** Galvanostatic discharge profile of 1-Naph-C6 and 2-Naph-C6 performed at 50 °C.



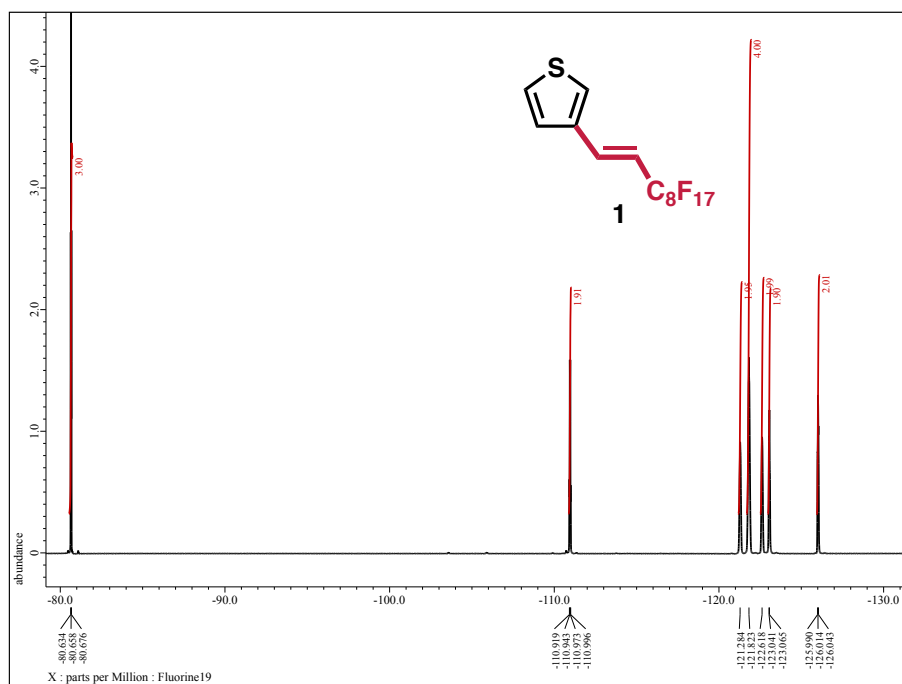


Figure 5.20 Compound 1 <sup>19</sup>F NMR (471 MHz, CDCl<sub>3</sub>)

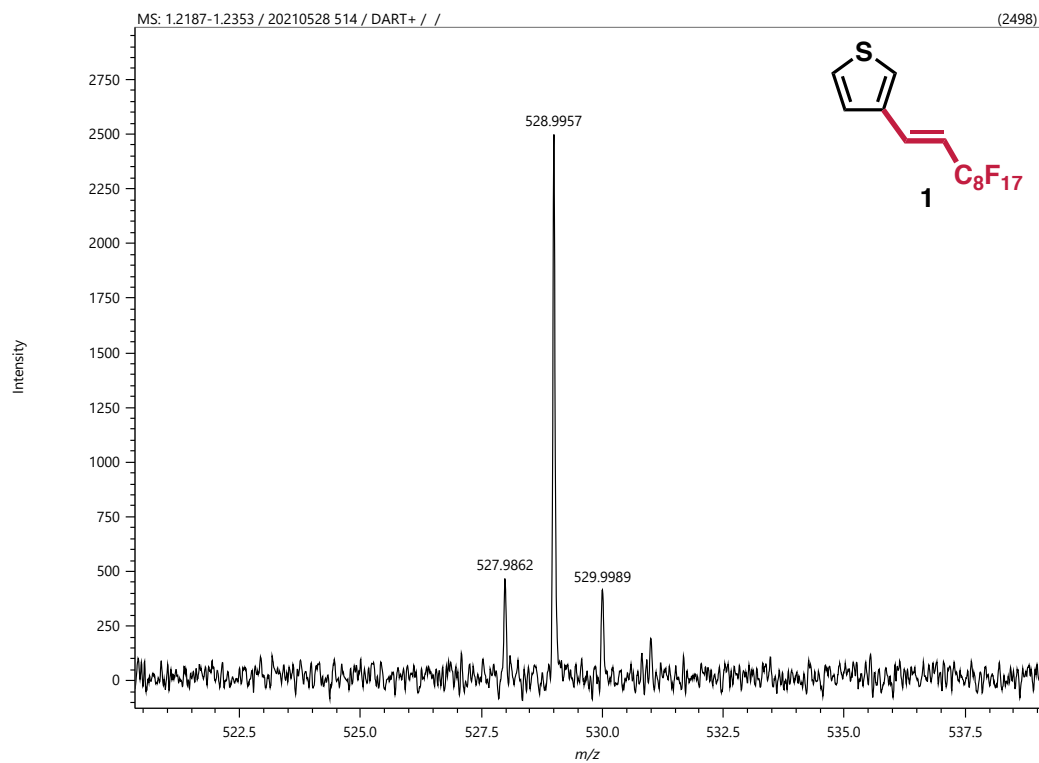


Figure 5.21 Compound 1 DART MS

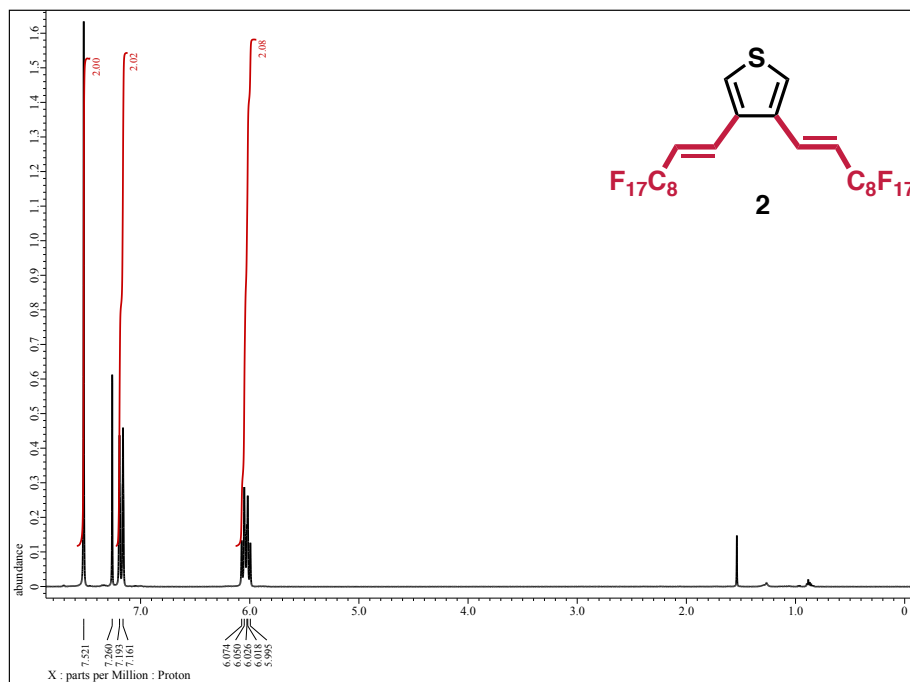


Figure 5.22 Compound 2  $^1\text{H}$  NMR (500 MHz,  $\text{CDCl}_3$ )

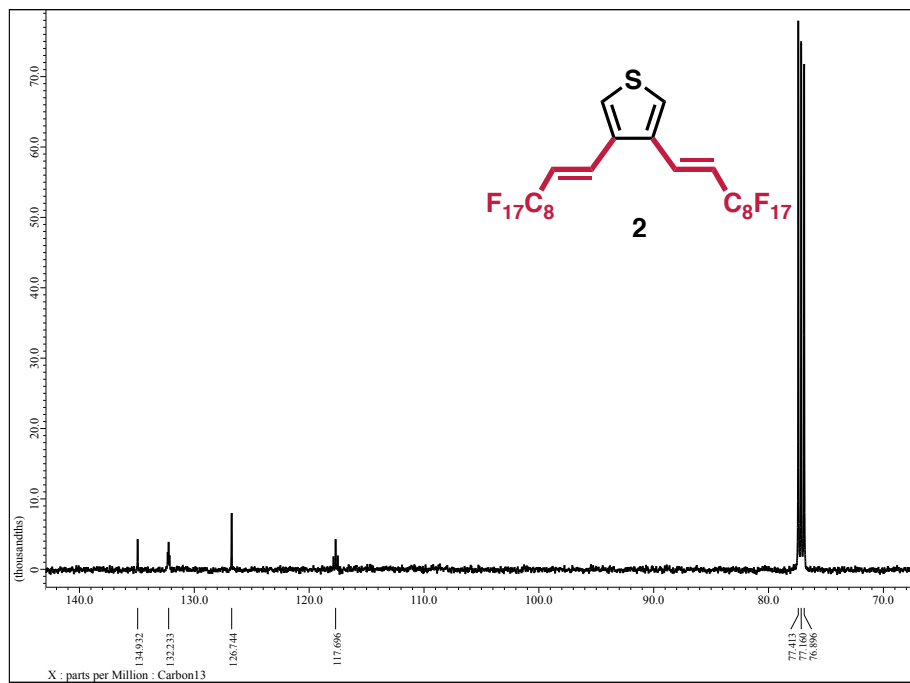


Figure 5.23 Compound 2  $^{19}\text{F}$  NMR (471 MHz,  $\text{CDCl}_3$ )

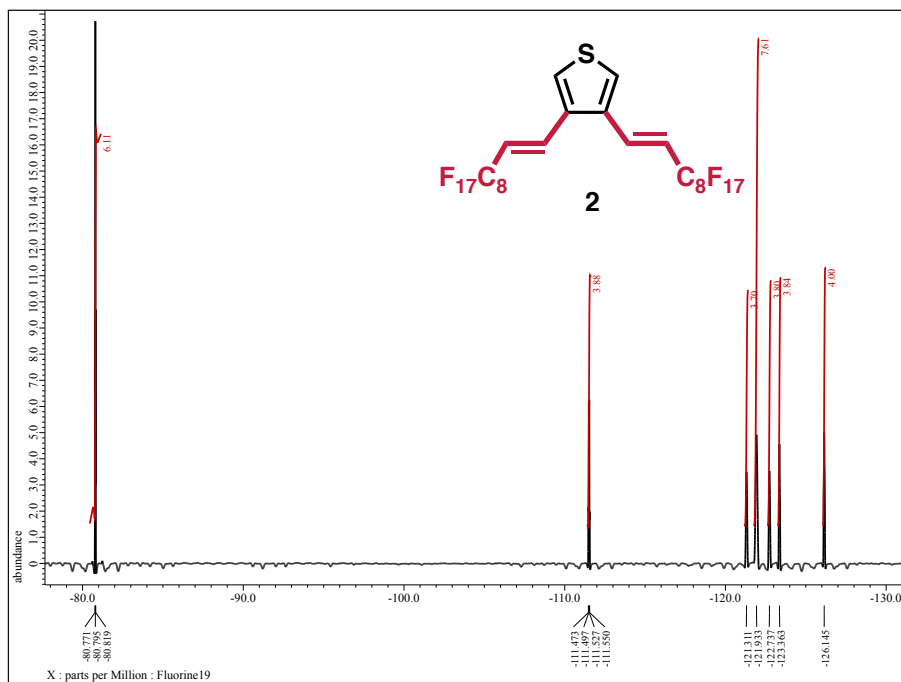


Figure 5.24 Compound 2 <sup>13</sup>C NMR (126 MHz, CDCl<sub>3</sub>)

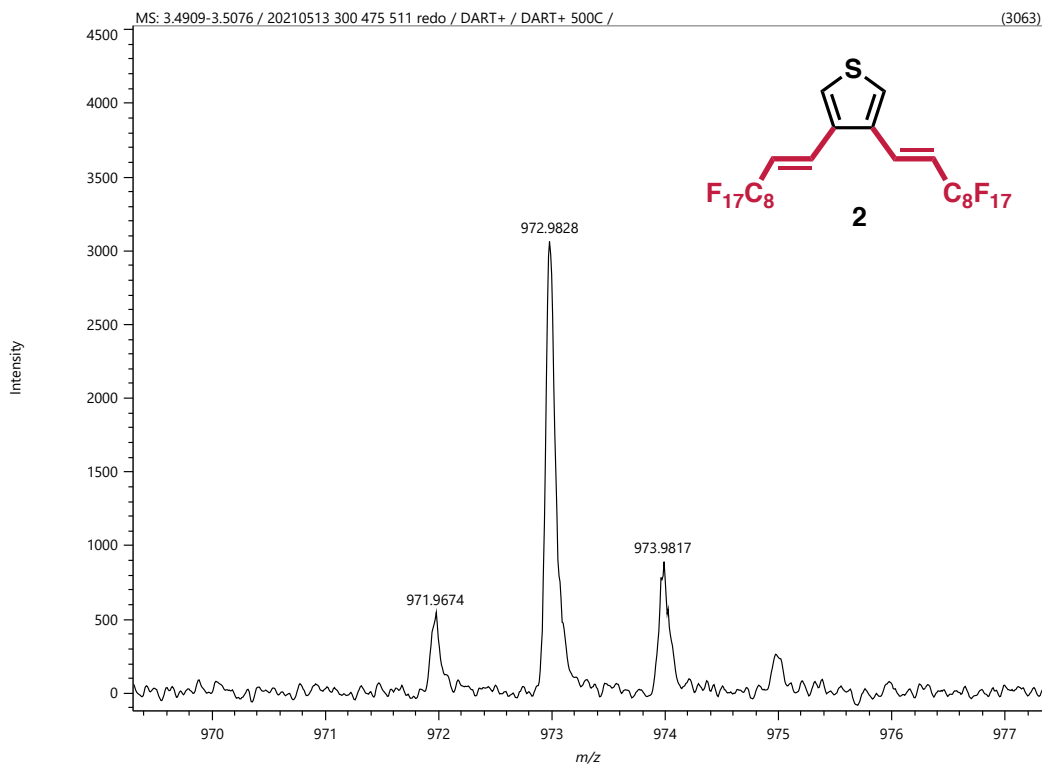


Figure 5.25 Compound 2 DART MS

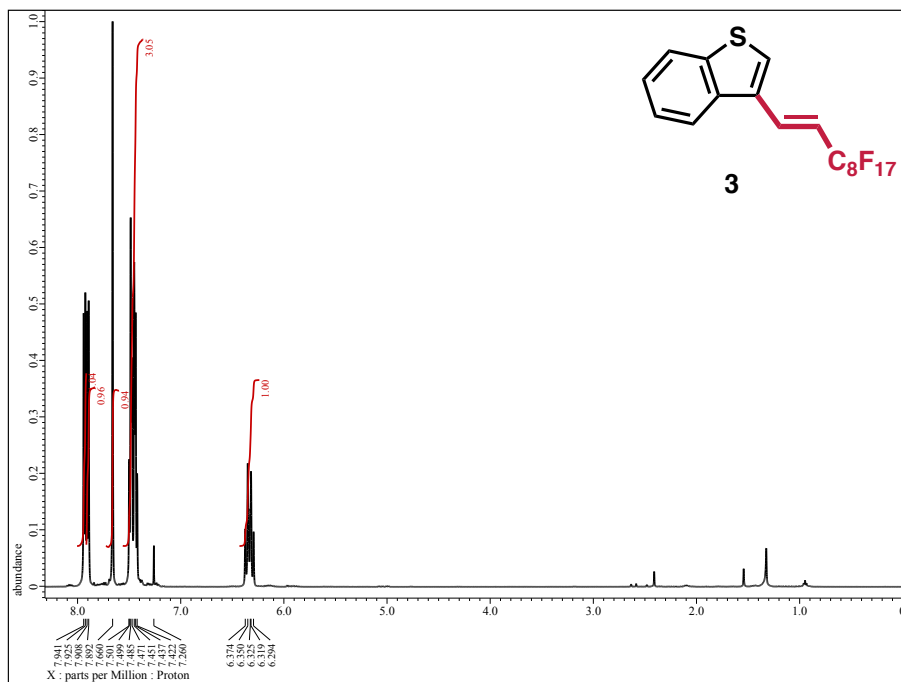


Figure 5.26 Compound 3  $^1\text{H}$  NMR (500 MHz,  $\text{CDCl}_3$ )

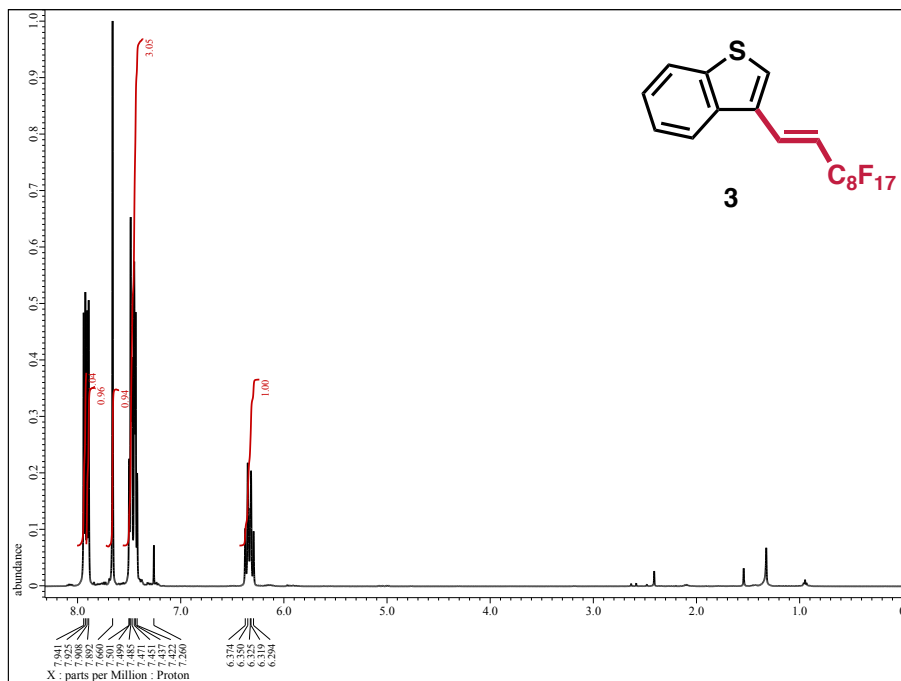


Figure 5.27 Compound 3  $^{13}\text{C}$  NMR (126 MHz,  $\text{CDCl}_3$ )

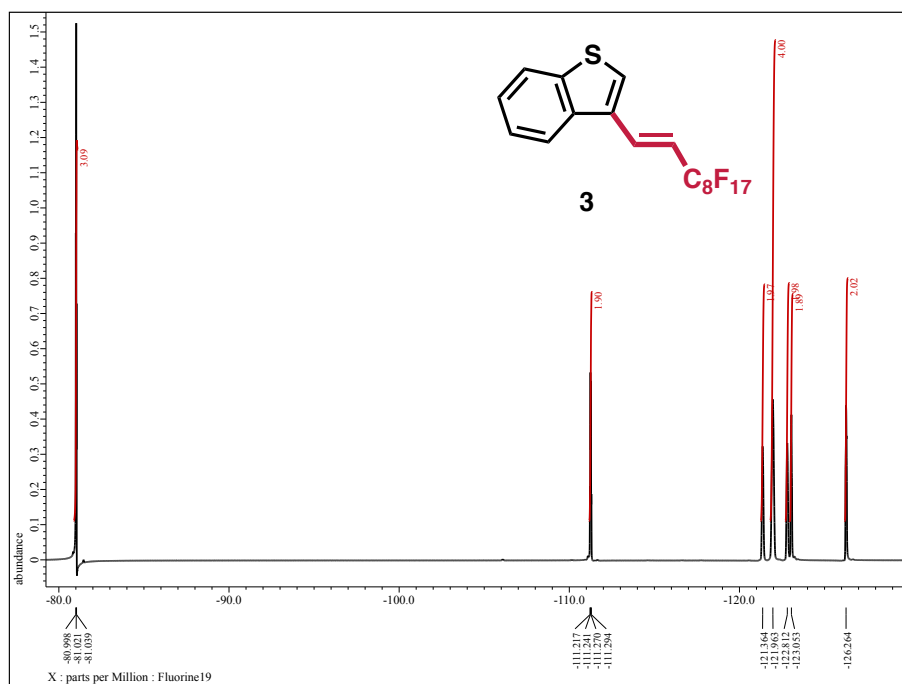


Figure 5.28 Compound **3**  $^{19}\text{F}$  NMR (471 MHz,  $\text{CDCl}_3$ )

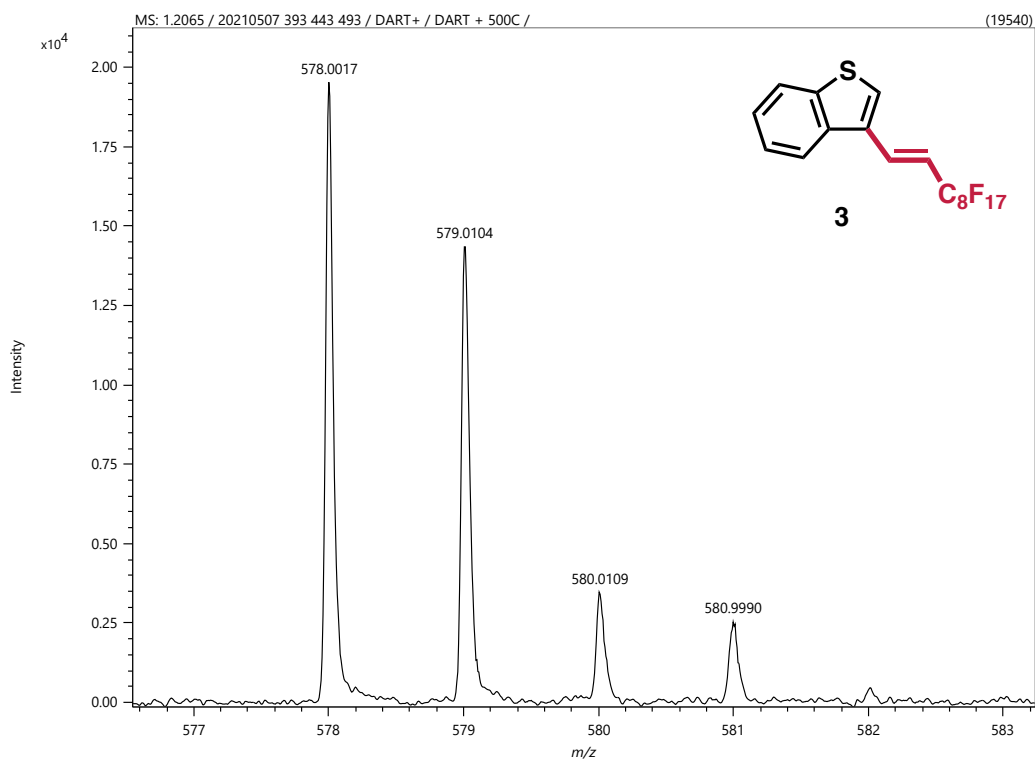


Figure 5.29 Compound **3** DART MS

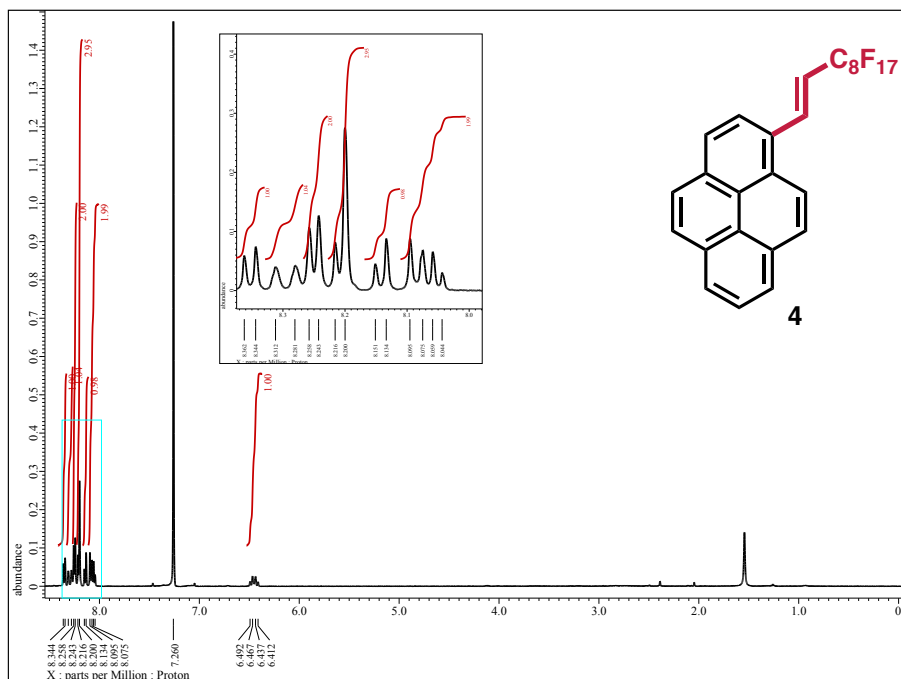


Figure 5.30 Compound 4  $^1\text{H}$  NMR (500 MHz,  $\text{CDCl}_3$ )

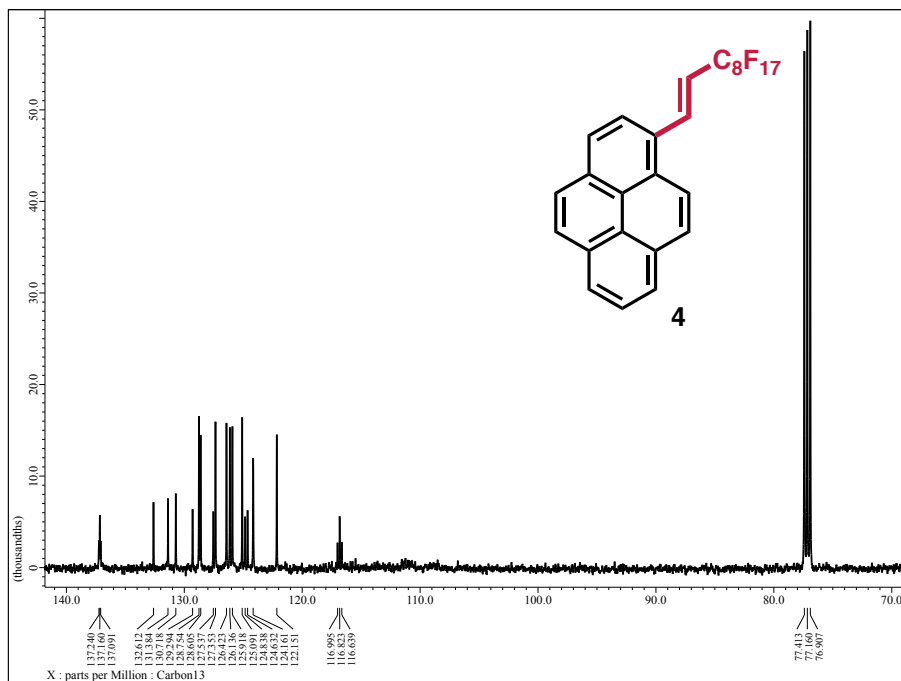


Figure 5.31 Compound 4  $^{13}\text{C}$  NMR (126 MHz,  $\text{CDCl}_3$ )



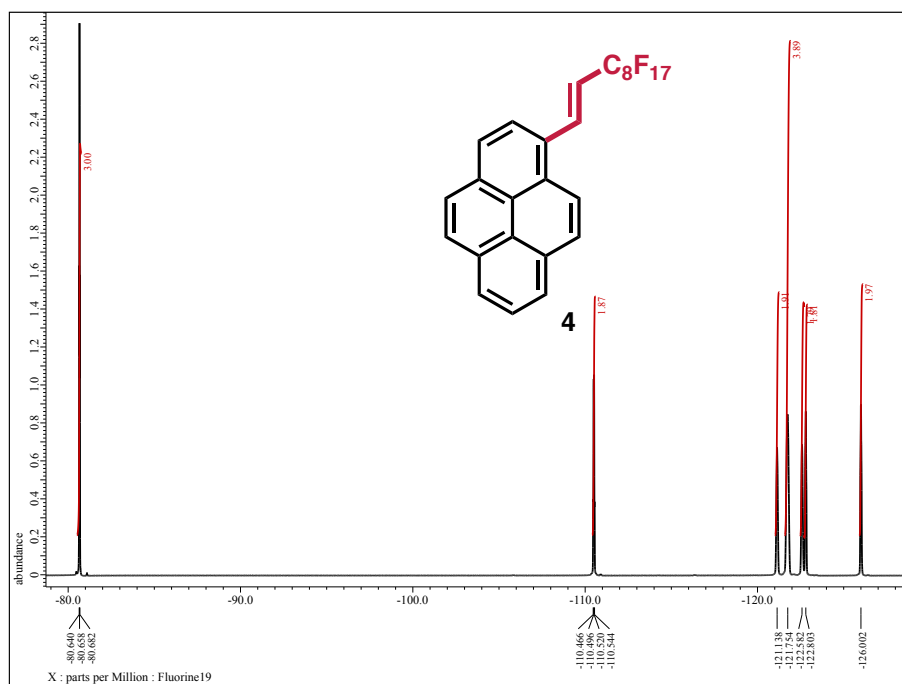


Figure 5.32 Compound **4**  $^{19}\text{F}$  NMR (471 MHz,  $\text{CDCl}_3$ )

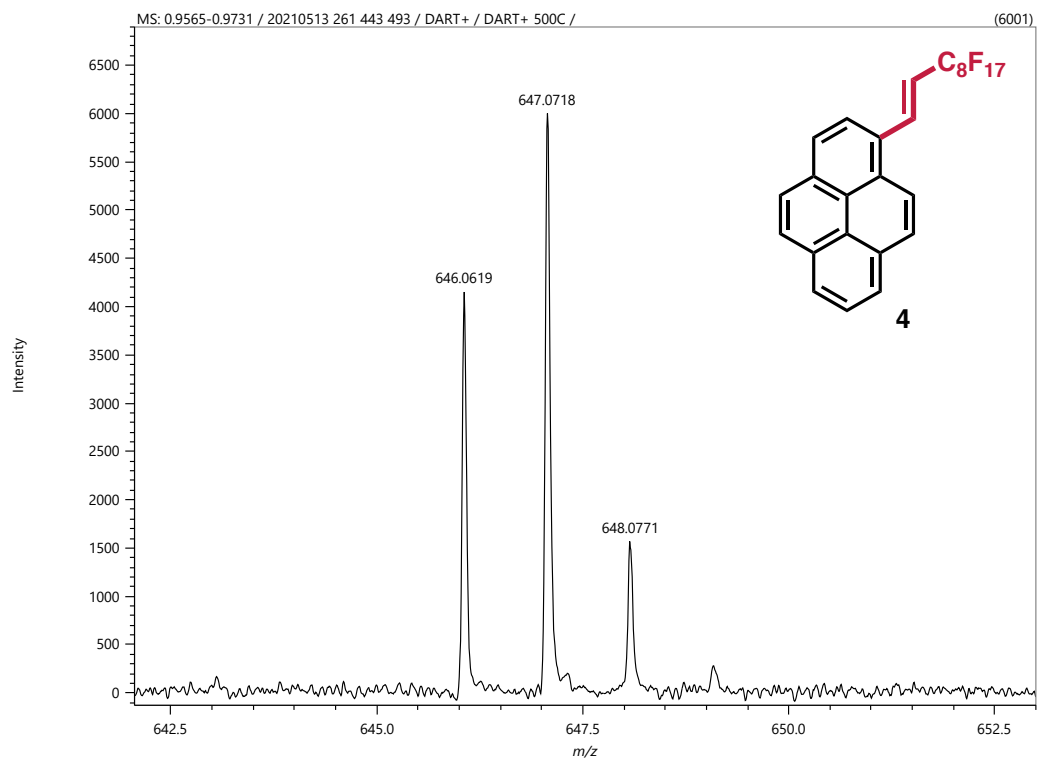


Figure 5.33 Compound **4** DART MS

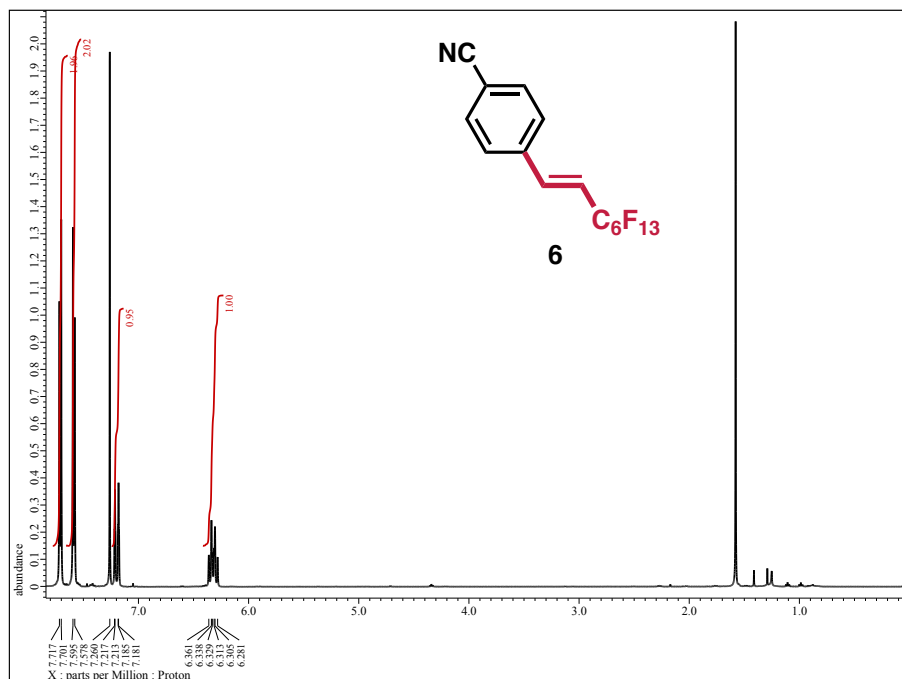


Figure 5.34 Compound 6 <sup>1</sup>H NMR (500 MHz, CDCl<sub>3</sub>)

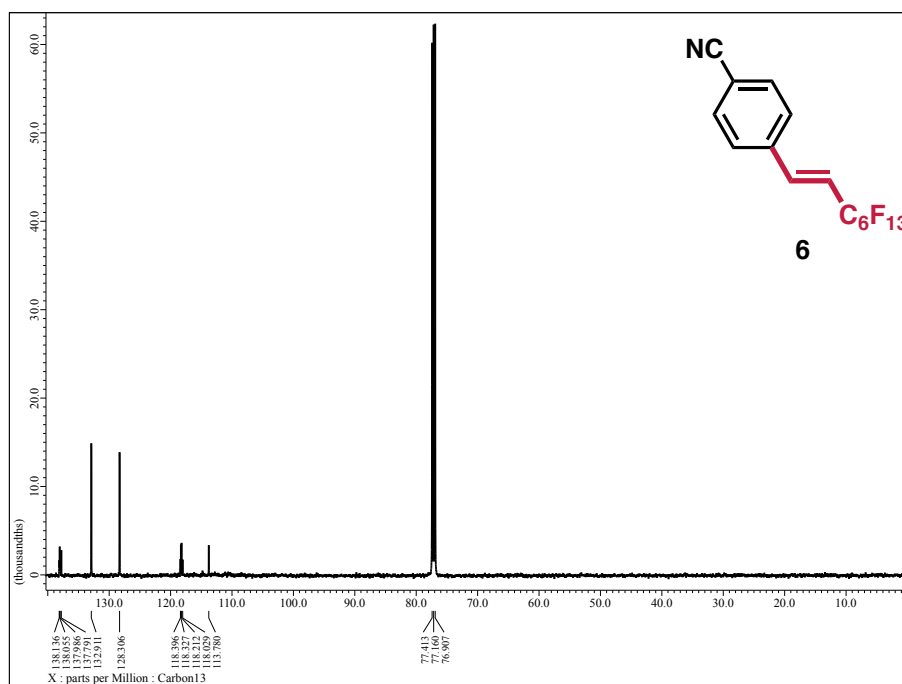


Figure 5.35 Compound 6 <sup>13</sup>C NMR (126 MHz, CDCl<sub>3</sub>)

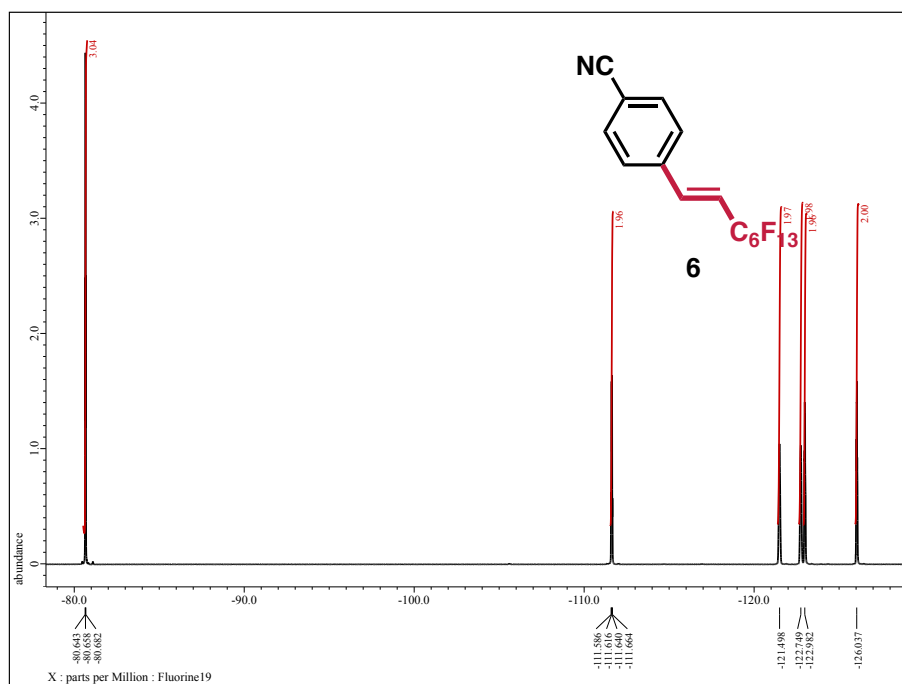


Figure 5.36 Compound **6**  $^{19}\text{F}$  NMR (471 MHz,  $\text{CDCl}_3$ )

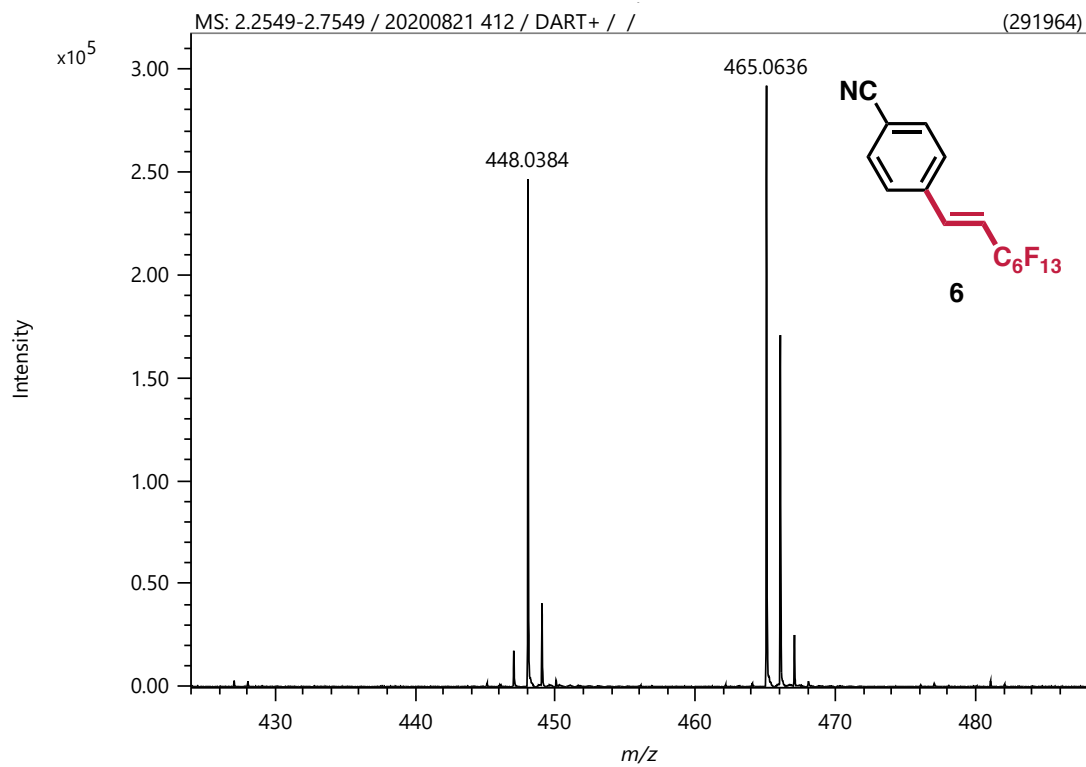


Figure 5.37 Compound **6** DART MS

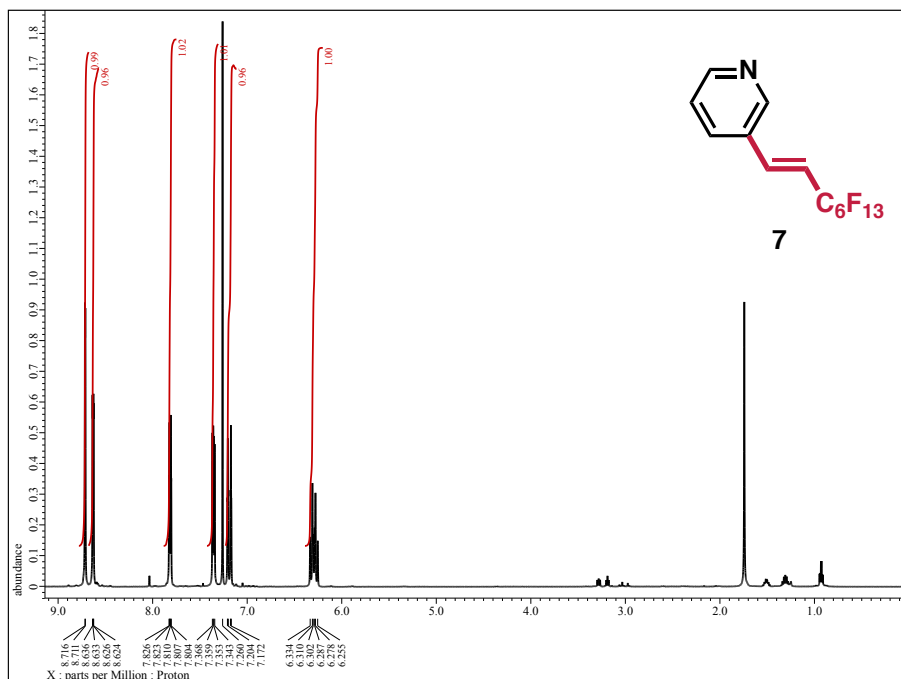


Figure 5.38 Compound 7  $^1\text{H}$  NMR (500 MHz,  $\text{CDCl}_3$ )

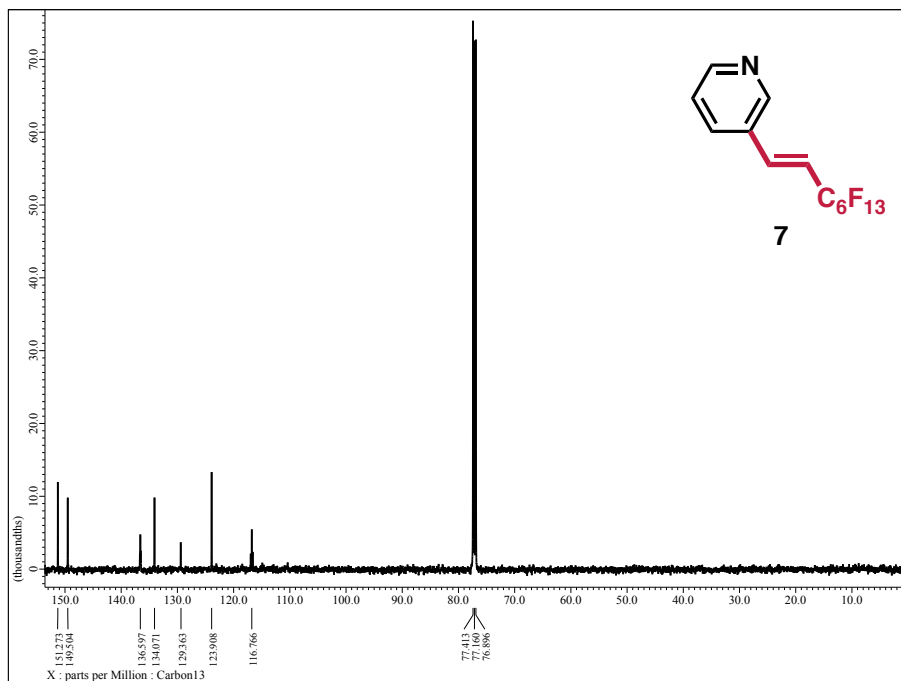


Figure 5.39 Compound 7  $^{13}\text{C}$  NMR (126 MHz,  $\text{CDCl}_3$ )



Figure 5.40 Compound 7  $^{19}\text{F}$  NMR (471 MHz,  $\text{CDCl}_3$ )

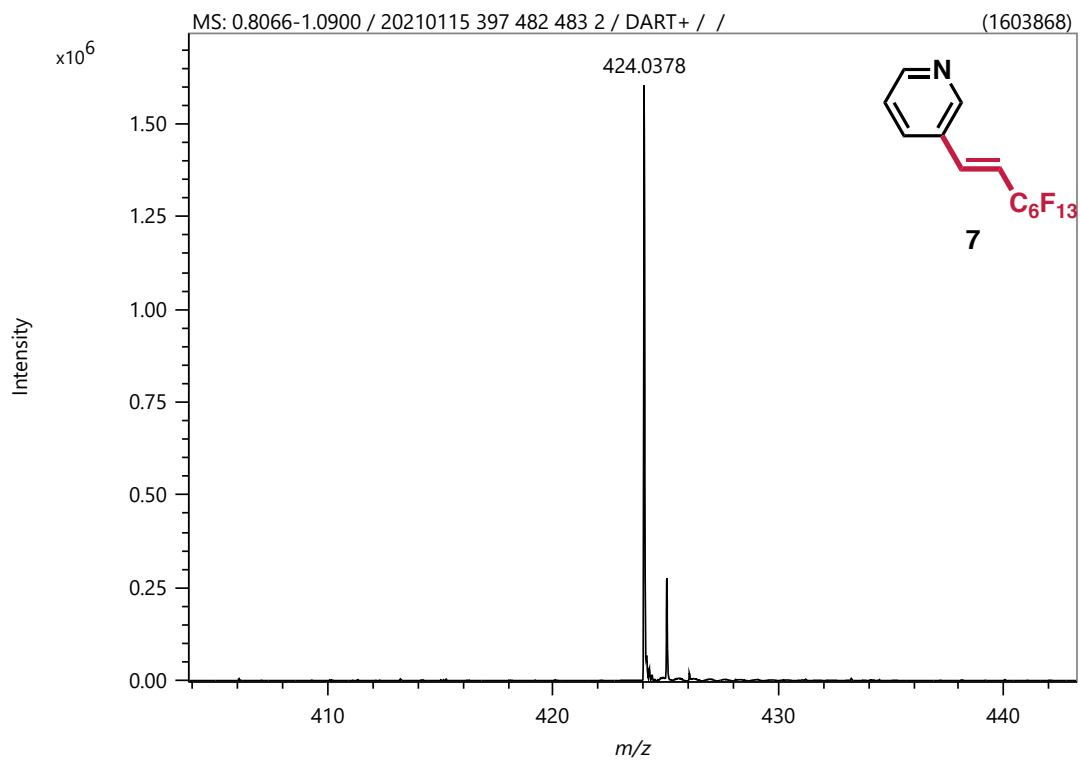


Figure 5.41 Compound 7 DART MS

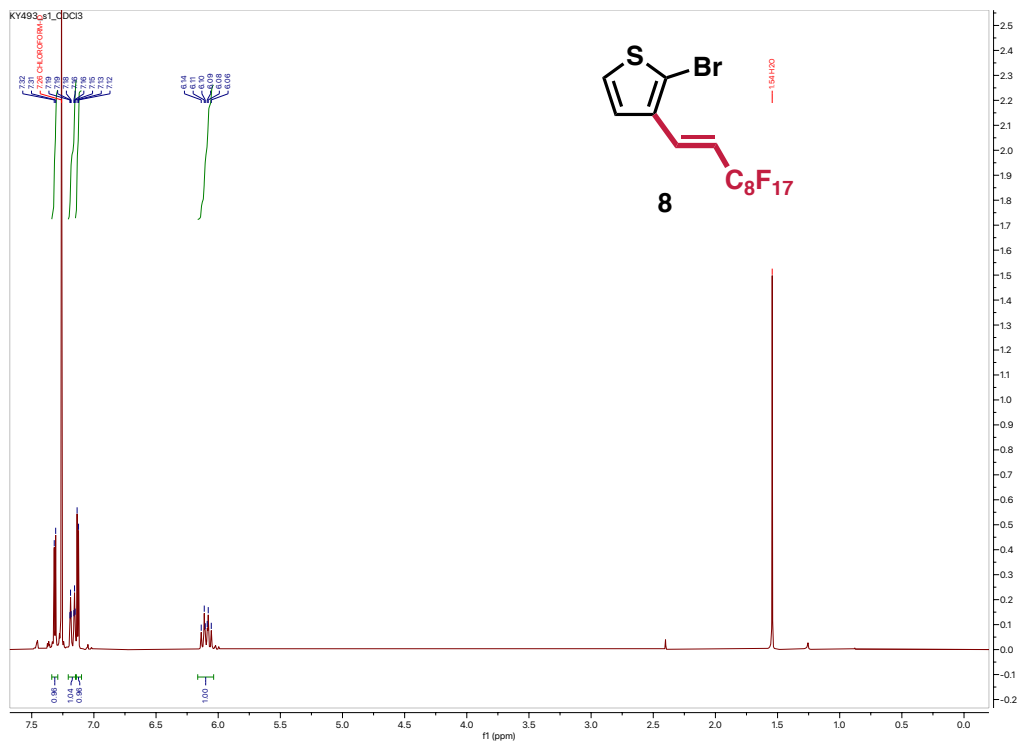


Figure 5.42 Compound 8  $^1\text{H}$  NMR (500 MHz,  $\text{CDCl}_3$ )

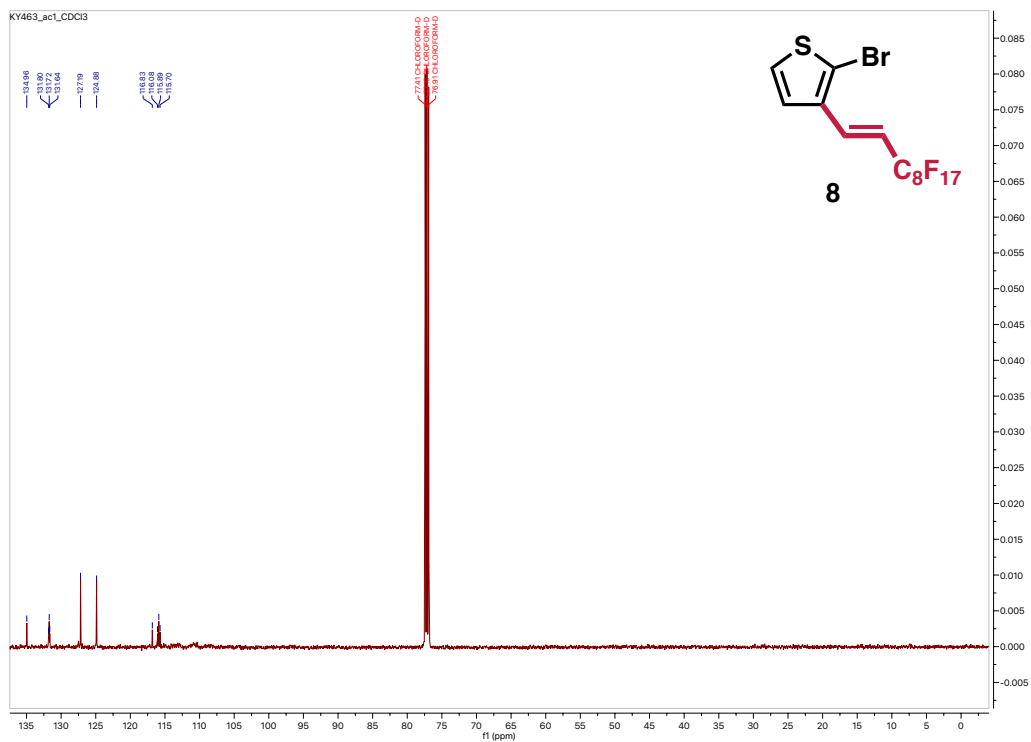


Figure 5.43 Compound 8  $^{13}\text{C}$  NMR (126 MHz,  $\text{CDCl}_3$ )

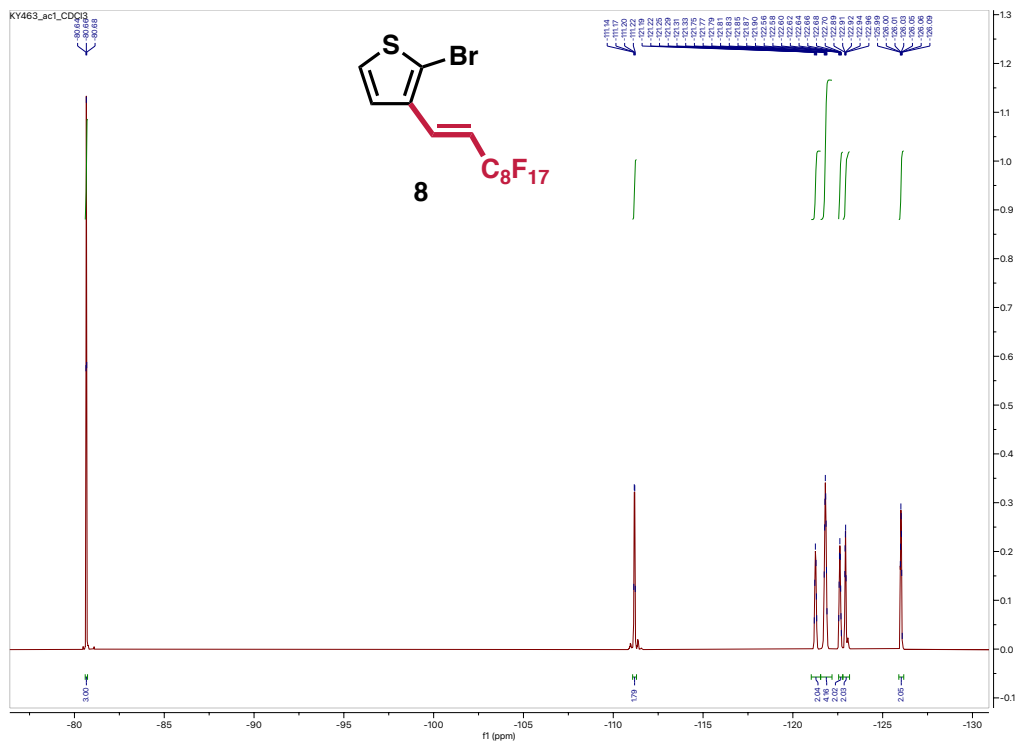


Figure 5.44 Compound 8 <sup>19</sup>F NMR (471 MHz, CDCl<sub>3</sub>)

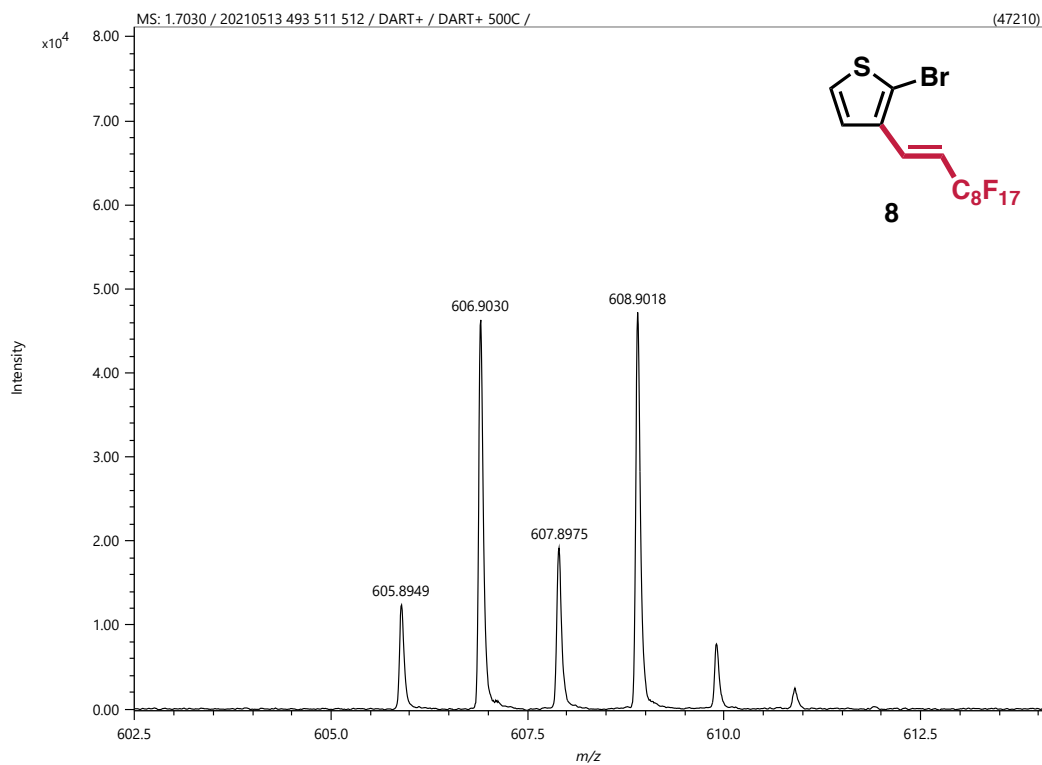


Figure 5.45 Compound 8 DART MS

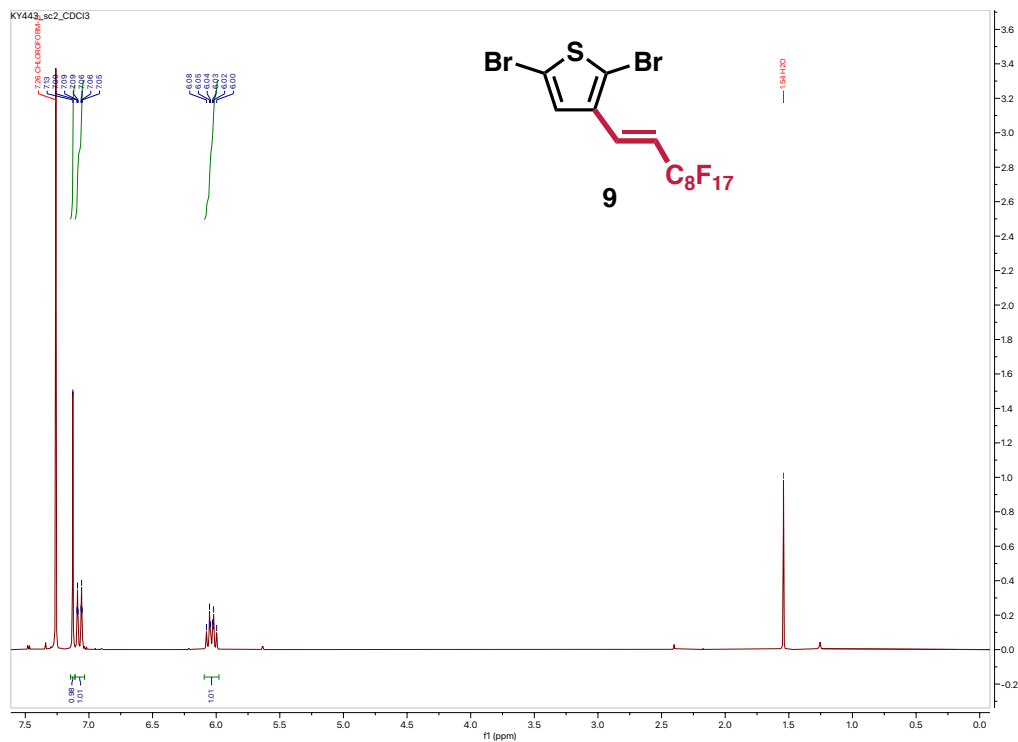


Figure 5.46 Compound **9**  $^1\text{H}$  NMR (500 MHz,  $\text{CDCl}_3$ )

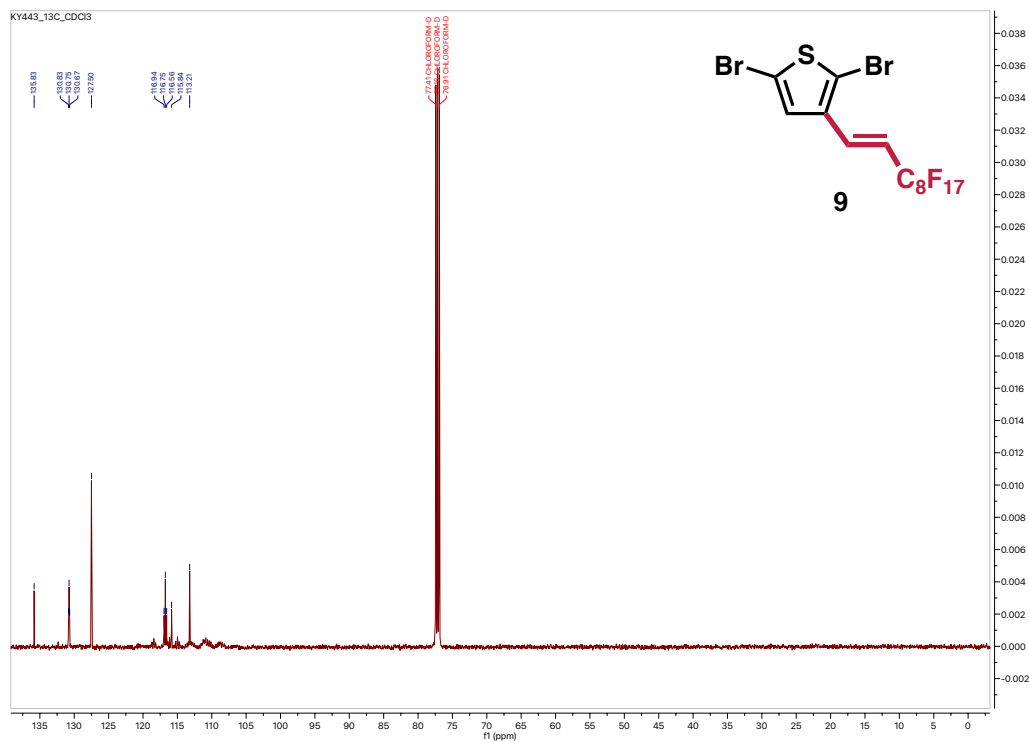


Figure 5.47 Compound **9**  $^{13}\text{C}$  NMR (126 MHz,  $\text{CDCl}_3$ )





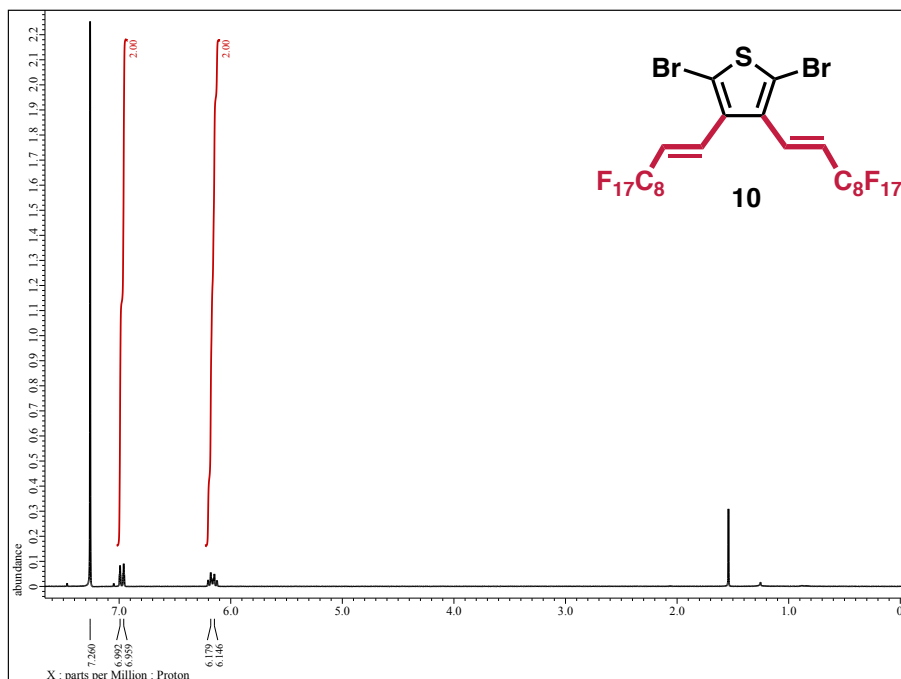


Figure 5.50 Compound 10  $^1\text{H}$  NMR (500 MHz,  $\text{CDCl}_3$ )

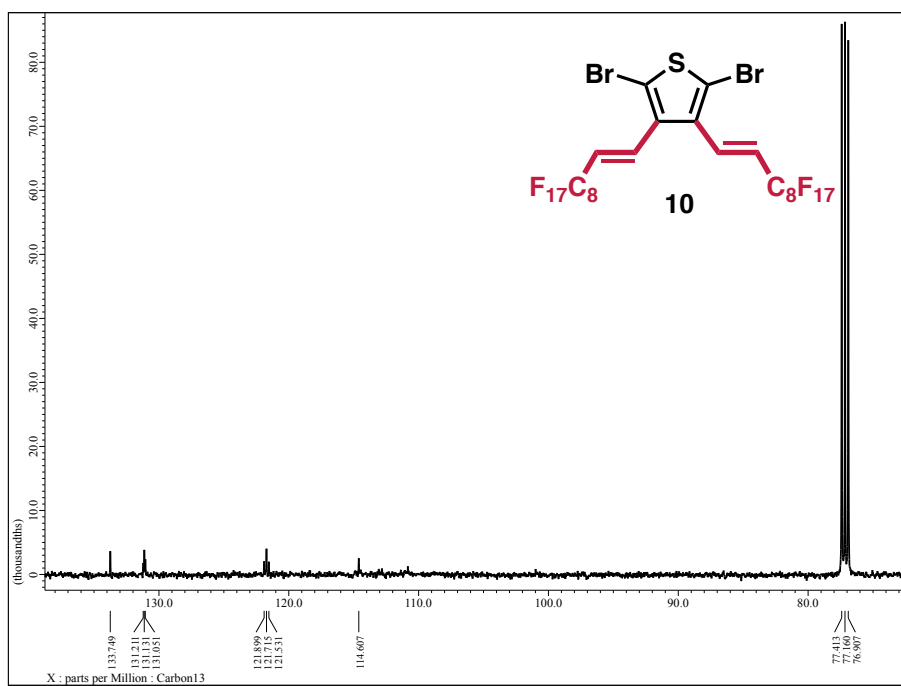
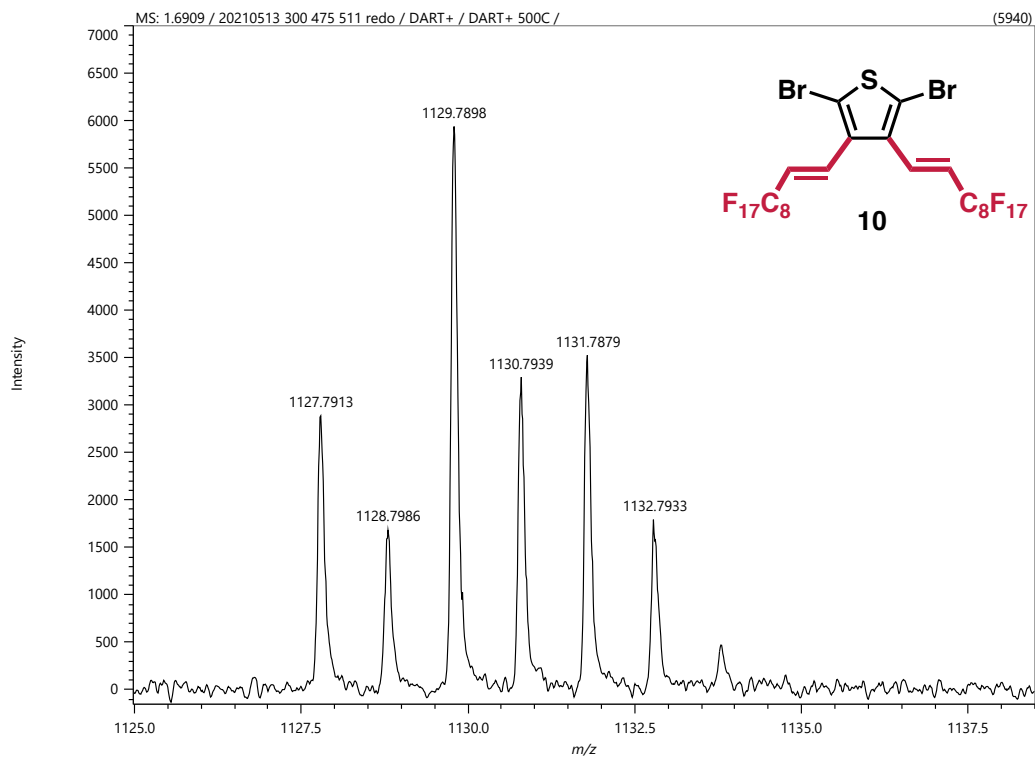
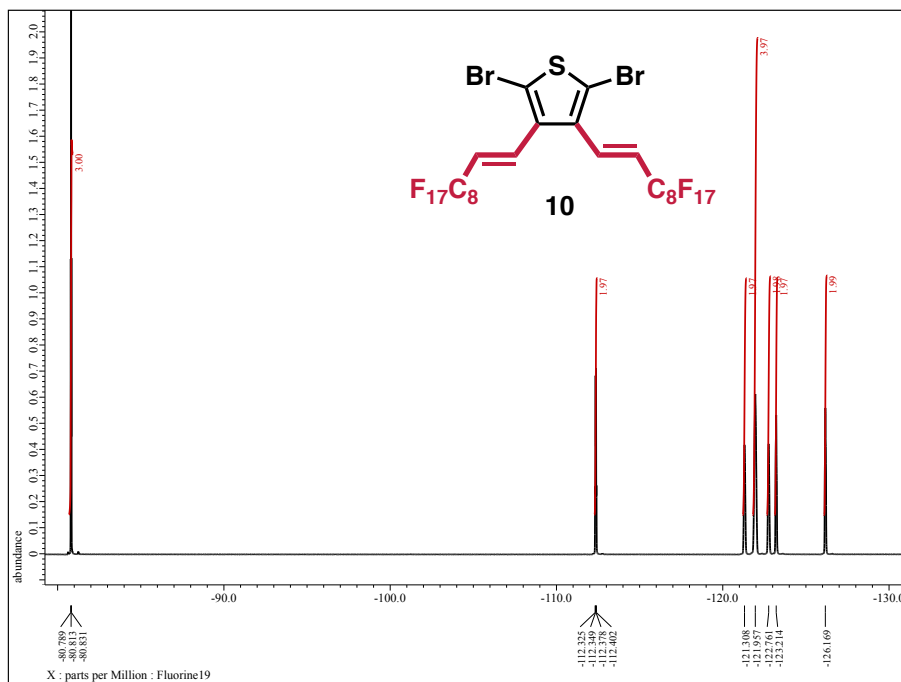


Figure 5.51 Compound 10  $^{13}\text{C}$  NMR (126 MHz,  $\text{CDCl}_3$ )



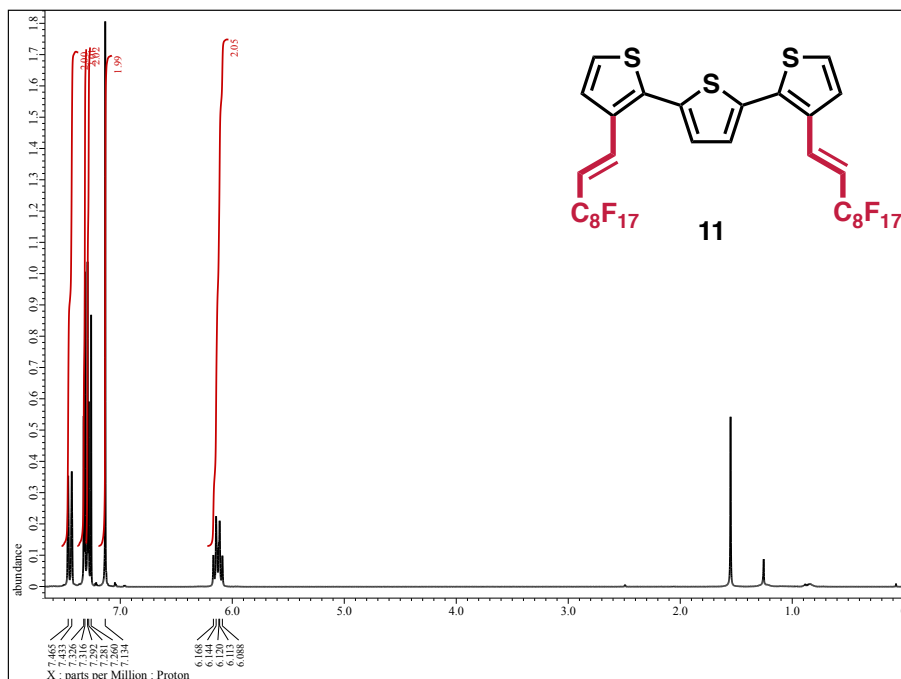


Figure 5.54 Compound 11 <sup>1</sup>H NMR (500 MHz, CDCl<sub>3</sub>)

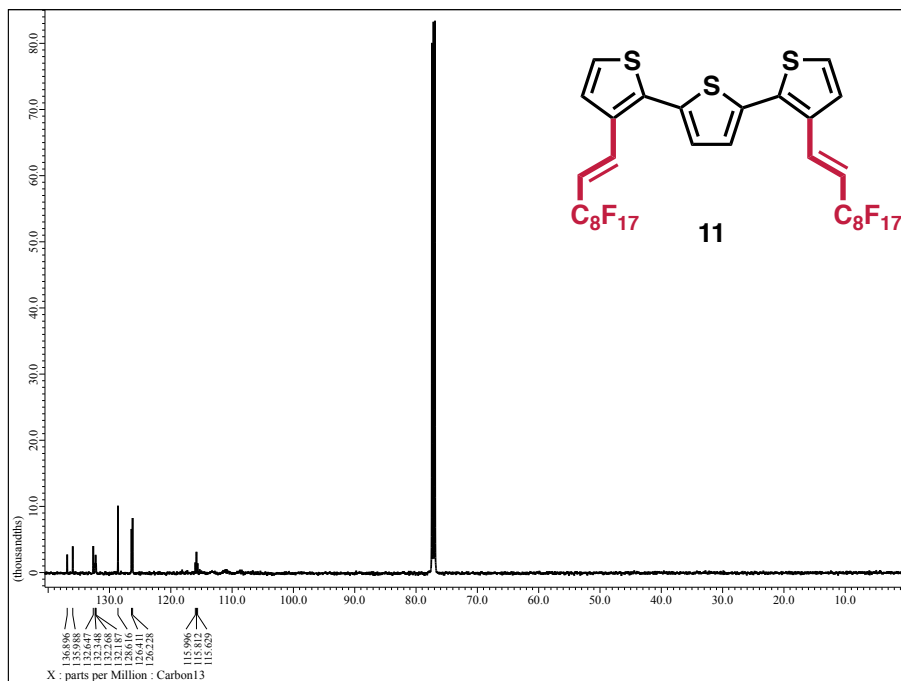


Figure 5.55 Compound 11 <sup>13</sup>C NMR (126 MHz, CDCl<sub>3</sub>)

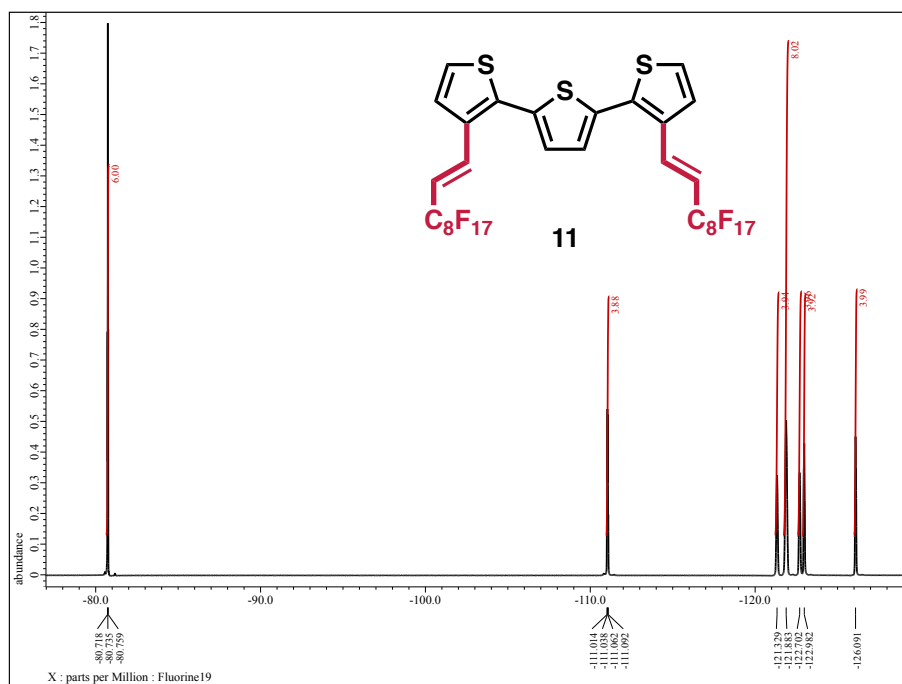


Figure 5.56 Compound **11** <sup>19</sup>F NMR (471 MHz, CDCl<sub>3</sub>)

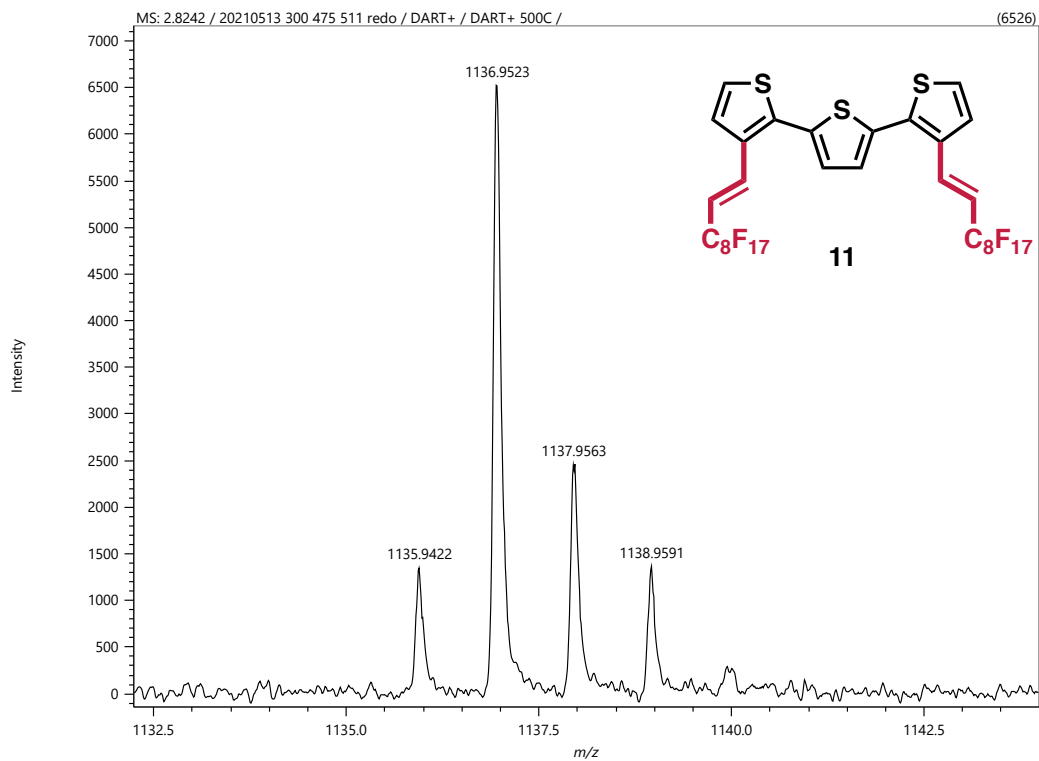


Figure 5.57 Compound **11** DART MS

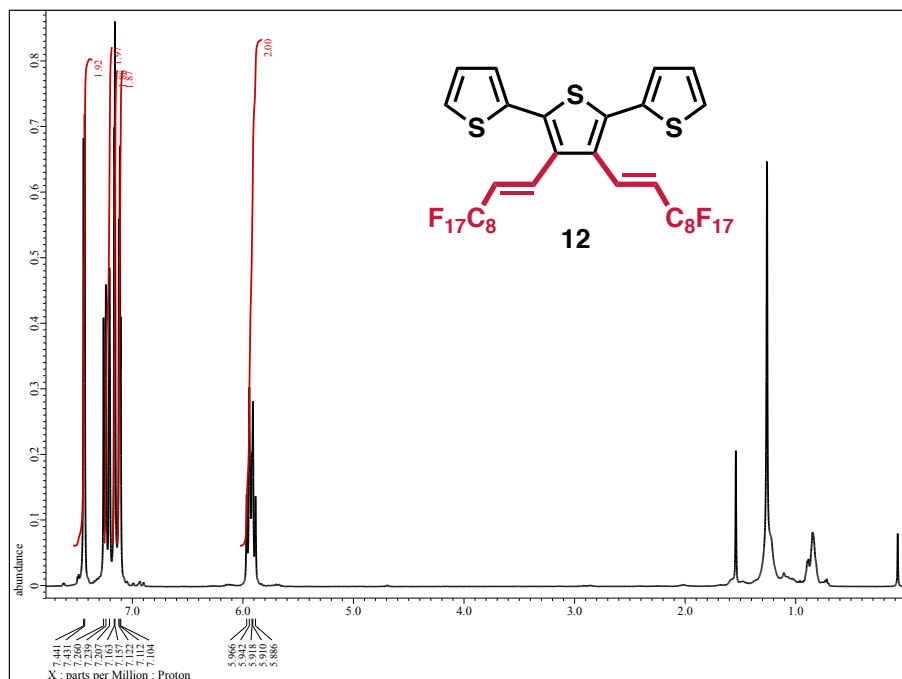


Figure 5.58 Compound 12 <sup>1</sup>H NMR (500 MHz, CDCl<sub>3</sub>)

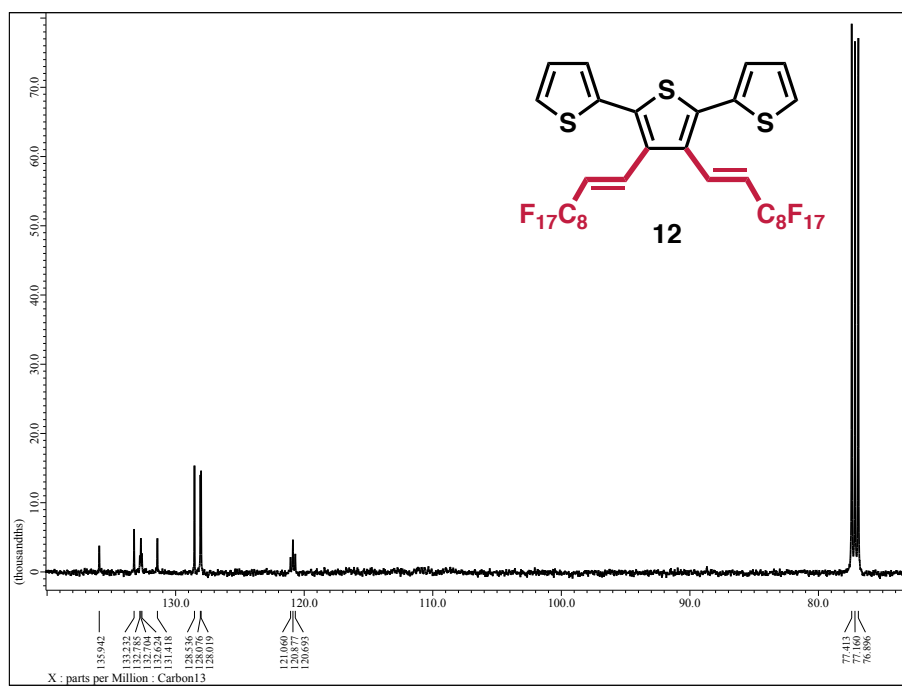


Figure 5.59 Compound 12 <sup>13</sup>C NMR (126 MHz, CDCl<sub>3</sub>)

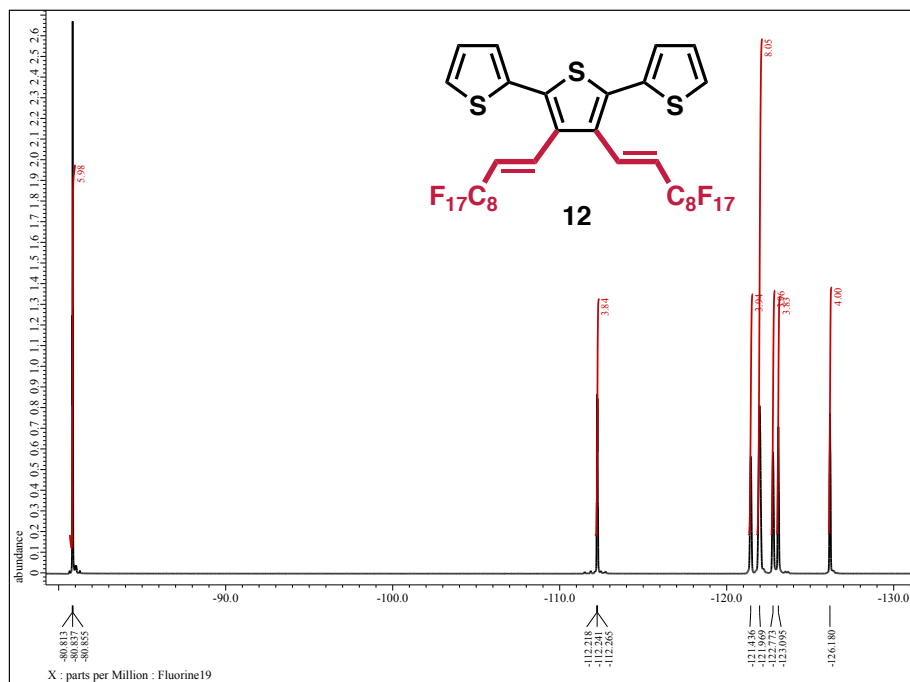


Figure 5.60 Compound **12**  $^{19}\text{F}$  NMR (471 MHz,  $\text{CDCl}_3$ )

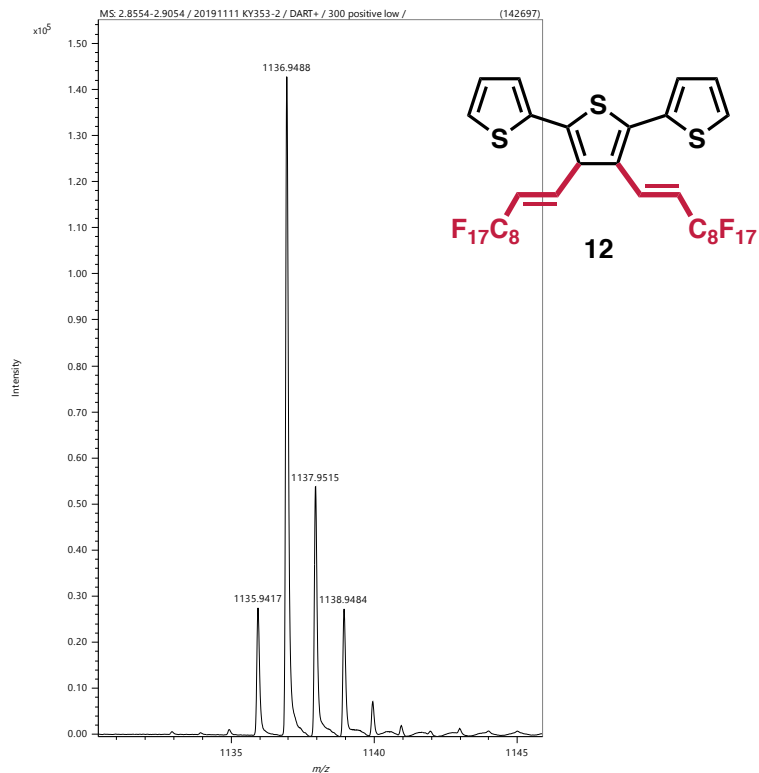


Figure 5.61 Compound **12** DART MS

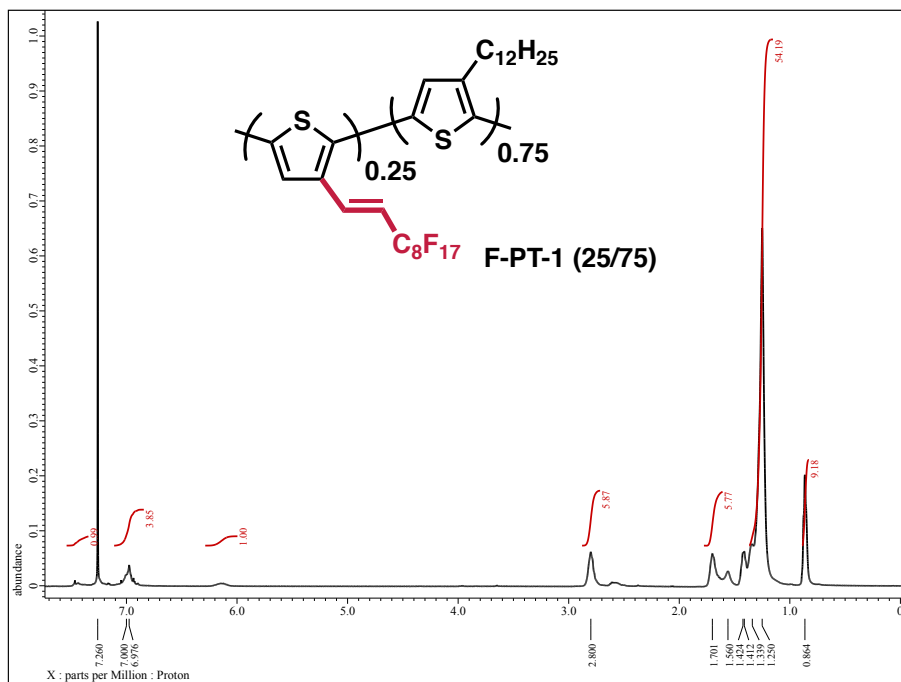


Figure 5.62 F-PT-1(25/75) <sup>1</sup>H NMR (500 MHz, CDCl<sub>3</sub>)

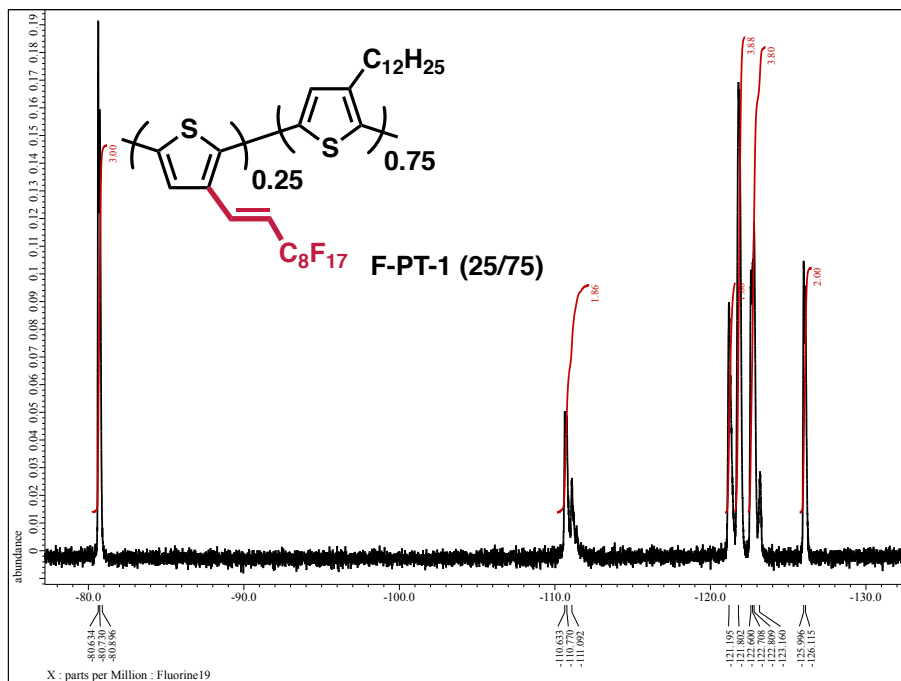


Figure 5.63 F-PT-1(25/75) <sup>19</sup>F NMR (471 MHz, CDCl<sub>3</sub>)





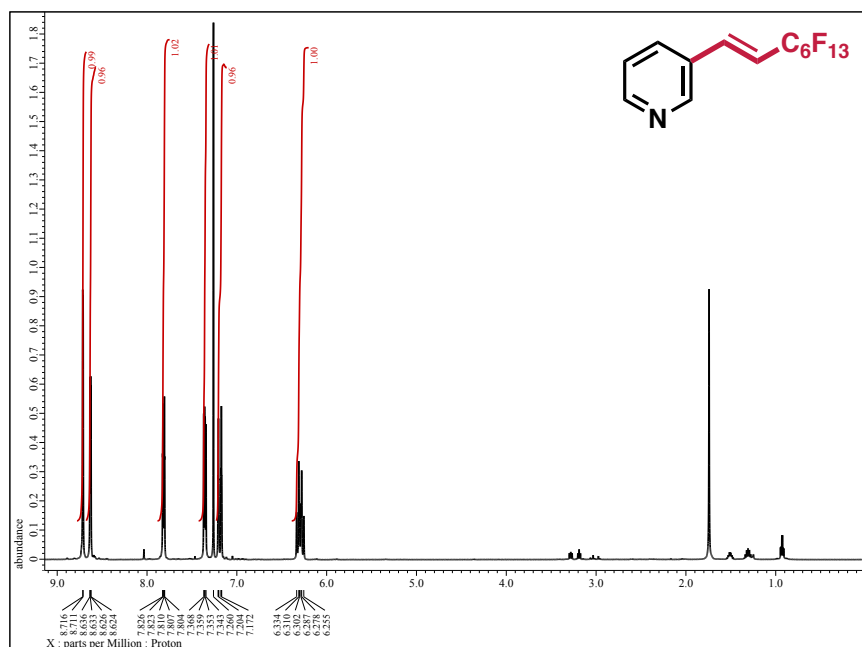


Figure 5.66 Compound Py-C6  $^1\text{H}$  NMR (500 MHz,  $\text{CDCl}_3$ , 20 °C)

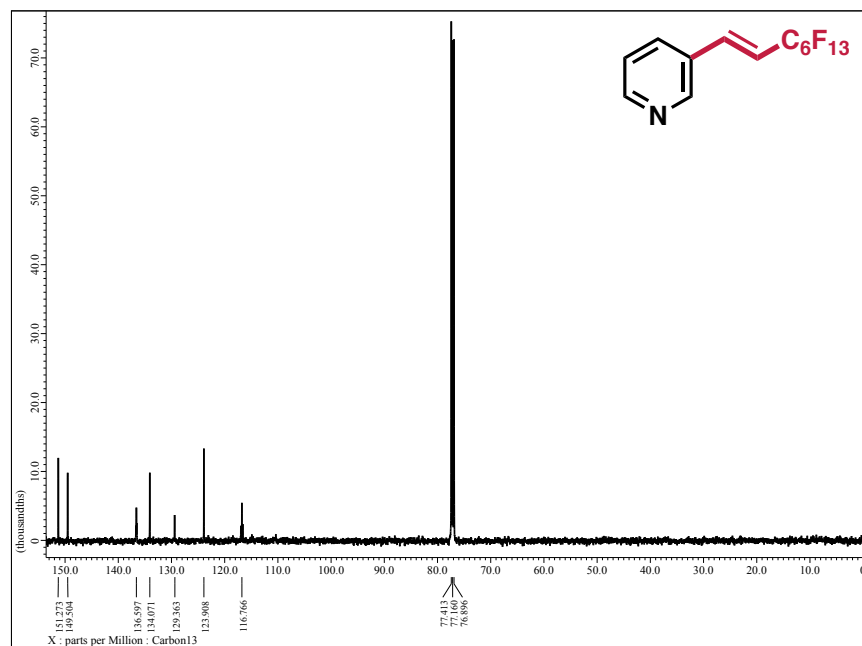
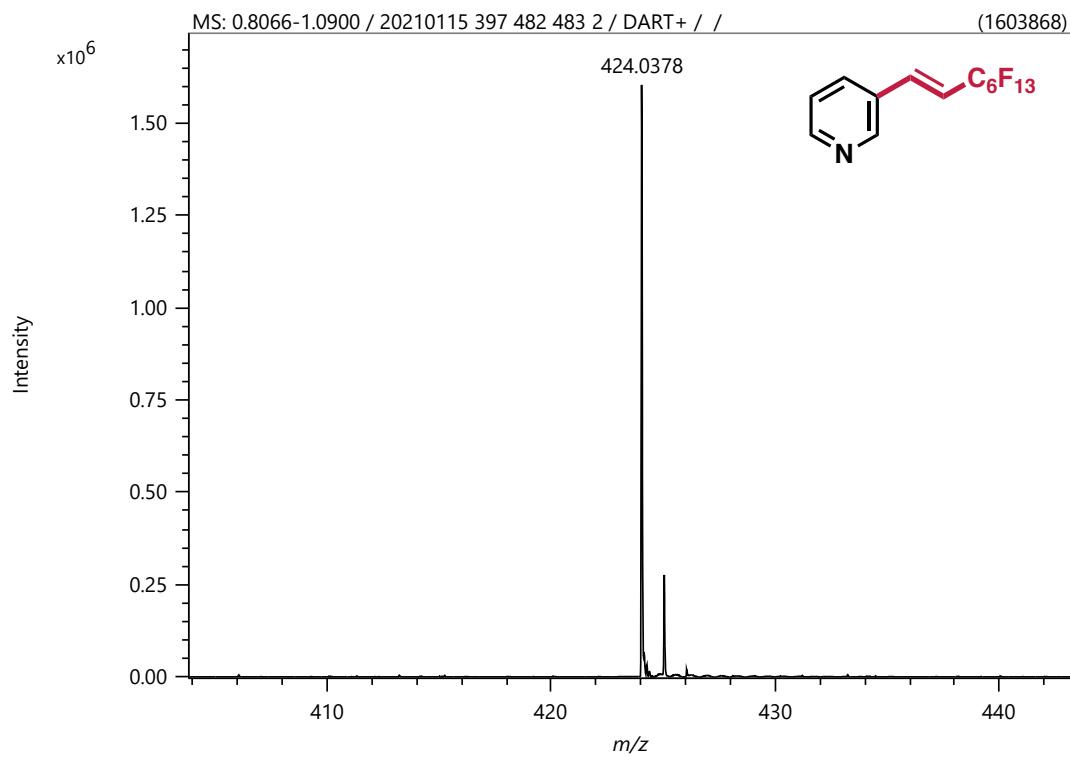


Figure 5.67 Compound Py-C6  $^{13}\text{C}$  NMR (126 MHz,  $\text{CDCl}_3$ , 20 °C)



**Figure 5.68** Compound **Py-C6**  $^{19}\text{F}$  NMR (471 MHz,  $\text{CDCl}_3$ , 20 °C)



**Figure 5.69** Compound **Py-C6** DART MS

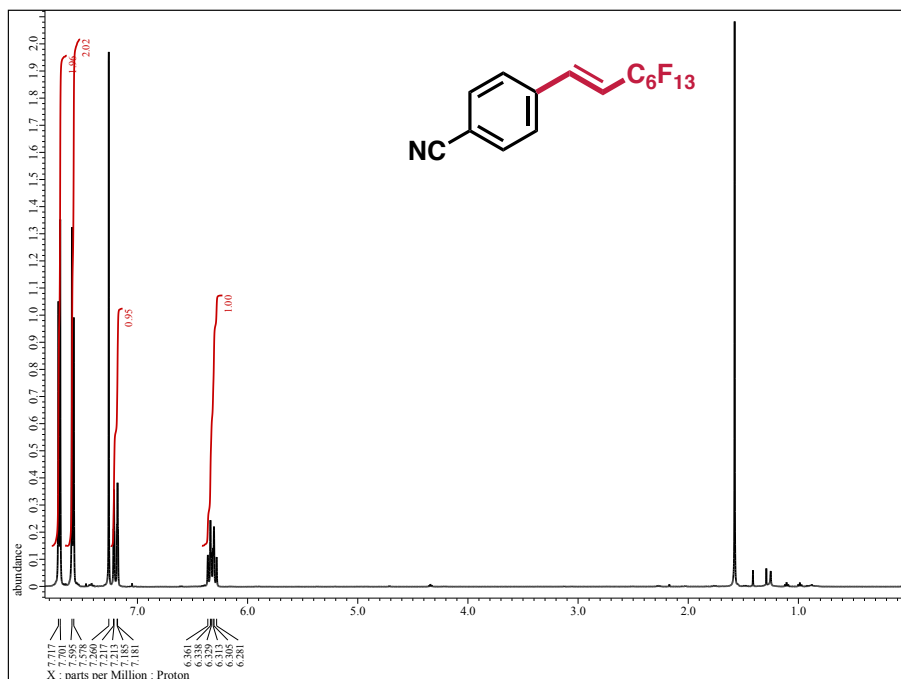


Figure 5.70 Compound Ph-CN-C6 (*p*) <sup>1</sup>H NMR (500 MHz, CDCl<sub>3</sub>, 20 °C)

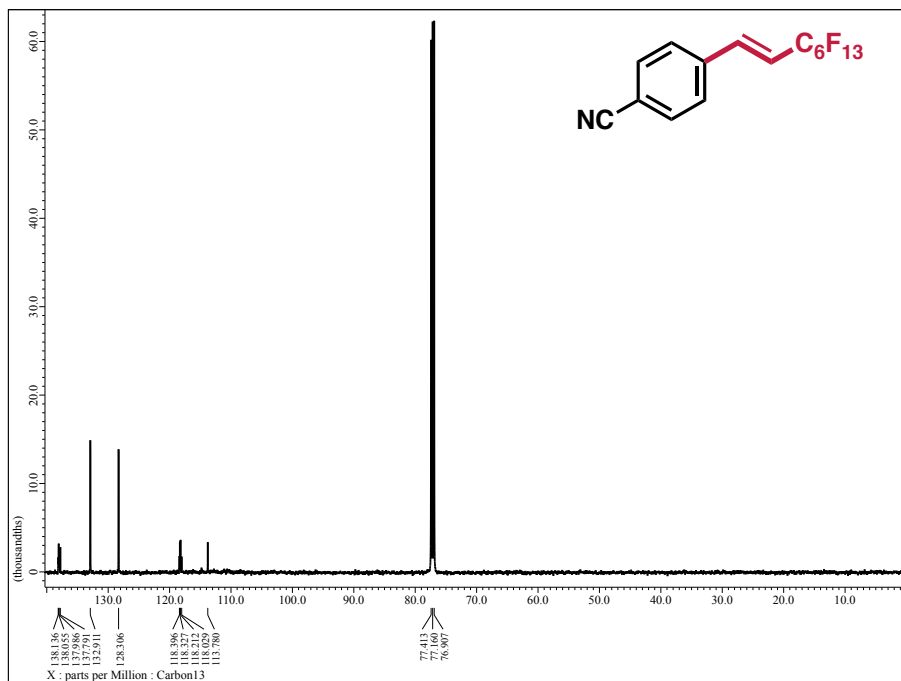
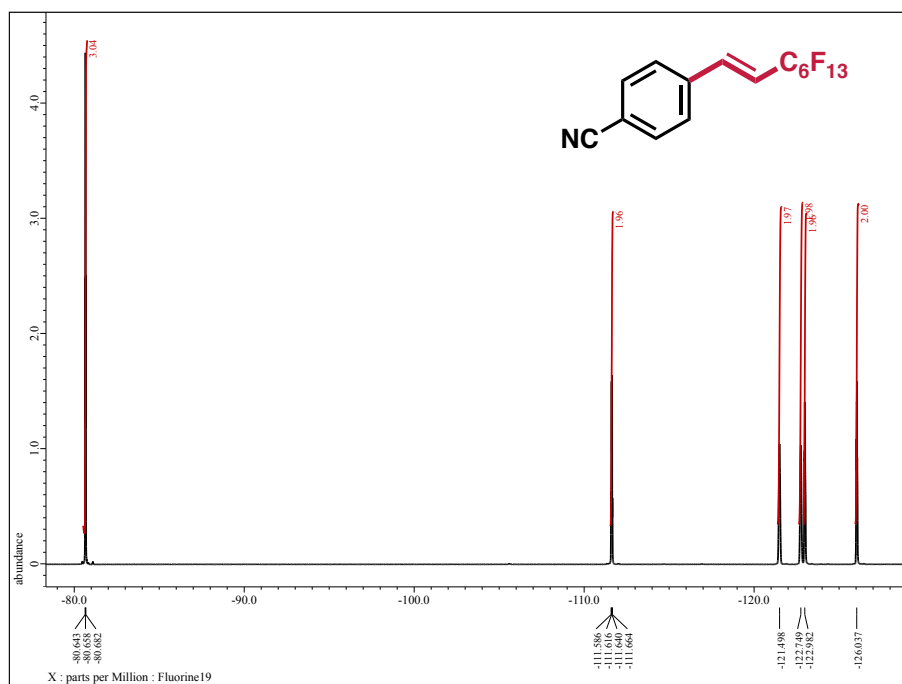
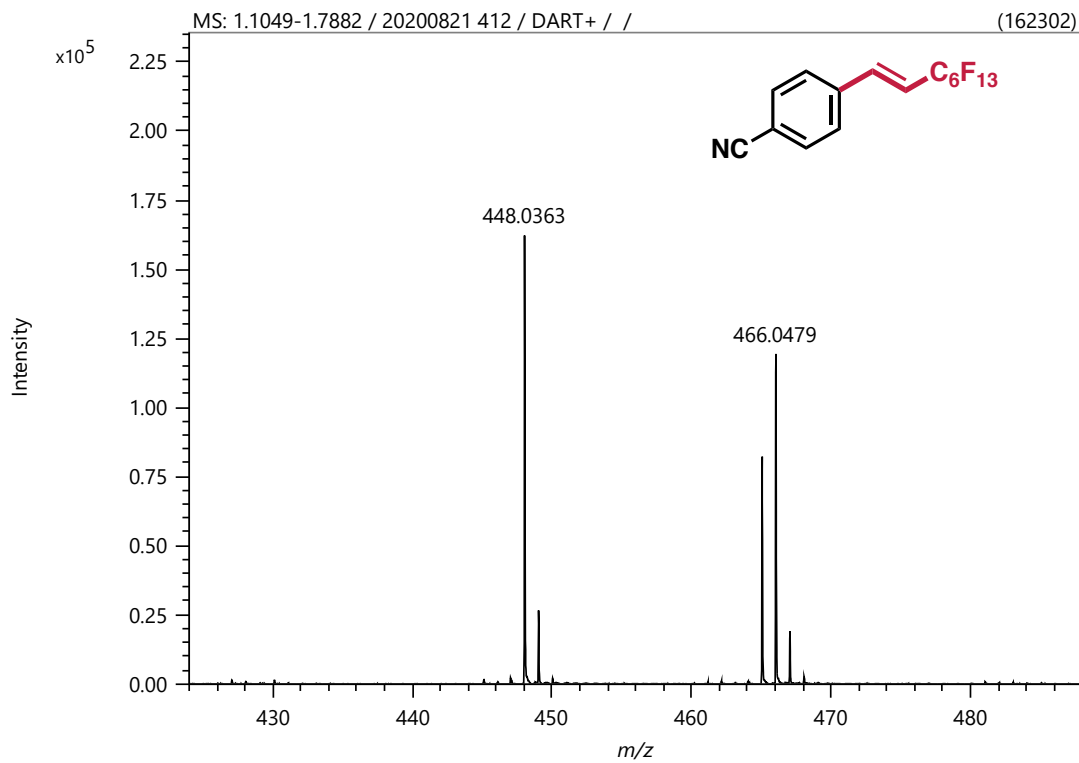


Figure 5.71 Compound Ph-CN-C6 (*p*) <sup>13</sup>C NMR (126 MHz, CDCl<sub>3</sub>, 20 °C)



**Figure 5.72** Compound **Ph-CN-C6 (p)**  $^{19}\text{F}$  NMR (471 MHz,  $\text{CDCl}_3$ , 20 °C)



**Figure 5.73** Compound **Ph-CN-C6 (p)** DART MS

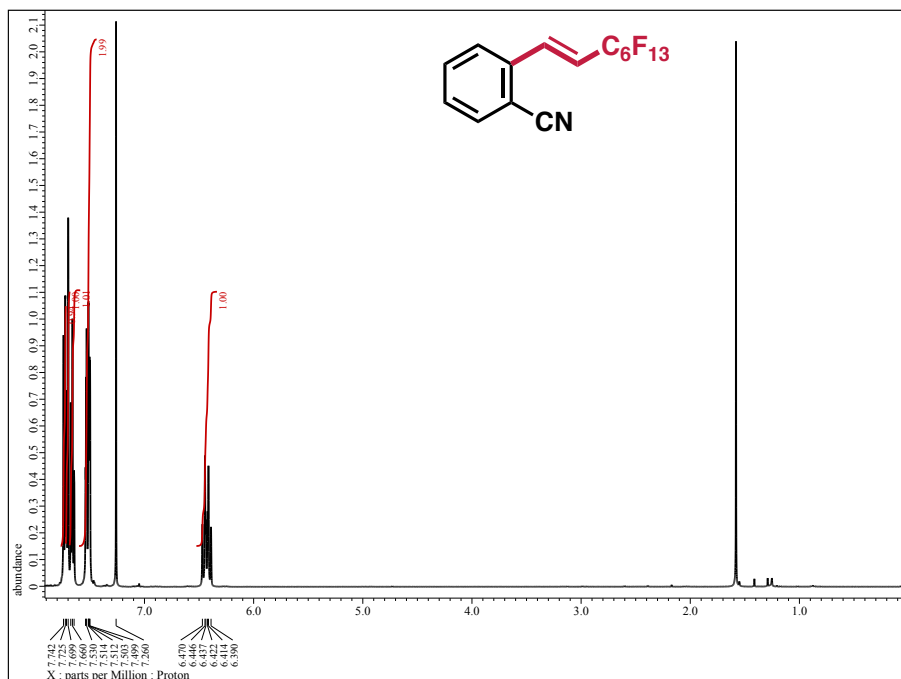


Figure 5.74 Compound Ph-CN-C6 (*o*) <sup>1</sup>H NMR (500 MHz, CDCl<sub>3</sub>, 20 °C)

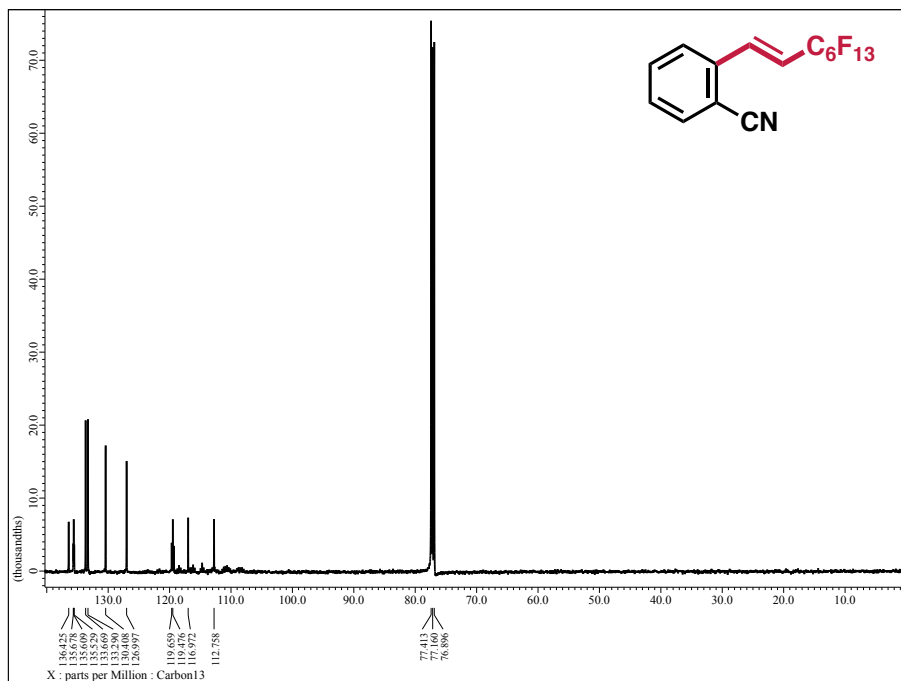
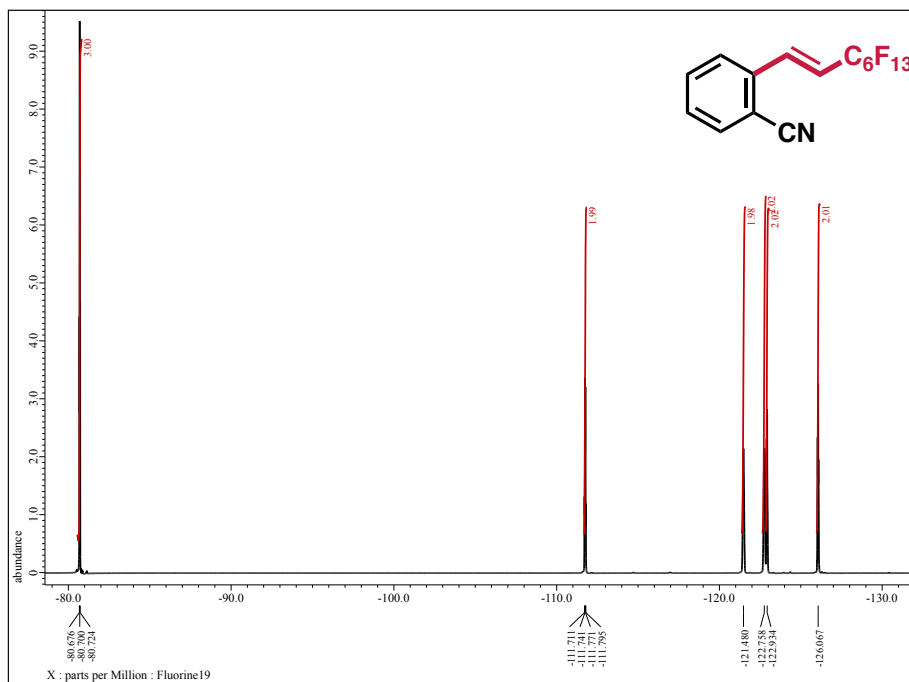
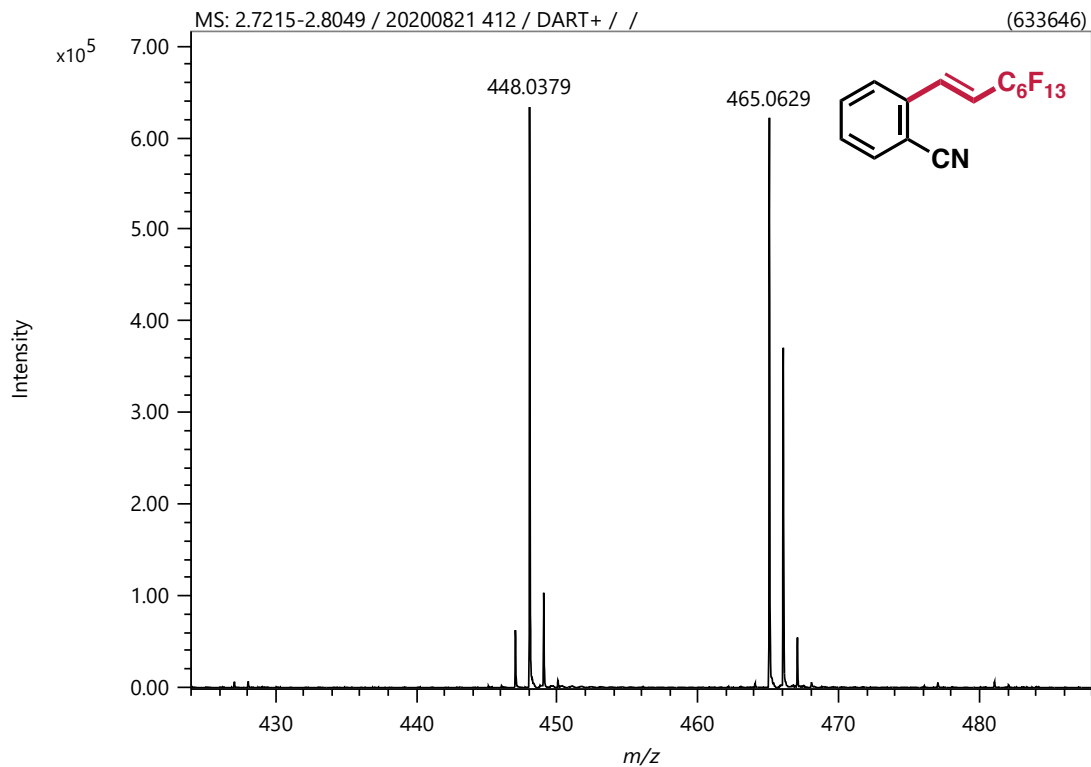


Figure 5.75 Compound Ph-CN-C6 (*o*) <sup>13</sup>C NMR (126 MHz, CDCl<sub>3</sub>, 20 °C)



**Figure 5.76** Compound **Ph-CN-C6 (o)**  $^{19}\text{F}$  NMR (471 MHz,  $\text{CDCl}_3$ , 20 °C)



**Figure 5.77** Compound **Ph-CN-C6 (o)** DART MS

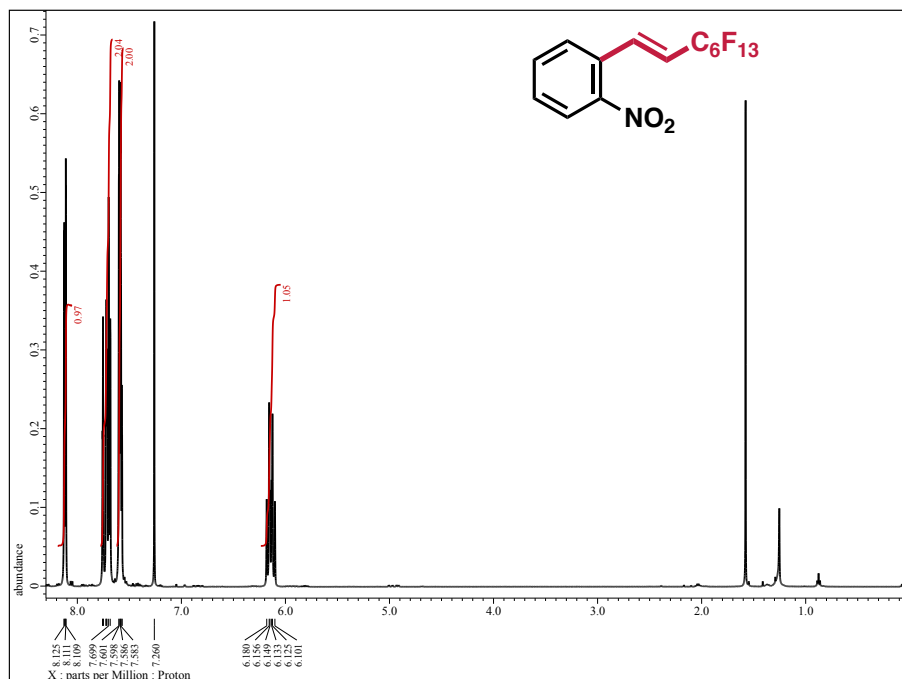


**Figure 5.78** Compound **Ph-NO<sub>2</sub>-C6 (o)** <sup>1</sup>H NMR (500 MHz, CDCl<sub>3</sub>, 20 °C)

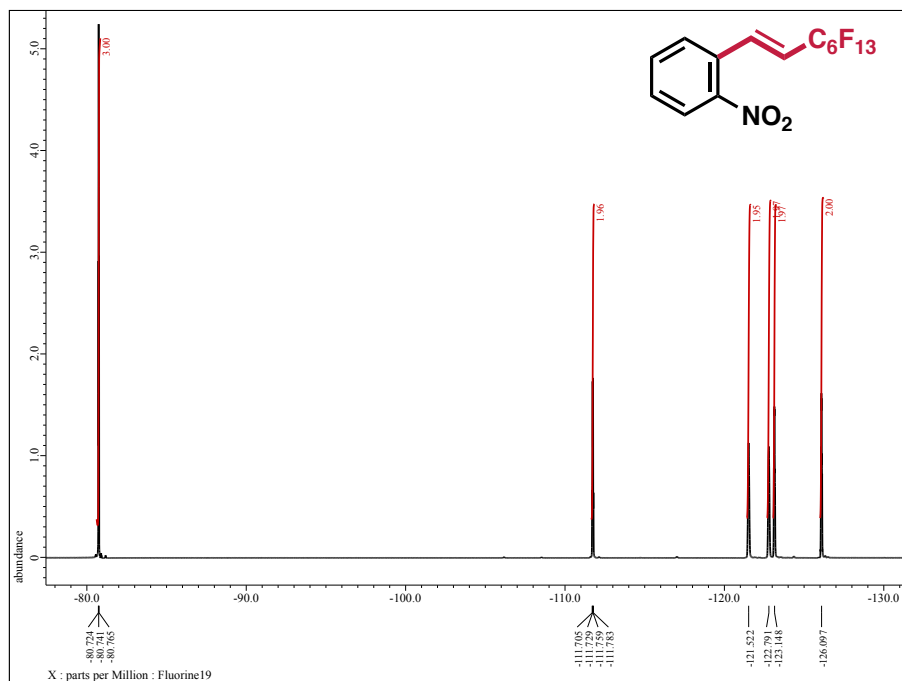


**Figure 5.79** Compound **Ph-NO<sub>2</sub>-C6 (o)** <sup>19</sup>F NMR (471 MHz, CDCl<sub>3</sub>, 20 °C)



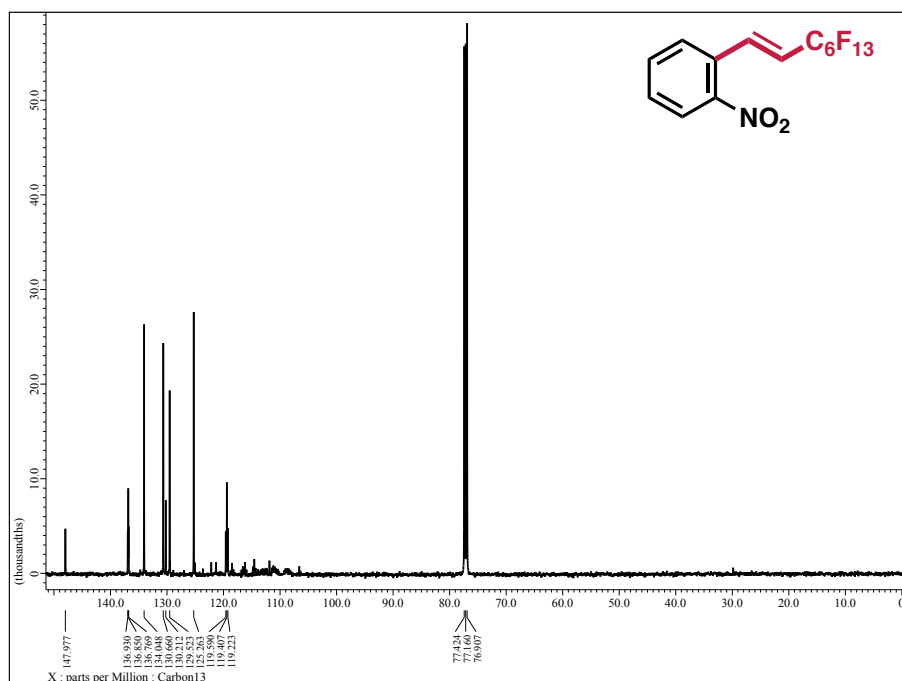


**Figure 5.80** Compound Ph-NO<sub>2</sub>-C6 (*o*) <sup>13</sup>C NMR (126 MHz, CDCl<sub>3</sub>, 20 °C)

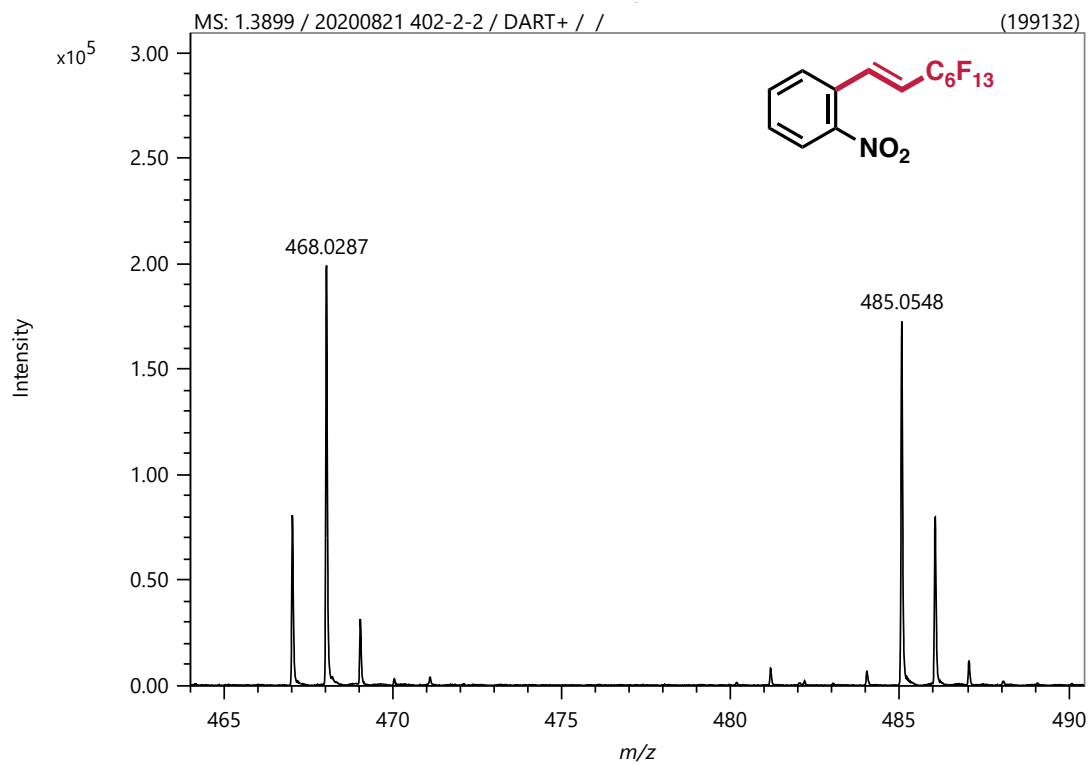


**Figure 5.81** Compound Ph-NO<sub>2</sub>-C6 (*o*) DART MS

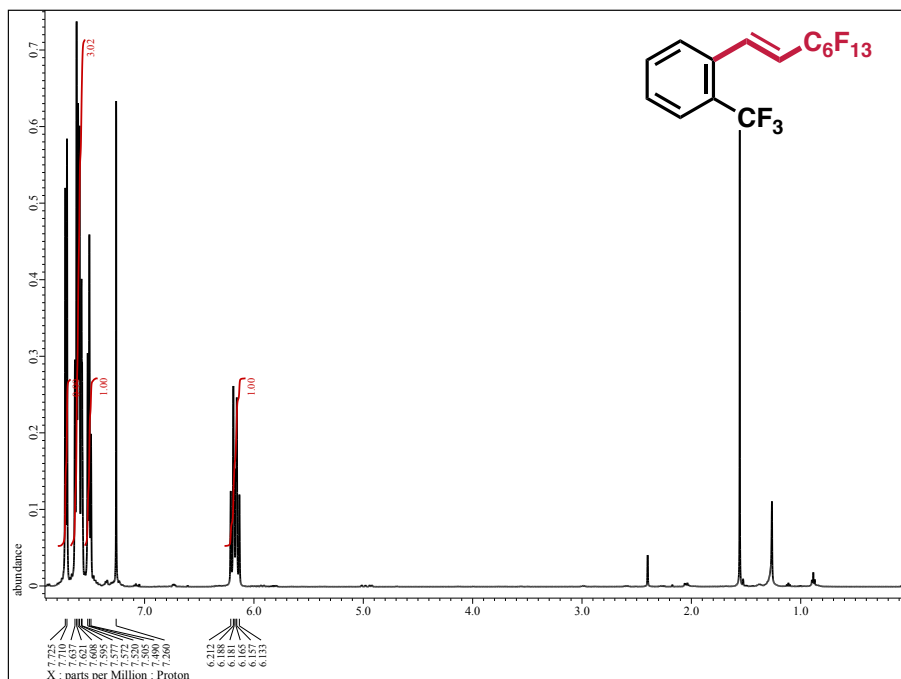


Figure 5.82 Compound Ph-CF<sub>3</sub>-C6 (*o*) <sup>1</sup>H NMR (500 MHz, CDCl<sub>3</sub>, 20 °C)

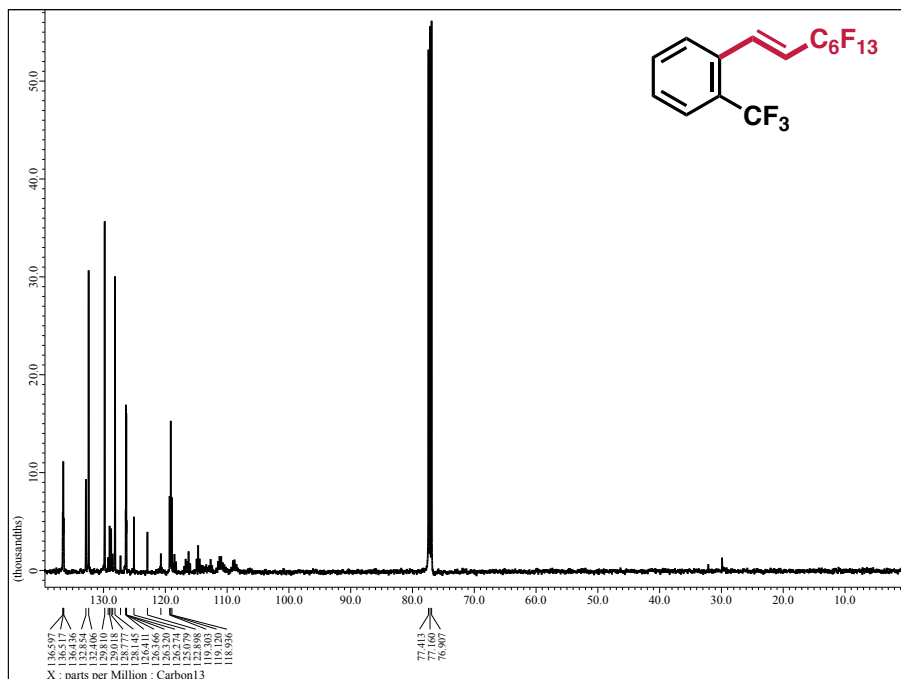
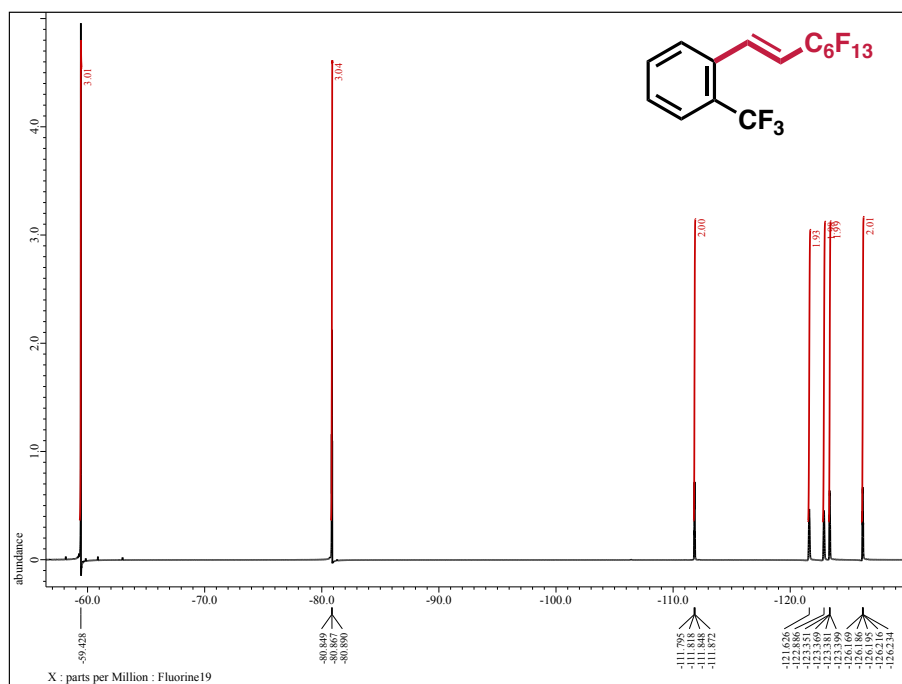
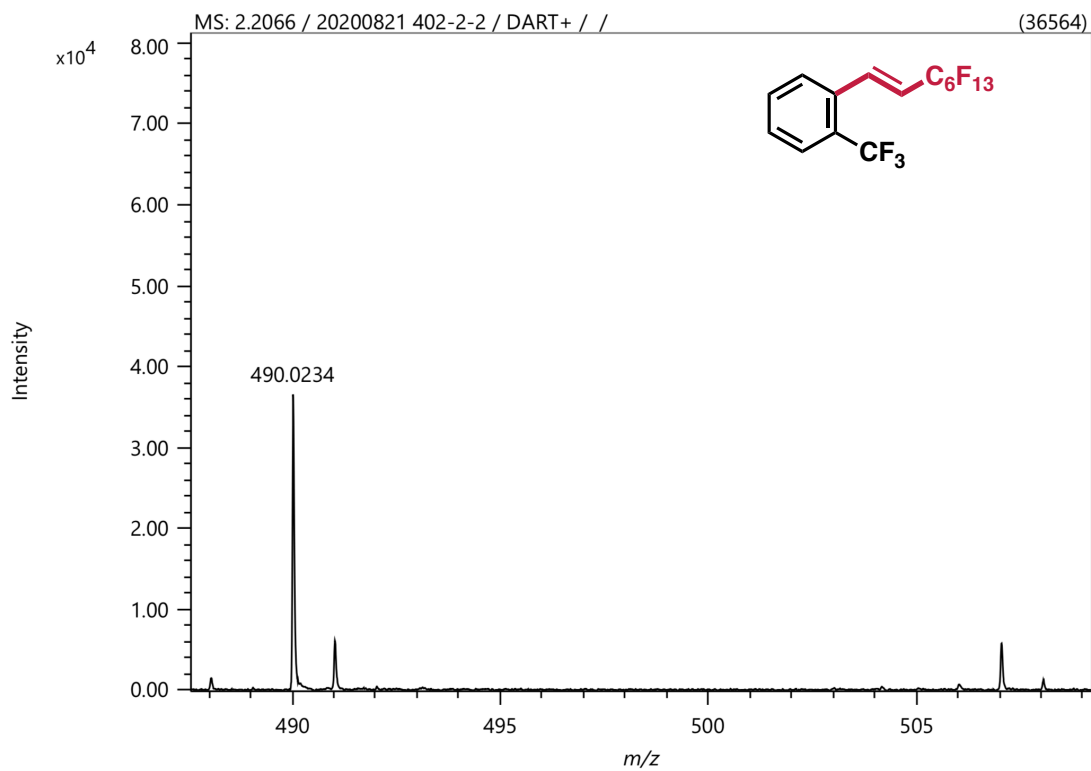


Figure 5.83 Compound Ph-CF<sub>3</sub>-C6 (*o*) <sup>13</sup>C NMR (126 MHz, CDCl<sub>3</sub>, 20 °C)



**Figure 5.84** Compound **Ph-CF<sub>3</sub>-C6 (o)** <sup>19</sup>F NMR (471 MHz, CDCl<sub>3</sub>, 20 °C)



**Figure 5.85** Compound **Ph-CF<sub>3</sub>-C6 (o)** DART MS

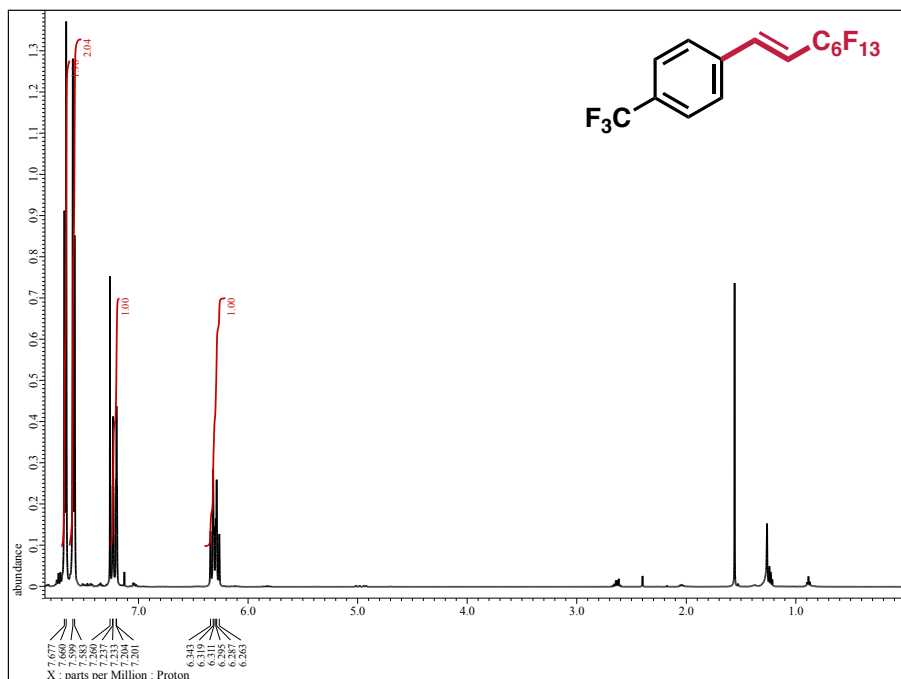


Figure 5.86 Compound  $\text{Ph-CF}_3\text{-C}_6(p)$   $^1\text{H NMR}$  (500 MHz,  $\text{CDCl}_3$ , 20 °C)

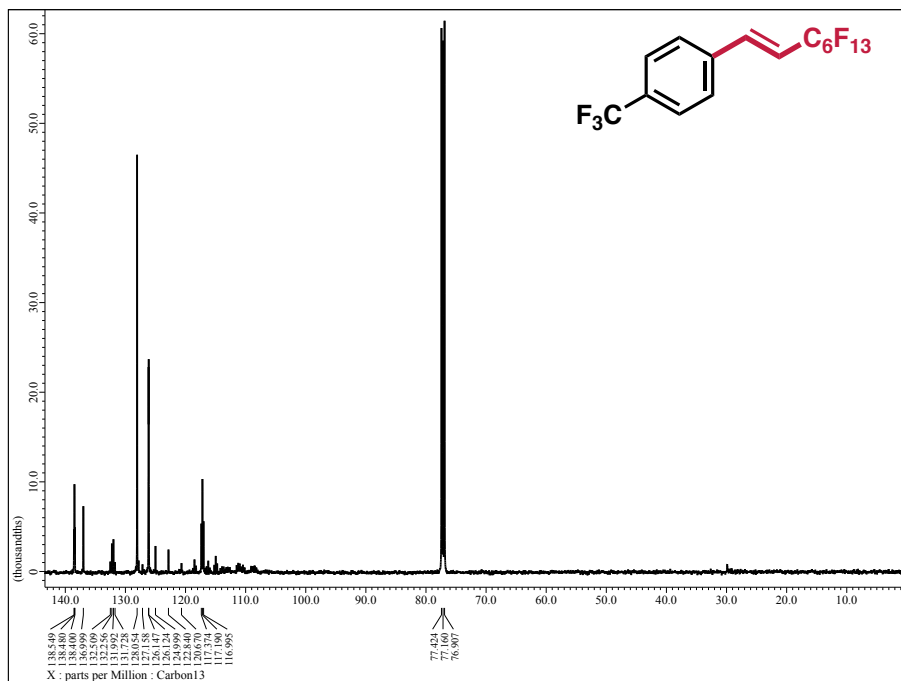
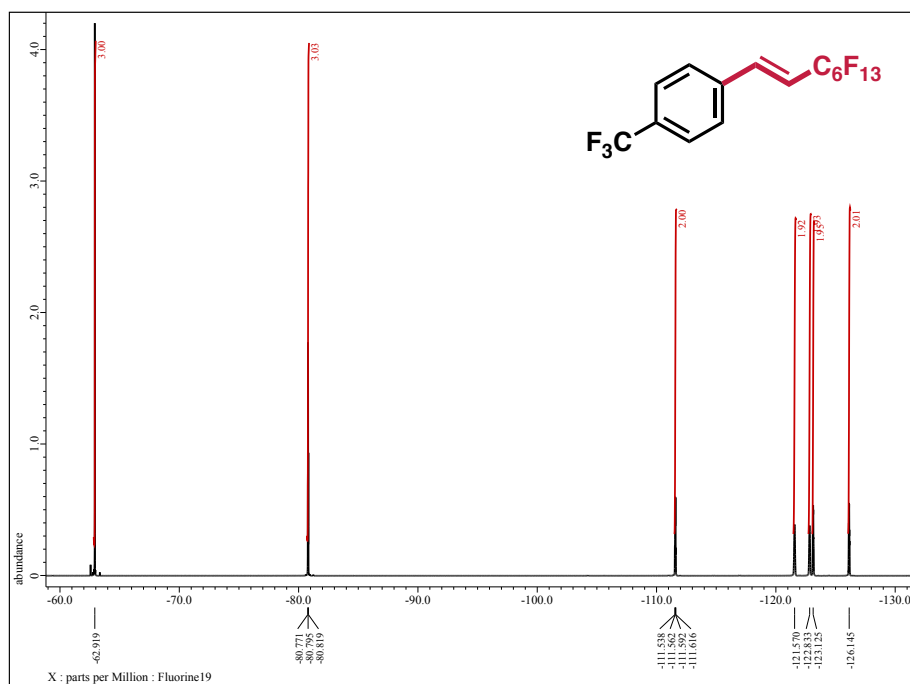
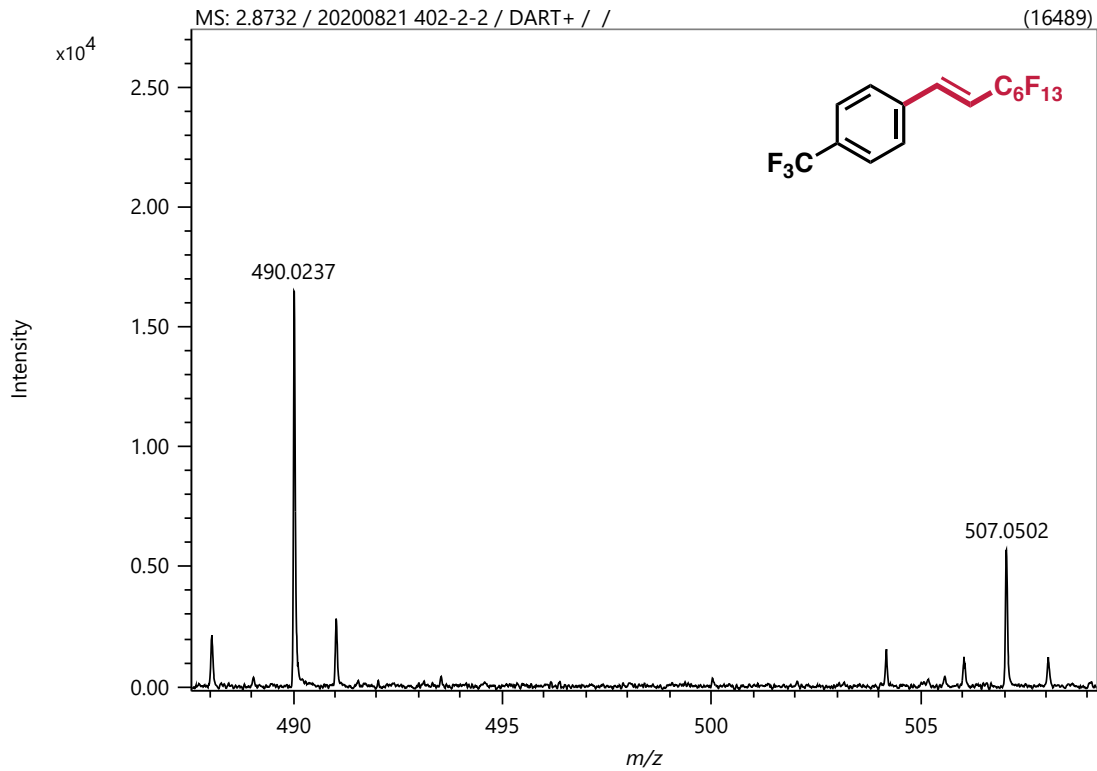


Figure 5.87 Compound  $\text{Ph-CF}_3\text{-C}_6(p)$   $^{13}\text{C NMR}$  (126 MHz,  $\text{CDCl}_3$ , 20 °C)



**Figure 5.88** Compound **Ph-CF<sub>3</sub>-C<sub>6</sub>(p)**  $^{19}\text{F}$  NMR (471 MHz, CDCl<sub>3</sub>, 20 °C)



**Figure 5.89** Compound **Ph-CF<sub>3</sub>-C<sub>6</sub>(p)** DART MS

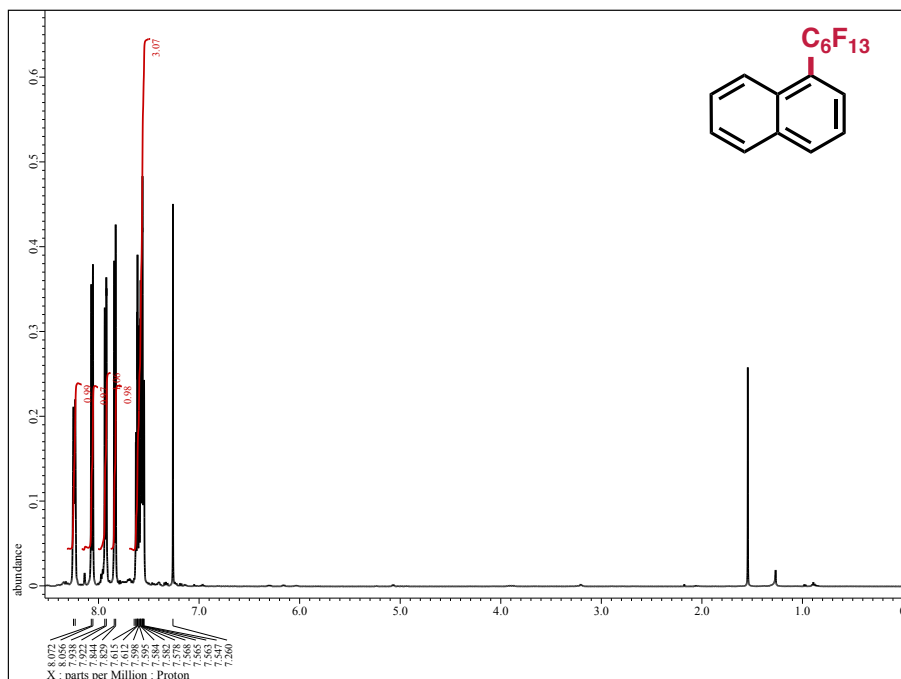


**Figure 5.90** Compound 1-Naph-C6  $^1\text{H}$  NMR (500 MHz,  $\text{CDCl}_3$ , 20 °C)

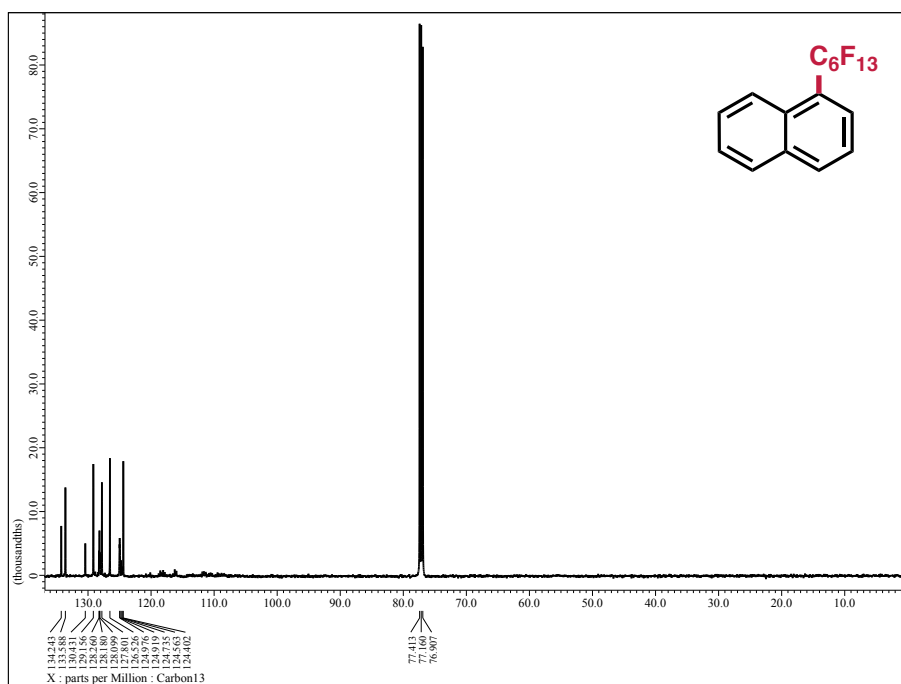


**Figure 5.91** Compound 1-Naph-C6  $^{13}\text{C}$  NMR (126 MHz,  $\text{CDCl}_3$ , 20 °C)

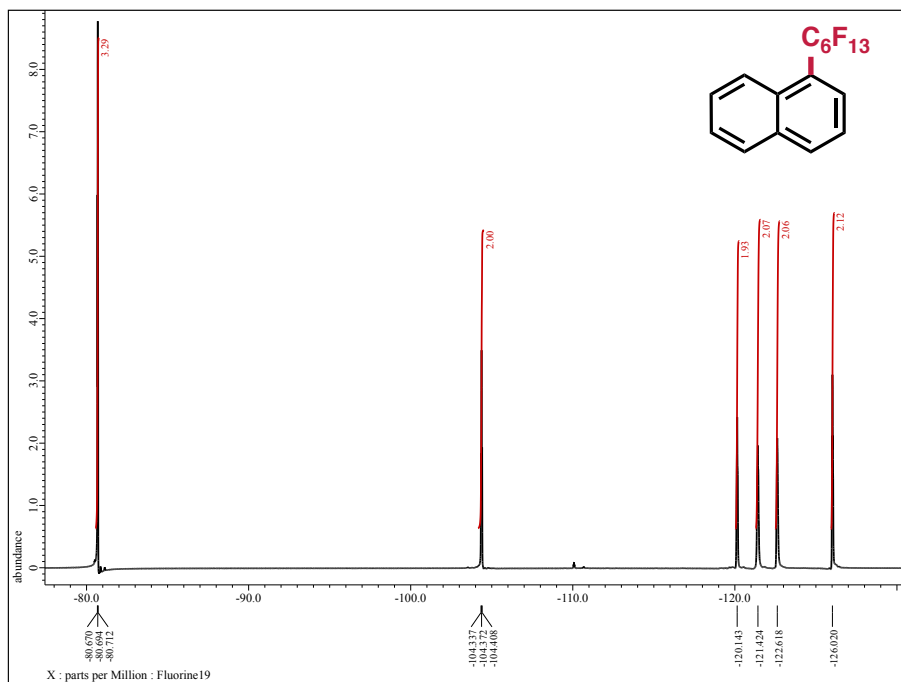


**Figure 5.92** Compound 1-Naph-C6 <sup>19</sup>F NMR (471 MHz, CDCl<sub>3</sub>, 20 °C)

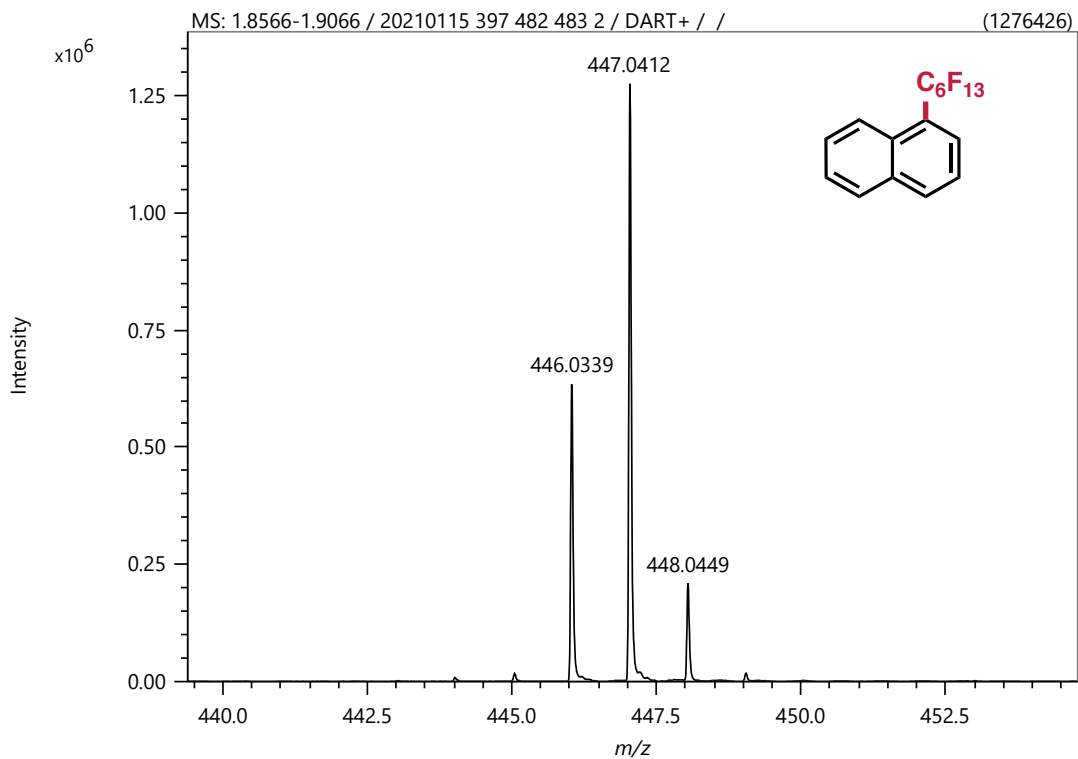


**Figure 5.93** Compound 1-Naph-C6 DART MS

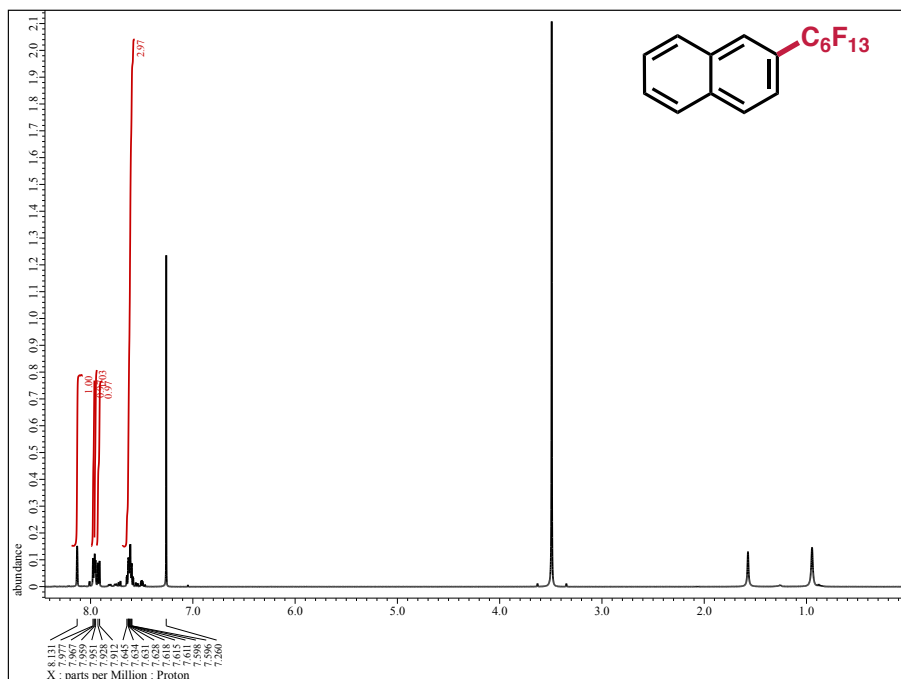


**Figure 5.94** Compound 2-Naph-C6  $^1\text{H}$  NMR (500 MHz,  $\text{CDCl}_3$ , 20 °C)

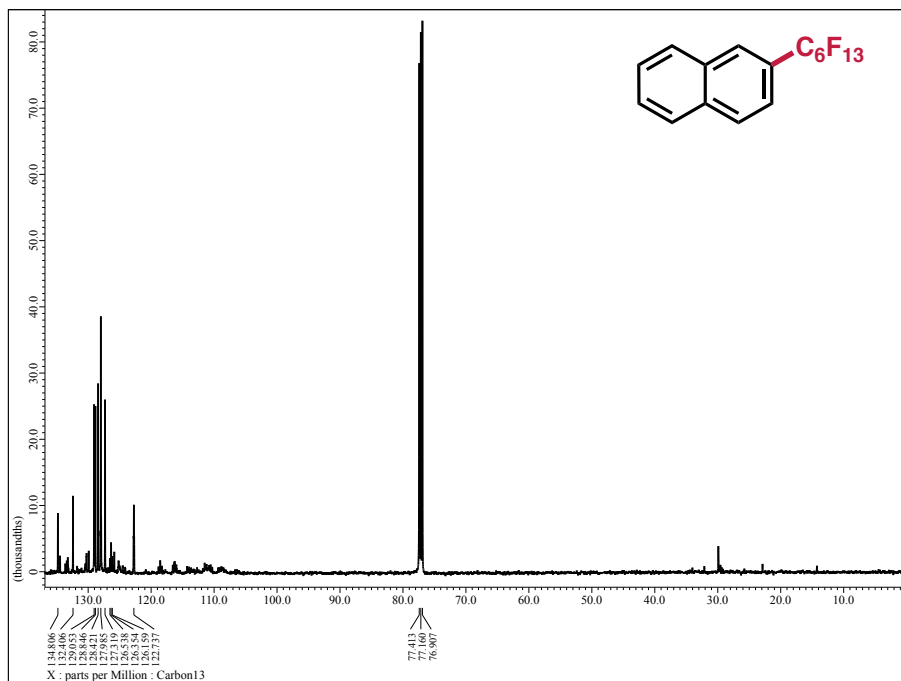


**Figure 5.95** Compound 2-Naph-C6  $^{13}\text{C}$  NMR (126 MHz,  $\text{CDCl}_3$ , 20 °C)



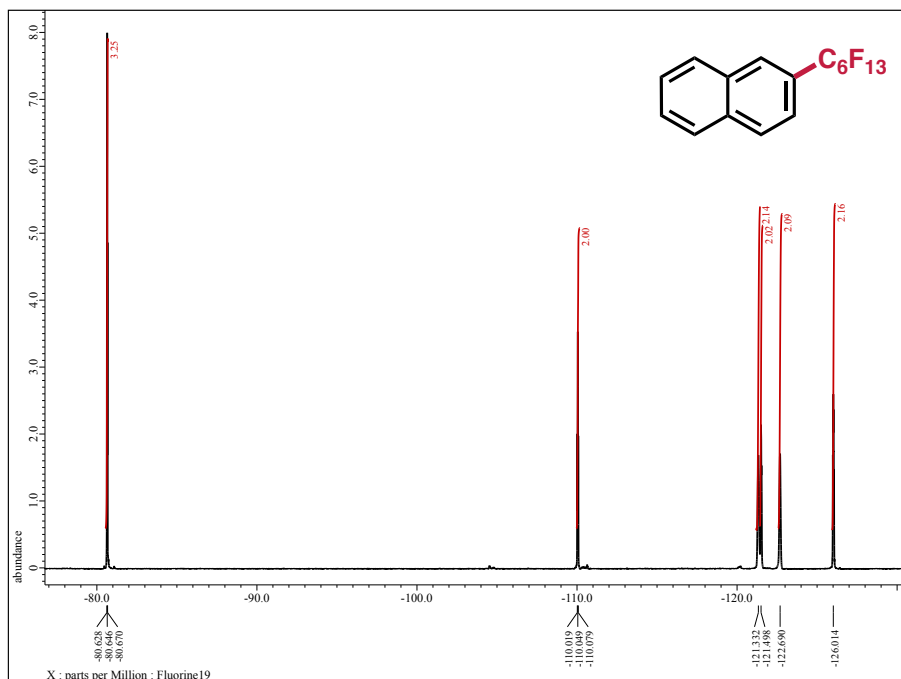


**Figure 5.96** Compound 2-Naph-C6  $^{19}\text{F}$  NMR (471 MHz,  $\text{CDCl}_3$ , 20  $^\circ\text{C}$ )

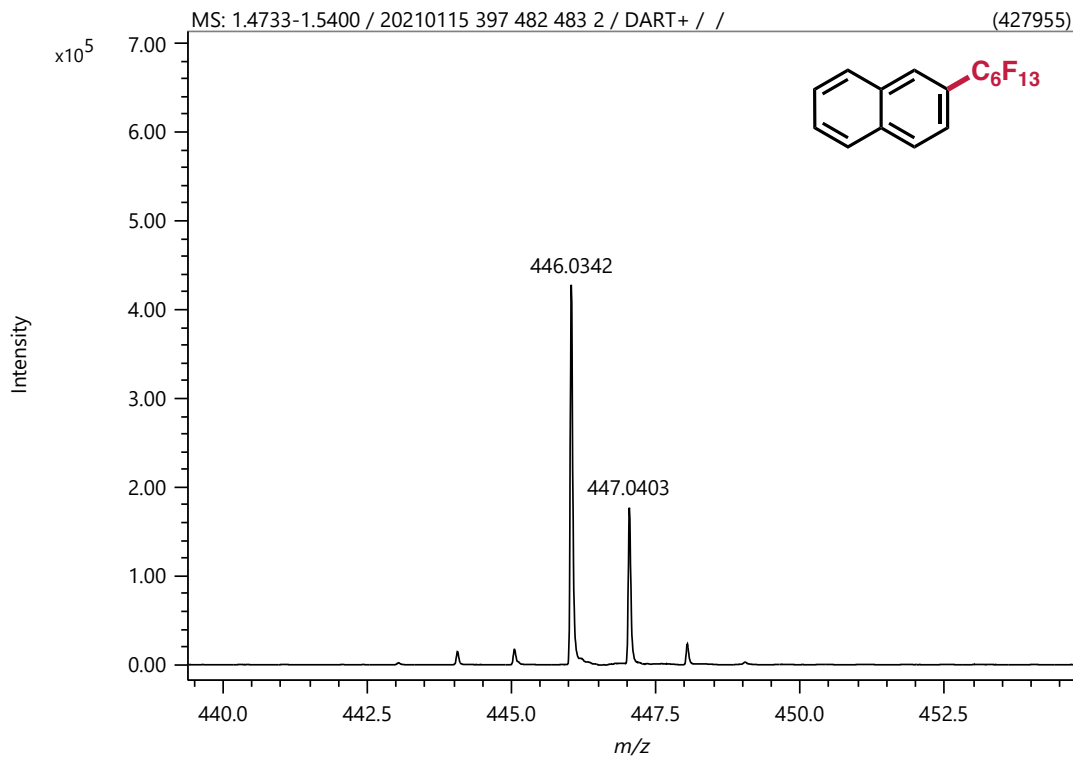


**Figure 5.97** Compound 2-Naph-C6 DART MS



## References

- (1) List of Elements of the Periodic Table - Sorted by Abundance in Earth's crust <https://www.science.co.il/elements/?s=Earth> (accessed Mar 30, 2021).
- (2) Puts, G. J.; Crouse, P.; Ameduri, B. M. Polytetrafluoroethylene: Synthesis and Characterization of the Original Extreme Polymer. *Chem. Rev.* **2019**, *119* (3), 1763–1805. <https://doi.org/10.1021/acs.chemrev.8b00458>.
- (3) G. de la Torre, B.; Albericio, F. The Pharmaceutical Industry in 2018. An Analysis of FDA Drug Approvals from the Perspective of Molecules. *Molecules* **2019**, *24* (4), 809. <https://doi.org/10.3390/molecules24040809>.
- (4) Fuchibe, K.; Morikawa, T.; Shigeno, K.; Fujita, T.; Ichikawa, J. Pinpoint-Fluorinated Phenacenes: New Synthesis and Solubility Enhancement Strategies. *Org. Lett.* **2015**, *17* (5), 1126–1129. <https://doi.org/10.1021/ol503759d>.
- (5) Sun, H.; Putta, A.; Kloster, J. P.; Tottempudi, U. K. Unexpected Photostability Improvement of Aromatics in Polyfluorinated Solvents. *Chem. Commun.* **2012**, *48* (99), 12085–12087. <https://doi.org/10.1039/c2cc35591d>.
- (6) Zhang, Q.; Kelly, M. A.; Bauer, N.; You, W. The Curious Case of Fluorination of Conjugated Polymers for Solar Cells. *Acc. Chem. Res.* **2017**, *50* (9), 2401–2409. <https://doi.org/10.1021/acs.accounts.7b00326>.
- (7) Schmidt, R.; Ling, M. M.; Oh, J. H.; Winkler, M.; Könemann, M.; Bao, Z.; Würthner, F. Core-Fluorinated Perylene Bisimide Dyes: Air Stable n-Channel Organic Semiconductors for Thin Film Transistors with Exceptionally High on-to-off Current Ratios. *Adv. Mater.* **2007**, *19* (21), 3692–3695. <https://doi.org/10.1002/adma.200701478>.
- (8) Kang, B.; Kim, R.; Lee, S. B.; Kwon, S.-K.; Kim, Y.-H.; Cho, K. Side-Chain-Induced Rigid Backbone Organization of Polymer Semiconductors through Semifluoroalkyl Side Chains. *J. Am. Chem. Soc.* **2016**, *138* (11), 3679–3686. <https://doi.org/10.1021/jacs.5b10445>.
- (9) Horváth, I. T.; Rábai, J. Facile Catalyst Separation without Water: Fluorous Biphasic Hydroformylation of Olefins. *Science* (80-. ). **1994**, *266* (5182), 72–75. <https://doi.org/10.1126/science.266.5182.72>.
- (10) Gladysz, J. A.; Emnet, C.; Rábai, J. Partition Coefficients Involving Fluorous Solvents. In *Handbook of Fluorous Chemistry*; Wiley, 2004; pp 56–100. <https://doi.org/10.1002/3527603905.ch6>.
- (11) Jeong, H.-G.; Lim, B.; Khim, D.; Han, M.; Lee, J.; Kim, J.; Yun, J.-M.; Cho, K.; Park, J.-W.; Kim, D.-Y. A Novel Thermally Reversible Soluble-Insoluble Conjugated Polymer with Semi-Fluorinated Alkyl Chains: Enhanced Transistor Performance by Fluorophobic Self-Organization and Orthogonal Hydrophobic Patterning. *Adv. Mater.* **2013**, *25* (44), 6416–6422. <https://doi.org/10.1002/adma.201301337>.
- (12) Lee, J.-K.; Fong, H. H.; Zakhidov, A. A.; McCluskey, G. E.; Taylor, P. G.; Santiago-Berrios, M.; Abruña, H. D.; Holmes, A. B.; Malliaras, G. G.; Ober, C. K. Semiperfluoroalkyl Polyfluorenes for Orthogonal Processing in Fluorous Solvents. *Macromolecules* **2010**, *43* (3), 1195–1198. <https://doi.org/10.1021/ma902179s>.
- (13) Lim, J.; Swager, T. M. Fluorous Biphasic Synthesis of a Poly(p-Phenyleneethynylene) and Its Fluorescent Aqueous Fluorous-Phase Emulsion. *Angew. Chemie - Int. Ed.* **2010**, *49* (41), 7486–7488. <https://doi.org/10.1002/anie.201003111>.
- (14) Takeda, Y.; Andrew, T. L.; Lobez, J. M.; Mork, A. J.; Swager, T. M. An Air-Stable Low-Bandgap n-Type Organic Polymer Semiconductor Exhibiting Selective Solubility in

- Perfluorinated Solvents. *Angew. Chemie Int. Ed.* **2012**, *51* (36), 9042–9046. <https://doi.org/10.1002/anie.201204066>.
- (15) Sletten, E. M.; Swager, T. M. Fluorofluorophores: Fluorescent Fluorous Chemical Tools Spanning the Visible Spectrum. *J. Am. Chem. Soc.* **2014**, *136* (39), 13574–13577. <https://doi.org/10.1021/ja507848f>.
- (16) Zarzar, L. D.; Sresht, V.; Sletten, E. M.; Kalow, J. A.; Blankschtein, D.; Swager, T. M. Dynamically Reconfigurable Complex Emulsions via Tunable Interfacial Tensions. *Nature* **2015**, *518* (7540), 520–524. <https://doi.org/10.1038/nature14168>.
- (17) Horváth, I. T.; Curran, D. P.; Gladysz, J. A. Fluorous Chemistry: Scope and Definition. In *Handbook of Fluorous Chemistry*; Wiley, 2004; pp 1–4. <https://doi.org/10.1002/3527603905.ch1>.
- (18) Vincent, J. M. Recent Advances of Fluorous Chemistry in Material Sciences. *Chem. Commun.* **2012**, *48* (93), 11382–11391. <https://doi.org/10.1039/c2cc34750d>.
- (19) Anton, D. Surface-Fluorinated Coatings. *Adv. Mater.* **1998**, *10* (15), 1197–1205. [https://doi.org/10.1002/\(SICI\)1521-4095\(199810\)10:15<1197::AID-ADMA1197>3.0.CO;2-F](https://doi.org/10.1002/(SICI)1521-4095(199810)10:15<1197::AID-ADMA1197>3.0.CO;2-F).
- (20) Chikamatsu, M.; Itakura, A.; Yoshida, Y.; Azumi, R.; Yase, K. High-Performance n-Type Organic Thin-Film Transistors Based on Solution-Processable Perfluoroalkyl-Substituted C<sub>60</sub> Derivatives. *Chem. Mater.* **2008**, *20* (24), 7365–7367. <https://doi.org/10.1021/cm802577u>.
- (21) Schmidt, R.; Oh, J. H.; Sun, Y.-S.; Deppisch, M.; Krause, A.-M.; Radacki, K.; Braunschweig, H.; Könemann, M.; Erk, P.; Bao, Z.; Würthner, F. High-Performance Air-Stable n-Channel Organic Thin Film Transistors Based on Halogenated Perylene Bisimide Semiconductors. *J. Am. Chem. Soc.* **2009**, *131* (17), 6215–6228. <https://doi.org/10.1021/ja901077a>.
- (22) Zhang, T.; Zhang, Q.; Tian, J. H.; Xing, J. F.; Guo, W.; Liang, X. J. Perfluorocarbon-Based Nanomedicine: Emerging Strategy for Diagnosis and Treatment of Diseases. *MRS Commun.* **2018**, *8* (2), 303–313. <https://doi.org/10.1557/mrc.2018.49>.
- (23) Rapoport, N. Phase-Shift, Stimuli-Responsive Perfluorocarbon Nanodroplets for Drug Delivery to Cancer. *Wiley Interdiscip. Rev. Nanomedicine Nanobiotechnology* **2012**, *4* (5), 492–510. <https://doi.org/10.1002/wnan.1176>.
- (24) El Bakkari, M.; Fronton, B.; Luguya, R.; Vincent, J. M. Reversible Fluorous Phase-Switching of Pyridyl-Tagged Porphyrins: Application to the Sensing of Histamine in Water. *J. Fluor. Chem.* **2006**, *127* (4-5 SPEC. ISS.), 558–564. <https://doi.org/10.1016/j.jfluchem.2005.11.019>.
- (25) Wang, C.; Wu, E.; Wu, X.; Xu, X.; Zhang, G.; Pu, L. Enantioselective Fluorescent Recognition in the Fluorous Phase: Enhanced Reactivity and Expanded Chiral Recognition. *J. Am. Chem. Soc.* **2015**, *137* (11), 3747–3750. <https://doi.org/10.1021/ja512569m>.
- (26) Shi, D.; Wang, X.; Yu, S.; Zhao, F.; Wang, Y.; Tian, J.; Hu, L.; Yu, X.; Pu, L. Fluorescent Recognition of 1,3-Diaminopropane in the Fluorous Phase - Greatly Enhanced Sensitivity and Selectivity. *European J. Org. Chem.* **2018**, *2018* (8), 1053–1059. <https://doi.org/10.1002/ejoc.201701703>.
- (27) Kim, S. H. Preface. In *Functional Dyes*; Kim, S.-H., Ed.; Elsevier Science: Amsterdam, 2006; pp v–vi. <https://doi.org/https://doi.org/10.1016/B978-044452176-7/50000-0>.
- (28) Feng, J.; Jiang, W.; Wang, Z. Synthesis and Application of Rylene Imide Dyes as Organic Semiconducting Materials. *Chem. - An Asian J.* **2018**, *13* (1), 20–30.

- <https://doi.org/10.1002/asia.201701424>.
- (29) Würthner, F.; Saha-Möller, C. R.; Fimmel, B.; Ogi, S.; Leowanawat, P.; Schmidt, D. Perylene Bisimide Dye Assemblies as Archetype Functional Supramolecular Materials. *Chem. Rev.* **2016**, *116* (3), 962–1052. <https://doi.org/10.1021/acs.chemrev.5b00188>.
- (30) Chen, L.; Li, C.; Müllen, K. Beyond Perylene Diimides: Synthesis, Assembly and Function of Higher Rylene Chromophores. *J. Mater. Chem. C* **2014**, *2* (11), 1938–1956. <https://doi.org/10.1039/C3TC32315C>.
- (31) Würthner, F.; Osswald, P.; Schmidt, R.; Kaiser, T. E.; Mansikkamaki, H.; Konemann, M. Synthesis and Optical and Electrochemical Properties of Core-Fluorinated Perylene Bisimides. *Org. Lett.* **2006**, *8* (17), 3765–3768. <https://doi.org/10.1021/ol0613416>.
- (32) Li, Y.; Tan, L.; Wang, Z.; Qian, H.; Shi, Y.; Hu, W. Air-Stable n-Type Semiconductor: Core-Perfluoroalkylated Perylene Bisimides. *Org. Lett.* **2008**, *10* (4), 529–532. <https://doi.org/10.1021/ol703046w>.
- (33) Ren, H.; Li, J.; Wang, R.; Wang, Q.; Liu, D. Synthesis and Characterization of Novel Perylenediimide-Cored Dendrimer with Fluorinated Shell. *Synth. Commun.* **2010**, *40* (5), 759–765. <https://doi.org/10.1080/00397910903013754>.
- (34) De Luca, G.; Liscio, A.; Melucci, M.; Schnitzler, T.; Pisula, W.; Clark, C. G.; Scolaro, L. M.; Palermo, V.; Müllen, K.; Samori, P. Phase Separation and Affinity between a Fluorinated Perylene Diimide Dye and an Alkyl-Substituted Hexa-Peri-Hexabenzocoronene. *J. Mater. Chem.* **2010**, *20* (1), 71–82. <https://doi.org/10.1039/b915484a>.
- (35) Partridge, B. E.; Leowanawat, P.; Aqad, E.; Imam, M. R.; Sun, H. J.; Peterca, M.; Heiney, P. A.; Graf, R.; Spiess, H. W.; Zeng, X.; Ungar, G.; Percec, V. Increasing 3D Supramolecular Order by Decreasing Molecular Order. A Comparative Study of Helical Assemblies of Dendronized Nonchlorinated and Tetrachlorinated Perylene Bisimides. *J. Am. Chem. Soc.* **2015**, *137* (15), 5210–5224. <https://doi.org/10.1021/jacs.5b02147>.
- (36) Yoshinaga, K.; Swager, T. M. Fluorofluorescent Perylene Bisimides. *Synlett* **2018**, *29* (19), 2509–2514. <https://doi.org/10.1055/s-0037-1610224>.
- (37) Partridge, B. E.; Leowanawat, P.; Aqad, E.; Imam, M. R.; Sun, H. J.; Peterca, M.; Heiney, P. A.; Graf, R.; Spiess, H. W.; Zeng, X.; Ungar, G.; Percec, V. Increasing 3D Supramolecular Order by Decreasing Molecular Order. A Comparative Study of Helical Assemblies of Dendronized Nonchlorinated and Tetrachlorinated Perylene Bisimides. *J. Am. Chem. Soc.* **2015**, *137* (15), 5210–5224. <https://doi.org/10.1021/jacs.5b02147>.
- (38) Qian, H.; Liu, C.; Wang, Z.; Zhu, D. S-Heterocyclic Annelated Perylene Bisimide: Synthesis and Co-Crystal with Pyrene. *Chem. Commun.* **2006**, *75* (44), 4587–4589. <https://doi.org/10.1039/b610765f>.
- (39) Curran, D. P. Fluorous Reverse Phase Silica Gel. A New Tool for Preparative Separations in Synthetic Organic and Organofluorine Chemistry. *Synlett* **2001**, No. 9, 1488–1496. <https://doi.org/10.1055/s-2001-16800>.
- (40) Gutierrez, G. D. Luminescent Organic Materials and Their Application in Solar Technologies, Massachusetts Institute of Technology, 2016.
- (41) van Shui-Pong, S.; Hammond, G. S. Amine Quenching of Aromatic Fluorescence and Fluorescent Exciplexes. *J. Am. Chem. Soc.* **1978**, *100* (12), 3895–3902. <https://doi.org/10.1021/ja00480a039>.
- (42) Che, Y.; Yang, X.; Loser, S.; Zang, L. Expedient Vapor Probing of Organic Amines Using Fluorescent Nanofibers Fabricated from an N-Type Organic Semiconductor. *Nano Lett.*

- 2008, 8 (8), 2219–2223. <https://doi.org/10.1021/nl080761g>.
- (43) Che, Y.; Zang, L. Enhanced Fluorescence Sensing of Amine Vapor Based on Ultrathin Nanofibers. *Chem. Commun.* **2009**, No. 34, 5106–5108. <https://doi.org/10.1039/b913138h>.
- (44) Liu, Y.; Wang, K. R.; Cuo, D. S.; Jiang, B. P. Supramolecular Assembly of Perylene Bisimide with  $\beta$ -Cyclodextrin Grafts as a Solid-State Fluorescence Sensor for Vapor Detection. *Adv. Funct. Mater.* **2009**, 19 (14), 2230–2235. <https://doi.org/10.1002/adfm.200900221>.
- (45) Peng, H.; Ding, L.; Liu, T.; Chen, X.; Li, L.; Yin, S.; Fang, Y. An Ultrasensitive Fluorescent Sensing Nanofilm for Organic Amines Based on Cholesterol-Modified Perylene Bisimide. *Chem. - An Asian J.* **2012**, 7 (7), 1576–1582. <https://doi.org/10.1002/asia.201100958>.
- (46) Sriramulu, D.; Valiyaveetil, S. Perylene Derivatives as a Fluorescent Probe for Sensing of Amines in Solution. *Dye. Pigment.* **2016**, 134, 306–314. <https://doi.org/10.1016/J.DYEPIG.2016.07.028>.
- (47) Herrmann, W. A.; Brossmer, C.; Reisinger, C.; Riermeier, T. H.; Öfele, K.; Beller, M. Palladacycles: Efficient New Catalysts for the Heck Vinylation of Aryl Halides. *Chem. - A Eur. J.* **1997**, 3 (8), 1357–1364. <https://doi.org/10.1002/chem.19970030823>.
- (48) Böhm, V. P. W.; Herrmann, W. A. Mechanism of the Heck Reaction Using a Phosphapalladacycle as the Catalyst: Classical versus Palladium(IV) Intermediates. *Chem. Eur. J.* **2001**, 7 (19), 4191–4197. [https://doi.org/10.1002/1521-3765\(20011001\)7:19<4191::AID-CHEM4191>3.0.CO;2-1](https://doi.org/10.1002/1521-3765(20011001)7:19<4191::AID-CHEM4191>3.0.CO;2-1).
- (49) Chen, W.; Xu, L.; Hu, Y.; Banet Osuna, A. M.; Xiao, J. New Approaches to Fluorinated Ligands and Their Application in Catalysis. *Tetrahedron* **2002**, 58 (20), 3889–3899. [https://doi.org/10.1016/S0040-4020\(02\)00213-2](https://doi.org/10.1016/S0040-4020(02)00213-2).
- (50) Chow, A. L.-F.; So, M.-H.; Lu, W.; Zhu, N.; Che, C.-M. Synthesis, Photophysical Properties, and Molecular Aggregation of Gold(I) Complexes Containing Carbon-Donor Ligands. *Chem. - An Asian J.* **2011**, 6 (2), 544–553. <https://doi.org/10.1002/asia.201000499>.
- (51) Würthner, F.; Thalacker, C.; Diele, S.; Tschierske, C. Fluorescent J-Type Aggregates and Thermotropic Columnar Mesophases of Perylene Bisimide Dyes. *Chem. - A Eur. J.* **2001**, 7 (10), 2245–2253. [https://doi.org/10.1002/1521-3765\(20010518\)7:10<2245::AID-CHEM2245>3.0.CO;2-W](https://doi.org/10.1002/1521-3765(20010518)7:10<2245::AID-CHEM2245>3.0.CO;2-W).
- (52) Kaiser, T. E.; Wang, H.; Stepanenko, V.; Würthner, F. Supramolecular Construction of Fluorescent J-Aggregates Based on Hydrogen-Bonded Perylene Dyes. *Angew. Chemie - Int. Ed.* **2007**, 46 (29), 5541–5544. <https://doi.org/10.1002/anie.200701139>.
- (53) Würthner, F.; Kaiser, T. E.; Saha-Möller, C. R. J-Aggregates: From Serendipitous Discovery to Supramolecular Engineering of Functional Dye Materials. *Angew. Chemie - Int. Ed.* **2011**, 50 (15), 3376–3410. <https://doi.org/10.1002/anie.201002307>.
- (54) Cao, W.; Sletten, E. M. Fluorescent Cyanine Dye J-Aggregates in the Fluorous Phase. *J. Am. Chem. Soc.* **2018**, 140 (8), 2727–2730. <https://doi.org/10.1021/jacs.7b11925>.
- (55) Company, F. M. Luminescent Greenhouse Collector for Solar Radiation W. H. Weber and John Lambe We Describe in This Letter a Planar Solar Collector Utilizing a Luminescent Medium to Absorb Radiation and Total Internal Reflection to Collect It. The Medium Strongly Absorbs. **1976**, 15 (10), 3–4.
- (56) Debije, M. G.; Verbunt, P. P. C. Thirty Years of Luminescent Solar Concentrator Research: Solar Energy for the Built Environment. *Adv. Energy Mater.* **2012**, 2 (1), 12–35. <https://doi.org/10.1002/aenm.201100554>.
- (57) Meinardi, F.; Ehrenberg, S.; Dharmo, L.; Carulli, F.; Mauri, M.; Bruni, F.; Simonutti, R.;

- Kortshagen, U.; Brovelli, S. Highly Efficient Luminescent Solar Concentrators Based on Earth-Abundant Indirect-Bandgap Silicon Quantum Dots. *Nat. Photonics* **2017**, *11* (3), 177–185. <https://doi.org/10.1038/nphoton.2017.5>.
- (58) Coropceanu, I.; Bawendi, M. G. Core/Shell Quantum Dot Based Luminescent Solar Concentrators with Reduced Reabsorption and Enhanced Efficiency. *Nano Lett.* **2014**, *14* (7), 4097–4101. <https://doi.org/10.1021/nl501627e>.
- (59) Zhao, Y.; Meek, G. A.; Levine, B. G.; Lunt, R. R. Near-Infrared Harvesting Transparent Luminescent Solar Concentrators. *Adv. Opt. Mater.* **2014**, *2* (7), 606–611. <https://doi.org/10.1002/adom.201400103>.
- (60) Rondão, R.; Frias, A. R.; Correia, S. F. H.; Fu, L.; de Zea Bermudez, V.; André, P. S.; Ferreira, R. A. S.; Carlos, L. D. High-Performance Near-Infrared Luminescent Solar Concentrators. *ACS Appl. Mater. Interfaces* **2017**, *9* (14), 12540–12546. <https://doi.org/10.1021/acsami.7b02700>.
- (61) Banal, J. L.; Zhang, B.; Jones, D. J.; Ghiggino, K. P.; Wong, W. W. H. Emissive Molecular Aggregates and Energy Migration in Luminescent Solar Concentrators. *Acc. Chem. Res.* **2017**, *50* (1), 49–57. <https://doi.org/10.1021/acs.accounts.6b00432>.
- (62) Zhang, B.; Banal, J. L.; Jones, D. J.; Tang, B. Z.; Ghiggino, K. P.; Wong, W. W. H. Aggregation-Induced Emission-Mediated Spectral Downconversion in Luminescent Solar Concentrators. *Mater. Chem. Front.* **2018**, *2* (3), 615–619. <https://doi.org/10.1039/c7qm00598a>.
- (63) Gutierrez, G. D.; Coropceanu, I.; Bawendi, M. G.; Swager, T. M. A Low Reabsorbing Luminescent Solar Concentrator Employing  $\pi$ -Conjugated Polymers. *Adv. Mater.* **2016**, *28* (3), 497–501. <https://doi.org/10.1002/adma.201504358>.
- (64) Müller, K.; Faeh, C.; Diederich, F. Fluorine in Pharmaceuticals: Looking Beyond Intuition. *Science* (80-. ). **2007**, *317* (5846), 1881 LP – 1886. <https://doi.org/10.1126/science.1131943>.
- (65) Rapoport, N. Drug-Loaded Perfluorocarbon Nanodroplets for Ultrasound-Mediated Drug Delivery. In *Therapeutic Ultrasound*; Escoffre, J.-M., Bouakaz, A., Eds.; Springer International Publishing: Cham, 2016; pp 221–241. [https://doi.org/10.1007/978-3-319-22536-4\\_13](https://doi.org/10.1007/978-3-319-22536-4_13).
- (66) Ragni, R.; Punzi, A.; Babudri, F.; Farinola, G. M. Organic and Organometallic Fluorinated Materials for Electronics and Optoelectronics: A Survey on Recent Research. *European J. Org. Chem.* **2018**, *2018* (27–28), 3500–3519. <https://doi.org/10.1002/ejoc.201800657>.
- (67) Gladysz, J. A.; Emnet, C. Fluorous Solvents and Related Media. *Handb. Fluorous Chem.* **2005**, 11–23. <https://doi.org/10.1002/3527603905.ch3>.
- (68) Kobayashi, N.; Fukuda, T. Chapter 1 - Recent Progress in Phthalocyanine Chemistry: Synthesis and Characterization. In *Functional Dyes*; Kim, S.-H., Ed.; Elsevier Science: Amsterdam, 2006; pp 1–45. <https://doi.org/https://doi.org/10.1016/B978-044452176-7/50002-4>.
- (69) Miller, M. A.; Sletten, E. M. A General Approach to Biocompatible Branched Fluorous Tags for Increased Solubility in Perfluorocarbon Solvents. *Org. Lett.* **2018**, *20* (21), 6850–6854. <https://doi.org/10.1021/acs.orglett.8b02976>.
- (70) Melville, O. A.; Lessard, B. H.; Bender, T. P. Phthalocyanine-Based Organic Thin-Film Transistors: A Review of Recent Advances. *ACS Appl. Mater. Interfaces* **2015**, *7* (24), 13105–13118. <https://doi.org/10.1021/acsami.5b01718>.
- (71) Baeg, K.-J.; Binda, M.; Natali, D.; Caironi, M.; Noh, Y.-Y. Organic Light Detectors:

- Photodiodes and Phototransistors. *Adv. Mater.* **2013**, *25* (31), 4267–4295. <https://doi.org/10.1002/adma.201204979>.
- (72) de la Torre, G.; Bottari, G.; Torres, T. Phthalocyanines and Subphthalocyanines: Perfect Partners for Fullerenes and Carbon Nanotubes in Molecular Photovoltaics. *Adv. Energy Mater.* **2017**, *7* (10), 1601700. <https://doi.org/10.1002/aenm.201601700>.
- (73) Oluwole, D. O.; Yagodin, A. V.; Mkhize, N. C.; Sekhosana, K. E.; Martynov, A. G.; Gorbunova, Y. G.; Tsivadze, A. Y.; Nyokong, T. First Example of Nonlinear Optical Materials Based on Nanoconjugates of Sandwich Phthalocyanines with Quantum Dots. *Chem. Eur. J.* **2017**, *23* (12), 2820–2830. <https://doi.org/10.1002/chem.201604401>.
- (74) Lo, P.-C.; Rodríguez-Morgade, M. S.; Pandey, R. K.; Ng, D. K. P.; Torres, T.; Dumoulin, F. The Unique Features and Promises of Phthalocyanines as Advanced Photosensitisers for Photodynamic Therapy of Cancer. *Chem. Soc. Rev.* **2020**, *49* (4), 1041–1056. <https://doi.org/10.1039/C9CS00129H>.
- (75) Gürol, I.; Gümüş, G.; Musluoğlu, E.; Arslan, Y.; Ahsen, V. Synthesis and Characterization of O- and S-Bridged Perfluoroalkylated Metal-Free and Zinc Phthalocyanines. *J. Porphyr. Phthalocyanines* **2013**, *17*, 555–563. <https://doi.org/10.1142/S1088424613500491>.
- (76) Mori, S.; Shibata, N. Synthesis and Application of Trifluoroethoxy-Substituted Phthalocyanines and Subphthalocyanines. *Beilstein J. Org. Chem.* **2017**, *13*, 2273–2296. <https://doi.org/10.3762/bjoc.13.224>.
- (77) Yoshinaga, K.; Delage-Laurin, L.; Swager, T. M. Fluorous Phthalocyanines and Subphthalocyanines. *J. Porphyr. Phthalocyanines* **2020**, *24* (08), 1074–1082. <https://doi.org/10.1142/S1088424620500182>.
- (78) Bilgiçli, A. T.; Günsel, A.; Kandaz, M.; Özkaya, A. R. Highly Selective Thioalcohol Modified Phthalocyanine Sensors for Ag(i) and Pd(ii) Based on Target Induced J- and H-Type Aggregations: Synthesis, Electrochemistry and Peripheral Metal Ion Binding Studies. *Dalt. Trans.* **2012**, *41* (23), 7047–7056. <https://doi.org/10.1039/c2dt30244f>.
- (79) Bayda, M.; Dumoulin, F.; Hug, G. L.; Koput, J.; Gorniak, R.; Wojcik, A. Fluorescent H-Aggregates of an Asymmetrically Substituted Mono-Amino Zn(II) Phthalocyanine. *Dalt. Trans.* **2017**, *46* (6), 1914–1926. <https://doi.org/10.1039/c6dt02651f>.
- (80) Eder, G. M.; Walker, B. R.; McGrier, P. L. Subphthalocyanine-Based Porous Organic Polymers. *RSC Adv.* **2017**, *7* (47), 29271–29274. <https://doi.org/10.1039/C7RA05544G>.
- (81) Adachi, K.; Chayama, K.; Watarai, H. Aggregation of Thioether-Substituted Subphthalocyanines with Palladium(II) at the Toluene–Water Interface. *Soft Matter* **2005**, *1* (4), 292–302. <https://doi.org/10.1039/B508648E>.
- (82) Faraday, M. I. Experimental Researches in Electricity.—Nineteenth Series. *Philos. Trans. R. Soc. London* **1846**, *136*, 1–20. <https://doi.org/10.1098/rstl.1846.0001>.
- (83) Wang, P.; Jeon, I.; Lin, Z.; Peeks, M. D.; Savagatrup, S.; Kooi, S. E.; Van Voorhis, T.; Swager, T. M. Insights into Magneto-Optics of Helical Conjugated Polymers. *J. Am. Chem. Soc.* **2018**, *140* (20), 6501–6508. <https://doi.org/10.1021/jacs.8b03777>.
- (84) Gangopadhyay, P.; Koeckelberghs, G.; Persoons, A. Magneto-Optic Properties of Regioregular Polyalkylthiophenes. *Chem. Mater.* **2011**, *23* (3), 516–521. <https://doi.org/10.1021/cm102215a>.
- (85) Vandendriessche, S.; Van Cleuvenbergen, S.; Willot, P.; Henrich, G.; Srebro, M.; Valev, V. K.; Koeckelberghs, G.; Clays, K.; Autschbach, J.; Verbiest, T. Giant Faraday Rotation in Mesogenic Organic Molecules. *Chem. Mater.* **2013**, *25* (7), 1139–1143. <https://doi.org/10.1021/cm4004118>.



- (86) Vleugels, R.; Steverlynck, J.; Brulot, W.; Koeckelberghs, G.; Verbiest, T. Faraday Rotation in Discotic Liquid Crystals by Long-Range Electron Movement. *J. Phys. Chem. C* **2019**, *123* (14), 9382–9387. <https://doi.org/10.1021/acs.jpcc.9b00607>.
- (87) Stephens, P. J.; Suëtaak, W.; Schatz, P. N. Magneto-Optical Rotatory Dispersion of Porphyrins and Phthalocyanines. *J. Chem. Phys.* **1966**, *44* (12), 4592–4602. <https://doi.org/10.1063/1.1726677>.
- (88) Shashoua, V. E. Magneto-Optical Rotation Spectra of Porphyrins and Phthalocyanines. *J. Am. Chem. Soc.* **1965**, *87* (18), 4044–4048. <https://doi.org/10.1021/ja01096a003>.
- (89) Wang, P.; Lin, S.; Lin, Z.; D. Peeks, M.; Van Voorhis, T.; M. Swager, T. A Semiconducting Conjugated Radical Polymer: Ambipolar Redox Activity and Faraday Effect. *J. Am. Chem. Soc.* **2018**, *140* (34), 10881–10889. <https://doi.org/10.1021/jacs.8b06193>.
- (90) Lim, C.-K.; Ju Cho, M.; Singh, A.; Li, Q.; Jin Kim, W.; Sub Jee, H.; L. Fillman, K.; H. Carpenter, S.; L. Neidig, M.; Baev, A.; T. Swihart, M.; N. Prasad, P. Manipulating Magneto-Optic Properties of a Chiral Polymer by Doping with Stable Organic Biradicals. *Nano Lett.* **2016**, *16* (9), 5451–5455. <https://doi.org/10.1021/acs.nanolett.6b01874>.
- (91) Buckingham, A. D.; Stephens, P. J. Magnetic Optical Activity. *Annu. Rev. Phys. Chem.* **1966**, *17* (1), 399–432. <https://doi.org/10.1146/annurev.pc.17.100166.002151>.
- (92) Swager, T. M.; Mirica, K. A. Introduction: Chemical Sensors. *Chem. Rev.* **2019**, *119* (1), 1–2. <https://doi.org/10.1021/acs.chemrev.8b00764>.
- (93) *Food Microbiology: Fundamentals and Frontiers, Third Edition*; Doyle, Beuchat, Eds.; American Society of Microbiology, 2007. <https://doi.org/10.1128/9781555815912>.
- (94) Bhunia, A. K. Biosensors and Bio-Based Methods for the Separation and Detection of Foodborne Pathogens. In *Advances in Food and Nutrition Research*; Academic Press Inc., 2008; Vol. 54, pp 1–44. [https://doi.org/10.1016/S1043-4526\(07\)00001-0](https://doi.org/10.1016/S1043-4526(07)00001-0).
- (95) McKillip, J. L.; Jaykus, L.-A.; Drake, M. Influence of Growth in a Food Medium on the Detection of Escherichia Coli O157:H7 by Polymerase Chain Reaction. *J. Food Prot.* **2002**, *65* (11), 1775–1779. <https://doi.org/10.4315/0362-028X-65.11.1775>.
- (96) Nakano, S.; Kobayashi, T.; Funabiki, K.; Matsumura, A.; Nagao, Y.; Yamada, T. PCR Detection of Bacillus and Staphylococcus in Various Foods. *J. Food Prot.* **2004**, *67* (6), 1271–1277. <https://doi.org/10.4315/0362-028X-67.6.1271>.
- (97) Notermans, S.; Wernars, K. Immunological Methods for Detection of Foodborne Pathogens and Their Toxins. *Int. J. Food Microbiol.* **1991**, *12* (1), 91–102. [https://doi.org/10.1016/0168-1605\(91\)90050-Y](https://doi.org/10.1016/0168-1605(91)90050-Y).
- (98) Zhang, Q.; Savagatrup, S.; Kaplonek, P.; Seeberger, P. H.; Swager, T. M. Janus Emulsions for the Detection of Bacteria. *ACS Cent. Sci.* **2017**, *3* (4), 309–313. <https://doi.org/10.1021/acscentsci.7b00021>.
- (99) Zhang, Q.; Zeininger, L.; Sung, K.-J. J.; Miller, E. A.; Yoshinaga, K.; Sikes, H. D.; Swager, T. M. Emulsion Agglutination Assay for the Detection of Protein-Protein Interactions: An Optical Sensor for Zika Virus. *ACS Sensors* **2019**, *4* (1), 180–184. <https://doi.org/10.1021/acssensors.8b01202>.
- (100) Zeininger, L.; Nagelberg, S.; Harvey, K. S.; Savagatrup, S.; Herbert, M. B.; Yoshinaga, K.; Capobianco, J. A.; Kollé, M.; Swager, T. M. Rapid Detection of Salmonella Enterica via Directional Emission from Carbohydrate-Functionalized Dynamic Double Emulsions. *ACS Cent. Sci.* **2019**, *5*, acscentsci.9b00059. <https://doi.org/10.1021/acscentsci.9b00059>.
- (101) Li, J.; Savagatrup, S.; Nelson, Z.; Yoshinaga, K.; Swager, T. M. Fluorescent Janus Emulsions for Biosensing of Listeria Monocytogenes. *Proc. Natl. Acad. Sci.* **2020**, *117* (22),

- 11923–11930. <https://doi.org/10.1073/pnas.2002623117>.
- (102) Li, J.; Concellón, A.; Yoshinaga, K.; Nelson, Z.; He, Q.; Swager, T. M. Janus Emulsion Biosensors for Anti-SARS-CoV-2 Spike Antibody. *ACS Cent. Sci.* **2021**, *7* (7), 1166–1175. <https://doi.org/10.1021/acscentsci.1c00173>.
- (103) Chevalier, A.; Renard, P.-Y.; Romieu, A. Straightforward Synthesis of Bioconjugatable Azo Dyes. Part 1: Black Hole Quencher-1 (BHQ-1) Scaffold. *Tetrahedron Lett.* **2014**, *55* (50), 6759–6763. <https://doi.org/10.1016/j.tetlet.2014.10.053>.
- (104) Chevalier, A.; Renard, P.-Y.; Romieu, A. Straightforward Synthesis of Bioconjugatable Azo Dyes. Part 2: Black Hole Quencher-2 (BHQ-2) and BlackBerry Quencher 650 (BBQ-650) Scaffolds. *Tetrahedron Lett.* **2014**, *55* (50), 6764–6768. <https://doi.org/10.1016/j.tetlet.2014.10.054>.
- (105) Claessens, C. G.; González-Rodríguez, D.; del Rey, B.; Torres, T.; Mark, G.; Schuchmann, H.-P.; von Sonntag, C.; MacDonald, J. G.; Nohr, R. S. Highly Efficient Synthesis of Chloro- and Phenoxy-Substituted Subphthalocyanines. *European J. Org. Chem.* **2003**, *2003* (14), 2547–2551. <https://doi.org/10.1002/ejoc.200300169>.
- (106) Meyer, F. Fluorinated Conjugated Polymers in Organic Bulk Heterojunction Photovoltaic Solar Cells. *Prog. Polym. Sci.* **2015**, *47*, 70–91. <https://doi.org/10.1016/j.progpolymsci.2015.04.007>.
- (107) Babudri, F.; Farinola, G. M.; Naso, F.; Ragni, R. Fluorinated Organic Materials for Electronic and Optoelectronic Applications: The Role of the Fluorine Atom. *Chem. Commun.* **2007**, No. 10, 1003–1022. <https://doi.org/10.1039/B611336B>.
- (108) Kim, Y.; Swager, T. M. Ultra-Photostable n-Type PPVs. *Chem. Commun.* **2005**, No. 3, 372–374. <https://doi.org/10.1039/b412948b>.
- (109) Wang, B.; Watt, S.; Hong, M.; Domercq, B.; Sun, R.; Kippelen, B.; Collard, D. M. Synthesis, Properties, and Tunable Supramolecular Architecture of Regioregular Poly(3-Alkylthiophene)s with Alternating Alkyl and Semifluoroalkyl Substituents. *Macromolecules* **2008**, *41* (14), 5156–5165. <https://doi.org/10.1021/ma702408h>.
- (110) Lee, M.-H.; Kang, M.; Jeong, H.-G.; Park, J.-J.; Hwang, K.; Kim, D.-Y. Effect of Semi-Fluorinated Alkyl Side Chains on Conjugated Polymers with Planar Backbone in Organic Field-Effect Transistors. *Macromol. Rapid Commun.* **2018**, *39* (23), 1800431. <https://doi.org/10.1002/marc.201800431>.
- (111) Pozzi, G.; Quici, S.; Fish, R. H. Perfluorocarbon Soluble Crown Ethers as Phase Transfer Catalysts. *Adv. Synth. Catal.* **2008**, *350* (14–15), 2425–2436. <https://doi.org/10.1002/adsc.200800393>.
- (112) Chen, W.; Xu, L.; Xiao, J. A General Method to Fluorous Ponytail-Substituted Aromatics. *Tetrahedron Lett.* **2001**, *42* (25), 4275–4278. [https://doi.org/10.1016/S0040-4039\(01\)00714-6](https://doi.org/10.1016/S0040-4039(01)00714-6).
- (113) Su, H. L.; Balogh, J.; Al-Hashimi, M.; Seapy, D. G.; Bazzi, H. S.; Gladysz, J. A. Convenient Protocols for Mizoroki-Heck Reactions of Aromatic Bromides and Polybromides with Fluorous Alkenes of the Formula H<sub>2</sub>CCH(CF<sub>2</sub>)<sub>n</sub>-1CF<sub>3</sub> (n = 8, 10). *Org. Biomol. Chem.* **2016**, *14* (42), 10058–10069. <https://doi.org/10.1039/c6ob01980c>.
- (114) Feng, J.; Cai, C. An Efficient Synthesis of Perfluoroalkenylated Aryl Compounds via Pincer-Pd Catalyzed Heck Couplings. *J. Fluor. Chem.* **2013**, *146*, 6–10. <https://doi.org/10.1016/j.jfluchem.2012.12.009>.
- (115) Darses, S.; Pucheault, M.; Genêt, J.-P. Efficient Access to Perfluoroalkylated Aryl Compounds by Heck Reaction. *European J. Org. Chem.* **2001**, *2001* (6), 1121–1128.

- [https://doi.org/10.1002/1099-0690\(200103\)2001:6<1121::AID-EJOC1121>3.0.CO;2-3](https://doi.org/10.1002/1099-0690(200103)2001:6<1121::AID-EJOC1121>3.0.CO;2-3).
- (116) Alameddine, B.; Savary, C.; Aebischer, O.; Jenny, T. Synthesis of Perfluoroalkylated Bulky Triarylamines. *Synthesis (Stuttg)*. **2007**, *2007* (2), 271–276. <https://doi.org/10.1055/s-2006-958953>.
- (117) Lee, D. S.; Cho, E. J. Fluoroalkenylation of Boronic Acids: Via an Oxidative Heck Reaction. *Org. Biomol. Chem.* **2019**, *17* (17), 4317–4325. <https://doi.org/10.1039/c9ob00332k>.
- (118) Wang, C.; Wu, X.; Pu, L. A Highly Fluorinated Chiral Aldehyde for Enantioselective Fluorescent Recognition in a Biphasic System. *Chem. - A Eur. J.* **2017**, *23* (45), 10749–10752. <https://doi.org/10.1002/chem.201702354>.
- (119) Prices listed on Synquest Labs, Inc. <http://www.synquestlabs.com/> (accessed Jun 1, 2021).
- (120) Yoshinaga, K.; Swager, T. M. Revisiting the Heck Reaction for Fluorous Materials Applications. *Synlett* **2021**, *Accepted*.
- (121) Geng, Y.; Tajima, K.; Hashimoto, K. Synthesis and Characterizations of Regioregular Poly(3-Alkylthiophene) with Alternating Dodecyl/1H,1H,2H,2H-Perfluorooctyl Side Chains. *Macromol. Rapid Commun.* **2011**, *32* (18), 1478–1483. <https://doi.org/10.1002/marc.201100275>.
- (122) Turner, D. J.; Anémian, R.; Mackie, P. R.; Cupertino, D. C.; Yeates, S. G.; Turner, M. L.; Spivey, A. C. Towards a General Solid Phase Approach for the Iterative Synthesis of Conjugated Oligomers Using a Germanium Based Linker - First Solid Phase Synthesis of an Oligo-(Triarylamine). *Org. Biomol. Chem.* **2007**, *5* (11), 1752–1763. <https://doi.org/10.1039/B703022C>.
- (123) Grand, C.; Zajackowski, W.; Deb, N.; Lo, C. K.; Hernandez, J. L.; Bucknall, D. G.; Müllen, K.; Pisula, W.; Reynolds, J. R. Morphology Control in Films of Isoindigo Polymers by Side-Chain and Molecular Weight Effects. *ACS Appl. Mater. Interfaces* **2017**, *9* (15), 13357–13368. <https://doi.org/10.1021/acsami.6b16502>.
- (124) Wang, Q.; Takita, R.; Kikuzaki, Y.; Ozawa, F. Palladium-Catalyzed Dehydrohalogenative Polycondensation of 2-Bromo-3-Hexylthiophene: An Efficient Approach to Head-to-Tail Poly(3-Hexylthiophene). *J. Am. Chem. Soc.* **2010**, *132* (33), 11420–11421. <https://doi.org/10.1021/ja105767z>.
- (125) Pankow, R. M.; Thompson, B. C. Approaches for Improving the Sustainability of Conjugated Polymer Synthesis Using Direct Arylation Polymerization (DArP). *Polym. Chem.* **2020**, *11* (3), 630–640. <https://doi.org/10.1039/C9PY01534E>.
- (126) Po, R.; Bianchi, G.; Carbonera, C.; Pellegrino, A. “All That Glisters Is Not Gold”: An Analysis of the Synthetic Complexity of Efficient Polymer Donors for Polymer Solar Cells. *Macromolecules* **2015**, *48* (3), 453–461. <https://doi.org/10.1021/ma501894w>.
- (127) Roncali, J. Synthetic Principles for Bandgap Control in Linear  $\pi$ -Conjugated Systems. *Chem. Rev.* **1997**, *97* (1), 173–206. <https://doi.org/10.1021/cr950257t>.
- (128) Huang, Y.; Wang, Y.; Sang, G.; Zhou, E.; Huo, L.; Liu, Y.; Li, Y. Polythiophene Derivative with the Simplest Conjugated-Side-Chain of Alkenyl: Synthesis and Applications in Polymer Solar Cells and Field-Effect Transistors. *J. Phys. Chem. B* **2008**, *112* (43), 13476–13482. <https://doi.org/10.1021/jp8055043>.
- (129) Lu, Y. C.; Gallant, B. M.; Kwabi, D. G.; Harding, J. R.; Mitchell, R. R.; Whittingham, M. S.; Shao-Horn, Y. Lithium-Oxygen Batteries: Bridging Mechanistic Understanding and Battery Performance. *Energy and Environmental Science*. The Royal Society of Chemistry March 20, 2013, pp 750–768. <https://doi.org/10.1039/c3ee23966g>.

- (130) Schmuck, R.; Wagner, R.; Hörpel, G.; Placke, T.; Winter, M. Performance and Cost of Materials for Lithium-Based Rechargeable Automotive Batteries. *Nat. Energy* **2018**. <https://doi.org/10.1038/s41560-018-0107-2>.
- (131) Liu, J.; Bao, Z.; Cui, Y.; Dufek, E. J.; Goodenough, J. B.; Khalifah, P.; Li, Q.; Yann Liaw, B.; Liu, P.; Manthiram, A.; Shirley Meng, Y.; Subramanian, V. R.; Toney, M. F.; Viswanathan, V. V.; Stanley Whittingham, M.; Xiao, J.; Xu, W.; Yang, J.; Yang, X.-Q.; Zhang, J.-G. Pathways for Practical High-Energy Long-Cycling Lithium Metal Batteries. *Nat. Energy* **4**. <https://doi.org/10.1038/s41560-019-0338-x>.
- (132) Beard, K. W. AN INTRODUCTION TO PRIMARY BATTERIES. In *Linden's Handbook of Batteries*; McGraw-Hill Education: New York, 2019.
- (133) Beard, K. W. GENERAL CHARACTERISTICS OF LITHIUM PRIMARY CELLS. In *Linden's Handbook of Batteries*; McGraw-Hill Education: New York, 2019.
- (134) Hills, A. J.; Hampson, N. A. The LiSOCl<sub>2</sub> Cell - a Review. *Journal of Power Sources*. Elsevier November 1, 1988, pp 253–271. [https://doi.org/10.1016/0378-7753\(88\)80102-2](https://doi.org/10.1016/0378-7753(88)80102-2).
- (135) Abraham, K. M. Chemical and Electrochemical Processes in Some Lithium–liquid Cathode Batteries. *J. Power Sources* **1991**, *34* (2), 81–101. [https://doi.org/10.1016/0378-7753\(91\)85028-U](https://doi.org/10.1016/0378-7753(91)85028-U).
- (136) Rangasamy, E.; Li, J.; Sahu, G.; Dudney, N.; Liang, C. Pushing the Theoretical Limit of Li-CF<sub>x</sub> Batteries: A Tale of Bifunctional Electrolyte. *J. Am. Chem. Soc.* **2014**, *136* (19), 6874–6877. <https://doi.org/10.1021/ja5026358>.
- (137) Zhang, Q.; Takeuchi, K. J.; Takeuchi, E. S.; Marschilok, A. C. Progress towards High-Power Li/CF<sub>x</sub> Batteries: Electrode Architectures Using Carbon Nanotubes with CF<sub>x</sub>. *Phys. Chem. Chem. Phys.* **2015**, *17* (35), 22504–22518. <https://doi.org/10.1039/C5CP03217B>.
- (138) Li, Y.; Khurram, A.; Gallant, B. M. A High-Capacity Lithium–Gas Battery Based on Sulfur Fluoride Conversion. *J. Phys. Chem. C* **2018**, *122* (13), 7128–7138. <https://doi.org/10.1021/acs.jpcc.8b00569>.
- (139) Gao, H.; Li, Y.; Guo, R.; Gallant, B. M. Controlling Fluoride-Forming Reactions for Improved Rate Capability in Lithium-Perfluorinated Gas Conversion Batteries. *Adv. Energy Mater.* **2019**, *9* (21), 1900393. <https://doi.org/10.1002/aenm.201900393>.
- (140) He, M.; Li, Y.; Guo, R.; Gallant, B. M. Electrochemical Conversion of Nitrogen Trifluoride as a Gas-to-Solid Cathode in Li Batteries. *J. Phys. Chem. Lett.* **2018**, *9* (16), 4700–4706. <https://doi.org/10.1021/acs.jpcclett.8b01897>.
- (141) Gao, H.; Gallant, B. M. Advances in the Chemistry and Applications of Alkali-Metal–Gas Batteries. *Nat. Rev. Chem.* **2020**, *4* (11), 566–583. <https://doi.org/10.1038/s41570-020-00224-7>.
- (142) Chen, G. J.; Tamborski, C. Polyfluoroalkylation of Bromoaromatic Compounds via Perfluoroalkylcopper Intermediates. *J. Fluor. Chem.* **1989**, *43* (2), 207–228. [https://doi.org/10.1016/S0022-1139\(00\)82940-1](https://doi.org/10.1016/S0022-1139(00)82940-1).
- (143) Probst, Joseph; Takeuchi, Esther S.; Smesko, S. A. ENHANCED CAPACITY LI/CF<sub>x</sub> ELECTROCHEMICAL CELL. US6451483, 2002.
- (144) Muffoletto, Barry C.; Kuvik, R. J. INTERNAL ELECTRODE AND ASSEMBLY METHOD FOR ELECTROCHEMICAL CELLS. 5250373, 1993.
- (145) Liu, T.; Vivek, J. P.; Zhao, E. W.; Lei, J.; Garcia-Araez, N.; Grey, C. P. Current Challenges and Routes Forward for Nonaqueous Lithium–Air Batteries. *Chem. Rev.* **2020**, *120* (14), 6558–6625. <https://doi.org/10.1021/acs.chemrev.9b00545>.

- (146) Kwak, W.-J.; Rosy, Sharon, D.; Xia, C.; Kim, H.; R. Johnson, L.; G. Bruce, P.; F. Nazar, L.; Sun, Y.-K.; A. Frimer, A.; Noked, M.; A. Freunberger, S.; Aurbach, D. Lithium–Oxygen Batteries and Related Systems: Potential, Status, and Future. *Chem. Rev.* **2020**, *120* (14), 6626–6683. <https://doi.org/10.1021/acs.chemrev.9b00609>.

# Curriculum Vitae

## Kosuke Yoshinaga

### Education

---

**Massachusetts Institute of Technology, Cambridge, MA** September 2016–Present  
Candidate for Doctor of Philosophy in Organic Chemistry; Department of Chemistry

**The University of Tokyo, Tokyo, JAPAN** April 2012–March 2016  
Bachelor of Engineering; Department of Chemistry and Biotechnology

### Research Experience

---

**Graduate Research Assistant** November 2016–Present  
Department of Chemistry, Massachusetts Institute of Technology, Cambridge, MA, USA  
Thesis Advisor: Prof. Timothy M. Swager

- Synthesize and characterize photophysical properties of “fluorofluorescent” dyes, designed to be fluorescent and soluble in fluoruous solvents. Contribute research expertise in dyes and organic synthesis in cross-departmental projects to enhance performances of lithium primary batteries and optical biosensors.
- Synthesize conjugated materials such as polyacetylenes, polythiophenes, and donor-acceptor polymers with high fluorine content for Faraday rotating materials, OFETs, and OPVs. Experiments studying the physical properties of these materials is ongoing.
- Led subgroup as captain for 2 years; restructured subgroup meetings to facilitate productive discussions; created a presentation archive for future member’s education purposes.

**Undergraduate Researcher** September 2014–June 2016  
Department of Chemistry and Biotechnology, The University of Tokyo, Tokyo, JAPAN  
Thesis Advisor: Prof. Takuzo Aida

- Synthesized metal-organic frameworks with a ligand containing a “benzyne” precursor and studied its post-synthetic modification. New structures were analyzed by X-ray diffraction.
- Rewarded early laboratory experience prior to 4<sup>th</sup> year, approved by faculty. My passion has led to initiate a departmental early laboratory experience program for motivated students.

### Teaching Experience

---

**Teaching Assistant** November 2016–Present  
Department of Chemistry, Massachusetts Institute of Technology, Cambridge, MA, USA  
Course: 5.43, Advanced Organic Chemistry (Fall 2016, Fall 2017)

## Publications

---

1. **Yoshinaga, K.**; Swager, T. M. Revisiting the Heck Reaction for Fluorous Materials Applications. *Synlett* **2021**, *Accepted*.
2. Ngo, Q. P.; He, M.; Concellón, A.; **Yoshinaga, K.**; Luo, S.-X.; Aljabri, N.; Swager, T. M. Reconfigurable Pickering Emulsions with Functionalized Carbon Nanotubes. *Langmuir* **2021**, *37*, 8204.
3. Li, J.; Concellón, A.; **Yoshinaga, K.**; Nelson, Z.; He, Q.; Swager, T. M. Janus Emulsion Biosensors for Anti-SARS-CoV-2 Spike Antibody. *ACS Cent. Sci.* **2021**, *7*, 1166.
4. Concellón, A.; Lu, R.-Q.; **Yoshinaga, K.**; Hsu, H.-F.; Swager, T. M. Electric-Field-Induced Chirality in Columnar Liquid Crystals. *J. Am. Chem. Soc.* **2021**, *143*, 9260.
5. Luo, S.-X. L.; Lin, C.-J.; Ku, K. H.; **Yoshinaga, K.**; Swager, T. M. Pentiptycene Polymer/Single-Walled Carbon Nanotube Complexes: Applications in Benzene, Toluene, and *o*-Xylene Detection. *ACS Nano* **2020**, *14*, 7297.
6. **Yoshinaga, K.**; Delage-Laurin, L.; Swager, T. M. Fluorous Phthalocyanines and Subphthalocyanines. *J. Porphy. Phthalocyanines* **2020**, *24*, 1074.
7. Ku, K. H.; Li, J.; **Yoshinaga, K.**; Swager, T. M. Dynamically Reconfigurable, Multifunctional Emulsions with Controllable Structure and Movement. *Adv. Mater.* **2019**, *31*, 1905569.
8. Zeininger, L.; Nagelberg, S.; Harvey, K. S.; Savagatrup, S.; Herbert, M. B.; **Yoshinaga, K.**; Capobianco, J. A.; Kolle, M.; Swager, T. M. Rapid Detection of Salmonella Enterica via Directional Emission from Carbohydrate-Functionalized Dynamic Double Emulsions. *ACS Cent. Sci.* **2019**, *5*, 789.
9. Li, J.; Savagatrup, S.; Nelson, Z.; **Yoshinaga, K.**; Swager, T. M. Fluorescent Janus Emulsions for Biosensing of *Listeria Monocytogenes*. *Proc. Natl. Acad. Sci.* **2020**, *117*, 11923.
10. Zhang, Q.; Zeininger, L.; Sung, K. J.; Miller, E. A.; **Yoshinaga, K.**; Sikes, H. D.; Swager, T. M. Emulsion Agglutination Assay for the Detection of Protein-Protein Interactions: An Optical Sensor for Zika Virus. *ACS Sensors* **2019**, *4*, 180.
11. **Yoshinaga, K.**; Swager, T. M. Fluorofluorescent Perylene Bisimides. *Synlett* **2018**, *29*, 2509.

## Patents

---

1. Swager, T. M.; Gallant, B.; **Yoshinaga, K.**; Gao, H.; Electrochemical Reduction of Halogenated Compounds. U.S. Patent Application Pending (Filed February 24, 2021).
2. Swager, T. M.; Li, J.; Savagatrup, S.; Nelson, Z.; **Yoshinaga, K.**; Zentner, C. Systems and Methods for Affecting Interactions of Electromagnetic Radiation with Janus Droplets for Sensitive Detection of Species. U.S. Patent Application No. 62/902,367 (Filed September 18, 2019).
3. Swager, T. M.; Johnson, H. S.; Zhang, Q.; Miller, E. A.; Sung, K.-J.; **Yoshinaga, K.** Systems Including Janus Droplets. U.S. Patent Applications No. 16/202,007 (Filed November 27, 2018).

## Presentations

---

1. Nelson, Z.; Han, J.; **Yoshinaga, K.**; Niroui, F.; Lang, J. H.; Bulovic, V.; Swager, T. M. Tuning Squitch Performance Through Molecular Design. 2019 E<sup>3</sup>S Annual Retreat, Berkeley, CA, USA, September 19–20, 2019, Poster Presentation.
2. **Yoshinaga, K.**; Swager, T. M. Synthesis and Applications of Fluorofluorescent Perylene Bisimides. 18<sup>th</sup> International Symposium on Novel Aromatics, Sapporo, Hokkaido, JAPAN, July 21–26, 2019, Poster Presentation.
3. **Yoshinaga, K.**; Swager, T. M. Synthesis and Applications of Fluorofluorescent Perylene Bisimides. 2019 MIT Chemistry Department Organic Retreat, Cambridge, MA, USA, June 10, 2019, Poster Presentation.
4. **Yoshinaga, K.**; Swager, T. M. Fluorofluorescent Perylene Bisimides: Synthesis, Properties, and Applications. MIT Materials Day, Cambridge, MA, USA, October 10, 2018, Poster Presentation.
5. **Yoshinaga, K.**; Gutierrez, G. D.; Achorn, O. B.; Swager, T. M. Fluorofluorescent Solar Concentrator: A Solution-Based Approach Towards Building-Integrated Photovoltaics. Meeting of the American Chemical Society, Boston, MA, USA, August 19–23, 2018, Poster Presentation.
6. **Yoshinaga, K.**; Sato, H.; Aida, T. Photochemically Reactive 'Benzyne' Metal-Organic Frameworks. International Supramolecular System Symposium 2015, Changchun, CHINA, September 6–9, 2015, Poster Presentation.

## Activities and Service

---

**Co-president, Chemistry Graduate Student Committee** July 2018–June 2020

- Led a student group of 10 people and strived for improving student quality of life.
- Hosted events ranging from 10–100 attendees to foster a sense of community within the department including orientations, social activities, and career developments.

**Career Panel Organizer** January 2020

- Invited professionals from the Greater Boston Area to speak with graduate students and postdoctoral fellows about careers possible with a doctoral degree in chemistry.
- Organized a panel session for International Students.

**Contributor for *Synfacts*** January 2017–December 2019

- Contributed 60 highlights on recent research publications on the synthesis of organic materials and unnatural products.

## Fellowship and Awards

---

- Funai Overseas Scholarship (February 2018–January 2020): Full Tuition and Insurance, Stipend \$2,500/month
- GSC Travel Grant (July 2019): Attended 18<sup>th</sup> International Symposium of Novel Aromatics.



## ACKNOWLEDGMENTS

First and foremost, my Ph.D. career could not have been any better without my advisor Professor Tim Swager. Thank you very much for your support not only in research, but also in mental health. You have not only been inspirational in research, but also led by example of what it means and what it takes to be a leader. You have mentioned choosing a Ph.D. advisor is like marrying someone. I am happy I have made the right choice choosing you as my advisor, and I am hoping for our relationship (marriage?) to continue. I would also like to thank Professor Jeremiah Johnson for serving as my thesis committee chairman and meeting with me to discuss my progress toward my Ph.D. throughout my graduate career. I am grateful to both him and Professor Bradley Olsen for taking the time to evaluate my progress toward the completion of my Ph.D. as well as to provide feedback on this thesis.

I was unbelievably fortunate to spend time and become friends with the most talented researchers at MIT and in the Swager group. I must admit I have learned more from Maggie He than from Tim about chemistry. I am thankful and sorry at the same time for taking so much of your time in answering my questions and brainstorming for research ideas. You played the biggest role in shaping the researcher I am today, and I was lucky to be assigned a desk next to you. I also want to thank Sibol Lin, Suchol Savagatrup, Vera Schroeder, and Constantin Voll for making my transition to the Swager group seamless. The best memories I have and the events I looked forward to in my first summer were the Wings Monday at Asgard and Burger Beer Tuesday at Champions. Special thanks to Greg Gutierrez for giving me special tips and advice to take over his project, even after his graduation.

This thesis could not have been written without the help of my wonderful colleagues, who have helped with the tedious peer review: a special thanks to Jessica Beard, Michelle Chen,

Richard Liu, Danny Wu, Leo Delage-Laurin, Jie Li, Alberto Concellón, Ru-Qiang Lu, and Haining Gao. I am also grateful to have learned so much from my wonderful group colleagues over the years: Lionel Moh, Tran Truong, Kathleen White, Wen Jie Ong, Byungjin Koo, Sarah Luppino, John Fennell, Intak Jeon, Frank He, Qifan Zhang, Zach Nelson, Cassie Zentner, Mason Wu, Joe Walish, Tomoyuki Ikai, Soichi Yokoyama, Bora Yoon, Cagatay Dengiz, Myles Herbert, Henry Sha, Yanchuan Zhao, Rong Zhu, Hongkun Lin, Che-Jen Lin, Yoonseob Kim, Yifan Li, Pan Wang, Seon-Jin Choi, Lukas Zeininger, Nathan Romero, Monika Stolar, Martin Peeks, Shohei Yumino, Cen Tang, Hanshen Xin, Kang Hee Ku. I would like to wish the best of luck to current group members Sam Etkind, Lennon Luo, Qilin He, Skye Ngo, Yifan Wu, Weize Yuan, Haosheng Feng, Kayla Storme, Ben McDonald, Máté Bezdek, Darryl Fong, Sheng Guo, Hari Vijayamohanan, Mingyu Liu.

In addition to the brilliant graduate students and postdocs, the Swager group is fortunate to have wonderful staff members to make the group a great place to work. Kathy Sweeney was the administrative assistant when I first joined the group and has greatly helped make my transition to the group smooth. Congratulations on your retirement! Rachael Fuller and Emily Wensberg has helped keeping the group organized and handled the overwhelming tasks that needed to be completed. Lastly, Brian Pretti has done a perfect job in keeping the lab in good shape and fulfilling even my smallest requests.

Transitioning to MIT from Japan was one of the biggest movements of my life, but the transition had been seamless thanks to those who also came to pursue their Ph.D. at MIT from Japan. Noriko Endo, Saki Ichikawa, Ryuji Takagi, and Qingyang “Seiyo” Wang were very kind and generous, and they taught me all I needed to know to be an MIT graduate student. I was

fortunate to have Akira Tanushi, Jeehyun Yang, and Qingbo “Seiha” Wang enroll in the same year, as we always supported each other throughout our Ph.D. journey.

Lastly, I would like to thank my family – my mother, father, and my brother Yosuke – for their support in making this Ph.D. possible. You were always interested in what I was working on and continued to check up on how I was doing. I was greatly encouraged to know you have my back and support me no matter what. And finally, to my fiancé Anna Yui, you deserve the most thanks of my Ph.D. career. You have been supportive of me no matter what our circumstances were. Though obtaining my Ph.D. at MIT has kept us far apart, I am looking forward to being together soon. And I hope we can support each other for the rest of our lives.